Clays and Clay Minerals, Vol. 62, No. 4, 243–252, 2014.

CRYSTAL CHEMISTRY AND SURFACE CONFIGURATIONS OF TWO IRON-BEARING TRIOCTAHEDRAL MICA-1*M* POLYTYPES

Chiara Elmi[1], Maria Franca Brigatti[1], Stephen Guggenheim[2,*], Luca Pasquali[3,4],
Monica Montecchi[3,4], and Stefano Nannarone[3,4]

[1] Dipartimento di Scienze Chimiche e Geologiche, Università di Modena e Reggio Emilia, Largo S. Eufemia 19, 41121 Modena, Italy
[2] Department of Earth and Environmental Sciences, University of Illinois at Chicago, 845 West Taylor Street, Chicago, Illinois, 60607-7059, USA
[3] Dipartimento di Ingegneria "Enzo Ferrari", Università di Modena e Reggio Emilia, Via Vignolese 905, 41125 Modena, Italy
[4] IOM INFM-CNR Area Science Park, Building MM, S.S. 14, Km 163.5, 34012, Basovizza (TS), Italy

Abstract—The crystal chemical features of the bulk and the uppermost (001) surface layers of freshly cleaved surfaces of two trioctahedral Fe-rich mica-1*M* (space group *C*2/*m*) polytypes, *i.e.* a tetra-ferriphlogopite from an alkaline-carbonatitic complex near Tapira, Belo Horizonte, Minas Gerais, Brazil, and an Fe^{2+}-bearing phlogopite containing less tetrahedral Fe^{3+} from the Kovdor carbonatite-bearing, alkaline-ultrabasic complex, Kola Peninsula, Russia, are explored here. Mineral-surface effects were investigated by X-ray Photoelectron Spectroscopy (XPS) and compared to the bulk structure derived from single-crystal X-ray diffraction data. Based on microprobe analysis and the X-ray study, the chemical formulae are $^{[XII]}(K_{0.99})^{[VI]}(Fe^{2+}_{0.08}Fe^{3+}_{0.15}Mg_{2.76}Ti_{0.01})^{[IV]}(Fe^{3+}_{0.82}Si_{3.18})O_{10.37}F_{0.24}(OH)_{1.39}$ and $^{[XII]}(K_{0.94}Na_{0.06})^{[VI]}(Fe^{2+}_{0.17}Fe^{3+}_{0.05}Mg_{2.75}Mn_{0.01}Ti_{0.05})^{[IV]}(Fe^{3+}_{0.16}Al_{0.84}Si_{3.00})O_{10.21}F_{0.35}(OH)_{1.44}$ for tetra-ferriphlogopite and Fe-bearing phlogopite, respectively. The tetrahedrally coordinated sites of the two minerals differ, where Fe-for-Si substitution is at 20.5% in tetra-ferriphlogopite and at 4% in Fe-bearing phlogopite.

The bulk study showed that Fe^{3+} substitution increases the tetrahedral sheet thickness and the mean tetrahedral edge lengths in tetra-ferriphlogopite compared to Fe-bearing phlogopite. The tetrahedral rotation angle (α) changes remarkably from tetra-ferriphlogopite ($\alpha = 10.5°$) to the Fe-bearing phlogopite ($\alpha = 8.5°$), thus indicating a significantly greater initial lateral sheet misfit (leading to a greater tetrahedral ring distortion) between the tetrahedral and the octahedral sheets in the tetra-ferriphlogopite compared to Fe-bearing phlogopite. The Fe^{3+} substitution for Si and the differences in lateral dimensions of the tetrahedral and octahedral sheets affect the tetrahedral flattening angle (τ), with $\tau = 109.9°$ for tetra-ferriphlogopite and $\tau = 110.7°$ for Fe-bearing phlogopite.

The binding energy (BE) of photoelectron peaks in XPS is dependent on the chemical state of atoms and on their local environment at the near surface. The Mg in both phlogopites is bonded to F, with the BE of Mg_{1s} increasing as coordinated oxygen atoms are substituted by fluorine. For Fe-rich phlogopite (BE = 1306.8 eV), the binding energy is greater than for tetra-ferriphlogopite (BE = 1305.9 eV), and this is consistent with the bulk composition having greater F-for-OH substitution in Fe-rich phlogopite ($F_{0.35}$ *vs.* tetra-ferriphlogopite, $F_{0.24}$ atoms per formula unit).

Key Words—Crystal Chemistry, Crystal Structure, Surface, Iron-bearing Trioctahedral Mica-1*M* Polytypes.

INTRODUCTION

Micas are common rock-forming minerals occurring in many geologic environments, where they can be used as powerful petrogenetic indicators (*e.g.* Brod *et al.*, 2001; Brigatti *et al.*, 2008; Reguir *et al.*, 2009; Laurora *et al.*, 2009). Bulk crystal chemistry and structure of micas, often by X-ray or neutron diffraction, are discussed extensively in the literature (*e.g.* Brigatti *et al.*, 1996a, 2001, 2008, 2011; Brigatti and Guggenheim, 2002; Fleet 2003; Guggenheim, 2011). However, the characterization of the crystal-chemical features of freshly cleaved surfaces and their physical properties are much less well defined (Bhattacharyya, 1993; Biino and Gröning, 1998a, 1998b; Biino *et al.*, 1999; and summaries in Guggenheim, 2011; Schoonheydt and Johnston, 2011). Commonly, a mineral surface differs from the bulk because of both composition (*e.g.* impurities) and structure (*i.e.* relaxation or reconstruction processes), probably following various interaction processes (*i.e.* oxidation, chemical substitutions, interactions with organic molecules, *etc.*) that are common in nature.

Mg-Fe trioctahedral micas form a solid-solution series, *i.e.* a structural and chemical series, extending from the phlogopite (Mg) to annite (Fe) end-members (Bailey, 1984). In the ideal phlogopite−annite join, Fe can be present only as Fe^{2+} although it often occurs as Fe^{3+} also. Depending on crystallization conditions, the

---

* E-mail address of corresponding author:
xtal@uic.edu

DOI: 10.1346/CCMN.2014.0620401

$Fe^{2+}/(Fe^{2+} + Fe^{3+})$ ratio can vary significantly, together with its distribution within the layer. Fe^{3+} can occupy both tetrahedral and octahedral positions, whereas Fe^{2+} is located at octahedral sites only (Lalonde *et al.*, 1991; Brigatti and Guggenheim, 2002; Brigatti *et al.*, 2011). Fe^{3+}-for-Si^{4+} tetrahedral substitution defines the phlogopite–tetra-ferriphlogopite and annite–tetra-ferriannite series (Brod *et al.*, 2001). For these micas, iron as Fe^{3+} and Fe^{2+} occupies octahedral sites also (Brigatti and Guggenheim, 2002).

The present study compares the crystal-structural and chemical data in the bulk and at the surface of two trioctahedral Fe-rich mica-1*M* polytypes which display important differences in $Fe^{3+}/(Fe^{2+}+Fe^{3+})$ ratio and anion composition: a tetra-ferriphlogopite from an alkaline-carbonatitic complex (Tapira, Belo Horizonte, Minas Gerals, Brazil) and a ferroan phlogopite from the Kovdor carbonatite-bearing alkaline-ultrabasic complex (Kola Peninsula, Russia).

The crystal chemistry and physical properties of Fe-bearing phlogopite from the Kovdor phlogopite deposit were discussed by Krasnova (2001) and Ferraris *et al.* (2001), whereas the crystal chemistry and structure of trioctahedral Fe^{3+}-rich micas from the Tapira carbonatite complex were discussed by Brigatti *et al.* (1996a, 1996b, 1999, 2001) and Cibin *et al.* (2005).

EXPERIMENTAL METHODS

Defining the chemical and structural relationships between the bulk and the surface of the two Fe-rich mica-1*M* polytypes required a multi-analytical approach involving electron microprobe analysis (EPMA), single crystal X-ray diffraction (SC-XRD), and X-ray photoelectron spectroscopy (XPS).

Chemical composition by electron microprobe analysis

The chemical compositions of both samples were determined on several crystal fragments using a Cameca SX 50 electron microprobe. The operating conditions were: accelerating voltage 20 kV, sample current 20 nA, and defocused beam diameter = 4 μm. The standards were: orthoclase (K), albite (Na), hematite (Fe), diopside (Si, Ca), $MnTiO_3$ (Mn, Ti), Al_2O_3 (Al), MgO (Mg), Cr_2O_3 (Cr), and CaF_2 (F). Analyses of >9 points on each fragment determined sample homogeneity and a statistically significant average. Compositional variations of each sample were within 3% of the estimated standard error for each element, thus indicating chemical homogeneity. FeO determination followed the procedure of Meyrowitz (1970). The F content was determined by the method of Foley (1989). No evidence of volatilization of F was observed.

Single-crystal X-ray diffraction data

Each crystal was mounted on a Bruker X8-Apex fully automated four-circle diffractometer with Kappa geometry, equipped with a fine focus Mo ceramic X-ray tube (λ = 0.7107 Å), and APEX 4K CCD detector. The data-collection strategy was obtained using the APEX2 software. For both crystals, preliminary lattice parameters and an orientation matrix were obtained from three sets of frames and refined during the integration process of the intensity data. Diffraction data were then collected with ω scans at different φ settings (φ–ω scan) (Bruker, 2003). Data were processed using *SAINT*+ (Bruker, 2003). The *SADABS* package (Sheldrick, 1996) was used to perform a semi-empirical absorption correction. Space-group determination and data merging were performed using *XPREP* (Sheldrick, 1997). Systematic extinctions on both crystals were consistent with space group *C*2/*m*. Subsequently, the crystal structure was refined with the package of programs SHELX-97 (Sheldrick, 1997).

Surface measurements

Chemical compositions of the (001) surfaces of tetra-ferriphlogopite and Fe-bearing phlogopite were determined by XPS analysis on freshly cleaved crystal fragments of ~5 mm × 5 mm × 0.25 mm. The XPS analyses were performed at a base pressure of 10^{-7} Pa using non-monochromatic Al Kα photons from a Vacuum Generators XR3 double anode X-ray source (operated at 15 kV, 18 mA). Spectra were recorded with a double pass cylindrical mirror analyzer (PHI 15-255G), operated at a constant pass energy of 50 eV (spot size = 2–4 mm).

The binding energy (BE) scale was calibrated (Barr *et al.*, 1997; Elmi *et al.*, 2010; 2011) with respect to the C_{1s} signal of adventitious carbon (a common contaminant for surfaces exposed to air) on each sample (fixed at BE = 284.8 eV). Owing to the high surface sensitivity of the XPS technique, determined by the inelastic mean free path of photoelectrons, the analysis is limited to only a few nanometers (1–3 nm) with an elemental concentration >0.1 atom.%. A preliminary identification of the elements present at the crystal surfaces included a fast survey scan (six scans at a pass energy of 100 eV), extended over a region which assured a sufficiently strong signal from the chemical species on each crystal.

Short sputtering of the sample surfaces was performed with an argon ion gun under an accelerating voltage of 0.5 kV to remove any possible contaminants from the outermost layer. Each sample was measured after 30 min of Ar^+ sputtering. An accurate determination of each element on the tetra-ferriphlogopite crystal surface was obtained in the region of the Si_{2p}, Mg_{1s}, Fe_{2p}, and K_{2p} core levels, whereas the concentration of each element on the Fe-bearing phlogopite was obtained in the region of Si_{2p}, Mg_{1s}, K_{2p}, Fe_{2p}, and Al_{2p}. No F signal from any surfaces was detected. No severe charging effects, which would compromise data acquisition, were observed.

RESULTS AND DISCUSSION

Mineral chemistry

The compositions reported in Table 1 were obtained by combining the results from the average of the microprobe point analyses and from the single-crystal structure refinement (by comparing the mean electron count and bond lengths of interlayer and octahedral cation sites). The tetra-ferriphlogopite chemical formula is $^{[XII]}(K_{0.99})^{[VI]}(Fe^{2+}_{0.08}Fe^{3+}_{0.15}Mg_{2.76}Ti_{0.01})^{[IV]}(Fe^{3+}_{0.82}Si_{3.18})O_{10.37}(F_{0.24}OH_{1.39})$ and the Fe-bearing phlogopite chemical formula is $^{[XII]}(K_{0.94}Na_{0.06})^{[VI]}(Fe^{2+}_{0.17}Fe^{3+}_{0.05}Mg_{2.75}Mn_{0.01}Ti_{0.05})^{[IV]}(Fe^{3+}_{0.16}Al_{0.84}Si_{3.00})O_{10.21}(F_{0.35}OH_{1.44})$. The chemical formulae are based on O_{12-x-y}, where x is the proportion of $(OH)^-$ groups per formula unit (p.f.u.) and y is F^- (atoms per formula unit, a.p.f.u.). The two minerals show an evident difference in tetrahedral composition, where Fe-for-Si substitution is at 20.5% in tetra-ferriphlogopite and at 4% in Fe-bearing phlogopite. A significantly higher $Fe^{3+}/(Fe^{2+}+Fe^{3+})$ ratio occurs in the octahedral sites of tetra-ferriphlogopite where the ratio is 0.65, compared to Fe-bearing phlogopite, with a $Fe^{3+}/(Fe^{2+}+Fe^{3+})$ ratio of 0.23.

Crystal chemistry and topology

The trioctahedral micas belong to space group $C2/m$ and are 1*M* polytypes (Table 2). Atomic positions of phlogopite-1*M* crystals from Brigatti *et al.* (1996b) were assumed as starting values. Neutral scattering factors were used for cation and anion positions. In the final cycles, anisotropic displacement parameters were refined for all atoms. Final refinements yielded an agreement factor $R = 3.43\%$ for tetra-ferriphlogopite and $R = 2.57\%$ for Fe-bearing phlogopite (Table 2). The final atomic coordinates, displacement parameters, calculated bond lengths (Table 3), and relevant structural parameters derived from structure refinement (Table 4) are reported. The large Fe^{3+} content in the tetrahedral site of tetra-ferriphlogopite produces a relatively high average T−O bond length ($\langle T-O \rangle$ = 1.6728 Å for tetra-ferriphlogopite and 1.6596 Å for Fe-bearing phlogopite) and larger cell-edge lengths (Table 2).

Tetra-ferriphlogopite has an appreciably greater tetrahedral volume (T_{volume} = 2.40 Å^3) than Fe-bearing phlogopite (T_{volume} = 2.34 Å^3). The average τ angle is smaller in tetra-ferriphlogopite (109.61º) than in Fe-bearing phlogopite (110.73º), and closer to the theoretical 109.47º value, indicating a regular tetrahedral site with tetrahedral cations located centrally. The mean tetrahedral basal edge length is greater in tetra-ferriphlogopite ($\langle O-O \rangle_{basal}$ = 2.725 (3) Å) than in Fe-bearing phlogopite ($\langle O-O \rangle_{basal}$ = 2.694(2) Å). The average distance between apical and basal tetrahedral oxygen atoms is 2.739 Å in tetra-ferriphlogopite and 2.726 Å in Fe-bearing phlogopite, which is a significantly smaller difference between the two samples than observed for $\langle O-O \rangle_{basal}$. The mean tetrahedral basal edge is related, at a first approximation, to the octahedral edge (*i.e.* average O3−O3 distance) by the following relationship:

Table 1. Averaged chemical composition[1] and structural formulae (a.p.f.u.) for tetra-ferriphlogopite and Fe-bearing phlogopite. Standard deviation in parenthesis.

Sample	Tetra-ferriphlogopite	Fe-bearing phlogopite		Tetra-ferriphlogopite	Fe-bearing phlogopite
	—— Wt.% ——			—— a.p.f.u. ——	
SiO_2	41.30(0.80)	40.40(0.95)	$^{[IV]}Si$	3.18	3.00
TiO_2	0.23(0.09)	0.91(.08)	$^{[IV]}Al$	0.00	0.84
Al_2O_3	0.00	9.58(0.13)	$^{[IV]}Fe^{3+}$	0.82	0.16
Cr_2O_3	b.d.t.	0.07(0.01)	$^{[IV]}\Sigma$	4.00	4.00
Fe_2O_3	16.70(0.30)	3.79(0.11)	$^{[VI]}Mg$	2.76	2.75
FeO	1.24	2.65	$^{[VI]}Fe^{3+}$	0.15	0.05
MnO	0.03(0.01)	0.09(0.01)	$^{[VI]}Fe^{2+}$	0.08	0.17
MgO	24.00(0.85)	24.85(.87)	$^{[VI]}Mn^{2+}$	0.00	0.01
Na_2O	0.03(0.01)	0.38(0.02)	$^{[VI]}Ti^{4+}$	0.01	0.05
K_2O	10.10(0.11)	9.98(0.13)	$^{[VI]}\Sigma$	3.00	3.03
F	0.98(0.28)	1.48(0.36)	$^{[XII]}Na$	0.00	0.06
H_2O	5.40	5.80	$^{[XII]}K$	0.99	0.94
Sum	100.01	99.98	$^{[XII]}\Sigma$	0.99	1.00
			F	0.24	0.35
			OH	1.39	1.44
			O	10.37	10.21
			Σ	12.00	12.00

---

[1] A least-squares method was utilized to combine chemical data from microprobe analysis and refinement data from single-crystal refinement (*i.e.* mean atomic count at octahedral and interlayer sites and mean octahedral (or interlayer) cation−oxygen bond distances). Tetrahedral sites are assumed to be filled by Si, Al, and Fe^{3+} to 4 cations per formula unit.

Table 2. Crystal, experimental, and refinement data for tetra-ferriphlogopite and Fe-bearing phlogopite.

	Tetra-ferriphlogopite	Fe-bearing phlogopite
Space group	$C2/m$	$C2/m$
a (Å)	5.380(1)	5.3296(1)
b (Å)	9.241(2)	9.2274(2)
c (Å)	10.315(3)	10.2943(2)
β(º)	100.08(2)	99.948(2)
Cell volume (Å^3)	505.0(2)	498.65(2)
Z	2	2
Crystal size (mm)	0.18 × 0.16 × 0.03	0.19 × 0.13 × 0.05
θ range (º)	4–38	4–55
Total reflections	2928	8458
Unique reflections	1107	3058
$R_{(int)}$ (%)	3.43	2.57
Reflections used	1107	3058
Miller index limits	$-9 \leqslant h \leqslant 8$	$-12 \leqslant h \leqslant 9$
	$-15 \leqslant k \leqslant 10$	$-21 \leqslant k \leqslant 20$
	$-16 \leqslant l \leqslant 17$	$-19 \leqslant l \leqslant 23$
No. of refined parameters	57	63
Goof	0.928	0.968
R_1 (%) [I>2σ(I)]	3.85	3.04
wR_2 (on F^2)	6.53	7.02
$\Delta\rho_{min}$ (e/Å^3)	−0.578	−0.432
$\Delta\rho_{max}$ (e/Å^3)	0.692	1.081

$R_1 = \Sigma||F_o| - |F_c||/\Sigma|F_o|$; $wR_2 = \{\Sigma[w(F_o^2 - F_c^2)^2]/\Sigma[w(F_o^2)^2]\}^{1/2}$; GooF $= \{\Sigma[w(F_o^2 - F_c^2)^2]/(n - p)\}^{1/2}$; $w = 1/[\sigma^2(F_o^2) + (aP)^2 + bP]$, where a = 0.0269, b = 0 for tetra-ferriphlogopite and a = 0.0422, b = 0 for Fe-bearing phlogopite. $P = (\max(F_o^2,0) + 2F_c^2)/3$; where n is the number of reflections and p is the number of parameters refined.

$\cos\alpha = \sqrt{3}/2 \times \langle O3 - O3\rangle/\langle O - O\rangle_{basal}$ (Brigatti and Guggenheim, 2002), where α is the tetrahedral rotation angle. The <O3–O3> octahedral mean edge distance is 3.093(3) Å in tetra-ferriphlogopite and 3.076(3) Å in Fe-bearing phlogopite. The observed tetrahedral rotation angle is 10.5º and 8.5º in tetra-ferriphlogopite and in Fe-bearing phlogopite, respectively. The larger value of 10.5º indicates that the lateral fit of the larger tetrahedral sheet to the smaller octahedral sheet is greater in tetra-ferriphlogopite than in Fe-bearing phlogopite. The above formula from Brigatti and Guggenheim (2002) predicts closely the observed α angles (at values of 10.6º and 8.6º, respectively). If the length of the edge of an ideally regular tetrahedron, with equal volume as determined for the two samples, is used in the formula instead of $\langle O-O\rangle_{basal}$, the predicted tetrahedral rotation angles are now 11.3º and 10.6º for tetra-ferriphlogopite and for Fe-bearing phlogopite, respectively. Because the tetrahedral flattening angle (τ) of 110.73º is larger than the ideal, this parameter reduces the lateral dimensions of the tetrahedral sheet, much like α but without tetrahedral ring distortions. However, the tetrahedral ring distortion significantly affects interlayer coordination. In particular, as the α angle increases, the effective coordination number (ECoN, Weiss *et al.*, 1992) of the interlayer cation decreases (8.9º in tetra-ferriphlogopite and 9.4º in Fe-bearing phlogopite). The difference between the inner (nearest oxygen atom neighbors) and outer (second nearest neighbors) distances around the interlayer cation increases (0.483 Å in tetra-ferriphlogopite and 0.383 Å in Fe-bearing phlogopite) and the interlayer separation increases (3.463 Å in tetra-ferriphlogopite and 3.451 Å in Fe-bearing phlogopite). These trends, well established for 1*M* micas (Brigatti and Guggenheim 2002), are also confirmed for the two samples here.

Octahedral sheet topology is similar for both samples, with tetra-ferriphlogopite showing slightly larger dimensions than those observed in Fe-bearing phlogopite (Table 3).

Surface features

Because of expected charge effects, the binding energy (BE) of the C_{1s} level was obtained from saturated-hydrocarbon contamination at 284.8 eV, thus providing an internal standard for the calibration of each spectrum. The precision of BE values was estimated at ±0.2 eV. An accurate determination of each element on the crystal surfaces was obtained in the region of the Si_{2p}, Mg_{1s}, K_{2p}, Al_{2p}, and Fe_{2p} core levels. The data obtained are reported in plots representing the number of emitted electrons *vs.* their characteristic binding energies. The XPS plots were fitted to Voigt peaks, after a Shirley background subtraction (Shirley, 1972).

In Fe-bearing phlogopites, Si is a tetrahedral cation with possible substitutions of Al^{3+} and/or Fe^{3+} in the tetrahedral site. The Si_{2p} binding energy in both samples (BE = 102.7 eV for tetra-ferriphlogopite and BE = 102.2 eV for Fe-bearing phlogopite) is consistent with

Table 3. Selected bond lengths (Å), mean electron count (m.e.c.) and parameters derived from structure refinement.

Sample	Tetra-ferriphlogopite	Fe-bearing phlogopite		Tetra-ferriphlogopite	Fe-bearing phlogopite
Tetrahedral sheet					
T–O1	1.668(1)	1.6621(3)	α (°)	10.5	8.5
T–O2	1.674(2)	1.6640(5)	Δz (Å)	0.003	0.002
T–O2′	1.678(1)	1.6617(5)	τ (°)	109.9	110.7
T–O3	1.671(2)	1.6506(4)	Si+Al (occupancy)	0.784(5)	0.989(2)
<T–O>	1.6728	1.6596	Fe (occupancy)	0.216(5)	0.011(2)
			Sheet thickness (Å)	2.266	2.263
Octahedral sheet					
M1–O3 (×4)	2.103(1)	2.0927(4)	ψ_{M1} (°)	58.9	58.6
M1–O4 (×2)	2.060(2)	2.0552(4)	ψ_{M2} (°)	58.9	58.7
<M1–O>	2.089	2.080	m.e.c. $_{M1}$	13.06(2)	12.67(1)
			m.e.c. $_{M2}$	12.63(3)	12.62(2)
M2–O3 (×2)	2.091(1)	2.0823(4)	Sheet thickness (Å)	2.160	2.162
M2–O3′ (×2)	2.104(1)	2.0925(4)			
M2–O4 (×2)	2.065(1)	2.0641(4)			
<M2–O>	2.087	2.080			
Interlayer					
A–O1 (×2)	2.959(2)	2.9856(8)	<A–O>$_{inner}$	2.952	2.985
A–O1′ (×2)	3.445(2)	3.3704(8)	<A–O>$_{outer}$	3.440	3.369
A–O2 (×4)	2.949(2)	2.9848(5)	Δ(A–O) (Å)	0.483	0.383
A–O2′ (×4)	3.430(2)	3.3672(6)	m.e.c.	19	17.96(1)
A–O4	4.046(2)		Interlayer separation (Å)	3.463	3.451

α (tetrahedral rotation angle) = $\Sigma_{i=1}^{6}\alpha_1/6$ where $\alpha_i = |120° - \phi_i|/2$ and where ϕ_i is the angle between basal edges of neighboring tetrahedra articulated in the ring. $\Delta z = [Z_{(O_{basal})\max} - Z_{(O_{basal})\min}]\,[c\sin\beta]$. τ (tetrahedral flattening angle) = $\Sigma_{i=1}^{3}(O_{basal}-\hat{T}-O_{basal})/3$. ψ (octahedral flattening angle) = $\cos^{-1}$ [octahedral thickness/(2<M–O, OH, F>)] (Donnay *et al.*, 1964). Tetrahedral thickness: $((zO4+2\times zO3)/3-(zO1+2\times zO2)/3)\times c\times\sin\beta$; octahedral thickness: $(1-2\times(zO4+2\times zO3)/3)\times c\times\sin\beta$; interlayer separation: $(2\times(zO1+2\times zO2)/3)\ )\times c\times\sin\beta$.

Table 4. Crystallographic coordinates and equivalent isotropic displacement parameters (Å^2 × 10^3). $U_{(eq)}$ is defined as one third of the trace of the orthogonalized U_{ij} tensor.

	x	*y*	*z*	$U_{(eq)}$	U_{11}	U_{22}	U_{33}	U_{23}	U_{13}	U_{12}
Tetra-ferriphlogopite (Space group: *C*2/*m*)										
O1	0.0034(4)	0	0.1703(2)	32(1)	37(1)	27(1)	30(12)	0	0(1)	0
O2	0.3328(3)	0.2227(2)	0.1706(2)	32(1)	35(1)	31(1)	29(1)	−5(1)	6(1)	−4(1)
O3	0.1302(2)	0.1674(1)	0.3913(1)	13(1)	9(1)	8(1)	21(1)	0(1)	2(1)	0(1)
O4	0.1344(3)	0.5	0.3984(2)	15(1)	12(1)	9(1)	25(1)	0	5(1)	0
T	0.0754(1)	0.1666(1)	0.2267(1)	12(1)	10(1)	5(1)	21(1)	0(1)	3(1)	0(1)
M1	0	0	0.5	11(1)	7(1)	5(1)	21(1)	0	3(1)	0
M2	0	0.3331(1)	0.5	10(1)	7(1)	3(1)	20(1)	0	3(1)	0
A	0	0.5	0	36(1)	36(1)	32(1)	39(1)	0	6(1)	0
Fe-bearing phlogopite (Space group: *C*2/*m*)										
O1	0.0138(2)	0	0.1703(1)	18(1)	26(1)	14(1)	13(1)	0	0(1)	0
O2	0.3282(1)	0.2286(1)	0.1701(1)	18(1)	17(1)	24(1)	14(1)	3(1)	4(1)	6(1)
O3	0.1303(1)	0.1668(1)	0.3910(1)	8(1)	8(1)	8(1)	10(1)	0(1)	2(1)	0(1)
O4	0.1327(1)	0.5	0.3981(1)	9(1)	8(1)	9(1)	10(1)	0	2(1)	0
T	0.0760(1)	0.1667(1)	0.2282(1)	8(1)	7(1)	7(1)	9(1)	0(1)	2(1)	0(1)
M1	0	0	0.5	8(1)	6(1)	7(1)	10(1)	0	2(1)	0
M2	0	0.3320(1)	0.5	8(1)	6(1)	6(1)	10(1)	0	2(1)	0
A	0	0.5	0	30(1)	35(1)	35(1)	21(1)	0	4(1)	0

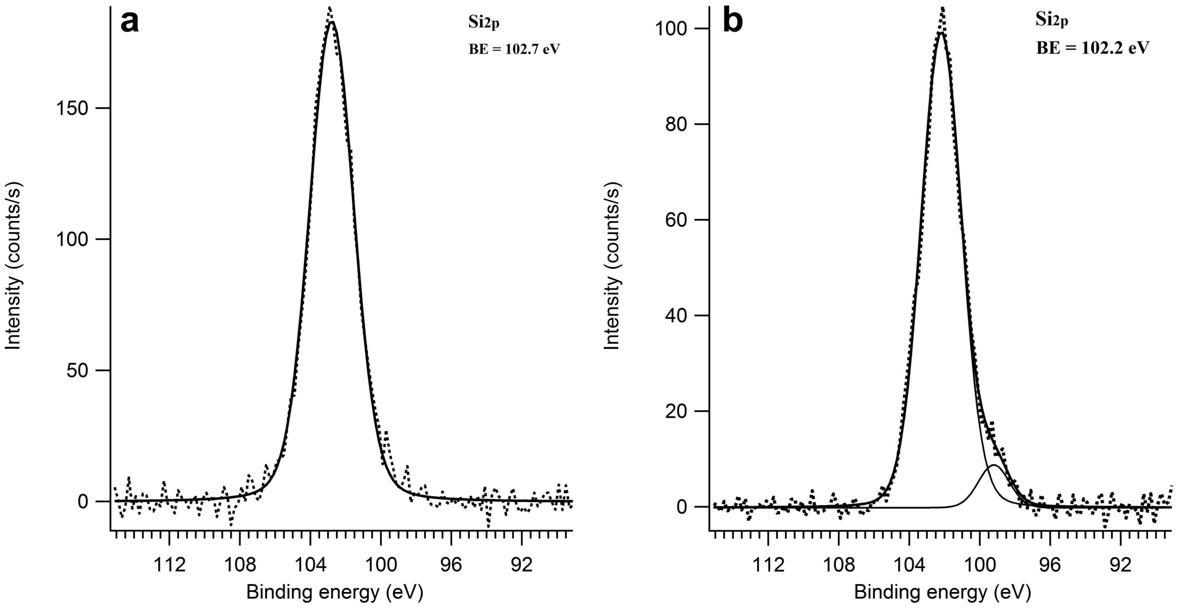

Figure 1. Si_{2p} spectrum of tetra-ferriphlogopite (a) and Fe-bearing phlogopite (b) displayed as a plot of electron binding energy *vs*. intensity (the number of electrons per second in a fixed and small energy interval). Dotted lines: experimental spectra; solid lines: fitted spectra.

tetrahedral coordination (Figure 1a,b) close to literature values obtained from other silicates (from 102.36 to 102.16 eV; Wagner *et al.*, 1982; Hasha *et al.*, 1988; Bhattacharyya, 1993; Biino and Gröning, 1998a).

Tetrahedrally coordinated Al is only present in Fe-bearing phlogopite. The Al_{2p} peak was located at BE = 74.2 eV with no evident asymmetries in the peak shape (Figure 2). The peak BE is close to values obtained by Hasha *et al.* (1988) for silico-aluminophosphates with Al in tetrahedral coordination (BE Al_{2p} values range from 74.2 to 75.3 eV), thus suggesting that in Fe-bearing phlogopite, Al is tetrahedrally coordinated also at the surface.

The Mg_{1s} spectra show a maximum at BE = 1305.9 eV for tetra-ferriphlogopite and at 1306.8 eV for Fe-bearing phlogopite (Figure 3a,b), thus confirming octahedral coordination (Mittal *et al.*, 2004; Elmi *et al.*, 2010, 2011).

The anion sites are occupied by OH and F. Furthermore, the OH site can be deprotonated to balance the layer charge. Nuclear magnetic resonance studies of Al-rich synthetic phlogopite (Fechtelkord *et al.*, 2003a, 2003b; Fechtelkord and Langner, 2013) demonstrated that OH^- and F^- ions form homogeneous domains. Usually, fluorine is located in Mg-rich octahedral and Si-rich tetrahedral clusters of the Mg-pure phlogopite structure. Several authors have observed that the Mg binding energy depends on the chemistry of the anion site as well as its local environment. In brucite ($Mg(OH)_2$, Haycock *et al.*, 1978) and Mg-Fe spinel ($MgFe_2O_4$, Mittal *et al.*, 2004) where Mg coordinates with OH groups or oxygen atoms, the binding energy is 1303.1 eV and 1302.7 eV, respectively. However, if oxygen is substituted by fluorine, the binding energy of Mg was observed to shift to higher values (MgF_2, BE = 1306.5 eV, Seyama and Soma, 1984). Considering values characterizing tetra-ferriphlogopite and Fe-bearing phlogopite (1305.9 eV and 1306.8 eV, respectively, Figure 3), Mg cations in Fe-bearing phlogopite seem to

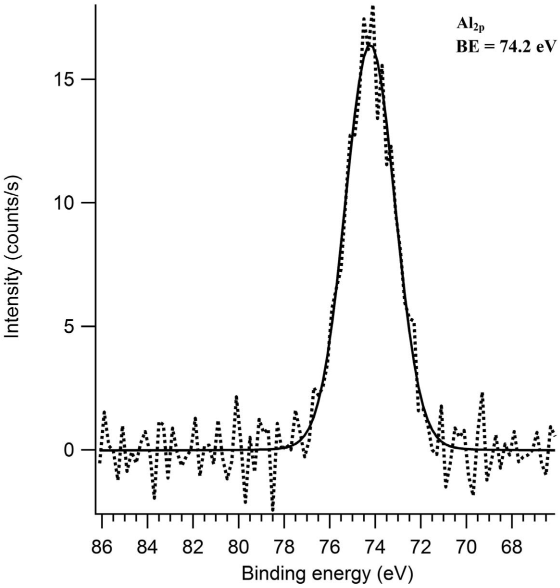

Figure 2. Al_{2p} spectrum of Fe-bearing phlogopite displayed as a plot of electron binding energy *vs*. intensity (the number of electrons per second in a fixed and small energy interval). Dotted lines: experimental spectra; solid lines: fitted spectra.

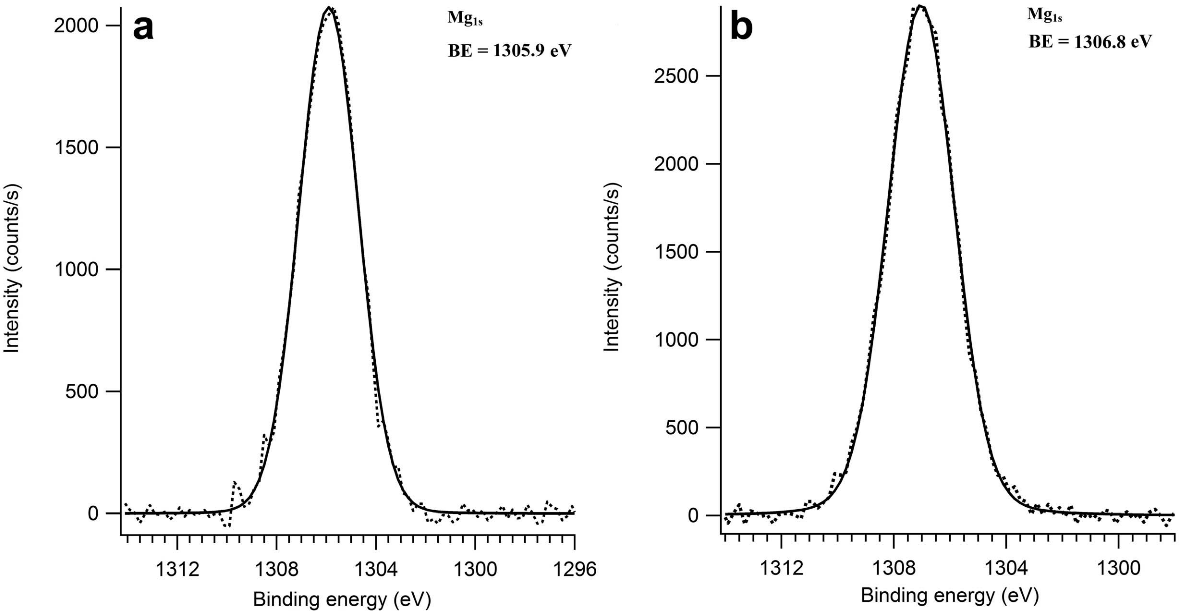

Figure 3. Mg_{1s} spectra of tetra-ferriphlogopite (a) and Fe-bearing phlogopite (b) displayed as a plot of electron binding energy *vs.* intensity (the number of electrons per second in a fixed and small energy interval). Dotted lines: experimental spectra; solid lines: fitted spectra.

be preferentially bonded to fluorine, rather than to OH groups. The larger value corresponds to Fe-bearing phlogopite showing greater F^- content.

The Fe_{2p} spectra are characterized by doublet structures relating to the spin orbit splitting between $2p_{1/2}$ and $2p_{3/2}$ states. The deconvolution of the $Fe_{2p3/2}$ peak (BE = 712.5 eV, in both samples) leads to two main components: one component is at BE = 710.7 eV with an associated satellite peak at BE = 716.0 eV, and the second component is at BE = 712.5 eV with an associated satellite peak at BE = 720.0 eV (Figure 4a,b). Because of the inability to determine the contribution of each component following a Gauss-Voigt deconvolution procedure, the main $2p_{3/2}$ peak maximum at BE = 712.5 eV represents the summation of the tetrahedral and octahedral Fe^{3+} components. This result is similar to that observed for magnetite by Grosvenor *et al.* (2004). The deconvolution of the $Fe_{2p1/2}$ peak indicates that the two main components are Fe^{2+} (BE = 724.2 eV and BE = 729.9 eV) and Fe^{3+} (BE = 726.2 and BE = 732.8 eV).

Several studies (Bronold *et al.*, 1992; Grosvenor *et al.*, 2004) demonstrated that, if the symmetry of a low-spin Fe^{2+} cation is decreased because of a loss of a ligand, the binding energy of its $2p_{3/2}$ peak increases. For the phlogopites examined here, the first component (label Fe^{2+}, Figure 4) at BE = 710.7 eV for both samples is related to Fe^{2+} in octahedral coordination, similar to olivine $(Mg,Fe)_2SiO_4$, where the BE is reported at 710.8 eV (Seyama and Soma, 1987).

The $K_{2p3/2}$ BE values are at 293.6 and 294.5 eV for tetra-ferriphlogopite and Fe-bearing phlogopite, respectively (Figure 5a,b). These values agree with those reported for muscovite (BE = 293.3 eV; Elmi *et al.*, 2013), where the K coordination at the surface is reduced from nine to eight (Zakaznova-Herzog *et al.*, 2008; Elmi *et al.*, 2013). Also in trioctahedral micas, the K coordination is slightly lower at the surface than that observed in the bulk (ECoN = 8.9 in tetra-ferriphlogopite and ECoN = 9.4 in Fe-bearing phlogopite). Strictly speaking, the information obtained from XPS relates to the outermost few repeat units of the crystals only. In margarite, muscovite, and sericite, the escape depth for all of the photoelectrons is ~15 Å at a pass energy of 100 eV (Johns and Gier, 2001). This is important for the analytical results from the present study because it confirms that, with respect to alkali and alkaline earth (K, Na) analysis, only the surface- and the first next interlayer-ions are considered. The reduction of the interlayer cation coordination, from nine to eight at the surface with respect to the bulk, may be an average of the outermost interlayer and the next interlayer at ~10 Å depth. This inference suggests that the interlayer cation coordination is subjected to a reduction of coordination to six and then a slight relaxation occurs. Nevertheless, future work may provide additional information from which a more decisive conclusion can be reached.

The $K_{2p1/2}$ binding energy values are 297.3 eV (tetra-ferriphlogopite) and 297.4 eV (Fe-bearing phlogopite). These values are greater than, for example, muscovite where K is in eight-fold coordination ($K_{2p1/2}$ BE = 295.5 eV). This energy shift is roughly related to the mean distance between K and inner oxygen atoms (2.952 and 2.985 Å in tetra-ferriphlogopite and Fe-bearing

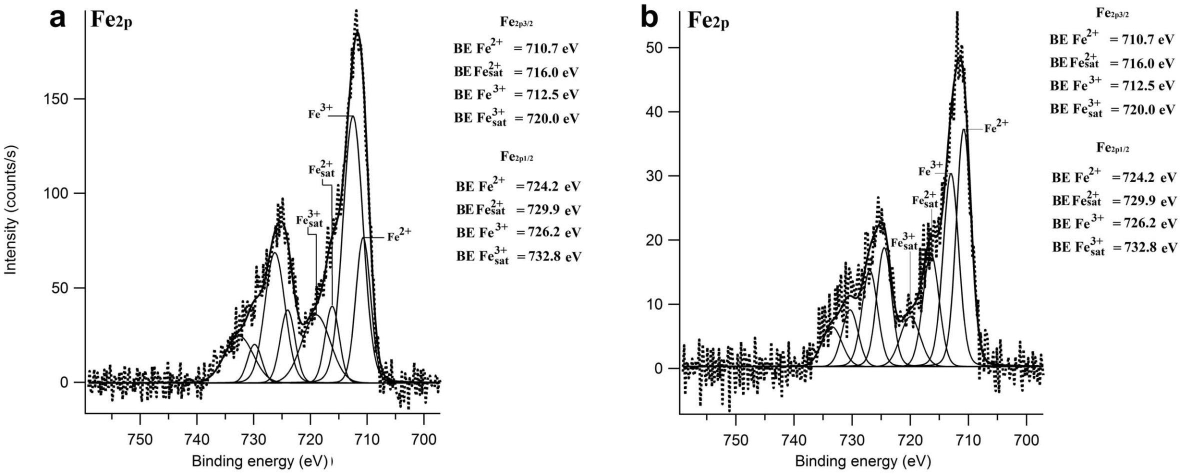

Figure 4. Fe_{2p} spectrum with the curve fit obtained for tetra-ferriphlogopite (a). The spectrum is displayed as a plot of electron binding energy *vs*. intensity (the number of electrons per second in a fixed and small energy interval). The Fe^{3+} and Fe^{2+} multiplet peaks are labeled on the spectrum. Fe^{3+}_{sat} and Fe^{2+}_{sat} refer to the associated satellite peaks of Fe^{3+} and Fe^{2+}, respectively. Fe_{2p} spectrum obtained for Fe-bearing phlogopite (b). Dotted lines: experimental spectra; solid lines: deconvoluted peaks. See text for additional explanations.

phlogopite, respectively, and 2.865 Å in muscovite). Although more data are required for confirmation, experimental data seem to suggest that, in the cleavage region of the crystal, the interlayer cation coordination is subjected to a reduction of coordination and then a slight relaxation effect.

In summary, the tetra-ferriphlogopite and Fe-rich phlogopite addressed here differ mainly because of Fe^{3+} in the tetrahedral site, the Fe^{3+}/Fe^{2+} ratio in octahedral sites, and the anion composition. In particular, the different tetrahedral compositions produce a significantly less distorted tetrahedral site in tetra-ferriphlogopite compared with Fe-rich phlogopite, as demonstrated by different values in the flattening angle, τ. The flattening angle is believed to be related to the relative misfit between the tetrahedral and octahedral sheets and thus, the size differences between tetrahedral Si, Al, and Fe^{3+}. A more regular tetrahedron, as found in tetra-ferriphlogopite apparently yields a 'stiffer' tetrahedron which would require more fixed basal oxygen distances, thus accounting for greater basal oxygen ring distortion, as measured by the tetrahedral rotation angle. The tetrahedral rotation angle impacts significantly on the coordination of the interlayer cation, reducing its coordination

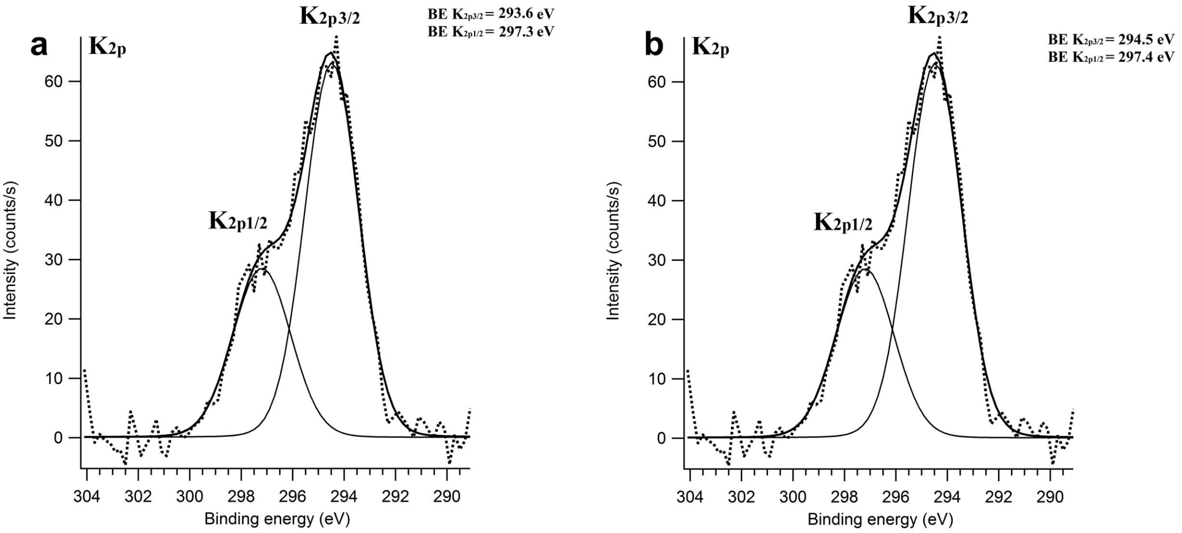

Figure 5. K_{2p} spectra of tetra-ferriphlogopite (a) and Fe-bearing phlogopite (b) displayed as a plot of electron binding energy *vs*. intensity (the number of electrons per second in a fixed and small energy interval). Dotted lines: experimental spectra; solid lines: deconvoluted peaks. See text for additional explanations.

number with increasing α. At the mineral surface, the coordination of the interlayer cation is reduced to eight oxygen atoms, unlike the coordination (six- and four-fold polyhedra) of the other cations at the surface, which maintain the same coordination as found in the bulk. The XPS investigation of the mineral surface identified differences in Mg binding energy between the two phlogopite samples. This difference is believed to be caused by different F^- contents, which are known to affect the binding energy of Mg.

ACKNOWLEDGMENTS

This work benefited from improvements suggested by two anonymous referees and by the Associate Editor, E. Ferrage. The authors acknowledge Fondazione Cassa di Risparmio di Modena (International Projects) for supporting this research.

REFERENCES

Bailey, S.W. (1984) Crystal chemistry of the true micas. Pp. 13–60 in: *Micas* (S.W. Bailey, editor). Reviews in Mineralogy, **13**, Mineralogical Society of America, Washington, D.C.

Barr, T.L., Seal, S., Wozniak, K., and Klinowaki, J. (1997) ESCA studies of the coordination state of aluminum in oxide environments. *Journal of Chemical Society, Faraday Transactions*, **93**, 181–186.

Bhattacharyya, K.G. (1993) XPS study of mica surfaces. *Journal of Electron Spectroscopy and Related Phenomena*, **63**, 289–306.

Biino, G.G. and Gröning, P. (1998a) Cleavage mechanism and surface chemical characterization of phengitic muscovite and muscovite as constrained by X-ray photoelectron spectroscopy. *Physics and Chemistry of Minerals*, **25**, 168–181.

Biino, G.G. and Gröning, P. (1998b) X-ray photoelectron spectroscopy (XPS) used as a structural and chemical surface probe on aluminosilicates minerals. *European Journal of Mineralogy*, **10**, 423–437.

Biino, G.G., Mannella, N., Kay, A., Mun, B., and Fadley, C. (1999) Surface chemical characterization and surface diffraction effects of real margarite (001): An angle-resolved XPS investigation. *American Mineralogist*, **84**, 629–638.

Brigatti, M.F. and Guggenheim, S. (2002) Mica crystal chemistry and the influence of pressure, temperature, and solid solution on atomistic models. Pp. 1–97 in: *Micas: Crystal Chemistry and Metamorphic Petrology* (A. Mottana, F.P. Sassi, J.B. Thompson Jr., and S. Guggenheim, editors). Reviews in Mineralogy and Geochemistry, **46**, Mineralogical Society of America and the Geochemical Society, Washington, D.C.

Brigatti, M.F., Medici, L., and Poppi, L. (1996a) Refinement of the structure of natural ferriphlogopite. *Clays and Clay Minerals*, **44**, 540–545.

Brigatti, M.F., Medici, L., Saccani, E., and Vaccaro, C. (1996b) Crystal-chemistry and petrologic significance of Fe^{3+}-rich phlogopite from the Tapira carbonatite complex, Brazil. *American Mineralogist*, **81**, 913–927.

Brigatti, M.F., Lalonde, A.E., and Medici, L. (1999) Crystal chemistry of $^{[4]}$Fe^{3+}-rich phlogopites: a combined single-crystal X-ray and Mössbauer study. Pp. 317–327 in: *Clays for our Future* (H. Kodama, A.R. Mermut, K. Torrance, editors). Proceedings of the 11th International Clay Conference, Ottawa, Mineralogical Association of Canada.

Brigatti, M.F., Medici, L., and Poppi, L. (2001) Crystal chemistry of trioctahedral micas-1M from the Alto Paranaíba igneous province, southeastern Brazil. *The Canadian Mineralogist*, **39**, 1933–1345.

Brigatti, M.F., Guidotti, C.V., Malferrari, D., and Sassi, F.P. (2008) Single-crystal X-ray studies of trioctahedral micas coexisting with dioctahedral micas in metamorphic sequences from western Maine. *American Mineralogist*, **93**, 396–408.

Brigatti, M.F., Malferrari, D., Laurora, A., and Elmi, C. (2011) Structure and mineralogy of layer silicates: recent perspectives and new trends. Pp. 1–71 in: *Layered Mineral Structures and their Application in Advanced Technologies* (M.F. Brigatti and A. Mottana, editors). EMU Notes in Mineralogy, **11**, European Mineralogical Union and the Mineralogical Society of Great Britain and Ireland.

Brod, J.A., Gaspar, J.C., de Araújo, D.P., Gibson, S.A., Thompson, R.N., and Junqueira-Brod, T.C. (2001) Phlogopite and tetra-ferriphlogopite from Brazilian carbonatite complexes: petrogenetic constraints and implications for mineral-chemistry systematics. *Journal of Asian Earth Sciences*, **19**, 265–296.

Bronold, M., Tomm, Y., and Jaegermann, W. (1992) Surface states on cubic d-band semiconductor pyrite (FeS_2). *Surface Science*, **314**, L931–L936.

Bruker (2003) *SMART and SAINT-Plus, version 6.01*. Bruker AXS Inc., Madison, Wisconsin.

Cibin, C., Mottana, A., Marcelli, A., and Brigatti, M.F. (2005) Potassium coordination in trioctahedral micas investigated by K-edge XANES spectroscopy. *Mineralogy and Petrology*, **85**, 67–87.

Donnay, G., Morimoto, N., Takeda, H., and Donnay, J.D.H. (1964) Trioctahedral one-layer micas: I. Crystal structure of a synthetic iron mica. *Acta Crystallographica*, **17**, 1369–1373.

Elmi, C., Brigatti, M.F., Pasquali, L., Montecchi, M., Laurora, A., Malferrari, D., and Nannarone, S. (2010) Crystal chemistry, surface morphology and X-ray photoelectron spectroscopy of Fe-rich osumilite from Mt. Arci, Sardinia (Italy). *Physics and Chemistry of Minerals*, **37**, 561–569.

Elmi, C., Brigatti, M.F., Pasquali, L., Montecchi, M., Laurora, A., Malferrari, D., and Nannarone, S. (2011) High-temperature vesuvianite: crystal chemistry and surface considerations. *Physics and Chemistry of Minerals*, **38**, 459–468.

Elmi, C., Brigatti, M.F., Guggenheim, S., Pasquali, L., Montecchi, M., Laurora, A., Malferrari, D., and Nannarone, S. (2013) Sodian muscovite-$2M_1$: crystal chemistry and surface features. *The Canadian Mineralogist*, **51**, 319–328.

Fechtelkord, M. and Langner, R. (2013) Aluminum ordering and clustering in Al-rich synthetic phlogopite: The influence of fluorine investigated by $\{^{19}F/^{1}H\}$ ^{29}Si CPMAS NMR spectroscopy. *American Mineralogist*, **98**, 120–131.

Fechtelkord, M., Behrens, H., Holtz, F., Fyfe, C.A., Groat, L.A., and Raudsepp, M. (2003a) Influence of F content on the composition of Al-rich synthetic phlogopite: Part I. New information on structure and phase-formation from ^{29}Si, ^{1}H, and ^{19}F MAS NMR spectroscopies. *American Mineralogist*, **88**, 47–53.

Fechtelkord, M., Behrens, H., Holtz, F., Bretherton, J.L., Fyfe, C.A., Groat, L.A., and Raudsepp, M. (2003b) Influence of F content on the composition of Al-rich synthetic phlogopite: Part II. Probing the structural arrangement of aluminum in tetrahedral and octahedral layers by ^{27}Al MQMAS and ^{1}H/^{19}F-^{27}Al HETCOR and REDOR experiments. *American Mineralogist*, **88**, 1046–1054.

Ferraris, G., Gula, A., Ivaldi, G., Nespolo, M., Sokolova, E., Uvarova, Y., and Khomyakov, A.P. (2001) First structure determination of a MDO-2*O* mica polytype associated with a 1*M* polytype. *European Journal of Mineralogy*, **13**, 1013–1023.

Fleet, M.E. (2003) *Rock-Forming Minerals, Volume 3A. Sheet Silicates: Micas*. 2nd edition, Geological Society, London.

Foley, S.F. (1989) Experimental constraints on phlogopites chemistry in lamproites: 2. The effect of pressure-temperature variations. *European Journal of Mineralogy*, **2**, 327–341.

Grosvenor, A.P., Kobe, B.A., Biesinger, M.C., and McIntyre, N.S. (2004) Investigation of multiplet splitting of Fe_{2p} XPS spectra and bonding in iron compounds. *Surface and Interface Analysis*, **36**, 1564–1574.

Guggenheim, S. (2011) An overview of order/disorder in hydrous phyllosilicates. Pp. 72–111: *Layered Mineral Structures and their Application in Advanced Technologies* (M.F. Brigatti and A. Mottana, editors). EMU Notes in Mineralogy, **11**, European Mineralogical Union and the Mineralogical Society of Great Britain and Ireland.

Hasha, D., de Saldarriaga, L., Saldarriaga, C., Hathway, P.E., Cox, D.F., and Davis, M. (1988) Studies of silicoaluminophosphates with the sodalite structure. *Journal of the American Chemical Society*, **110**, 2127–2135.

Haycock, D.E., Kasrai, M., Nicholls, C.J., and Urch, D.S. (1978) The electronic structure of magnesium hydroxide (brucite) using X-ray emission, X-ray photoelectron, and auger spectroscopy. *Journal of the Chemical Society, Dalton Transactions*, **12**, 1791–1796

Johns, W.D. and Gier, S. (2001) X-ray photoelectron spectroscopic study of layer charge magnitude in micas and illite-smectite clays. *Clay Minerals*, **36**, 355–367.

Krasnova, N.I. (2001) The Kovdor phlogopite deposit, Kola Peninsula, Russia. *The Canadian Mineralogist*, **39**, 33–44.

Lalonde, A.E., Rancourt, D.G., and Chao, G.Y. (1991) Fe-bearing trioctahedral micas from Mont Saint-Hilaire, Québec, Canada. *Mineralogical Magazine*, **60**, 447–460.

Laurora, A., Malferrari, D., Brigatti, M.F., Mottana, A., Caprilli, E., Giordano, G., and Funiciello, R. (2009) Crystal chemistry of trioctahedral micas in the top sequences of the Colli Albani volcano, Roman Region, Central Italy. *Lithos*, **113**, 507–520.

Meyrowitz, R. (1970) New semi-microprocedure for determination of ferrous iron in refractory silicate minerals using a sodium metafluoborate decomposition. *Analytical Chemistry*, **42**, 1110–1113.

Mittal, V.K., Bera, S., Nithya, R., Srinivasan, M.P., Velmurugan, S., and Narasimhan, S.V. (2004) Solid state synthesis of Mg-Ni ferrite and characterization by XRD and XPS. *Journal of Nuclear Materials*, **335**, 302–310.

Reguir, E.P., Chakhmouradian, A.R., Halden, N.M., Malkovets, V.G., and Yanga, P. (2009) Major- and trace-element compositional variation of phlogopite from kimberlites and carbonatites as a petrogenetic indicator. *Lithos*, **112S**, 372–384.

Schoonheydt, R.A. and Johnston, C.T. (2011) The surface properties of clay minerals. Pp. 337–373 in: *Layered Mineral Structures and their Application in Advanced Technologies* (M.F. Brigatti and A. Mottana, editors). EMU Notes in Mineralogy, **11**, European Mineralogical Union and the Mineralogical Society of Great Britain and Ireland.

Seyama, H. and Soma, M. (1984) X-ray photoelectron spectroscopic study of montmorillonite containing exchangeable divalent cations. *Journal of the Chemical Society, Faraday Transactions 1: Physical Chemistry in Condensed Phases*, **80**, 237–248

Seyama, H. and Soma, M. (1987) Fe_{2p} spectra of silicate minerals. *Journal of Electron Spectroscopy and Related Phenomena*, **42**, 97–101.

Sheldrick, G.M. (1996) *SADABS*. University of Göttingen, Germany.

Sheldrick, G.M. (1997) *SHELXL97. Program for the Refinement of Crystal Structures*. University of Göttingen, Germany.

Shirley, D.A. (1972) Effect of atomic and extra-atomic relaxation on atomic binding energies. *Chemical and Physical Letters*, **16**, 220–5.

Wagner, C.D., Passoja, D.E., Hillery, H.F., Kinisky, T.G., Six, H.A., Jansen, W.T., and Taylor, J.A. (1982) Auger and photoelectron line energy relationship in aluminum-oxygen and silicon-oxygen compounds. *Journal of Vacuum Science and Technology*, **21**, 933–944.

Weiss, Z., Rieder, M., and Chmielovà, M. (1992) Deformation of coordination polyhedra and their sheets in phyllosilicates. *European Journal of Mineralogy*, **4**, 665–682.

Zakaznova-Herzog, V.P., Nesbitt, H.W., Bancroft, G.M., and Tsese, J.S. (2008) Characterization of leached layers on olivine and pyroxenes using high-resolution XPS and density functional calculations. *Geochimica et Cosmochimica Acta*, **72**, 69–86.

(*Received 25 February 2013; revised 13 November 2013; Ms. 745; AE: J.W. Stucki*)

Clays and Clay Minerals, Vol. 62, No. 4, 253–266, 2014.

ASSESSMENT OF PEDOGENIC GIBBSITE AS A PALEO-$P\mathrm{CO_2}$ PROXY USING A MODERN ULTISOL

JASON C. AUSTIN* AND PAUL A. SCHROEDER
University of Georgia, Department of Geology, Athens, GA 30602-2501 USA

Abstract—The stable carbon isotope composition of CO_2 occluded in the gibbsite structure is proposed as a potential atmospheric paleo-PCO_2 proxy. Analysis of pedogenic gibbsite from a modern Ultisol in the Piedmont of Georgia, USA, was conducted to test the basis for this concept and to help constrain the parameters used to describe physical and biological processes affecting such factors as the respiration rate of CO_2. Co-variation of the $\delta^{13}C$ and $\delta^{18}O$ values with depth along a gradient parallel to the mixing line between the atmosphere and the soil organic material implies that diffusion is the process that determines the stable isotope composition of soil CO_2. In the upper 40 cm, the measured $\delta^{13}C$ values are not consistent with the expected diffusive depth profile assumed in paleo-PCO_2 models. The isotope signature is reset downward in the depth profile with a concentration of the most atmosphere-like $\delta^{13}C$ and $\delta^{18}O$ values occurring at the top of the Bt horizon by some as-yet-unknown process. Bioturbation, recrystallization, and physical translocation are potential explanations for this observation. Regardless of the process at work, the net effect is an apparent two-component mixing curve between the top of the Bt horizon and deep within the saprolite. In cases where the A horizon is eroded but the Bt horizon is preserved it is possible that $\delta^{13}C$ values of gibbsite-occluded CO_2 can serve as a proxy for atmospheric paleo-PCO_2. Careful textural study of all paleosols is therefore essential to match stable carbon isotope signatures with the horizons preserved. Understanding of modern dynamics and preservation of these isotopic signatures may also be important for those that employ other carbonate proxies.

Key Words—Paleo-PCO_2 Proxies, Pedogenic Gibbsite, Soil CO_2 Diffusion, Stable Carbon Isotopes, Stable Oxygen Isotopes, Ultisol.

INTRODUCTION

A review of proxy-based estimates of paleo-PCO_2 through geologic time reveals a large range of error associated within individual methods and a large range of estimates between methods (Royer *et al.*, 2001). Paleo-PCO_2 proxies using marine phytoplankton and a stomatal index have small estimated errors (200 and 50 ppmv, respectively) but are temporally limited to Cretaceous and younger samples. In addition, these proxies are reliable only under relatively low atmospheric PCO_2 conditions (1250 and 340 ppmv, respectively) (Farrimond *et al.*, 1986; Woodward and Bazzaz, 1988; Marlowe *et al.*, 1990; Freeman and Hayes, 1992; Van Der Burgh *et al.*, 1993; Kurschner *et al.*, 1996; Kump and Arthur, 1999; Pagani *et al.*, 1999; Royer *et al.*, 2001). Pedogenic carbonates provide information over the much longer history of soils on earth (*i.e.* the Phanerozoic) formed in arid environments. However, uncertainty in estimating the concentration of CO_2 in the soil results in large errors. When compared to other methods such as the GEOCARB model (Berner and Kothavala, 2001) the pedogenic carbonate method appears to over-estimate paleo-PCO_2 (Breecker *et al.*, 2009); the latter authors suggested that better agreement is possible if seasonal biases for time of mineralization are factored into model assumptions. Pedogenic goethite has also been used as a proxy but is limited to Fe-rich, wet climates mutually exclusive of arid calcrete-forming environments (Yapp and Poths, 1992, 1996). Direct comparison of proxy-derived paleo-PCO_2 estimates are limited by the effective time and spatial ranges of each proxy. Other, independent proxies effective over broad age ranges would therefore be helpful. Recent work modeling the stable carbon isotope composition of a carbonate-like component associated with pedogenic gibbsite suggests that this mineral has the potential to fill the proxy need (Schroeder *et al.*, 2006; Austin, 2011).

The pedogenic gibbsite proxy employs the same Fickian diffusion model developed for pedogenic carbonates by Cerling (1984) and is described in detail by Austin (2011) who used both analytical and numerical approaches to evaluate errors. Briefly, the diffusion model takes the form:

$$\frac{\partial C_s^*}{\partial t} = D_s^* \frac{\partial^2 C_s^*}{\partial z^2} + \phi_s^*(z) \quad (1)$$

where C is the concentration of CO_2 in the soil, D is the diffusion coefficient, t is time, z is depth, and ϕ is the production rate of CO_2 in the soil as a function of depth. Subscript ‘s’ refers to the soil and * refers to bulk CO_2 as

---

* E-mail address of corresponding author:
jaycaustin@live.com
DOI: 10.1346/CCMN.2014.0620402

opposed to ^{12}C or ^{13}C. The general solution of this equation is

$$C_s^*(z) = S(z) + C_a^* \tag{2}$$

where $S(z)$ is the concentration of CO_2 in the soil and C_a^* is the bulk concentration of CO_2 in the atmosphere. The production rate function can take different forms depending on the assumptions made about how CO_2 production varies with depth (ϕ_s^* in equation 1) (Cerling, 1999). The pedogenic gibbsite proxy is most sensitive to the soil respiration rate, which is dependent on the diffusion coefficient and soil CO_2 production rate, and the $\delta^{13}C$ value of the soil organic material (SOM) that is producing CO_2 in the soil. To assess the applicability of the model to CO_2 occluded in the gibbsite structure, a field test was conducted on an active Ultisol for comparison to a similar data set (Schroeder and Melear, 1999). The field test also enabled a more detailed evaluation of the general applicability of modeling assumptions related to the physical properties of the soil including porosity, tortuosity, and the $\delta^{13}C$ value of the soil biomass. The utility of the model will be increased if the general assumptions for parameters such as soil bulk density, tortuosity, and CO_2 production rate worked equally well for two sites with similar soil types and vegetation.

CO_2 collected during the dehydration of gibbsite is assumed to be liberated from defect sites where it is trapped during mineral formation in the soil. Bidentate carbonate anions have been shown to adsorb strongly to the surface of goethite and gibbsite (Su and Suarez, 1997). The nature of CO_2 incorporation differs from the cases of soil carbonate and goethite where the CO_2 is assumed to be part of the mineral structure. Infrared (IR) spectroscopy suggests that carbonate is present in goethite as a solid solution and is accommodated in an open channel parallel to the c^* axis (Yapp and Poths, 1990). The crystalline structure of gibbsite does not have the required space to accommodate a carbonate ion. In addition, the charge imbalance resulting from the exchange of an OH^- with a CO_3^{2-} ion prohibits a solid solution. A constant ratio yield (*i.e.* CO_2 to H_2O) during mineral dehydration/decarbonation at ~230ºC under vacuum demonstrates the stoichiometric breakdown of the goethite structure (Yapp and Poths, 1986). $Fe(O_{1-X},(CO_3)_X)OH$ (where X = moles of occluded CO_2) as shown by the reaction

$$Fe(O_{1-X})(CO_3)_XOH \rightarrow \tfrac{1}{2}\,Fe_2O_3 + \tfrac{1}{2}\,H_2O + XCO_2 \tag{3}$$

Alternatively as,

$$(1-X)FeOOH + XFeCO_3OH \rightarrow \tfrac{1}{2}\,Fe_2O_3 + \tfrac{1}{2}\,H_2O + XCO_2 \tag{4}$$

Similar stoichiometric responses for CO_2 yields from gibbsite have also been documented (Schroeder and Melear, 1999). The reaction below shows the stoichiometric C/H yielded at ~230ºC under vacuum.

$$Al(OH)_3XCO_2 \rightarrow \tfrac{1}{2}\,Al_2O_3 + \tfrac{3}{2}\,H_2O + XCO_2 \tag{5}$$

Values for X in goethite are related to F, which is defined as the molar ratio of CO_2:H_2O. Constant values of F during step-wise extraction of natural goethite range up to 0.01 (Yapp and Poths, 1991; Yapp, 1997) and values for natural gibbsite range up to 0.005 (Tabor and Yapp, 2005). Note that if similar numbers of moles of carbon are occluded in both minerals, then the C/H is smaller for gibbsite because of the greater water yield. Due to the presence of three possible OH^- sites for CO_3^{2-} anion bonding in gibbsite as compared to the single O^{2-} site in goethite, it is expected that on a molar basis gibbsite will have a greater capacity for carbon sequestration. In fact, comparison of CO_2 yield (µmoles CO_2/mg sample) for published values of both goethite and gibbsite shows that the ratio of gibbsite CO_2: goethite CO_2 is ~3:1 (Tabor and Yapp, 2005; Yapp and Poths, 1991).

The $\delta^{13}C$ values observed by Schroeder and Melear (1999) suggest diffusion-controlled soil atmosphere mixing. Analytical and numerical modeling predicted a soil respiration rate which is an order of magnitude slower than the measured rate (Schroeder *et al.*, 2006). The present study proposes that the concomitant $\delta^{18}O$ composition of the CO_2 may give additional insight into the process controlling the isotopic signatures of CO_2 occluded in gibbsite and the possibility to detect exchange of isotopes with the environment after mineral formation, a process that could compromise the $\delta^{13}C$ proxy.

The $\delta^{18}O$ compositions of soil CO_2 have been studied extensively because they are useful for modeling the carbon cycle, where it has been shown that the soil is a large reservoir that contributes CO_2 to the atmosphere (Hesterberg and Siegenthaler, 1991; Miller *et al.*, 1999; Stern *et al.*, 1999). The oxygen isotopic composition of CO_2 produced in soil by plant and microbial respiration is expected to be in equilibrium with soil water because the soil water is assumed to be the same inside and outside the roots (Cuntz *et al.*, 2003). The $\delta^{18}O$ value of soil CO_2 is controlled by diffusion through the soil and the isotope exchange reaction between soil water and soil gas CO_2. $^{12}C^{16}O^{18}O$ has a slower diffusivity than $^{12}C^{16}O_2$ due to its greater mass. Differences in mass-dependent diffusion rates result in an enrichment of 8.7‰ in soil CO_2 if diffusion is the only process controlling the $\delta^{18}O$ value (Miller *et al.*, 1999). The relatively rapid exchange of oxygen atoms occurs in the reaction,

$$^{12}C^{16}O^{16}O + H_2^{18}O \rightarrow {}^{12}C^{16}O^{18}O + H_2{}^{16}O \tag{6}$$

Quasi-equilibrium exists between the soil water and the enriched soil CO_2. Experimental work under rate-limiting conditions showed that this reaction will reach equilibrium in 110 s at 25ºC (Stern *et al.*, 1999). In soils however, this reaction usually does not reach equilibrium due to the transport-limiting nature of the soil pore networks (Hsieh *et al*., 1998). Therefore, the expected $\delta^{18}O$ of the soil CO_2 is expected to be enriched by some amount less than 8.7‰ compared to soil water, depending on the rate of the isotope exchange reaction.

Note that in experiments conducted on goethite, the $\delta^{18}O$ values of CO_2 extracted during dehydration varied as a function of the reaction rate (Yapp, 2003). The variation is the result of exchange between the liberated CO_2 and H_2O. A similar result has been shown for kaolinite and dickite (Girard and Savin, 1996). Fractionation of oxygen isotopes during dehydration calls into question the validity of conclusions regarding the co-variation of $\delta^{18}O$ and $\delta^{13}C$ values in this study. The $\delta^{18}O$ data are presented here and the implications of these questions are discussed in detail.

The purpose of the present study was to examine the $\delta^{13}C$ and $\delta^{18}O$ compositions of CO_2 occluded in gibbsite in an active soil profile with the aim of assessing the validity of using this signature as a paleoclimate proxy in paleosols.

SITE DESCRIPTION AND METHODS

The sampling location is a moderately dense deciduous forest located in the J. Phil Campbell Natural Resource Conservation Center, Watkinsville, Georgia, USA, which has been operated by the USDA-ARS since 1937 (33º51′55″N, 83º27′23″W). Historical aerial photography and anecdotal evidence from local farmers confirm that the ~3.5 acre (1.4 hectare) plot has been fenced and managed as a forest for more than a century and escaped cotton management and tillage. Plants using a C_3 photosynthetic carbon fixation pathway are assumed to be the only input of respired CO_2. This site was selected specifically to mitigate contributions from carbon isotope pools that may have been generated using other pathways (*i.e.* C_4). The parent-rock material is the Athens Gneiss and the soil is identified as CYB2 (Cecil series soil eroded, with up to 2% slope) (Robertson, 1968). This field location was also chosen for its relatively high landscape position, to minimize colluvial inputs from other locations in the watersheds sited at the experiment station.

Soil material was excavated from a 1 m^2 square area at discrete depth layers (*e.g.* 0−5 cm, 5−10 cm, *etc.*). Each layer was removed using a hand trowel and packed into 5-gallon buckets, which were then closed and sealed and stored in the field before processing at the laboratory. The sample at the top of the O_a horizon (0−5 cm depth) was taken after removal of large, loose, leaf litter which consisted mostly of organic material with some mineral material. Minor sampling overlap occurred between the 5−10 cm and 10−20 cm segments due to heterogeneities in the pit. Beyond 20 cm, to a depth of 100 cm, the pit was dug over a period of three months with more accurate depth control. Additional samples beyond 100 cm depth were collected from three peripheral auger cores extracted ~1 m from the pit edges. Auger core samples were used along with the pit sample splits to determine percent sand, silt, and clay (by weight) using standard sieve and settling-tube methods. Bulk-sample stable carbon isotope composition and percent organic carbon analysis was performed prior to chemical treatment at the University of Georgia Stable Isotope & Soil Biology Lab (http://swpa.uga.edu) using standard tin capsules, micro-Dumas combustion, a Thermo Finnigan Delta V, Isotope Ratio Mass Spectrometer (Bremen, Germany) coupled to a Carlo Erba NA1500 CHN Analyzer (Milan, Italy) *via* a Thermo Finnigan Conflo III Interface, and standards (relative to Vienna Pee Dee Belemnite).

The <2 μm size fraction was treated chemically with 0.5 M HCl and 30% H_2O_2 following the methods described by Yapp and Poths (1996) and Schroeder and Melear (1999) to produce ~300−500 g of sample mass. X-ray diffraction (XRD) analyses were performed using a Bruker D8 Advanced diffractometer (Co radiation). All samples were examined before and after chemical treatments to verify that no change in mineralogy had occurred as a result of the chemical treatment. No peaks for carbonates in the original diffraction patterns of any sample material were observed. Ratios of gibbsite (002) peak height to the kaolinite (001) peak height were calculated and defined as the mineral index (Figure 1) to allow comparison of the relative abundance of gibbsite at different depths in the soil.

The treated sample material was heated in a step-wise procedure to allow for the collection of CO_2 liberated from the mineral structure during the thermal breakdown of gibbsite and goethite following the procedure of Schroeder and Melear (1999) in the University of Georgia Stable Isotope Laboratory. During sample collection, the CO_2 was separated cryogenically from the co-evolved H_2O using a dry ice ethanol mixture.

The CO_2 collected was analyzed by conventional dual inlet mass spectrometry using a Finnigan MAT 252 (Thermo, USA) instrument equipped with a microvolume coldfinger for the stable carbon and oxygen isotope ratios. The volume of CO_2 analyzed ranged from 20 to <1 micromoles (μmol). The stable carbon isotope ratios were plotted to determine the plateau $\delta^{13}C$ value, which indicates stoichiometric breakdown and that the CO_2 originates from a single pool assumed to be trapped CO_2 in the gibbsite structure.

RESULTS

Textural analysis returned values typical of the regional Cecil-series soil, with the maximum % clay (63%) occurring at the top of the Bt horizon (30−50 cm) (Figure 1, Table 1). The wt.% organic carbon reached a maximum of 6% at the surface and the $\delta^{13}C$ value of the

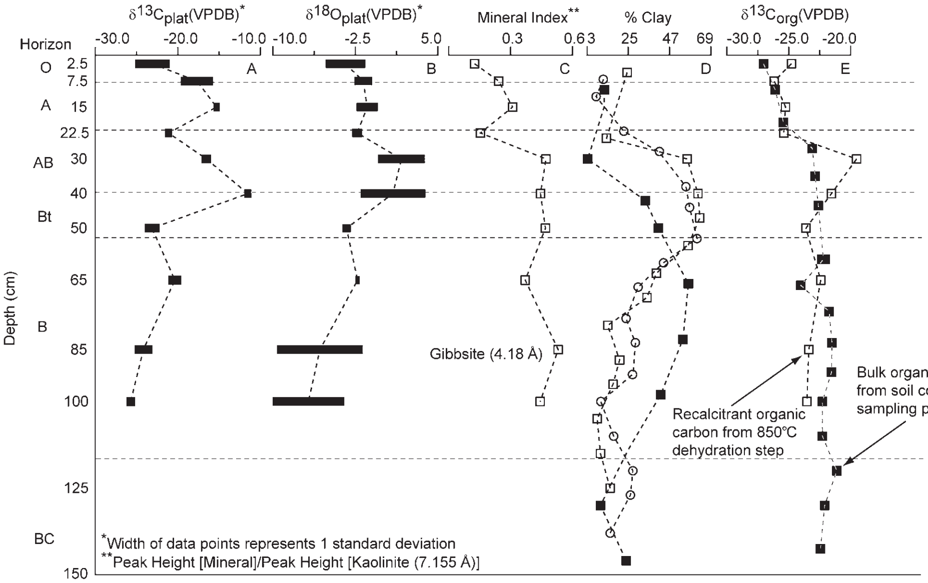

Figure 1. Compilation of all data collected from the field site: (A) δ^{13}C values of plateaus from the dehydration process (the width of the box represents variability in the results from multiple analyses); (B) δ^{18}O values of plateaus from the dehydration process (the width of the box represents variability in the results from multiple analyses); (C) mineral index defined as the XRD peak height of gibbsite as a ratio with kaolinite peak height; (D) percentage of clay determined from three soil cores located 1 m from the soil pit; (E) δ^{13}C values of bulk SOM (filled squares) and the recalcitrant carbon collected during the final 850ºC heat treatment (open squares).

bulk untreated soil material is −27.5‰, consistent with a C_3-dominated environment. Organic carbon δ^{13}C values increase with increasing depth as seen in other studies (Bowen and Beerling, 2004) (Figure 1). At the conclusion of the step-wise dehydration process, a final 850ºC step served to completely dehydrate all remaining gibbsite in the sample (Table 2). The carbon collected during this step may be recalcitrant organic carbon that was not removed during the chemical treatment or the initial oxidation step. The δ^{13}C value of recalcitrant carbon is used as a proxy for the δ^{13}C value of the organic material in the soil when using this method to estimate paleo-PCO_2 (Yapp and Poths, 1996). Although the δ^{13}C values of the 850ºC step are, on average, more depleted than bulk SOM by 3.5‰, with the exception of two samples, the close agreement between the bulk SOM and recalcitrant carbon δ^{13}C values reinforces the use of this CO_2 as an acceptable estimate for soil organic carbon.

X-ray diffraction analysis further showed that the majority of the <2 μm material in the soil is kaolin and gibbsite with minor amounts of goethite and hydroxy-interlayered vermiculite (HIV) (Figure 2). A mica phase exists in the 0−5 cm and 20−25 cm samples and is indicative of the foliated gneissic parent material. Shallow samples also contained more goethite than the other samples; gibbsite is the dominant oxy-hydroxide phase present, however. The upper 5−10 cm of the soil contained the largest amounts of HIV. The presence of HIV (which can potentially host interlayer organics), along with the greater bulk organic content, accounted for increased yield of CO_2 from the samples taken at shallow depths. CO_2 yields at 0−5 cm varied between 35 and 80 μmoles g^{-1}, whereas at depths >5 cm (when HIV did not dominate the mineral assemblage) yields were <20 μmoles g^{-1} with little variability amongst all deeper samples (Table 3).

To ensure that the CO_2 collected during the dehydration of gibbsite was representative of the trapped CO_2, the ratio of moles of CO_2 to moles of H_2O (F value, nCO_2/nH_2O) was plotted *vs.* the progress of dehydration (Figure 3). As discussed previously, when the CO_2 is released from the mineral structure the F value should remain constant. CO_2 collected from 0−5 cm did not show a constant F value during any part of the dehydration process. Combined with the large and variable CO_2 yield of these samples, the large organic content of the upper 5 cm of the soil, and the presence of HIV, the CO_2 collected is concluded to have originated from multiple sources and the δ^{13}C values are, therefore, not useful proxies (Figure 3, sample 0005). The rest of the samples did show constant F values and the CO_2 from the plateaus identified were assumed, therefore, to be representative of CO_2 trapped in the gibbsite structure (Figure 3). δ^{13}C values of the plateaus for the remaining samples showed enrichment from the surface to 40 cm followed by the expected depletion with depth (Figure 1) (Table 2). Similarly, the measured δ^{18}O values were most enriched at 30 cm and became more depleted with depth. Keeping in mind the caveat that there may be

Table 1. Percent clay and total carbon and $\delta^{13}C$ values for untreated bulk-soil samples from two cores adjacent to the soil pit and from the soil pit itself.

Sample ID		Depth (cm)	% Clay	% Total C	$\delta^{13}C$ (‰ VPDB)
C11530	Core 1	23	12.2	1.30	−25.78
C14450		47	34.0	0.95	−25.21
C15066		58	41.1	0.43	−24.67
C16682		74	57.0	0.44	−25.25
C18298		90	54.1	0.40	−25.86
C1114130		122	42.3	0.11	−24.35
C1114130		122	24.9	0.12	−23.59
C30005	Core 3	3	6.8	5.71	−27.05
C30515		8		1.53	−26.10
C31524		20	13.4	0.71	−25.43
C32430		27	56.4	0.59	−23.70
C33040		35	62.1	0.43	−22.87
C34047		44	63.1	0.32	−22.61
C35563		59	56.9	0.12	−22.32
C35563		59	40.0	0.12	−22.05
C36370		67	34.9	0.31	−24.02
C37078		74	14.1	0.09	−21.74
C37888		83	20.4	0.13	−21.51
C38895		92	16.9	0.07	−21.55
C395105		100	8.4	0.15	−22.28
C3105115		110	10.2	0.10	−22.28
C3115125		120	15.3	0.09	−21.12
C3125135		130		0.09	−22.10
C3135150		143		0.10	−22.44
FS0005	Soil Pit	3		0.95	−26.07
FS0515		10		0.32	−22.58
FS1020		15		0.25	−20.29
FS2025		23		0.22	−21.55
FS32025		23		0.83	−26.23
FS2535		30		0.17	−17.40
FS3545		40		0.09	−18.03
FS4555		50		0.10	−19.92
FS5575		65		0.10	−20.08
FS5575		65		0.07	−20.07
FS7595		85		0.09	−20.64
FS95105		100		0.09	−20.61

Table 2. Mineral index, plateau $\delta^{13}C$ and $\delta^{18}O$ values of treated samples, and $\delta^{13}C$ values of the 850ºC dehydration step.

				Plateau $\delta^{13}C$ (‰ VPDB)			Plateau $\delta^{18}O$ (‰ VPDB)			850ºC $\delta^{13}C$ (‰ VPDB)	
Sample ID	Depth (cm)	Mineral index	*n*	$\delta^{13}C$	s.d.	*n*	$\delta^{18}O$	s.d.	*n*	$\delta^{13}C$	s.d.
0005	3	0.13	5	−23.3	2.2	5	−3.3	1.8	4	−24.6	2.2
0515	8	0.24	3	−17.5	2.1	3	−1.8	0.8	2	−26	0.2
1020	15	0.31	3	−15.3	0.3	3	−1.2	1.0	2	−25.1	2.6
2025	23	0.15	3	−21.1	0.4	3	−2.5	0.5	2	−25.2	0.4
2535	30	0.47	3	−16.5	0.6	3	1.3	2.1	3	−19.3	0.7
3545	40	0.44	3	−11.5	0.4	3	0.9	2.9	3	−21.4	0.2
4555	5	0.47	3	−23.1	0.9	3	−3.3	0.4	1	−23.4	
5575	65	0.37	3	−20.4	0.8	3	−2.5	0.8	2	−22.2	0.5
7595	85	0.53	3	−24.2	1.1	3	−5.8	3.9	3	−23.2	1
95105	100	0.44	3	−25.7	0.5	3	−9.2	3.3	3	−23.3	0.7

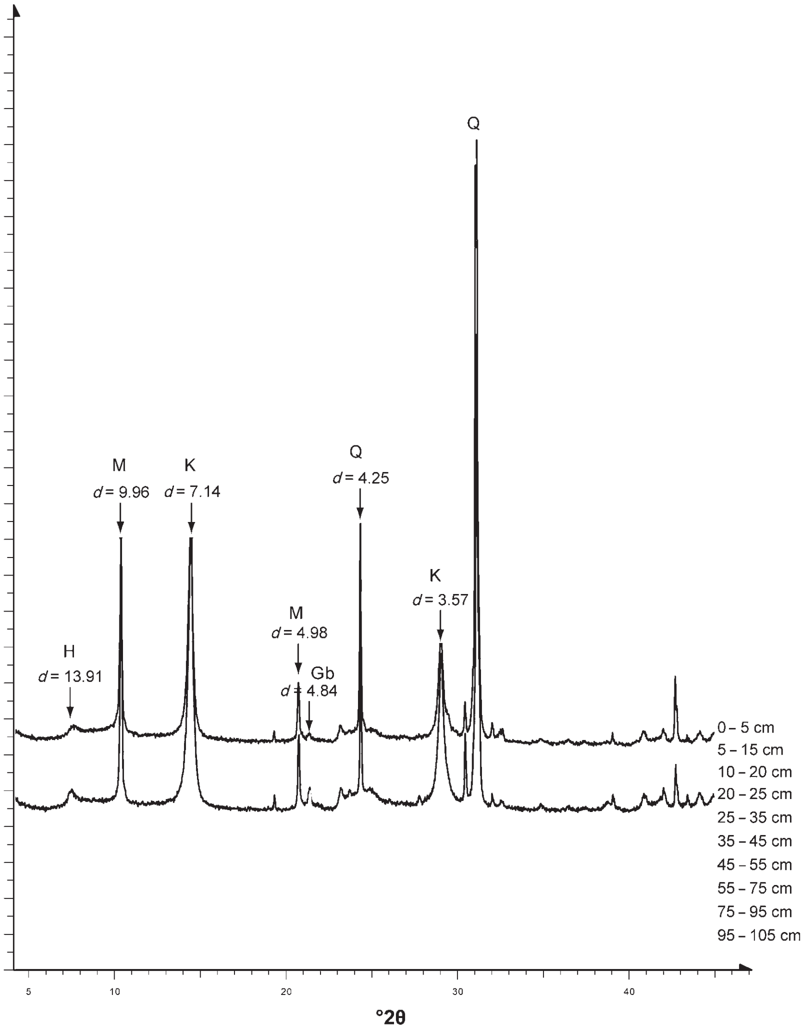

Figure 2. XRD patterns (Co radation) of the <2 μm size fraction of soil material (after chemical treatment). H = hydroxy interlayer vermiculite, M = mica, K = kaolinite, Gb = gibbsite, Q = quartz.

isotope exchange between the CO_2 and H_2O during sample collection, $\delta^{18}O$ values below this depth followed the expected depth profile for diffusion.

Examining the patterns of stable carbon and oxygen isotopic composition trends with depth for the entire soil profile, the one-dimensional (1D) Fickian diffusion-process could not describe the results. Generally, three regions of the soil profile appeared to reflect different carbon occlusion processes. In the upper portion of the soil, above the Bt horizon, the $\delta^{13}C$ values changed from relatively depleted (*i.e.* close to the value of SOM) to a maximum enrichment in the A horizon (15 cm). Values were more depleted near the AB horizon (22 cm). Between the AB and Bt horizons (22–40 cm), there was a large enrichment of ^{13}C with maximum enrichment of both oxygen and carbon isotopes corresponding with the top of the Bt horizon (1.3 and −11.5 VPDB, respectively). At depths > 40 cm, $\delta^{13}C$ values returned to those expected deep in the soil for a 1D Fickian diffusion process.

DISCUSSION

The $\delta^{13}C$ value of CO_2 in the soil pore space is understood to be controlled by the diffusive mixing of CO_2 produced at depth in the soil and CO_2 influx from the atmosphere (Cerling, 1984, 1991; Cerling *et al.*, 1989). CO_2 respired in the soil, by plant roots and microbes, has an initial $\delta^{13}C$ value that corresponds to the photosynthetic pathway used by the plants. The degree of mixing with the atmosphere is determined by the rate of CO_2 flux through the soil. These two factors, therefore, have the greatest degree of influence over final $\delta^{13}C$ value of the pore space CO_2 (Cerling, 1991; Austin, 2011). The soil CO_2 efflux rate is a product of the concentration gradient between the atmosphere and the soil pore space and the tortuosity of the soil pore space.

The $\delta^{18}O$ value of soil CO_2 is also understood to be controlled by the factors discussed above as they affect diffusion in addition to the isotope exchange between

Table 3. Gibbsite dehydration CO_2 and H_2O yields.

Sample ID	Sample weight (g)	Weight lost (g)	Step	Time (min)	CO_2 yield (μmol)	CO_2 release rate (μmol/min)	H_2O yield (μmol)	F	$\delta^{13}C$	$\delta^{13}C$ s.d.	$\delta^{18}O$	$\delta^{18}O$ s.d.
000501	0.554	0.051	1	45	4.9	0.11	85.8	0.06	−19.4	0.024	−2.3	0.036
			2	45	2.3	0.05	49.1	0.05	−19.9	0.004	−3.3	0.077
			3	45	2.0	0.04	23.6	0.08	−19.4	0.061	−3.6	0.042
			4	60	2.5	0.04	26.9	0.09	−19.6	0.024	−2.7	0.055
			5	120	2.6	0.02	18.6	0.14	−20.9	0.027	−3.8	0.039
			6	59	11.5	0.19	717.1	0.02				
000502	0.731	0.069	1	45	4.8	0.11			−23.1	0.045	−4.6	0.046
			2	45	8.0	0.18	34.6	0.23	−23.0	0.029	−2.3	0.078
			3	45	6.1	0.14	29.2	0.21	−23.8	0.035	−2.1	0.035
			4	60	11.9	0.20	26.8	0.44	−24.7	0.021	−1.8	0.020
			5	120	14.4	0.12	46.3	0.31	−25.0	0.074	−2.1	0.078
			6	30	30.1	1.00	81.0	0.37	−24.7	0.035	−4.6	0.030
000503	0.620	0.058	1	45	6.1	0.14	56.7	0.11	−21.6	0.024	0.1	0.060
			2	45	5.5	0.12	51.5	0.11	−21.1	0.039	−0.1	0.033
			3	45	3.2	0.07			−23.9	0.025	−1.3	0.069
			4	60	6.5	0.11	33.1	0.20	−23.8	0.027	−1.4	0.049
			5	120	8.4	0.07	38.8	0.22	−25.8	0.055	−1.7	0.061
			6	30	31.0	1.03	285.8	0.11	−21.4	0.084	−4.7	0.088
000504	0.508	0.050	1	45	3.0	0.07	24.4	0.12	−24.8	0.048	−6.1	0.058
			2	45	7.5	0.17	39.5	0.19	−24.5	0.019	−5.3	0.023
			3	45	8.0	0.18	36.9	0.22	−24.6	0.016	−5.6	0.033
			4	60	11.4	0.19	35.0	0.33	−24.9	0.029	−7.1	0.044
			5	120	16.0	0.13	44.8	0.36	−25.2	0.015	−7.8	0.028
			6	30	14.0	0.47	51.3	0.27	−26.2	0.022	−9.9	0.028
000505	0.697	0.064	1	45	6.3	0.14	36.5	0.17				
			2	48	8.6	0.18	49.8	0.17	−23.7	0.032	−3.6	0.027
			3	42	5.7	0.14			−24.6	0.028	−3.4	0.055
			4	60	10.9	0.18	43.7	0.25	−25.6	0.044	−4.2	0.045
			5	120	15.4	0.13	44.7	0.34	−25.7	0.055	−3.3	0.031
			6	30	20.7	0.69	62.1	0.33	−26.1	0.024	−5.5	0.049
051501	0.573	0.081	1	45	2.3	0.05	42.5	0.05	−14.3	0.023	−3.4	0.030
			2	45	3.0	0.07	55.3	0.05	−15.3	0.015	−2.6	0.066
			3	45	2.2	0.05	33.1	0.07	−15.0	0.083	−1.8	0.199
			4	60	3.1	0.05			−21.1	0.030	−2.7	0.077
			5	120	6.3	0.05	78.4	0.08	−22.7	0.027	−0.3	0.062
			6	30	6.7	0.22	98.3	0.07	−26.1	0.036	−9.7	0.040
051502	0.541	0.076	1	42	1.8	0.04			−15.6	0.014	−2.6	0.042
			2	48	2.8	0.06	36.3	0.08	−18.0	0.025	−1.0	0.024
			3	45	2.4	0.05	27.1	0.09	−20.2	0.041	−0.2	0.108
			4	60	2.9	0.05	37.8	0.08	−22.7	0.010	−2.7	0.046
			5	120	8.5	0.07						
			6	30								
051503	0.668	0.096	1	45	4.3	0.10	255.9	0.02	−13.9	0.018	−1.1	0.036
			2	45	3.7	0.08	103.9	0.04	−15.1	0.027	−0.7	0.115
			3	45	1.9	0.04	40.6	0.05	−18.3	0.013	−1.0	0.026
			4	60	2.7	0.05	54.0	0.05	−21.6	0.027	−2.6	0.049
			5	120	3.3	0.03	122.6	0.03	−23.8	0.016	−2.5	0.051
			6	30	10.8	0.36	64.7	0.17	−25.8	0.024	−5.2	0.048
102001	0.607		1	45	2.8	0.06			−12.1	0.018	−1.2	0.029
			2	45	3.2	0.07	75.5	0.04	−11.9	0.020	−0.5	0.027
			3	45	1.9	0.04	41.0	0.05	−13.9	0.020	−0.2	0.026
			4	60	2.5	0.04	51.2	0.05	−17.2	0.043	−2.0	0.107
			5	120	2.8	0.02	48.8	0.06				
			6	30	4.4	0.15	48.4	0.09	−23.3	0.014	−7.6	0.025
102002	0.919	0.136	1	45	5.7	0.13	201.1	0.03				
			2	45	6.2	0.14	188.9	0.03	−11.5	0.016	−1.6	0.049
			3	45	2.7	0.06	75.2	0.04	−13.2	0.051	0.3	0.126
			4	60	3.3	0.06	83.9	0.04	−16.7	0.025	−1.4	0.051
			5	120	3.6	0.03	71.5	0.05				
			6	30		0.00	63.2	0.00	−26.9	0.032	−13.7	0.117
102003	0.662	0.098	1	45	2.4	0.05	102.0	0.02	−13.4	0.030	−3.0	0.057
			2	45	4.1	0.09	46.8	0.09	−12.6	0.019	−2.1	0.050
			3	45	3.1	0.07	82.0	0.04	−13.9	0.018	−1.2	0.021
			4	60	2.8	0.05			−17.0	0.033	−2.9	0.032
			5	120	3.3	0.03	75.3	0.04	−18.7	0.033	−1.2	0.094
			6	30								

Table 3 (*contd.*)

Sample ID	Sample weight (g)	Weight lost (g)	Step	Time (min)	CO$_2$ yield (μmol)	CO$_2$ release rate (μmol/min)	H$_2$O yield (μmol)	F	δ^{13}C	δ^{13}C s.d.	δ^{18}O	δ^{18}O s.d.
202501	0.825	0.094	1	45	2.1	0.05	106.1	0.02	−14.9	0.021	−2.0	0.069
			2	45	3.1	0.07	75.1	0.04	−16.4	0.007	−1.7	0.029
			3	45	2.1	0.05	41.0	0.05	−21.2	0.039	−2.8	0.057
			4	60	3.1	0.05			−20.7	0.011	−2.6	0.035
			5	120	3.5	0.03	51.0	0.07	−21.8	0.031	−2.5	0.044
			6	30	7.6	0.25	62.3	0.12	−25.0	0.031	−7.0	0.046
202502	0.578	0.067	1	45	4.5	0.10	229.1	0.02	−14.0	0.045	0.6	0.125
			2	45	2.9	0.06	65.7	0.04	−18.3	0.031	−1.5	0.026
			3	45	1.8	0.04	39.2	0.05				
			4	60	3.6	0.06	56.9	0.06	−20.7	0.018	−2.6	0.035
			5	120	3.5	0.03	42.9	0.08	−20.1	0.017	−3.1	0.022
			6	30	7.5	0.25			−25.5	0.055	−5.8	0.068
202503	0.579	0.067	1	45	1.5	0.03	54.9	0.03	−15.9	0.011	−1.9	0.027
			2	45	2.9	0.06	48.3	0.06	−17.1	0.024	0.8	0.035
			3	45	1.8	0.04	30.3	0.06	−19.1	0.016	−0.1	0.088
			4	60	2.5	0.04	40.8	0.06	−21.5	0.019	−2.5	0.030
			5	120	3.2	0.03	66.2	0.05	−21.5	0.016	−1.4	0.048
			6	30								
253501	0.639	0.149	1	45	2.6	0.06	336.2	0.01	−16.2	0.027	0.5	0.071
			2	45	3.2	0.07	298.6	0.01	−12.0	0.026	1.3	0.039
			3	45	0.7	0.02	27.0	0.03	−14.8	0.018	0.9	0.013
			4	60	1.5	0.03	44.3	0.03	−17.2	0.017	−0.8	0.066
			5	120	2.1	0.02	39.7	0.05				
			6	30	2.8	0.09	35.0	0.08	−19.6	0.014	−4.7	0.068
253502	0.742	0.115	1	45	2.5	0.06	229.0	0.01	−11.0	0.027	4.7	0.043
			2	45	2.3	0.05	98.9	0.02	−11.9	0.036	0.9	0.118
			3	45	1.4	0.03	44.5	0.03	−15.2	0.020	0.9	0.087
			4	60	2.1	0.04			−17.9	0.052	2.0	0.102
			5	120	2.4	0.02			−18.2	0.034	−0.6	0.038
			6	30	6.1	0.20	57.0	0.11	−19.8	0.017	−3.2	0.058
253503	0.909	0.141	1	45	2.2	0.05			−13.1	0.044	2.4	0.094
			2	45	3.5	0.08	72.2	0.05	−14.4	0.043	4.2	0.087
			3	45	2.5	0.06	43.6	0.06	−16.7	0.025	4.8	0.047
			4	60	3.3	0.06	58.0	0.06	−18.5	0.031	2.3	0.042
			5	120	4.0	0.03	57.2	0.07				
			6	30	4.4	0.15	54.2	0.08	−18.5	0.040	−3.0	0.061
354501	0.715	0.115	1	45	2.6	0.06	516.0	0.01	−14.9	0.020	1.9	0.080
			2	45	1.7	0.04	134.2	0.01	−10.9	0.004	1.7	0.018
			3	45	0.6	0.01	38.2	0.02	−17.6	0.016	−1.2	0.030
			4	60	1.0	0.02	63.6	0.02	−13.2	0.030	2.8	0.043
			5	120	1.0	0.01	51.5	0.02	−15.1	0.049	2.4	0.127
			6	30	8.2	0.27	112.1	0.07	−21.5	0.030	−7.4	0.051
354502	0.911	0.326	1	45	3.1	0.07	569.1	0.01	−13.2	0.023	−0.7	0.022
			2	45	1.2	0.03	101.8	0.01	−10.9	0.088	−0.8	0.243
			3	45	0.8	0.02	51.2	0.02	−12.0	0.026	0.7	0.042
			4	60	1.1	0.02	82.0	0.01	−13.5	0.033	−3.1	0.048
			5	120								
			6	30	25.1	0.84			−21.5	0.023	−7.5	0.065
455501	0.833		1	45	2.0	0.04	49.5	0.04	−18.2	0.005	−2.0	0.049
			2	45	1.6	0.04	53.0	0.03	−20.8	0.009	−3.1	0.023
			3	45	1.0	0.02	29.1	0.03	−22.5	0.015	−1.6	0.029
			4	60	1.8	0.03	40.1	0.04	−24.5	0.024	−4.0	0.071
			5	120	1.9	0.02	32.9	0.06	−23.8	0.010	−2.3	0.022
			6	30								
455502	0.983	0.148	1	45	1.0	0.02	60.8	0.02				
			2	45	2.1	0.05	44.0	0.05	−22.0	0.027	−3.1	0.016
			3	45	1.2	0.03	31.9	0.04	−24.9	0.033	−3.5	0.076
			4	60	2.3	0.04	41.1	0.06	−25.5	0.006	−4.4	0.053
			5	120	2.4	0.02	39.6	0.06	−23.7	0.011	−4.4	0.017
			6	30	14.5	0.48	24.5	0.59				
455503	1.038	0.160	1	45	1.6	0.04	52.0	0.03	−19.3	0.021	−2.7	0.011
			2	45	2.1	0.05	42.6	0.05	−21.6	0.022	−3.5	0.013
			3	45	1.4	0.03	36.5	0.04	−22.7	0.021	−3.4	0.032
			4	60	2.4	0.04	45.2	0.05	−23.6	0.024	−4.0	0.062
			5	120	2.4	0.02	42.3	0.06	−22.4	0.027	−3.2	0.045
			6	30	7.7	0.26	38.0	0.20	−23.4	0.057	−8.3	0.062

Table 3 (*contd.*)

Sample ID	Sample weight (g)	Weight lost (g)	Step	Time (min)	CO_2 yield (μmol)	CO_2 release rate (μmol/min)	H_2O yield (μmol)	F	$\delta^{13}C$	$\delta^{13}C$ s.d.	$\delta^{18}O$	$\delta^{18}O$ s.d.
557501	0.935	0.128	1	35	0.7	0.02	39.5	0.02	−19.0	0.011	−2.9	0.024
			2	45	0.8	0.02	25.4	0.03	−20.9	0.037	−2.5	0.015
			3	45	0.8	0.02	34.3	0.02	−21.6	0.022	−1.4	0.019
			4	60								
			5	120	1.3	0.01	28.7	0.05	−21.2	0.040	−2.4	0.126
			6	30	2.0	0.07	19.7	0.10	−22.5	0.013	−9.0	0.025
557502	1.033	0.147	1	45	0.8	0.02	45.9	0.02	−18.1	0.029	−2.6	0.091
			2	45	1.2	0.03	39.7	0.03	−19.1	0.040	−2.6	0.059
			3	45	0.9	0.02	32.7	0.03	−19.8	0.021	−1.6	0.066
			4	60	1.1	0.02	37.8	0.03	−21.1	0.025	−3.2	0.132
			5	120	1.3	0.01	34.6	0.04	−20.4	0.002	−2.4	0.031
			6	30	1.6	0.05	24.5	0.07	−21.9	0.036	−7.5	0.108
557503	0.940	0.120	1	45								
			2	45	0.3	0.01			−19.7	0.009	−3.4	0.029
			3	45	0.4	0.01			−20.0	0.050	6.5	0.129
			4	60	0.2	0.00			−22.6	0.023	−4.3	0.014
			5	120	0.2	0.00			−21.5	0.038	−3.0	0.083
			6	30	0.2	0.01						
759501	1.005	0.111	1	45	2.4	0.05			−19.7	0.016	−2.1	0.037
			2	45	2.8	0.06			−21.3	0.017	−1.9	0.061
			3	45	0.4	0.01			−24.1	0.067	−2.9	0.170
			4	60	2.2	0.04			−24.5	0.022	−4.0	0.040
			5	120	3.6	0.03			−21.8	0.059	−3.8	0.195
			6	30	6.4	0.21			−22.4	0.043	−6.5	0.026
759502	0.916	0.145	1	45	3.8	0.08			−21.5	0.012	−4.1	0.026
			2	45	1.5	0.03			−25.5	0.023	−8.6	0.023
			3	45	0.4	0.01			−25.5	0.045	−10.3	0.046
			4	60	1.1	0.02			−24.5	0.036	−13.1	0.122
			5	120	1.2	0.01			−23.3	0.037	−13.6	0.060
			6	30	28.0	0.93						
759503	0.976	0.156	1	45	3.7	0.08			−21.9	0.011	−1.4	0.027
			2	45	1.9	0.04			−30.3	0.055	−9.4	0.139
			3	45	1.4	0.03			−23.8	0.006	−3.5	0.028
			4	60	0.6	0.01			−22.3	0.032	−5.1	0.086
			5	120	9.2	0.08			−19.1	0.043	−0.1	0.069
			6	30	28.0	0.93			−22.9	0.029	−11.0	0.051
9510501	0.977	0.142	1	45	2.8	0.06			−19.7	0.017	−4.8	0.041
			2	45	1.1	0.02			−26.1	0.021	−7.1	0.045
			3	45	0.9	0.02			−26.2	0.046	−4.8	0.089
			4	60	1.2	0.02			−26.1	0.008	−5.5	0.040
			5	120	1.3	0.01			−23.4	0.013	−6.2	0.034
			6	30	28.0	0.93			−24.0	0.060	−10.1	0.080
9510502	0.999	0.145	1	45	2.9	0.06			−19.6	0.012	−7.1	0.037
			2	45	1.0	0.02			−26.4	0.167	−13.0	0.250
			3	45								
			4	60	0.9	0.02			−23.9	0.038	−12.4	0.100
			5	120	0.9	0.01			−21.8	0.024	−11.1	0.042
			6	30					−23.4	0.022	−10.2	0.035
9510503			1	45	2.9	0.06			−19.5	0.019	−6.9	0.030
			2	45	0.9	0.02						
			3	45	0.8	0.02			−26.0	0.031	−9.5	0.022
			4	60	0.9	0.02			−25.6	0.050	−11.3	0.141
			5	120	1.0	0.01			−23.8	0.013	−12.4	0.100
			6	30								

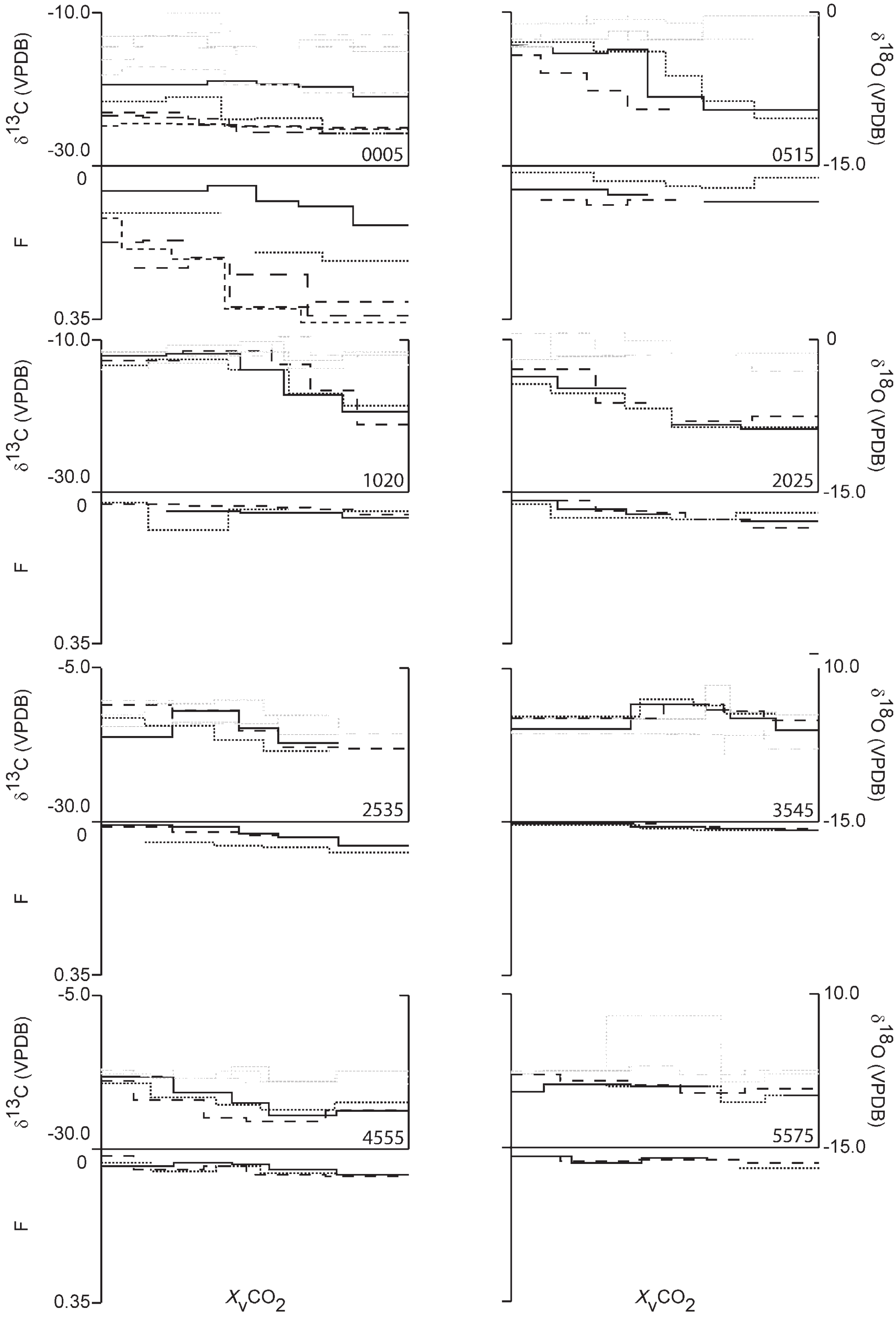

Figure 3. Dehydration and decarbonation steps for sample replicates. Solid, dashed, and dotted lines represent xxxx01, xxxx02, and xxxx03, respectively, where xxxx is the sample ID as labeled on each horizontal axis (see also Table 3). X_VCO_2 is the fraction of the total CO_2 yield at each step. $\delta^{13}C$ is plotted in black and $\delta^{18}O$ is plotted in gray.

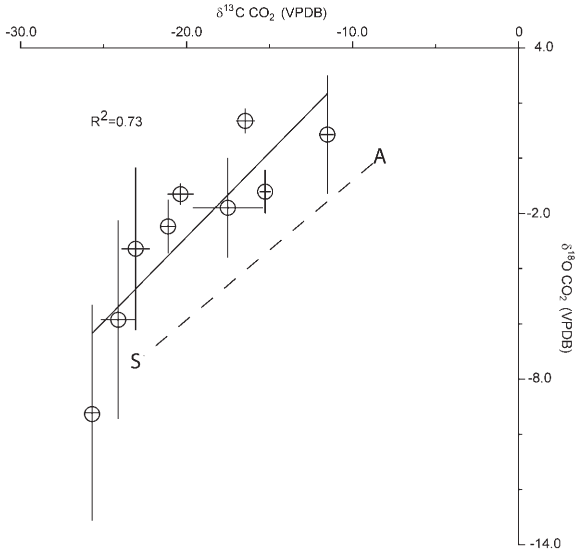

Figure 4. $\delta^{13}C$ *vs.* $\delta^{18}O$ of the plateau samples for each depth. Error bars represent one standard deviation of all plateau samples at each depth (Figure 3), $R^2 = 0.73$ ($p < 0.01$). S represents the average SOM value as determined by all samples collected during the 850ºC heat treatment in the dehydration procedure. A represents an average value for atmospheric CO$_2$ (Chen *et al.*, 2013). The line between atmosphere and SOM is arbitrary and represents linear mixing between the two reservoirs.

soil CO$_2$ and H$_2$O (Stern *et al.*, 1999). Because the factors affecting these two isotopes are similar, correlation between the $\delta^{13}C$ and $\delta^{18}O$ values of CO$_2$ occluded in the gibbsite structure with a possible shift in the $\delta^{18}O$ value due to isotope exchange seems likely. A linear relationship existed between the $\delta^{13}C$ and $\delta^{18}O$ values of CO$_2$ measured in this study ($R^2 = 0.73$) (Figure 4) and was offset roughly parallel to a hypothetical mixing line between the atmosphere (Chen *et al.*, 2013) and the SOM, indicating that the process was controlled by diffusion. A process other than diffusion must be responsible for the offset, however.

Fractionation resulting from oxygen exchange between the CO$_2$ and transition states as the CO$_2$ moves through the mineral structure during dehydration must be considered. Fractionation of oxygen isotopes of CO$_2$ occluded in goethite has been modeled as a function of the reaction rate, where the greatest extent of fractionation occurs in association with slow reaction rate (Yapp, 2003). Gibbsite dehydration was assumed to proceed *via* a similar process, by the reaction

$$2Al(OH)_3 \rightarrow 2AlO(OH)^* + 2H_2O \rightarrow 2AlO(OH)^* \rightarrow Al_2O_3 + H_2O \tag{5}$$

where AlO(OH)* represents a transition state. A reasonable inference is that a similar reaction rate-controlled fractionation might occur. Using the method described by Yapp (2003), ln$X$s(H$_2$) was plotted *vs*. the cumulative reaction time to determine the reaction rate (Figure 5). $X_s(H_2)$ was used to determine the progress of the reaction and is defined as the fraction of the total H$_2$ remaining in the sample. All samples in this study showed very similar reaction rates. If it was further assumed that the magnitude of fractionation for gibbsite was similar to goethite for a given difference in reaction rate, the measured $\delta^{18}O$ values relative to each other were expected to be within 1‰ of the relative values of the original unfractionated CO$_2$ $\delta^{18}O$ values. Therefore,

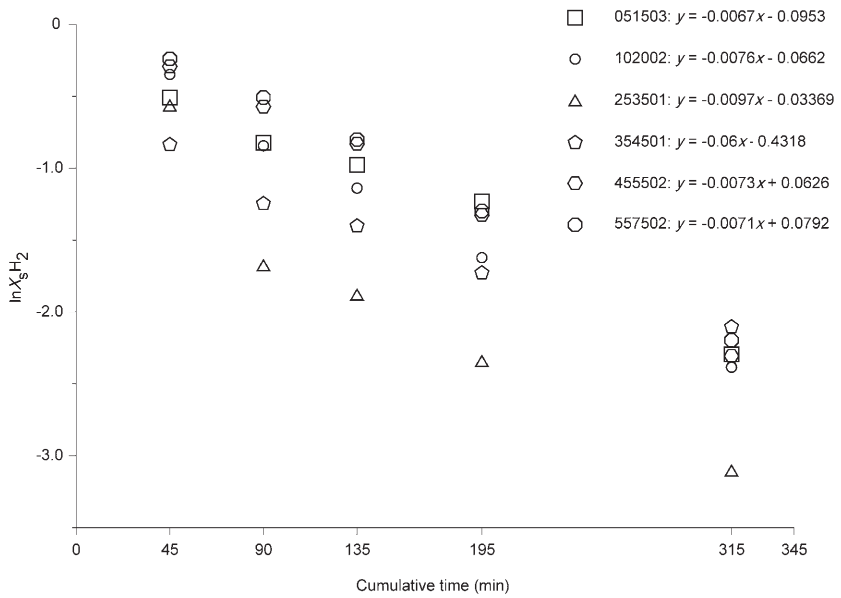

Figure 5. Ln$X_s(H_2)$ *vs*. cumulative dehydration time for gibbsite samples 051503, 102002, 253501, 35450, 455502, and 557502. R^2 for all samples >0.97 except 253501 ($R^2 = 0.92$) and 354501 ($R^2 = 0.86$). See Yapp (2003) and the text.

while the absolute values measured were not useful, the relative values were, and were used to establish the relationship between δ^{13}C and δ^{18}O. Until the structural δ^{18}O value of gibbsite is measured, this discussion will continue using these assumptions.

In addition to fractionation during dehydration, the difference between the measured mixing line and the theoretical mixing line could represent isotope exchange between CO_2 and H_2O in the soil pore space prior to inclusion in the mineral structure. As shown by Stern (1999), the amount of exchange is dependent on the residence time of the CO_2 in the soil pore space. Therefore, the degree of change from the assumed pore space CO_2 δ^{18}O value may have implications for inferring the soil diffusion conditions during mineral formation. For example, a relatively small difference between the mixing line for atmosphere and SOM may represent high soil respiration rates, precluding isotope exchange. Conversely, a large shift implies a slow respiration rate, allowing for more isotope exchange. Until the reality of fractionation during sample collection is resolved, exchange and diffusion fractionation effects cannot be quantified.

Finally, the δ^{18}O value of SOM or the atmosphere or both may change over time. Determining the magnitude of change was complicated by the uncertainty of the sequence of formation and transport of gibbsite in the soil compared to the age of the active soil-forming processes. Cosmogenic ^{10}Be estimates of the soil residence time of the Southern Piedmont ranged between 1.3 and 3.1 million years (Bacon *et al.*, 2012). Radiogenic carbon dates of pedogenic gibbsite measured at Panola Mountain, Georgia showed at least two distinct populations deep in the soil on a millennial time scale (Schroeder *et al.*, 2001). Differences between mineral 'ages' and soil residence time suggested that mineral populations are reforming continuously in the soil. Therefore, CO_2 occluded in gibbsite near the surface should be representative of the relatively recent past environment (*i.e.* <10,000 y). Atmospheric CO_2 δ^{13}C has been depleted by ~1.2‰ over the past 250 y (post-industrial revolution) by the release of depleted organic carbon into the atmosphere by the burning of fossil fuels (Francey *et al.*, 1999). δ^{18}O of atmospheric CO_2 for time scales of soil formation is influenced by climate, as it relates to changes in precipitation, and the carbon cycle, as it relates to changes in plant type and respiration (Welp *et al.*, 2011).

While the correlation between δ^{13}C and δ^{18}O values indicated that diffusion was controlling the isotopic compositions of soil CO_2, the depth profile of δ^{13}C values did not match the progressive decrease with depth expected in a diffusion-controlled profile. The depth profile of δ^{13}C values in the upper 40 cm showed an erratic increase from the surface to the top of the Bt horizon. At depths >40 cm, the profile appears to follow the expected diffusion-controlled profile. This implies that there is some process other than diffusion controlling the profile shape above the Bt horizon. Because the correlation of δ^{13}C and δ^{18}O implied that diffusion was the controlling process and the δ^{13}C values of the gibbsite-occluded CO_2 at 40 cm are most similar to the atmosphere, the implication is that transport and mixing of gibbsite above the Bt horizon is responsible for the unexpected depth profile. Mixing in the upper portion made utilization of the pedogenic gibbsite proxy more difficult but may provide insight into the processes and timing of events in soils regarding dissolution, formation, and transport, particularly in deep intensely weathered soils. Measuring the radiocarbon content of occluded gibbsite CO_2 and its distribution down profile will provide insight into the extent of mixing recorded by the gibbsite at different depths in the soil.

Regarding the preservation of a weathering profile in the rock record (*i.e.* a paleosol), carbon-rich, poorly consolidated O, A, and upper AB horizons are likely to have low preservation potential. Thus, paleosols preserved in the rock record were probably decapitated during the erosional and subsequent depositional events that deposited unconformable sequences above. The more clay-rich lower AB and Bt horizons are more likely to be preserved. If these horizons are studied for their gibbsite CO_2 δ^{13}C values, the mixing curve (*i.e.* asymptotic values are approached with depth) still potentially harbors information about the original SOM pool and the atmosphere with which it mixed. The key to using gibbsite preserved in ancient soil is observing the soil textural properties to be sure about the horizons being sampled. The USDA-ARS study site used here is unique in that the only mixing of the soil has been bioturbation and tree-throw (no tilling). Also minimized at this site was the introduction of an enriched C_4 carbon pool. The present authors suggest that the signal recorded and preserved here reflects a more pre-human like condition, where rapid erosion or changes in carbon input have probably not taken place. In contrast, most landscapes in the southeastern United States have experienced intense cultivation, which affects mixing and can lead to erosion of the A horizon and its gibbsite-hosted carbon signal (*i.e.* accelerated erosion). Human-induced factors have not been considered in previous occluded gibbsite carbon studies, which were sampled at a site that probably did undergo significant erosion and agricultural tilling (Schroeder and Melear, 1999). For this reason, managed, tilled, and eroded landscapes, with a concentration of enriched carbon isotopes at the top of the preserved Bt horizon, may serendipitously appear more like a paleosol than an undisturbed soil.

CONCLUSIONS

Co-variation of the stable carbon and oxygen isotopic composition of carbonate occluded in the pedogenic gibbsite structure parallel to a mixing line between the atmosphere and SOM indicates that the process which controls these compositions is probably diffusive mixing. The difference in the depth profile of measured $\delta^{13}C$ values and the expected diffusion-controlled profile suggests that other transport processes have occurred after mineral formation. In the shallow soil active mixing by physical or biological processes makes interpretation of the depth profile of stable carbon isotope composition difficult. As a result, care should be taken when using paleosol proxies to identify the soil type and horizons, especially in soils with Bt horizons which indicate a concentration of alluvial clay, or with A, E, or B horizons which may be mixed due to bioturbation. Restricting samples to the region below the Bt horizon removes the upper portion of the profile, which allows for more precise PCO_2 estimates, but until the systematics of mixing can be determined and modeled reliably, estimates using deep soil only will have errors comparable to current paleosol methods.

ACKNOWLEDGMENTS

The authors thank Julie Cox for her help with the redesign of the isotope extraction line, which was essential to the success of this project. The manuscript was improved significantly by the thoughtful comments of two anonymous reviewers. Support was provided by The Clay Minerals Society, NSF-EAR-0501690, EAR-IF-0929912, and EAR-1331846.

REFERENCES

Austin, J.C. (2011) Soil CO_2 efflux simulations using Monte Carlo method and implications for recording paleo-atmospheric PCO_2 in pedogenic gibbsite. *Palaeogeography Palaeoclimatology Palaeoecology*, **305**, 280–285.

Bacon, A.R., Richter, D.D., Bierman, P., and Rood, D.H. (2012) Coupling meteoric ^{10}Be with pedogenic losses of ^{9}Be to improve soil residence time estimates on an ancient North American interfluve. *Geology*, **40**, 847–850.

Berner, R.A. and Kothavala, Z. (2001) GEOCARB III: A revised model of atmospheric CO_2 over Phanerozoic time. *American Journal of Science*, **301**, 182–204.

Bowen, G.J. and Beerling, D.J. (2004) An integrated model for soil organic carbon and CO_2: Implications for paleosol carbonate pCO_2 paleobarometry. *Global Biogeochemical Cycles*, **18**, GB1026 1021–1012.

Breecker, D.O., Sharp, Z.D., and McFadden, L.D. (2009) Seasonal bias in the formation and stable isotopic compostition of pedogenic carbonate in modern soils from central New Mexico, USA. *Geological Society of America Bulletin*, **121**, 630–640.

Cerling, T.E. (1984) The stable isotopic composition of modern soil carbonate and its relationship to climate. *Earth and Planetary Science Letters*, **71**, 229–240.

Cerling, T.E. (1991) Carbon dioxide in the atmosphere: evidence from Cenozoic and Mesozoic Paleosols. *American Journal of Science*, **291**, 377–400.

Cerling, T.E., Quade, J., and Bowman, J.R. (1989) Carbon isotopes in soils and palaeosols as ecology and palaeoecology indicators. *Nature*, **341**, 138–139.

Chen, Q., Zhu, R., and Xu, H. (2013) Stable isotopes of carbon dioxide in the marine atmosphere along a hemispheric course from China to Antartica. *Atmospheric Environment*, **80**, 342–346.

Cuntz, M., Ciais, P., Hoffmann, G., and Knorr, W. (2003) A comprehensive global three-dimensional model of $\delta^{18}O$ in atmospheric CO_2: 1. Validation of surface processes. *Journal of Geophysical Research*, **108**, 4528, doi: 10.1029/2002JD003153.

Farrimond, P., Eglinton, G., and Brassell, S.C. (1986) Alkenones in Cretaceous black shales, Blake-Bahama Basin, western North Atlantic. *Organic Geochemistry*, **10**, 897–903.

Francey, R.J., Allison, C.E., Etheridge, D.M., Trudinger, C.M., Enting, I.G., Leuenberger, M., Langerfelds, R.L., Michel, E., and Steele, L.P. (1999) A 1000-year high precision record of $\delta^{13}C$ in atmospheric CO_2. *Tellus*, **51B**, 170–193.

Freeman, K.H. and Hayes, J.M. (1992) Fractionation of carbon isotopes by phytoplankton and estimates of ancient CO_2 levels. *Global Biogeochemical Cycles*, **6**, 185–198.

Hesterberg, R. and Siegenthaler, U. (1991) Production and stable isotopic composition of CO_2 in a soil near Bern, Switzerland. *Tellus*, **43B**, 197–205.

Hsieh, J.C.C., Savin, S.M., Kelly, E.F., and Chadwick, O.A. (1998) Measurement of soil-water $\delta^{18}O$ values by direct equilibration with CO_2. *Geoderma*, **82**, 255–268.

Kump, L.R. and Arthur, M.A. (1999) Interpreting carbon-isotope excursions: carbonates and organic matter. *Chemical Geology*, **161**, 181–198.

Kurschner, W.M., Van Der Burgh, J., Visscher, H., and Dilcher, D.L. (1996) Oak leaves as biosensors of late Neogene and early Pleistocene paleoatmospheric CO_2 concentrations. *Marine Micropaleontology*, **27**, 299–312.

Marlowe, I.T., Brassell, S.C., Eglinton, G., and Green, J.C. (1990) Long-chain alkenones and alkyl alkenoates and the fossil coccolith record of marine sediments. *Chemical Geology*, **88**, 349–375.

Miller, J.B., Yakir, D., White, J.W.C., and Tans, P.P. (1999) Measurement of $^{18}O/^{16}O$ in the soil-atmosphere CO_2 flux. *Global Biogeochemical Cycles*, **13**, 761–774.

Pagani, M., Freeman, K.H., and Arthur, M.A. (1999) Late Miocene atmospheric CO_2 concentrations and the expansion of C_4 grasses. *Science*, **285**, 876–879.

Robertson, S.M. (1968) Soil Survey of Clarke and Oconee Counties, Georgia. Department of Agriculture, U.S.A.

Royer, D.L., Berner, R.A., and Beerling, D.J. (2001) Phanerozoic atmospheric CO_2 change: evaluating geochemical and paleobiological approaches. *Earth Science Reviews*, **54**, 349–392.

Schroeder, P.A. and Melear, N.D. (1999) Stable carbon isotope signatures preserved in authigenic gibbsite from a forested granitic-regolith: Panola Mountain, Georgia, USA. *Geoderma*, **91**, 261–279.

Schroeder, P.A., Melear, N.D., Bierman, P., Kashgarian, M., and Caffee, M.W. (2001) Apparent gibbsite growth ages for regolith in the Georgia Piedmont. *Geochimica et Cosmochimica Acta*, **65**, 381–386.

Schroeder, P.A., Austin, J.C., and Dowd, J.F. (2006) Estimating long-term soil respiration rates from carbon isotopes occluded in gibbsite. *Geochimica et Cosmochimica Acta*, **70**, 5692–5697.

Stern, L., Baisden, W.T., and Amundson, R. (1999) Processes controlling the oxygen isotope ratio of soil CO_2: Analytic and numerical modeling. *Geochimica et Cosmochimica Acta*, **63**, 799–814.

Su, C.M. and Suarez, D.L. (1997) In situ infrared speciation of absorbed carbonate on aluminum and iron oxide. *Clays and Clay Minerals*, **45**, 814–825.

Tabor, N.J. and Yapp, C.J. (2005) Incremental vacuum dehydration-decarbonation experiments on a natural gibbsite (α-$Al(OH)_3$): CO_2 abundance and $\delta^{13}C$ values. *Geochimica et Cosmochimica Acta*, **69**, 519–527.

Van Der Burgh, J., Visscher, H., Dilcher, D.L., and Kurschner, W.M. (1993) Paleoatmospheric signatures in Neogene fossil leaves. *Science*, **260**, 1788−1790.

Welp, L.R., Keeling, R.F., Meijer, H.A.J., Bollenbacher, A.F., Piper, S.C., Yoshimura, K., Francey, R.J., Allison, C.E., and Wahlen, M. (2011) Interannual variability in the oxygen isotopes of atmospheric CO_2 driven by El Nino. *Nature*, **477**, 579−582.

Woodward, F.I. and Bazzaz, F.A. (1988) The responses of stomatal density to CO_2 partial pressure. *Journal of Experimental Botany*, **39**, 1771−1781.

Yapp, C.J. (1997) An assessment of isotopic equilibrium in goethites from a bog iron deposit in a lateritic regolith. *Chemical Geology*, **135**, 159−171.

Yapp, C.J. (2003) A model for $^{18}O/^{16}O$ variations in CO evolved from goethite during the solid-state α-FeOOH to α-Fe_2O_3 phase transition. *Geochimica et Cosmochimica Acta*, **67**, 1991−2004.

Yapp, C.J. and Poths, H. (1986) Carbon in natural goethites. *Geochimica et Cosmochimica Acta*, **50**, 1213−1220.

Yapp, C.J. and Poths, H. (1990) Infrared spectral evidence for a minor Fe(III) carbonate bearing component in natural goethite. *Clays and Clay Minerals*, **38**, 442−444.

Yapp, C.J. and Poths, H. (1992) Ancient atmospheric CO_2 pressures inferred from natural goethites. *Nature*, **355**, 342−344.

Yapp, C.J. and Poths, H. (1996) Carbon isotopes in continental weathering environments and variations in ancient atmospheric CO_2 pressure. *Earth and Planetary Science Letters*, **137**, 71−82.

(*Received 1 April 2014; revised 2 September 2014; Ms. 755; AE: H. Dong*)

Clays and Clay Minerals, Vol. 62, No. 4, 267–285, 2014.

MINERALOGY, GEOCHEMISTRY, AND GENESIS OF MUDSTONES IN THE UPPER MIOCENE MUSTAFAPAŞA MEMBER OF THE ÜRGÜP FORMATION IN THE CAPPADOCIA REGION, CENTRAL ANATOLIA, TURKEY

TACİT KÜLAH[1], SELAHATTİN KADİR[1,*], ALİ GÜREL[2], MUHSİN EREN[3], AND NERGİS ÖNALGİL[1]

[1] Eskişehir Osmangazi University, Department of Geological Engineering, TR-26480 Eskişehir, Turkey
[2] Niğde University, Department of Geological Engineering, TR-51200 Niğde, Turkey
[3] Mersin University, Department of Geological Engineering, TR-33343 Mersin, Turkey

Abstract—The Upper Miocene Mustafapaşa member of the Ürgüp Formation in the Cappadocia region consists predominantly of mudstones, sandstone, and conglomerate lenses with ignimbrite and basalt intercalations. The mudstones are an important source of raw materials for the ceramics industry in Turkey. A detailed mineralogical, geochemical, and genesis study of these materials has not been performed previously and the present study aims to fill that gap. The characteristics of mudstones of the Mustafapaşa member were examined using X-ray diffraction, scanning and transmission electron microscopy, energy dispersive spectroscopy, and chemical analyses. Weathering products of ophiolitic and pyroclastic rocks were transported into the tectonically subsided zone where they accumulated as fluvial and lacustrine deposits. Weathering in the mudstones is evidenced by smectite flakes associated with relict pyroxene, rod-like amphibole, feldspar, and volcanic glass. The chemical composition of mudstones and their distribution suggest that the depositional basin was supplied with ophiolitic material in the south and ignimbrite material in the north. This interpretation is based on an increase in the quantity of feldspar and opal-A and a decrease in the Fe_2O_3+MgO/Al_2O_3+SiO_2 ratio from south to north in the study area. The northward increases in Light Rare Earth Elements/Heavy Rare Earth Elements, La/Yb, Zr/Ni and Zr/Co ratios and Nb, Ba, Rb, Sr, and Eu in the mudstones of the Mustafapaşa member with positive Eu anomalies suggest that the Fe, Mg, Al, and Si required to form smectite were supplied mainly through the decomposition of amphiboles, pyroxenes, feldspars, and volcanic glass during weathering processes. After the deposition of mudstones, relative increases in evaporation-controlled Ca, K, and Al in pore water favored the partial dissolution of Ca-bearing minerals and smectite flakes and *in situ* precipitation of calcite and traces of illite fibers under alkaline micro-environmental conditions during early diagenesis.

Key Words—Cappadocia, Ignimbrite, Mudstone, Ophiolite, Smectite, Turkey, Weathering.

INTRODUCTION

The study area occupies ~400 km^2 in the Cappadocia region in central Anatolia (Turkey), which contains widespread argillaceous sediments of the Upper Miocene Mustafapaşa member of the Ürgüp Formation. In recent decades, extensive attention to the sedimentology, mineralogy, and geochemistry of mudstones has led to significant advances relating to cement, ceramics, and shale gas (*e.g.* Casciello *et al.*, 2011; Chermak and Schreiber, 2014; Osborn *et al.*, 2014; Taylor and Macquaker, 2014). Most published studies of the area are related to volcanism, mineralogy-petrography, and tectonics (Pasquarè, 1968; Pasquarè *et al.*, 1988; Batum, 1975, 1978; Innocenti *et al.*, 1975; Besang *et al.*, 1977; Ercan *et al.*, 1987, 1989; Göncüoğlu and Toprak, 1992; Le Pennec *et al.*, 1994; Druitt *et al.*, 1995; Schumacher and Mues-Schumacher, 1996; Gevrek, 1997; Türkecan *et al.*, 2003; Viereck-Götte and Gürel, 2003; Le Pennec *et al.*, 2005). Less work has been done on the mineralogy and distribution of Pliocene clay-rich sediments in vertical stacked paleosol levels among ignimbrites (Gürel and Kadir, 2006). The geology and mineralogy of the Upper Miocene and paleosol and carbonate levels and their vertical distributions are used as clues to determine the paleoclimatic conditions of Anatolia and the Mediterranean region (Gürel and Kadir, 2008; Kadir *et al.*, 2013; Göz *et al.*, 2014). To date, no detailed study has been carried out of the mineralogy, geochemistry, and genesis of these smectitic materials in the Upper Miocene Mustafapaşa member of the Cappadocia Basin. The implications of ophiolitic and volcanic sources for deposits which contain several hundred million tons of clay reserves of potential raw material (for use in cement, ceramics, and elsewhere) also need to be understood. The present study focuses on the mineralogy and geochemistry of the mudstone of the Mustafapaşa member and associated sediments and interprets the genetic relationship between argillaceous sediments and ophiolitic rocks and the Yeşilhisar conglomerate, including ophiolitic components and ignimbrites.

---

* E-mail address of corresponding author:
skadir_esogu@yahoo.com
DOI: 10.1346/CCMN.2014.0620403

MATERIALS AND METHODS

In the field, representative stratigraphic sections were measured to study the lateral and vertical variations in the Mesozoic ophiolitic rocks, the Oligo-Miocene Yeşilhisar conglomerate, the mudstone of the Upper Miocene Mustafapaşa member, and the ignimbrite. One hundred and seventeen (117) characteristic samples were collected from these units (Figure 3). Fresh and partially altered samples were examined under a polarizing microscope (Leitz Laborlux 11 Pol).

The mineralogical characteristics of the samples were determined by powder X-ray diffraction (XRD) at the Turkish Petroleum Corporation (TPAO, Ankara, Turkey) using a Rigaku Geigerflex instrument. The XRD analyses were performed using CuKα radiation with a scanning speed of 1º2θ min^{-1}. Randomly oriented mounts of powdered whole-rock samples were scanned to determine the mineralogy of each bulk sample. Samples for clay analyses (<2 µm) were prepared by separating the clay fraction using sedimentation and centrifuging the suspension after an overnight dispersion in distilled water. The clay particles were dispersed using ultrasonic vibration for ~15 min. Oriented specimens of the <2 µm fractions were prepared from each sample using the following procedure: drying with air, solvating with ethylene glycol at 60ºC for 2 h, and thermal treatment at 550ºC for 2 h. Semi-quantitative abundances of rock-forming minerals were obtained using Brindley's (1980) external standard method. The relative abundances of clay-mineral fractions were determined using their basal reflections and the mineral intensity factors of Moore and Reynolds (1989).

Scanning electron microscopy (SEM) studies were performed at Eskişehir Osmangazi University (Turkey) using a JEOL JSM 84A instrument equipped with an EDX detector. Representative clay-dominated bulk samples were prepared for SEM analyses by adhering the fresh, broken surface of each sample to an aluminum sample holder with double-sided tape and coating thinly (350 Å) with gold using a Giko ion coater. Transmission electron microscopy (TEM) studies were performed at Anadolu University (Eskişehir, Turkey) using a JEOL JEM-21007 instrument. The clay particles for TEM analyses were dispersed using an ultrasonic ethanol bath for ~30 min. One drop of each clay suspension was placed on carbon-coated copper grids and dried at room temperature.

Chemical analyses of 29 ophiolite and related Yeşilhisar conglomerate, mudstone and ignimbrite whole-rock samples were performed at Acme Analytical Laboratories Ltd. (Vancouver, Canada) using inductively coupled plasma-atomic emission spectroscopy (ICP-AES) for major and trace elements and inductively coupled plasma-mass spectrometry (ICP-MS) for rare-earth elements (*REE*). The detection limits for the analyses were between 0.01 and 0.1 wt.% for major elements, 0.1 and 5 ppm for trace elements, and 0.01 to 0.5 ppm for *REE*.

Smectite structural formulae were determined for the chemical analyses of <2 µm clay fractions of smectite (confirmed by XRD). The samples were prepared by separating the clay fraction using sedimentation followed by centrifugation of the suspension after an overnight dispersion in distilled water. They were then analyzed using ICP-AES at Acme Analytical Laboratories Ltd. (Vancouver, Canada). The structural formulae of smectite were calculated from chemical analyses based on the 22 oxygen atom content of the unit cell (Moore and Reynolds, 1989).

GEOLOGICAL SETTING AND DEPOSITIONAL ENVIRONMENT

Geological setting

The basement rocks of the Cappadocia region comprise Mesozoic ophiolitic rocks consisting of serpentinized peridotites and pyroxenites, isotropic gabbros, diabasic dikes, and extrusive rocks (Dilek and Whitney, 1997). The ophiolitic rocks were thrust onto Paleozoic metamorphic rocks, including gneiss and marble. The region was later subjected to an extensional tectonic regime from the Middle Miocene until the Early Pliocene, which caused the occurrence of a depressional basin in central Anatolia (Toprak, 1998). This subsided basin is filled with fluvial and lacustrine sediments and pyroclastic rocks.

The Oligo-Miocene Yeşilhisar conglomerate typically comprises ophiolitic and metamorphic rock fragments and Neogene sediments. The Yeşilhisar conglomerate overlies discordantly the basement rocks (Figures 1 and 2) and is overlain unconformably by Neogene sediments of the Ürgüp Formation (Pasquarè, 1968). The Upper Miocene Mustafapaşa member is the oldest sedimentary unit in the Ürgüp Formation, which consists of massive and layered mudstones and conglomerates and sandstones of fluvial and lacustrine origin. The Mustafapaşa member overlies ophiolitic basement rocks near the Akköy and Keşlik villages and the Yeşilhisar conglomerate to the south of Yeşilhisar. The sediments of the Mustafapaşa member near the Damsa Valley south of Ürgüp are intercalated locally with the Kavak ignimbrite, a welded, thickly bedded, dark gray Sarımadentepe ignimbrite, and Damsa Valley basaltic lava. The Mustafapaşa member is overlain conformably by Late Miocene to Pliocene volcaniclastic and sedimentary units, which are overlain discordantly by Quaternary ashfall deposits, white travertine, and alluvium (Figure 2, Viereck-Götte *et al.*, 2010).

Description of the lithology

In the study area, the following lithologies have been distinguished in the Oligo-Miocene and Upper Miocene sediments (Figures 3, 4).

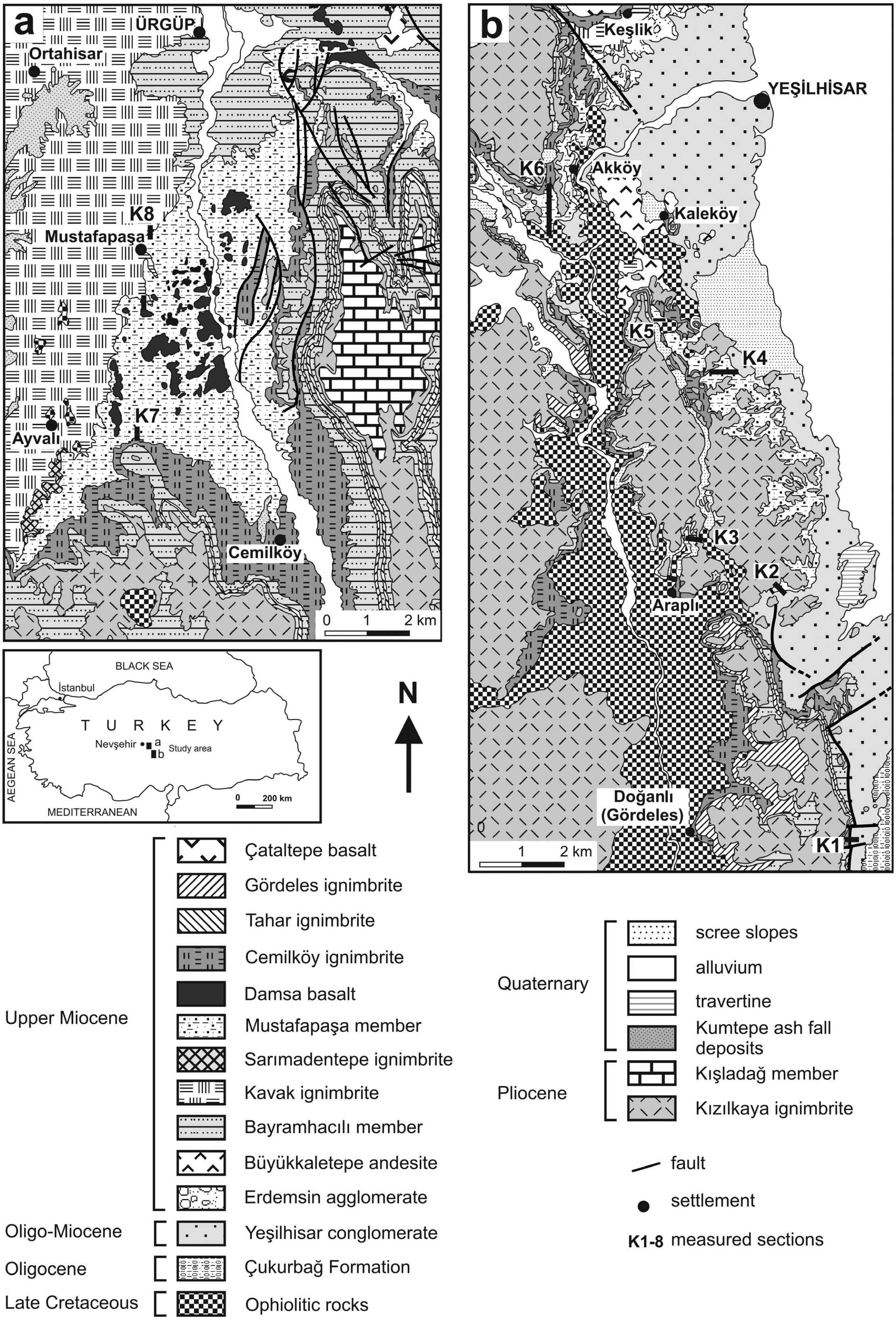

Figure 1. Simplified geological map of the Cappadocia region (after Pasquarè, 1968).

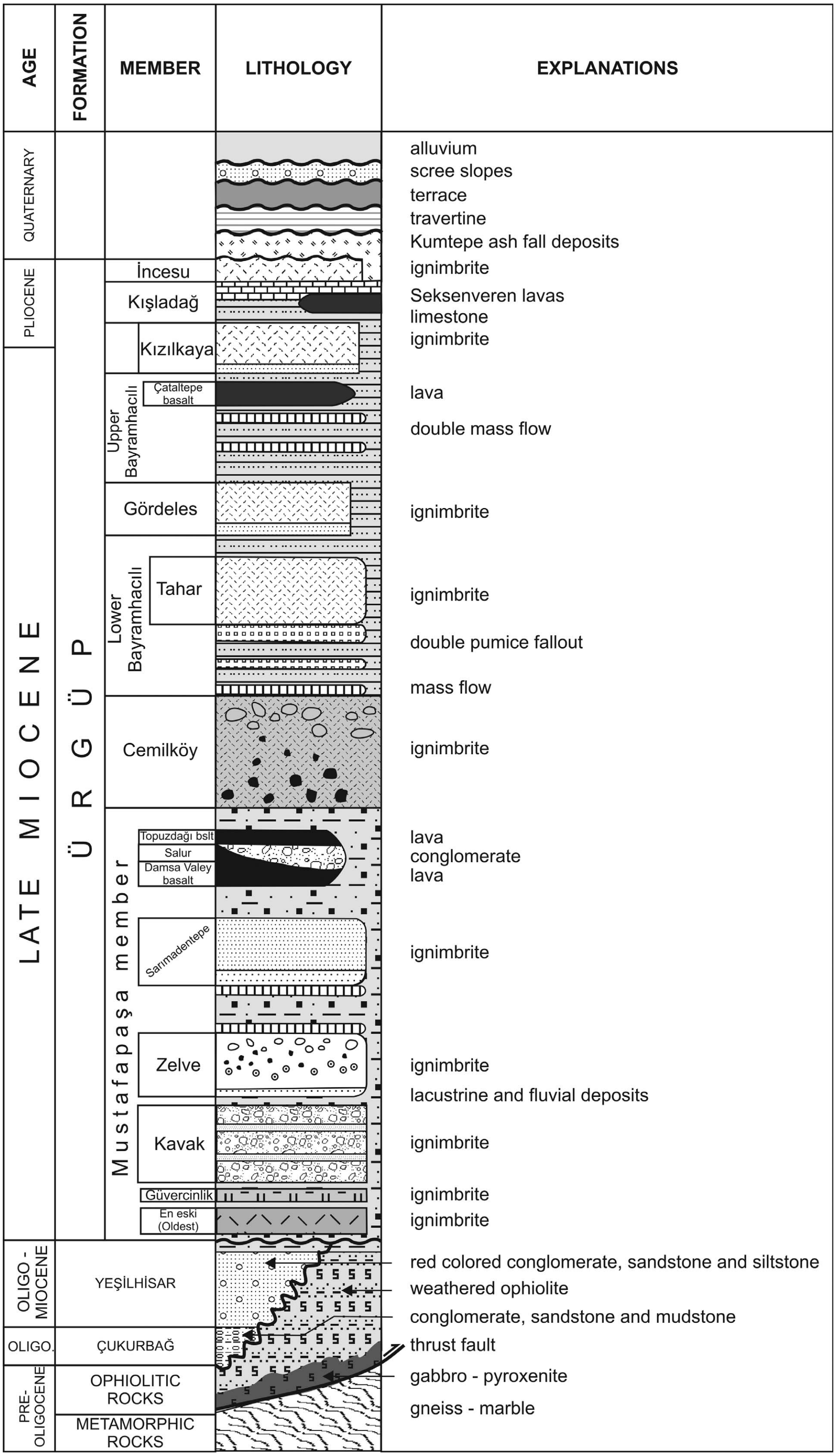

Figure 2. Generalized stratigraphic column of the study area (after Viereck-Götte *et al.*, 2010).

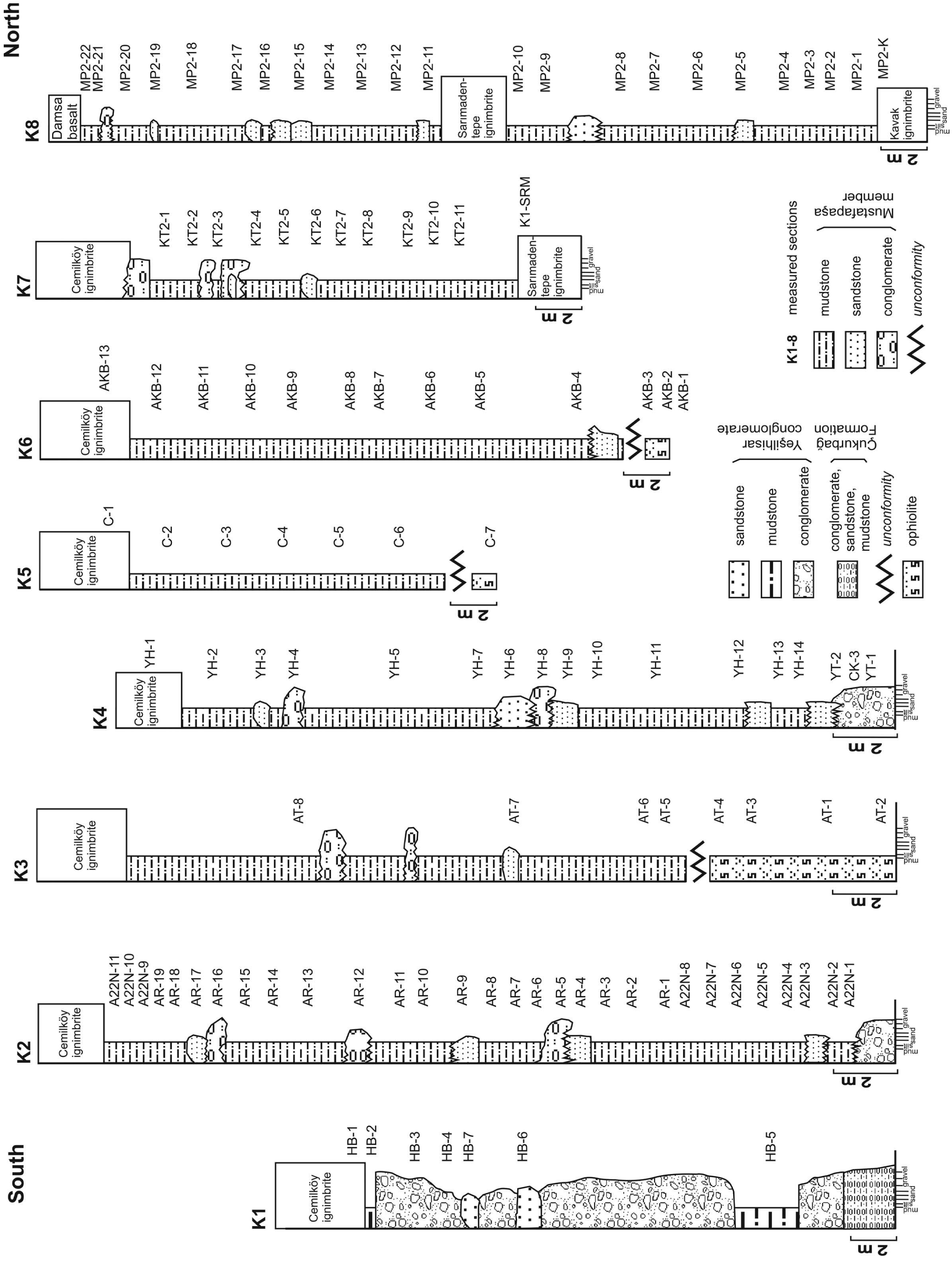

Figure 3. Distribution of the principal lithologies in the study area (see Figure 1 for section locations and Table 1 for the mineralogical compositions of the selected samples).

Conglomerate. This facies appears in two stratigraphic levels characterized by thick-bedded fluvial sediments of the Yeşilhisar conglomerate (Figure 4a,b) and channel filling in the mudstone of the Mustafapaşa member. The Yeşilhisar conglomerate consists almost entirely of conglomerates, including ophiolitic and metamorphic rock fragments. The pebbles are well rounded and their size varies from a few cm to 20–30 cm. To the north, metamorphic components predominate in these conglomerates. The matrix of the conglomerate consists of red, sandy, silty, and argillaceous material. This lithology appears in an area ~40 km long and 10 km wide. The channel-filling conglomerates in the mudstone of the Mustafapaşa member are characterized by massive, gray, unsorted, and sub-rounded conglomerates. The conglomerates are mainly matrix-supported. The average size of the clasts is ~10 cm. The thickness of the conglomerate varies from 20 to 50 cm. This conglomerate channel has a lenticular character with a cross-section ~2 m wide.

Sandstone. This facies consists of greenish-gray, medium- to fine-grained, medium-bedded sandstones with plant rootlets. The facies is ~50 cm thick and several km long.

Mudstone. This massive and layered mudstone facies appears in two stratigraphic levels characterized by different colors (Figure 4c,d). The lower level is generally greenish-gray, but the upper level is brownish-red. The facies includes plant rootlets and desiccation cracks. The mudstone is ~70 m thick, 10 km wide, and 60 km long.

Description of stratigraphic sections

Eight stratigraphic sections were analyzed from south to north in the study area, and the results are described below (Figure 3, K1–K8).

Hacibekirli section (K1). The Yeşilhisar conglomerate unconformably overlies the Çukurbağ Formation, which is overlain by the Cemilköy ignimbrite (Gürel *et al.*,

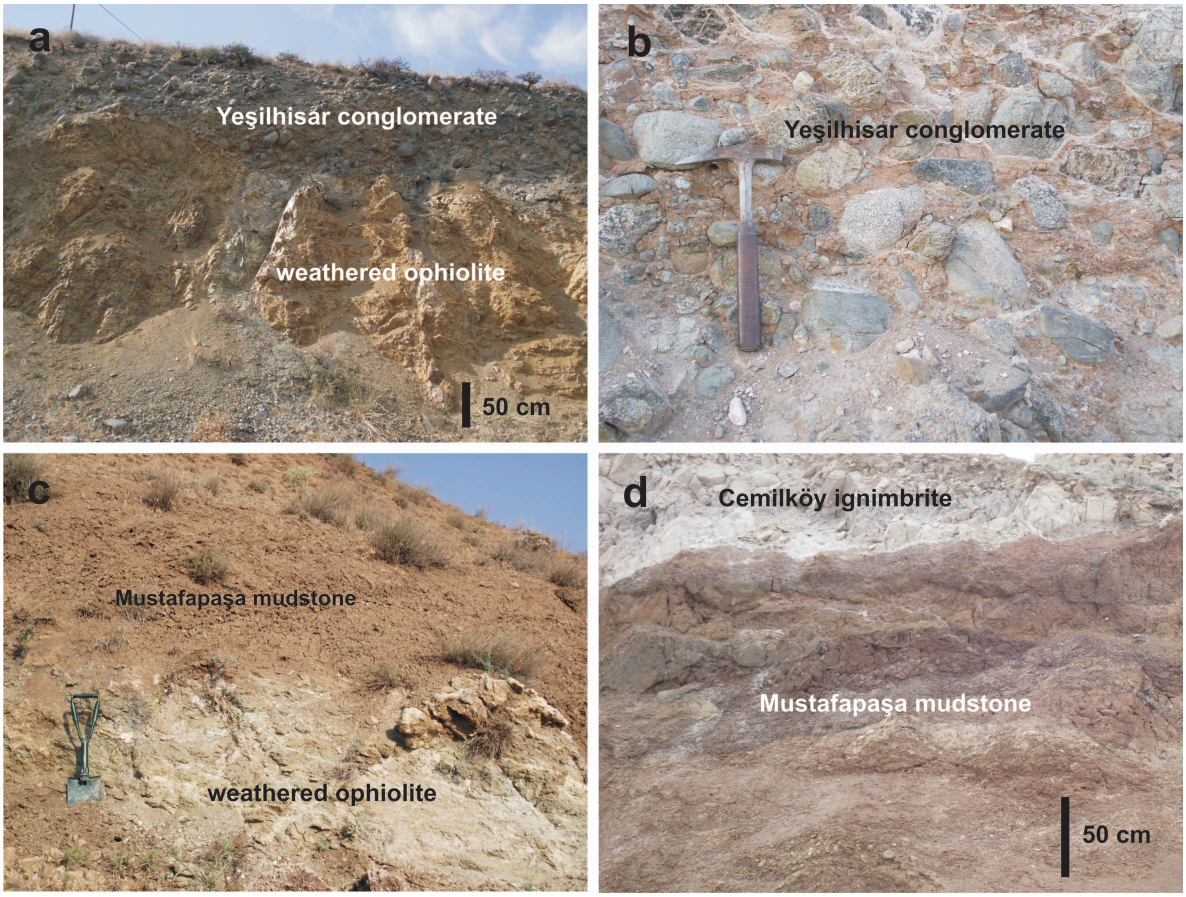

Figure 4. Field view of: (a) the weathered ophiolitic unit and the overlying Yeşilhisar conglomerate; (b) close-up view of ophiolite-sourced pebbles in a matrix of mudstone in the Yeşilhisar conglomerate; (c) mudstone of the Mustafapaşa member on the weathered ophiolitic units; and (d) close-up view of the Mustafapaşa mudstone with intercalated sandstone lenses and overlain by the Cemilköy ignimbrite.

2007; Figure 3). The section consists predominantly of ophiolitic conglomerate and sandstone and mudstone horizons. These units are overlain by the Cemilköy ignimbrite.

Araplı Pass section (K2). This section begins with the Yeşilhisar conglomerate, which overlies unconformably ophiolitic rocks and is overlain unconformably by mudstones, sandstones, and conglomerates of the Mustafapaşa member (Figure 4a). The Yeşilhisar conglomerate consists of pebbles and cobbles derived predominantly from ophiolitic basement rocks, such as gabbro, pyroxenite, and serpentinite and minor amounts of marble and gneiss (Figure 4b). This section is covered by the Cemilköy ignimbrite.

Araplı section (K3). The ophiolitic basement rocks show signs of weathering. This unit is overlain unconformably by the Mustafapaşa member deposits which consist of mudstones intercalated with sandstones and conglomerate lenses (Figure 4c). The Cemilköy ignimbrite occurs in the uppermost part of this section (Figure 4d).

Yeşilhisar section (K4). This section begins with an ophiolitic unit that is overlain unconformably by the Yeşilhisar conglomerate, which is overlain unconformably by the sediments of the Mustafapaşa member. This section is covered by the Cemilköy ignimbrite.

Çevliktaş Tepe section and Akköy section (K5, K6). The ophiolitic basement rocks are overlain unconformably, mainly by mudstone deposits of the Mustafapaşa member, which is overlain by the Cemilköy ignimbrite.

Kolkollu Tepe section (K7). This section begins with the Sarımadentepe ignimbrite, which is overlain by Mustafapaşa member sediments and topped by the Cemilköy ignimbrite. The thicknesses and frequency of occurrence of conglomerate lenses in the Mustafapaşa member are less than in the southern area. A reddish color is predominant in the Mustafapaşa-member sediments compared with those of previously described sections.

Mustafapaşa section (K9). This section begins with the Kavak ignimbrite, which is overlain by Mustafapaşa-member sediments composed of mudstones intercalated with sandstone and conglomerate lenses and the Sarımadentepe ignimbrite. This section is topped by the Damsa Valley basalt.

PALEOGEOGRAPHY

Tectonic activity during the Oligocene caused the uplift and emergence of the region, after which ophiolitic basement rocks and ignimbrites were subjected to moderate to intensive weathering. Weathering products were eroded, transported, and deposited in the subsided basin. The Yeşilhisar conglomerate, consisting mainly of ophiolitic components, was deposited close to the source area in these valleys. Thin lacustrine sediments were deposited in areas to the north. Polygenetic volcanoes were active in the Late Miocene and their pyroclastic products, such as the Kavak and Sarımadentepe ignimbrites, were intercalated with mudstones in the northern part of the study area (Pasquarè, 1988; Toprak, 1998; Le Pennec *et al.*, 2005). During the arid climatic conditions at the beginning of the Late Miocene, the lacustrine areas were subjected to flash flooding, which caused the deposition of mud and the development of mud flats. Argillaceous sediments then formed in the region (Kadir *et al.*, 2013). According to the profiles examined, the main lithofacies consist of massive and layered mudstones, which occur in three sections: the very shallow part of the lake (southern lake margin, Figure 3, K1, K2), the central part of study area around Akköy (Figure 3, K3, K4, P5, K6), and a shallow-lake environment (north, Figure 3, K7, K8). In the depressional basin, the main paleo-flow direction was generally determined to have been from south to north, based on field observations such as pebble orientation, planar and trough cross-beddings in sandstones, and the mineralogical compositions of detrital sediments.

RESULTS

Mineralogical and petrographical determinations

Ophiolitic rocks are generally composed of serpentinized amphibole, pyroxene, and accessory olivine (Dilek and Furnes, 2014). The Yeşilhisar conglomerate includes components derived mainly from basement rocks. These components consist of serpentinized and Fe (oxyhydr)-oxide-bearing amphibole, pyroxene, and olivine minerals with partial to extensive alteration (Nahon *et al.*, 1982; Delvigne, 1998). Volcanic rocks include plagioclase and amphibole phenocrysts in a volcanic glass groundmass. Feldspars and amphiboles are altered, and the volcanic glass is devitrified.

The XRD results of the bulk samples from the measured profiles are given in Table 1. Smectite is dominant in all of the samples from the sections of the Mustafapaşa member and is accompanied by feldspars, quartz, amphiboles, pyroxenes, calcite, local olivine, and traces of illite/mica, kaolinite, chlorite, and serpentine. The quantities of feldspar and opal-A increase from south to north in the study area.

Smectite is identified by a sharp basal reflection at 14.48–14.91 Å, which shifts to 17.51–17.65 Å following ethylene-glycol treatment and collapses to 10.08–10.13 Å after heating at 550ºC for 2 h (Figure 5). The d_{060} value of smectite is 1.50 Å, suggesting a dioctahedral character (Moore and Reynolds, 1989). Illite/mica is identified by reflections

Table 1. Mineralogical composition and abundance of samples in the measured sections. Sections and their samples are ordered from north to south.

Sample	Rock type	smc	ilt/mc	kln	chl	srp	am	px	ol	fds	qz	op	cal
North													
K8													
MP2-22	Mudstone	++++	acc							acc	+	acc	acc
MP2-21	Mudstone	+++	acc		acc	acc				+	+	+	
MP2-20	Mudstone	+++								+	+	+	
MP2-16	Mudstone	+++		acc						+	+	acc	
MP2-14	Mudstone	+++		acc		acc				+	+	+	
MP2-10	Mudstone	+++	acc	+	acc					+	acc	+	
MP2-7	Mudstone	+		acc						+++	acc	+	acc
MP2-4	Mudstone	+++		acc				acc		+	acc	+	
MP2-3	Mudstone	++			acc				acc	++	acc	acc	
K7													
KT2-1	Mudstone	+++	acc							+	+	+	
KT2-2	Mudstone	+++	acc							++	+	+	
KT2-3	Mudstone	+++		+						+++	+	acc	
KT2-5	Mudstone	++++	acc	acc						++	acc	+	
KT2-7	Mudstone	++++	acc	acc						+	acc	+	
KT2-8	Mudstone	++++								acc	+	acc	acc
KT2-10	Mudstone	+++								acc	acc	acc	+
KT2-11	Mudstone	+++								+	acc	+	acc
Middle													
K6													
AKB-11	Mudstone	++++								acc	+	+	
AKB-10	Mudstone	++++								acc	+	+	
AKB-9	Mudstone	++	acc							acc	+		++
AKB-7	Mudstone	+++	acc		+					acc	+	acc	+
AKB-5	Mudstone	++	acc		acc					acc	+		++
AKB-4	Mudstone	++		acc	acc			+		+	+		++
K5													
C-2	Mudstone	+++	acc		acc	acc				+	+	acc	
C-3	Mudstone	+++								acc	+	acc	+
C-4	Mudstone	++			acc		acc			+	+		++
C-5	Mudstone	++				acc				+	+	+	
K4													
YH-2	Mudstone	++	acc		acc			acc		+	+	acc	++
YH-5	Mudstone	++			acc					acc	+		+
YH-7	Mudstone	++	acc	acc	+					acc	+		+
YH-10	Mudstone	++	acc		acc		acc			+	+		+
YH-11	Mudstone	++			acc		+		acc	+	+	acc	acc
YH-13	Mudstone	+++		acc	acc		+			acc	+	acc	++
K3													
AT-5	Mudstone	+++		acc						acc	+		+
AT-8	Mudstone	++								+	+		acc
South													
K2													
A22N-11	Mudstone	++++								acc	+		
A22N-4	Mudstone	++++									+		
K1													
HB-2	Mudstone	+++								acc	+		
HB-3	Matrix of Yeşilhisar conglomerate	++++					acc		acc	acc	+		acc
HB-5	Mudstone	++++	acc	acc						acc	+		acc

smc: smectite, ilt/mc: illite/mica, kln: kaolinite, chl: chlorite, srp: serpentine, am: amphibole, px: pyroxene, ol: olivine; fds: feldspar, qz: quartz, op: opal-A, cal: calcite. acc: accessory, +: relative abundance of mineral.

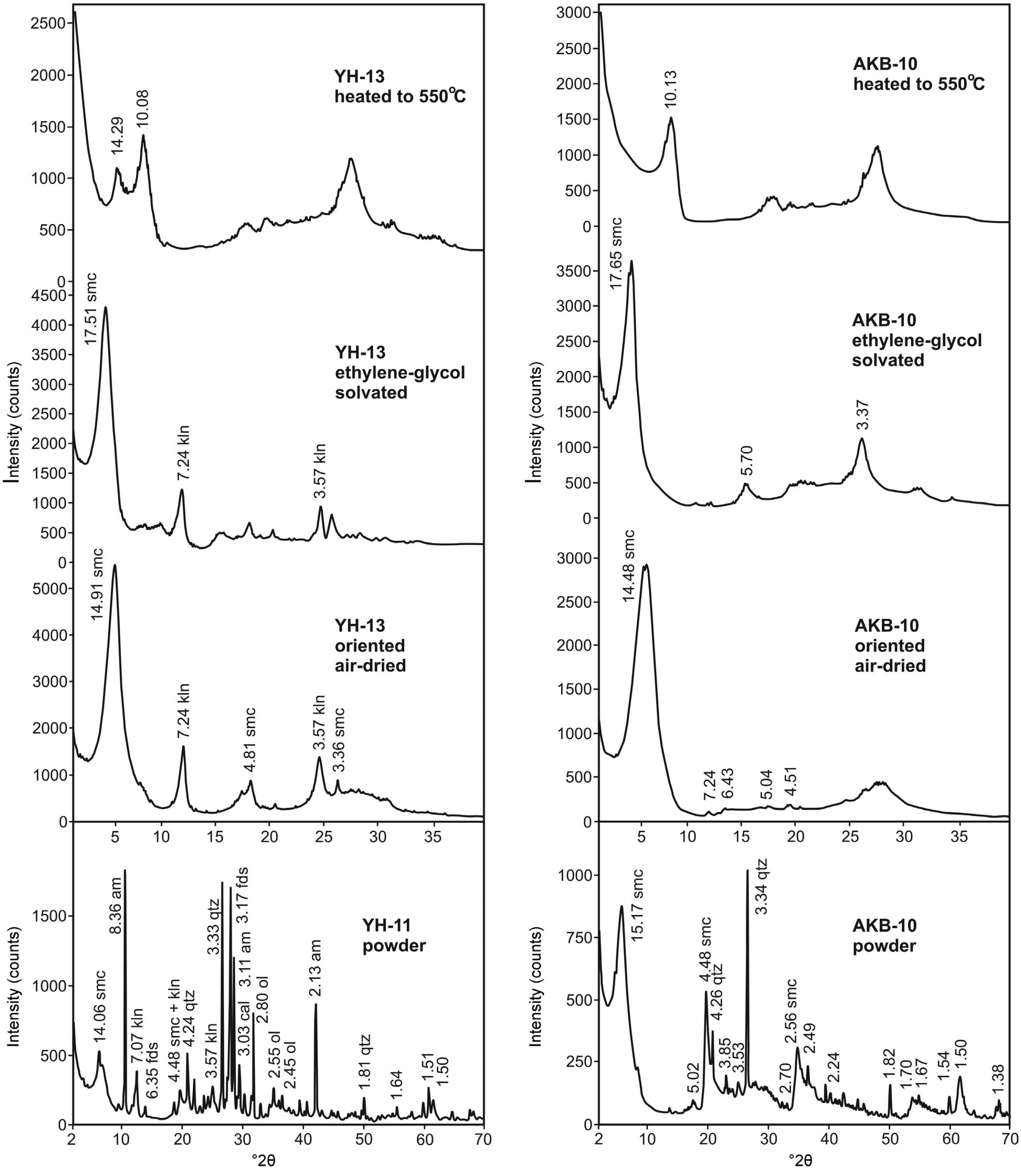

Figure 5. XRD patterns of smectite-rich mudstone samples (YH-11, YH-13, AKB-10). smc: smectite, kln: kaolinite, fds: feldspar, qz: quartz, am: amphibole, ol: olivine, cal: calcite.

at 10.0 and 5.0 Å, which are not affected by the ethylene-glycol treatment but undergo a slight shift toward a higher angle when heated to 550ºC because of dehydroxylation. Kaolinite has peaks at 7.24 and 3.57 Å and serpentine has peaks at 7.63 Å. Sharp peaks appear in amphibole at 8.36 and 3.11 Å, in pyroxene at 2.90 Å, in olivine at 2.80 Å, in quartz at 3.34 and 4.26 Å, in feldspar at 3.18 Å, and in calcite at 3.03 Å. An increase in the XRD background intensity in some of the samples may indicate the presence of opal-A (Iijima and Tada, 1981).

Amphibole is associated with accessory chlorite, serpentine, and olivine and is found mainly in weathered ophiolitic units, related to weathered units of the Araplı area in the southern region of the studied area. Illite and feldspar increase northward near the Akköy area.

SEM-EDX AND TEM DETERMINATIONS

Scanning electron microscope images indicate that flaky smectite predominates in the mudstone and matrix of the Yeşilhisar conglomerate samples (Figure 6). Flaky smectite crystals (up to 2−7 μm in diameter) appear in the samples with irregular outlines and are locally edged with fibrous illite (Figure 6a−h). Amphiboles with rod-like forms (~10 μm long) and pyroxene relics are associated with smectite in the mudstones from the southern part of the study area (Figure 6c,d). Smectite in the northern mudstones occur as authigenic flakes and include relict crystals, such as feldspar and devitrified volcanic glass (Figure 6e,f). In addition, irregular flaky smectite in the central mudstone encloses authigenic euhedral micritic calcite crystals (1−7 μm in diameter) as regular pore fillings (Figure 6g,h).

Energy dispersive analyses of the smectite flakes have large peaks for Si, Al, Fe, and Ca and low Al and Mg (Figure 7a). Energy dispersive analyses of rod and rod-bundle amphibole crystals yielded Si, Ca, and Fe and low Al, whereas the pyroxene precursor exhibits high Ca, Fe, and Si and low Mg resembling augite-type pyroxenes (Figure 7b,c). Relics of feldspars exhibit high peaks for Si, smaller peaks for Al, and very faint peaks for K and Ca (Figure 7d). The altered volcanic rocks consist mainly of Si with very small peaks for Al, Mg, K, Ca, and Na (Figure 7e). Rhombic calcite crystals exhibit strong peaks for Ca (Figure 7f).

Transmission electron microscope analyses indicate that the smectite particles occur as wavy fan- and lens-like plate packets arranged in a well oriented order (Figure 8a−f). In addition, there are discontinuous, bent and non-oriented packs of smectite particles (Figure 8b−f). Smectite plates edge rod-like crystals of amphiboles in the mudstones (Figure 8d−f). The sharp edges of the individual fibers suggest moderate to high crystallinity. The smectite plates have a diameter of 300−600 nm.

Geochemistry

Chemical analyses of representative samples of ophiolite and the associated Yeşilhisar conglomerate matrix, mudstones, and ignimbrites in the Cappodocia region are given in Table 2 (please see an extended version of this table which has been deposited with the Editor in Chief and is available from http://www.clays.org/JOURNAL/JournalDeposits.html). The variations in the major and trace-element profiles appear to be related to ophiolitic and volcanic provenances (Table 2, plus extended version, deposited). Therefore, SiO_2, K_2O, TiO_2, ΣREE, and Zr values increase and Fe_2O_3 and MgO values decrease northward in the mudstones of the Mustafapaşa member. The loss on ignition is an important indicator of weathering and is proportional to the amount of calcite and clay minerals. Large amounts of Cr, Ni, and Co are found in the ophiolitic rocks with average values of 1850, 1917, and 98.5 ppm, respectively. The Cr, Ni, and Co contents decrease from the south to the middle to the north with average values in the mudstones of the Mustafapaşa member of 548, 475, and 40 ppm; 402, 226, and 26 ppm; and 136, 46, and 15 ppm, respectively. In addition, the Ba, Rb, and Sr contents of the sediments of the Mustafapaşa member display local increases northward.

SiO_2 has a positive correlation with K_2O, and ΣREE correlates positively with Zr in the mudstone samples (Figure 9a,b). A plot of Zr/Ni *vs.* Zr/Co shows a northward increase in Zr content relative to Ni and Co (Figure 10).

The whole-rock *REE* contents of samples from the study area were normalized to the North American Shale Composite (NASC) values (Gromet *et al.*, 1984) (Figure 11). Light *REE*s (*LREE*s), such as La, Ce, and Nd, are enriched relative to the increase in concentrations of medium *REE*s (*MREE*s) and heavy *REE*s (*HREE*s) based on the increase in La_N/Yb_N ratios from 0.41 to 5.96 in mudstones from south to north in the study area (Table 1, Figure 11a−c). However, *LREE*s were leached relative to the *MREE*s and *HREE*s in mudstone samples close to the ophiolitic units and related Yeşilhisar conglomerates in the southern region (Table 1, Figure 11a,d). Nb/Ti increases parallel to the increase in La/Yb northward (Figure 12). The *LREE*/*HREE* ratio is enriched in ignimbrite samples (Figure 11e).

The averages [$(Eu/Eu^*)_{NASC}$= 0.98−1.67 and $(Ce/Ce^*)_{NASC}$ = 0.75−1.06] show positive Eu and negative Ce anomaly values, respectively (Table 2, deposited). The $(Yb/Yb^*)_{NASC}$ ratios range from 0.80 to 1.17 and are positive, revealing a relatively immobile character.

The structural formulae of smectite were calculated from chemical analyses of the clay fractions of samples A22N-11, AKB-11, and KT2-8 (Table 3). The average structural formula was estimated to be $(Si_{7.59}Al_{0.41})(Al_{2.34}Fe_{0.93}Mg_{0.76}Ti_{0.06}Mn_{0.013})(Ca_{0.29}Na_{0.03}K_{0.20})O_{20}(OH)_4$. The tetrahedral site is filled by Si, which is substituted by a small amount of Al. Al is the predominant cation in the octahedral site and is accompanied by Fe^{3+}, Mg, and traces of Ti and Mn. Ca, Na, and K were deemed exchangeable interlayer cations. The average tetrahedral charge/octahedral charge ratio (xt/xo) is 1.00. These values indicate that the smectite is montmorillonite, similar to that reported by Güven (1988) and Inoue *et al.* (2004).

DISCUSSION

The basement rocks in the study area consist of Paleozoic and Mesozoic gneiss, marble, and ophiolitic rocks. Long-term weathering of ophiolite and ignimbrite units from the Early Eocene to the Late Miocene produced an enormous amount of argillaceous material that was later transported and deposited in the depressional basin

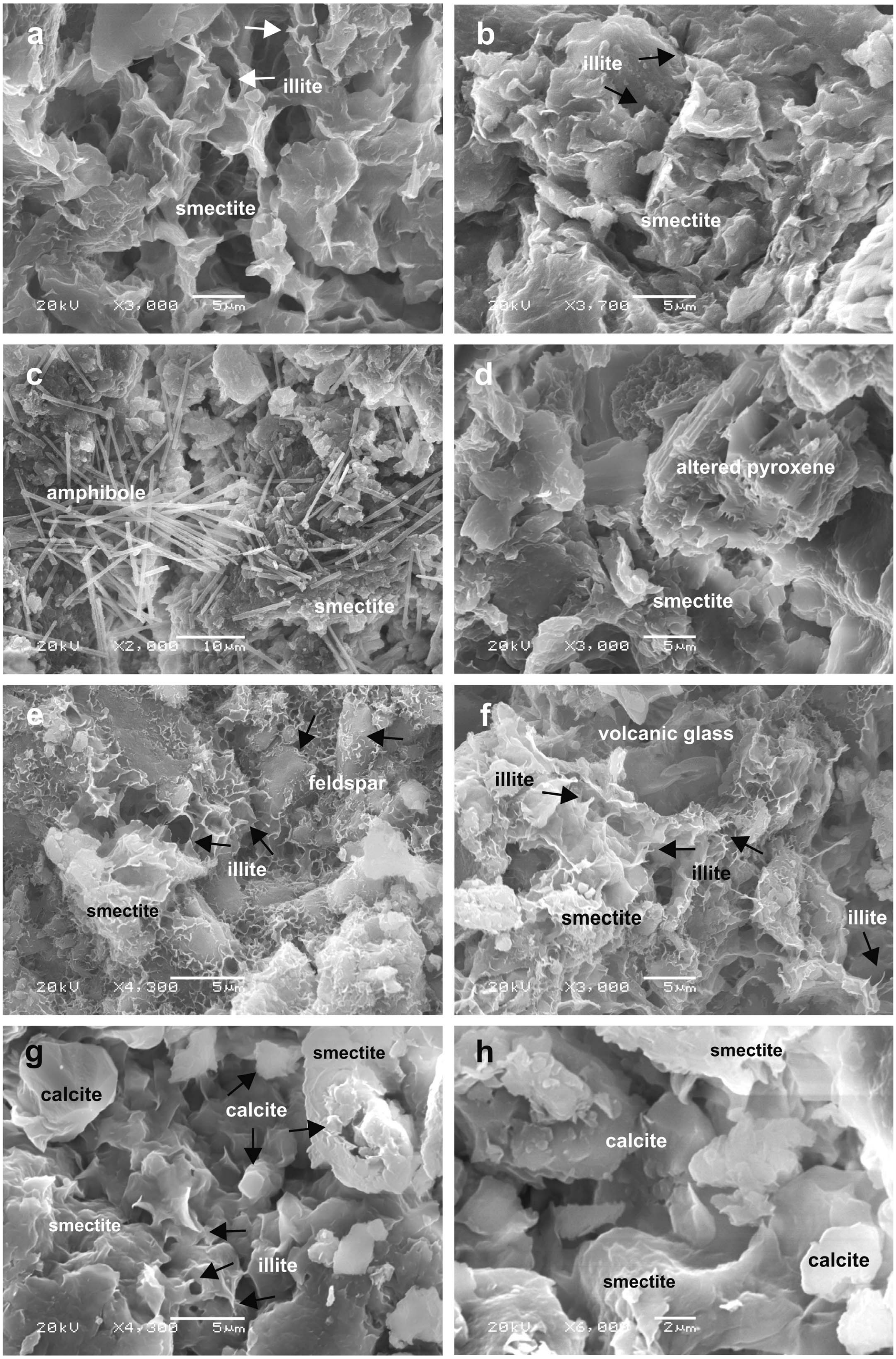

Figure 6. SEM images: (a,b) irregular cornflake-shaped smectite in southern mudstones (YH11, A22N-11); (c) smectite flakes with rod-like amphibole crystals (YH-13); (d) altered pyroxene edging smectite flakes (KT2-8); (e,f) authigenic growth of smectite on and between altered feldspar crystals and devitrified volcanic glass (AKB-13); (g,h) authigenic growth of calcite crystals in pores of irregular smectite and smectite-edged illite (AKB-8).

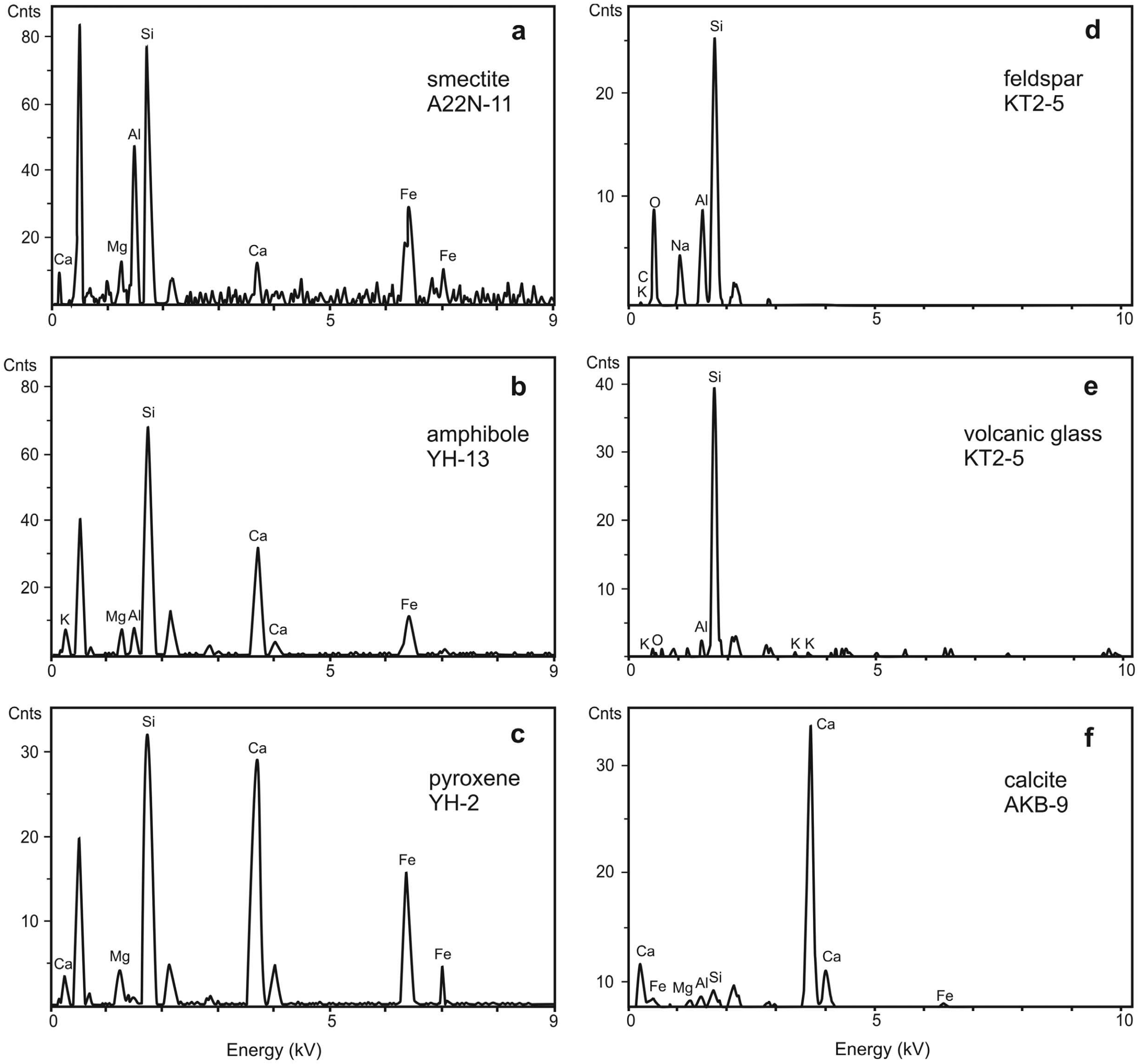

Figure 7. EDX analyses of smectite and precursors in mudstone samples.

as fluvial and lacustrine deposits. Evidence of weathering is seen in smectite flakes in the mudstones, which are associated with relict pyroxenes, rod-like amphiboles, feldspars, and volcanic glass (Figure 6). The suggestion of a detrital origin for the smectitic mudstone is based mainly on its repetition in stratigraphic sections and its matrix form in conglomerates, associated discrete minerals derived from ophiolitic and volcanogenic rocks (Hong *et al*., 2007, 2012) and micromorphologies of smectite flakes with irregular boundaries.

Changes in the concentrations of Fe_2O_3+MgO, Al_2O_3, and SiO_2 in the mudstones of the Mustafapaşa member are caused by vertical and lateral variations in lithologies. The presence of Fe_2O_3+MgO in the sediments may indicate detrital pyroxene, amphibole, and Fe (oxyhydr)oxide phases from ultramafic units exposed in the south and SiO_2 and Al_2O_3 from volcanogenic materials, such as feldspars and opal-A in the northern region. Therefore, smectitic mudstones from the southern region contain more Fe±Mg and less Si±Al and Ca+K+Na than either the middle or northern parts (Table 3). After the deposition of smectitic mudstones, the local concentration of Ca and K (along with Al) in the pore water resulted in *in situ* formation of calcite cement filling the micropores.

The edging of irregular smectite flakes by trace illite developed as a result of a dissolution and precipitation mechanism under alkaline micro-environmental conditions during early diagenesis (Braide and Huff, 1986; Erhenberg, 1991; Meunier and Velde, 2004; Ziegler, 2006). The presence of trace kaolinite in the northern part was caused by the relative increase of altered feldspars, amphiboles, and volcanic glass in the volcanic input throughout the sequence.

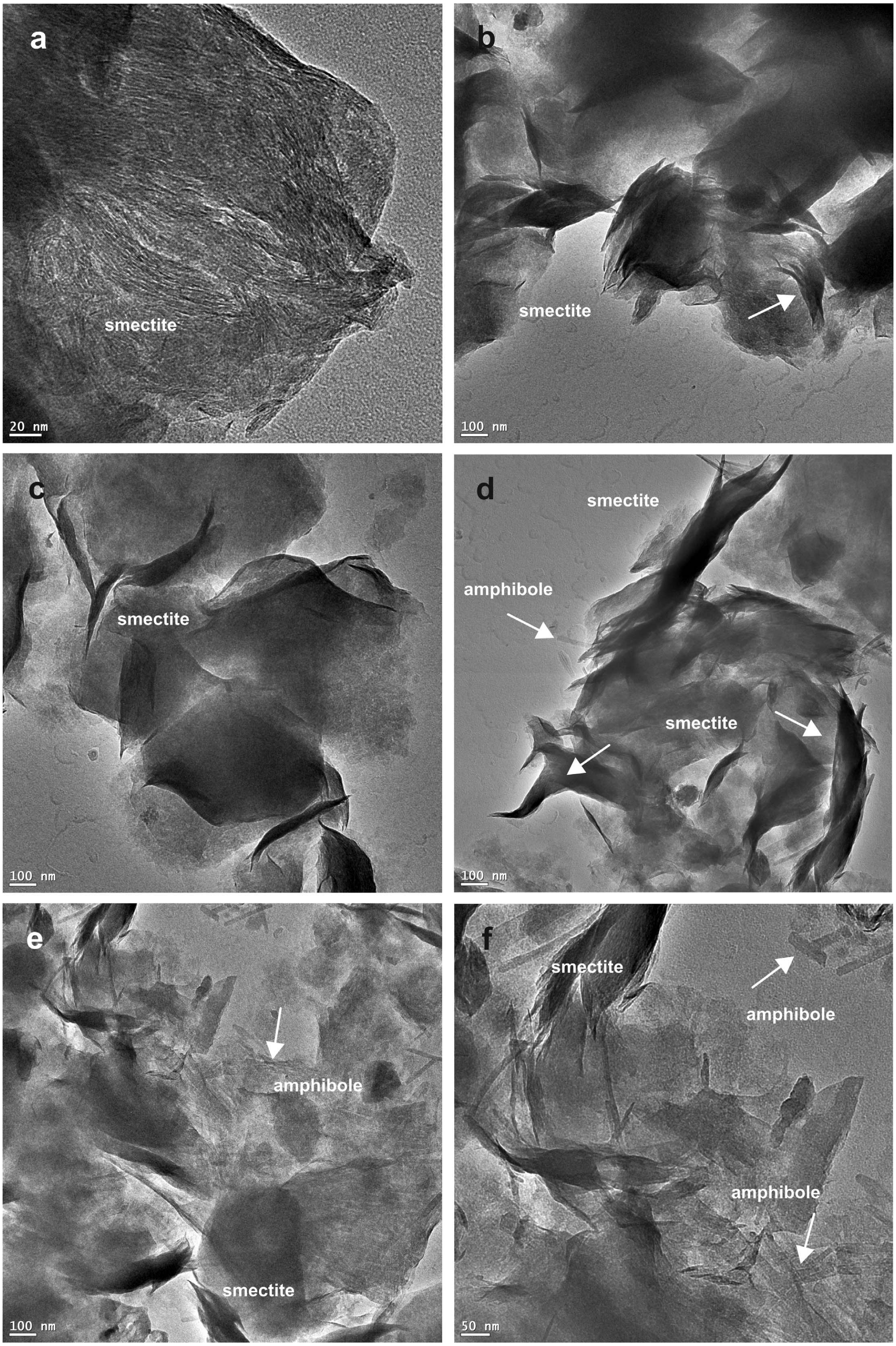

Figure 8. TEM images showing: (a) smectite plates, plate bundles (A22N-11); (b–d) wavy fan- and lens-like smectite plate packets (A22N-11, AKB-11); (d–f) smectite plates edging rod-like amphiboles (AKB-11), and (c–d) smectite plates edging fibrous materials resembling illite (A22N-11, AKB-11).

Table 2. Major oxides (wt.%), trace elements (ppm), and *REE* contents (ppm) of ophiolite, the Yeşilhisar conglomerate matrix, mudstones, and ignimbrites in the study area.

Major oxides (wt.%)	Ophiolite	Yeşilhisar matrix	Mudstone			Ignimbrite
			South	Middle	North	
	Avg. (*n* = 3)	(*n* = 1)	Avg. (*n* = 4)	Avg. (*n* = 11)	Avg. (*n* = 8)	Avg. (*n* = 2)
SiO_2	39.04	58.57	50.35	44.70	57.87	70.2
Al_2O_3	1.1	19.04	16.95	11.70	15.22	14.29
ΣFe_2O_3	8.05	4.58	9.12	6.23	6.11	1.73
MgO	36.51	2.15	4.38	4.24	1.57	0.39
CaO	0.16	1.26	2.71	11.68	3.1	1.76
Na_2O	0.003	1.83	2.09	1.24	1.57	2.33
K_2O	–	0.41	0.56	0.92	1.74	3.64
TiO_2	0.006	0.68	0.50	0.58	0.56	0.26
P_2O_5	–	0.02	0.04	0.08	0.11	0.03
MnO	0.07	0.02	0.07	0.09	0.06	0.05
LOI	13.8	11.2	13.2	18.3	12.0	5.2
Total	99.37	99.88	99.86	99.84	99.83	99.90
Trace elements (ppm)						
Ba	5	61	50.25	144.3	609	760.5
Be	0.33	2	1	1.7	1.5	2
Co	98.53	34.8	40.05	26	14.8	3.5
Cr	1850	590	547.5	401.8	136.25	80
Cs	–	0.9	3.43	6.3	3.4	4.9
Ga	0.73	17.3	13.48	10.9	14.2	13.5
Hf	–	2.4	1.4	2.3	3.8	4.2
Nb	–	2.6	3.1	6	8.8	4.2
Ni	1917	567	474.8	226.3	46	34
Rb	0.16	10.4	29.3	42.3	76.4	122.8
Sc	8	44	27.5	18.3	12.1	3.5
Sn	0.33	–	–	0.4	0.6	–
Sr	5	72.2	100.4	216.3	222.3	217.4
Ta	–	0.2	0.26	0.4	0.6	0.9
Th	–	1.5	1.9	5.4	12.7	21.9
U	0.3	0.4	1.9	1.6	2.6	6.45
V	37.3	255	127.5	109	72	5.5
W	0.43	–	1.05	1.6	2.2	2.7
Zr	0.4	77.1	51.2	85.2	145.7	148
Y	0.2	38.9	10.25	15.4	19.5	15.6
La	0.13	9.8	4.7	15.1	24.6	36.9
Ce	0.13	26.1	10.3	26.7	44.4	60.4
Pr	–	3.87	1.17	3.29	4.87	5.93
Nd	–	19.5	5.33	12.7	17.8	20
Sm	–	5.82	1.29	2.63	3.20	3.05
Eu	–	1.96	0.42	0.73	0.85	0.64
Gd	–	7.26	1.58	2.65	3.10	2.6
Tb	–	1.23	0.26	0.42	0.50	0.39
Dy	–	7.30	1.77	2.73	3.20	2.44
Ho	–	1.52	0.37	0.55	0.68	0.52
Er	–	4.62	1.09	1.56	1.93	1.59
Tm	–	0.60	0.16	0.22	0.30	0.26
Yb	0.23	3.77	1.16	1.55	2.16	1.89
Lu	–	0.56	0.18	0.23	0.34	0.29
TOT/C	0.1	0.03	0.24	2.42	0.26	0.15
TOT/S	–	0.03	0.25	0.04	0.004	–
Mo	0.07	0.2	0.9	0.3	0.2	1.5
Cu	12.73	30.3	56.46	24.8	13.0	3.3
Pb	0.33	3.2	3.8	8.24	5.8	1.7
Zn	18.3	52	52.5	38.6	19.5	7.5
Ni	2017.8	377.3	315.7	204.0	20.7	32.7
As	3.1	4.7	8.1	6.9	14.8	–
Cd	–	–	–	0.05	–	–
Sb	–	–	0.05	0.12	0.03	–

Table 2 (*contd.*)

Major oxides (wt. %)	Ophiolite Avg. (n = 3)	Yeşilhisar matrix (n = 1)	Mudstone South Avg. (n = 4)	Mudstone Middle Avg. (n = 11)	Mudstone North Avg. (n = 8)	Ignimbrite Avg. (n = 2)
Bi	–	–	0.05	0.07	0.11	0.05
Ag	–	–	–	–	–	–
Au (ppb)	2.6	–	0.9	1.2	1.5	1.2
Hg	0.003	–	0.02	0.02	0.001	–
Tl	–	–	–	0.08	0.1	–
Se	–	0.6	–	–	0.01	–
Σ*REE*	0.69	132.8	40.03	86.46	127.4	152.5
Σ*LREE*	0.26	59.27	21.50	59.40	91.70	123.2
Σ*MREE*	0.2	25.09	5.69	9.71	11.5	10.4
Σ*HREE*	0.1	9.55	2.59	5.45	4.73	4.82
Eu/Eu*	1.75	1.30	1.26	1.26	1.20	1.04
Ce/Ce*	0.63	0.89	0.92	0.83	0.87	0.97
Yb/Yb*	0.89	1.02	1.09	1.09	1.06	1.32
La_N/Yb_N	0.3	0.25	0.41	0.94	5.96	14.42

n: number of samples.
Σ*REE* = the sum of (La–Lu)+Y; Σ*LREE* = the sum of La–Nd; Σ*MREE* = the sum of (Sm–Ho); Σ*HREE* = the sum of (Er–Lu); Ce/Ce*= $2Ce_N/(La_N+Pr_N)$, Eu/Eu* = $2Eu_N/(Sm_N+Gd_N)$, Yb/Yb* = $2Yb_N/(Tm_N+Lu_N)$, where N refers to a NASC-normalized value (Gromet *et al.*, 1984).

The *LREE*s/*HREE*s in a NASC-normalized pattern and the $(La/Yb)_N$ ratios are correlated positively with the concentration of smectite in the mudstone deposits and increase from south to north, indicating an increasing contribution of volcanic materials in that direction. Therefore, the fractionation of amphibole and feldspar resulted in the adsorption of *LREEs* onto the smectite and Fe (oxyhydr)oxide phases, similar to that reported by Christidis (1998) and Jeans *et al.* (2000). However, the depletion of *LREE*s relative to *MREE*s and *HREE*s in mudstones from the southern region suggests that they benefited from the alteration of amphibole and pyroxene that originated from the ophiolitic basement rock (Cullers and Graf, 1983; Nyakairu and Koeberl, 2001). A positive Eu anomaly value suggests that the accumulation and alteration of plagioclase originated from the input of interlayered volcanic units (Nance and Taylor, 1977).

The parallel northward increase in the Nb/Ti abundance ratio relative to the La/Yb ratio suggests that Nb and La are concentrated with increasing smectite-dominated mudstone deposits derived mainly from ophiolite and related Yeşilhisar conglomerates and volcanic source rocks. This was confirmed by a northward parallel increase in the Zr/Ni ratio relative to the Zr/Co ratio and a positive correlation of Zr with Σ*REE* in the mudstone samples. This suggests that Σ*REE* have a similar geochemical behavior associated with the molecular structure of smectite, which increases northward with Zr. This interpretation is also supported by an increase in Ba, Rb, and Sr in the mudstones of the Mustafapaşa member to the north, close to the Kavak and Sarımadentepe ignimbrites, and by the increase in Ni, Co, and Cr in the mudstones in the south, near the ophiolitic basement units. Intermediate values of these data are present in the mudstones in the middle area.

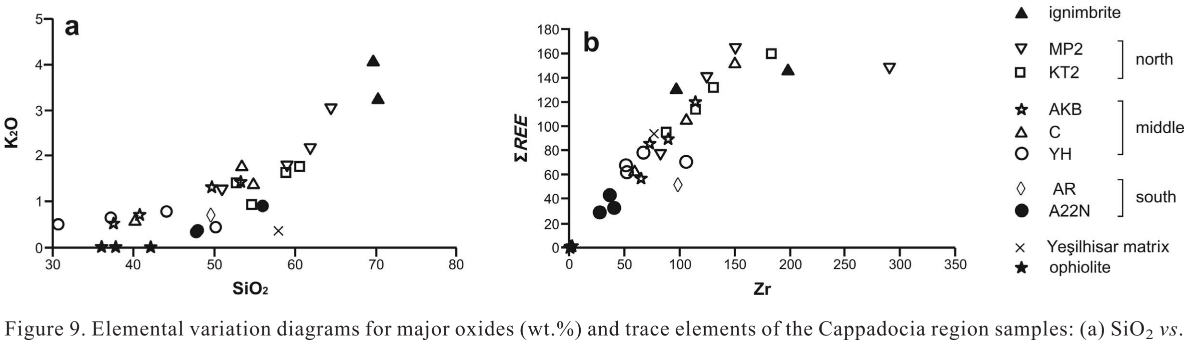

Figure 9. Elemental variation diagrams for major oxides (wt.%) and trace elements of the Cappadocia region samples: (a) SiO_2 *vs.* K_2O; (b) Zr *vs.* Σ*REE*.

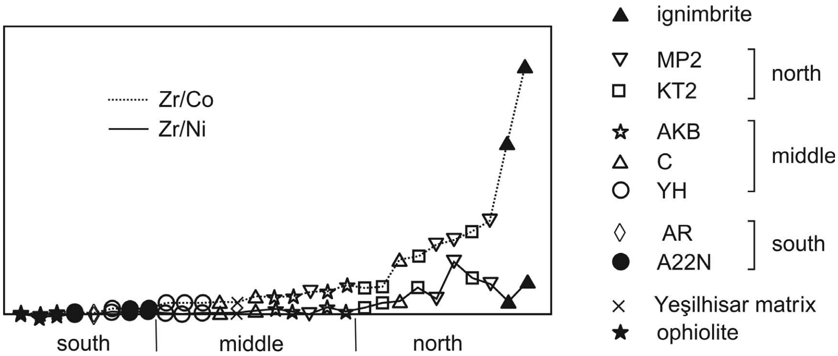

Figure 10. Plots of Zr/Ni *vs*. Zr/Co for the smectite-dominated mudstone samples from the south, middle, and north of the study area.

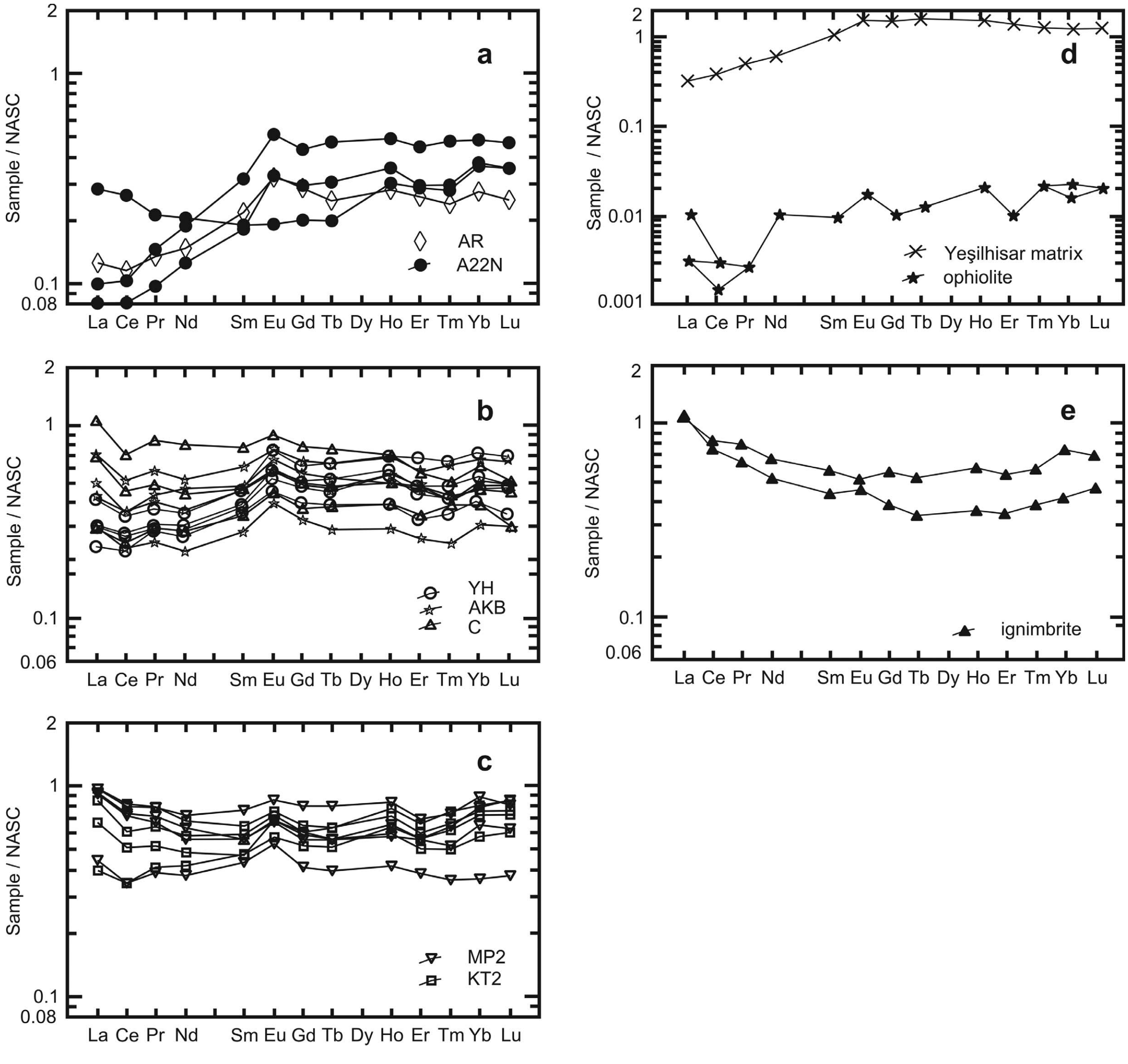

Figure 11. NASC-normalized *REE* patterns (Gromet *et al.*, 1984) from the smectite-dominated mudstone samples from: (a) the south; (b) the middle; (c) the north, and (d,e) north of the study area.

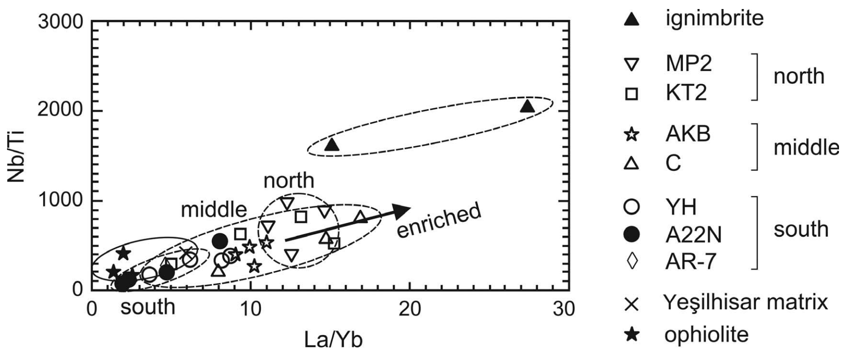

Figure 12. Plots of La/Nb *vs.* Nb/Ti for the smectite-dominated mudstone samples from the south, middle, and north of the study area.

Table 3. Chemical compositions (wt.%) and structural formulae for pure smectite samples.

Major oxides (wt.%)	A22N-11 South	AKB-11 Middle	KT2-8 North	Average
SiO_2	49.20	50.93	51.0	50.38
Al_2O_3	15.30	15.80	15.30	15.47
ΣFe_2O_3	11.08	6.19	7.31	8.20
MgO	2.84	4.09	3.17	3.37
CaO	1.62	1.58	2.20	1.80
Na_2O	0.03	0.07	0.18	0.09
K_2O	0.84	1.42	0.94	1.07
MnO	0.06	0.10	0.07	0.08
TiO_2	0.42	0.53	0.59	0.51
LOI	18.2	19.0	19.0	18.73
Total	99.59	99.71	99.76	99.69
SiO_2/Al_2O_3	3.22	3.22	3.33	3.26
Tetrahedral				
Si	7.45	7.65	7.68	7.59
Al	0.55	0.35	0.32	0.41
Σ	8.00	8.00	8.00	8.00
Octahedral				
Al	2.18	2.45	2.39	2.34
Fe	1.26	0.70	0.83	0.93
Mg	0.65	0.92	0.72	0.76
Ti	0.05	0.06	0.07	0.06
Mn	0.009	0.02	0.01	0.013
Σ	4.15	4.15	4.02	4.11
Interlayer				
Ca	0.262	0.254	0.355	0.29
Na	0.009	0.01	0.052	0.03
K	0.162	0.272	0.180	0.20
Σ	0.433	0.536	0.587	0.52
Tetrahedral charge	0.550	0.350	0.320	0.41
Octahedral charge	0.170	0.450	0.610	0.41
Total charge	0.720	0.800	0.930	0.82
Interlayer charge	0.690	0.800	0.930	0.81
xt/xo	3.24	0.78	0.52	1.00

xt/xo = tetrahedral charge/octahedral charge ratio.

However, a slight to moderate negative Ce anomaly in mudstones and ophiolites suggests the substitution of Ce by Fe in iron-oxide/hydroxide phases under oxidizing and reducing sedimentation environments (Fulignati *et al.*, 1999; Karakaya, 2009; Zhou *et al.*, 2013). This suggestion was supported by the alternation of green, yellow, and dark red mudstones, reflecting the fluctuation of reducing and oxidizing conditions in the depositional environment (Eren and Kadir, 2013).

CONCLUSIONS

The development of flaky smectite and smectite ± illite with relict pyroxenes, amphiboles, feldspars, and volcanic glass suggests that the weathering of ophiolitic units in the south and volcanic units in the north contributed to the accumulation of detrital smectite-dominated fluvial and lacustrine mudstone deposits of the Mustafapaşa member in a tectonic depressional basin. Serpentinized and Fe (oxyhydr)oxide-bearing pyroxenes and amphiboles, and the alteration of feldspars, originated from the weathering of ophiolitic units, related Yeşilhisar conglomerates, and ignimbrites. Increases in the *LREE*s/*HREE*s, $(La/Yb)_N$, Zr/Ni, and Zr/Co ratios and Ba, Rb, and Sr in the mudstones in the northern Mustafapaşa member with a positive Eu anomaly suggest that the decomposition of detrital materials from ophiolitic and volcanogenic material were the main sources of Fe±Mg, Al, and Si for the smectite in mudstones in the study area. Therefore, the change in the chemical composition of smectite fractions in the depressional basin is related mainly to the proximity to the source area.

ACKNOWLEDGMENTS

The present study was supported financially by the Scientific Research Projects Fund of Eskişehir Osmangazi University in the framework of Project 201015030 and constitutes part of the PhD thesis of the first author. The authors are much indebted to anonymous reviewers for their extremely careful and constructive reviews which improved the quality of the paper significantly. The authors are also grateful to Associate Editor, Warren D. Huff, and Editor in Chief, Michael A. Velbel, for their insightful editorial comments and suggestions.

REFERENCES

Batum, I. (1975) Petrographische und geochemische Untersuchungen in den Vulkangebieten Göllü Dağ und Acıgöl (Zentralanatolien/Türkei). PhD thesis, Freiburg University, Germany, 101 pp.

Batum, I. (1978) Geology and petrography of the Göllüdağ and Acıgöl volcanics in the southwestern Nevşehir. *Bulletin of Earth Sciences Application and Research Centre of Hacettepe University*, **4**, 50–69. (In Turkish with English abstract.)

Besang, C., Eckhardt, F.J., Harre W., Kreuzer, H., and Müller, P. (1977) Radiometrische Altersbestimmungen an Neogenen eruptivgesteinen der Turkei. *Geologisches Jahrbuch*, **B25**, 3–36.

Braide, S.P. and Huff, W.D. (1986) Clay mineral variation in Tertiary sediments from the eastern Flank of the Niger Delta. *Clay Minerals*, **21**, 211–224.

Brindley, G.W. (1980) Quantitative X-ray analysis of clays. Pp. 411–438 in: *Crystal Structures of Clay Minerals and their X-ray Identification* (G.W. Brindley and G. Brown, editors). Monograph **5**, Mineralogical Society, London.

Casciello, E., Cosgrove, J.W., Cesarano, M., Romero, E., Queralt, I., and Vergés, J. (2011) Illite-smectite patterns in sheared Pleistocene mudstones of the southern Apennines and their implications regarding the process of illitization: a multiple analysis. *Journal of Structural Geology*, **33**, 1699–1711.

Chermak, J.A. and Schreiber, M.E. (2014) Mineralogy and trace element geochemistry of gas shales in the United States: Environmental implications. *International Journal of Coal Geology*, **126**, 32–44.

Christidis, G.E. (1998) Comparative study of the mobility of major and trace elements during alteration of an andesite and a rhyolite to bentonite, in the islands of Milos and Kimolos, Aegean, Greece. *Clays and Clay Minerals*, **46**, 379–399.

Cullers, R.L. and Graf, J. (1983) Rare earth elements in igneous rocks of the continental crust: intermediate and silicic rocks, ore petrogenesis. Pp. 275–312 in: *Rare-Earth Geochemistry* (P. Henderson, editor). Elsevier, Amsterdam.

Delvigne, J.E. (1998) *Micromorphology of Mineral Alteration and Weathering. The Canadian Mineralogist*, Special Publication, 494 pp.

Dilek, Y. and Furnes, H. (2014) Ophiolites and their origins. *Elements*, **10**, 93–100.

Dilek, Y. and Whitney, D.L. (1997) Counterclockwise *P-T*-t trajectory from the metamorphic sole of a Neo-Tethyan ophiolite (Turkey). *Tectonophysics*, **280**, 295–310.

Druitt, T.H., Brenchley, P.J., Gökten, Y.E., and Francaviglia, V. (1995) Late Quaternary rhyolitic eruptions from the Acıgöl complex, Central Turkey. *Journal of Geological Society*, London, **152**, 655–667.

Ercan, T., Köse, C., Akbaşli, A., and Yildirim, T. (1987) Orta Anadolu'da Nevşehir-Niğde-Konya dolayındaki volkanik kökenli gaz çıkışları. *Cumhuriyet Üniversitesi Mühendislik Fakültesi Dergisi – Seri A, Yerbilimleri*, **4**, 57–63.

Ercan, T., Yeğingil, Z., and Biggazi, G. (1989) Obsidiyen tanımı ve özellikleri, Anadolu'daki dağılımı ve Orta Anadolu obsidiyenlerinin jeokimyasal nitelikleri. *Jeomorfoloji Dergisi*, **17**, 71–83.

Eren, M. and Kadir, S. (2013) Colour origin of red sandstone beds within the Hüdai Formation (Early Cambrian), Aydıncık (Mersin), southern Turkey". *Turkish Journal of Earth Sciences*, **22**, 563–573.

Erhenberg, S.N. (1991) Kaolinized, potassium-leached zones at the contacts of the Garn Formation, Haltenbanken, mid-Norwegian continental shelf. *Marine and Petroleum Geology*, **8**, 250–269.

Fulignati, P., Gioncada, A., and Sbrana, A. (1999) Rare-earth element (REE) behaviour in the alteration facies of the active magmatic-hydrothermal system of Vulcano (Aeolian Islands, Italy). *Journal of Volcanology and Geothermal Research*, **88**, 325–342.

Gevrek, A.İ. (1997) Aksaray doğusu, Ihlara-Derinkuyu yöresindeki volkaniklastiklerin sedimentolojisi. Doktora Tezi, Ankara Üniversitesi Fen Bilimleri Enstitüsü, 178 pp. (in Turkish, unpublished).

Göncüoğlu, C. and Toprak, V. (1992) Neogene and Quaternary volcanism of Central Anatolia: a volcano-structural evaluation. *Bulletin de la Section de Volcanologie, Société Géologique de France*, **26**,1–6.

Göz, E., Kadir, S., Gürel, A., and Eren, M. (2014) Geology, mineralogy, geochemistry, and depositional environment of a Late Miocene/Pliocene fluvio-lacustrine succession, Cappadocian Volcanic Province, central Anatolia, Turkey. *Turkish Journal of Earth Sciences*, **23**, 386–411.

Gromet, L.P., Dymek, R.F., Haskin, L.A., and Korotev, R.I. (1984) The 'North American Shale Composite': its compilation, major and trace element characteristics. *Geochimica et Cosmochimica Acta*, **48**, 2469–2482.

Gürel, A. and Kadir, S. (2006) Geology, mineralogy and origin of clay minerals of the Pliocene fluvial-lacustrine deposits in the Cappadocian Volcanic Province, Central Anatolia, Turkey. *Clays and Clay Minerals*, **54**, 555–570.

Gürel, A. Ciftci, E., and Kerey, I.E. (2007) Sedimentological characteristics of the Cukurbağ formation deposited along the Ecemis Fault Zone (Central Anatolia, Turkey). *Journal of the Geological Society of India*, **70**, 59–72.

Gürel, A. and Kadir, S. (2008) Geology and mineralogy of Late Miocene clayey sediments in the southeastern part of the Central Anatolian Volcanic Province, Turkey. *Clays and Clay Minerals*, **56**, 307–321.

Güven, N. (1988) Smectites. Pp. 497–559 in: *Hydrous Phyllosilicates* (S.W. Bailey, editor). Reviews in Mineralogy, **19**, Mineralogical Society of America, Washington, D.C.

Hong, H., Li, Z., Xue, H., Zhu, Y., Zhang, K., and Xiang, S. (2007) Oligocene clay mineralogy of the Linxia Basin: evidence of paleoclimatic evoution subsequent to the initial stage uplift of the Tibetan Plateau. *Clays and Clay Minerals*, **55**, 491–503.

Hong, H., Wang, C., Zeng, K., Zhang, K., Yin, K., and Li, Z. (2012) Clay mineralogy of the Zhada sediments: Evidence for climatic and tectonic evolution since ~9 Ma in Zhada, southwestern Tibet. *Clays and Clay Minerals*, **60**, 240–253.

Iijima, A. and Tada, R. (1981) Silica diagenesis of Neogene diatomaceous and volcaniclastic sediments in northern Japan. *Sedimentolgy*, **28**, 185–200.

Innocenti, F., Mazzuoli, R., Pasquarè, G., Radicati Di Brozolo, F., and Villari, L. (1975) The Neogene calcalkaline volcanism of Central Anatolia: geochronological data on Kayseri-Niğde area. *Geological Magazine*, **112**, 349–360.

Inoue, A., Meunier, A., and Beaufort, D. (2004) Illite–smectite mixed-layer minerals in felsic volcaniclastic rocks from drill cores, Kakkonda, Japan. *Clays and Clay Minerals*, **52**, 66–84.

Jeans, C.V., Wray, D.S., Merriman, R.J., and Fisher, M.J. (2000) Volcanogenic clays in Jurassic and Cretaceous strata of England and the North Sea Basin. *Clay Minerals*, **35**, 25–55.

Kadir, S., Gürel, A., Senem, H., and Külah, T. (2013) Geology of Late Miocene clayey sediments and distribution of palaeosol clay minerals in the northeastern part of the Cappadocian Volcanic Province (Araplı-Erdemli), central Anatolia, Turkey. *Turkish Journal of Earth Sciences*, **22**, 427–443.

Karakaya, N. (2009) REE and HFS element behaviour in the alteration facies of the Erenler Dağı Volcanics (Konya, Turkey) and kaolinite occurrence. *Journal of Geochemical Exploration*, **101**, 185–208.

Le Pennec, J.L., Bourdier, J.L., Froger, J.L., Temel, A., Camus, G., and Gourgaud, A. (1994) Neogene ignimbrites of the Nevşehir Plateau (Central Anatolia): stratigraphy, distribution and source constraints. *Journal of Volcanology and Geothermal Research*, **63**, 59–87.

Le Pennec, J.L., Temel, A., Froger, J.L., Sen, S., Gourgaud, A., and Bourdier, J.L. (2005) Stratigraphy and age of the Cappadocia ignimbrites, Turkey: reconciling field constraints with paleontologic, radiochronologic, geochemical and paleomagnetic data. *Journal of Volcanology and Geothermal Research*, **141**, 45–64.

Meunier, A. and Velde, B. (2004) *Illite, Origin, Evolution and Metamorphism*. Springer-Verlag, Berlin, Heidelberg, New York, 286 pp.

Moore, D.M. and Reynolds, R.C. (1989) *X-ray Diffraction and the Identification and Analysis of Clay Minerals*. Oxford University Press, New York, 332 pp.

Nahon, D., Paquet, H., and Delvigne, J. (1982) Lateritic weathering of ultramafic rocks and the concentration of nickel in the western Ivory Coast. *Economic Geology*, **77**, 1159–1175.

Nance, W.B. and Taylor, S.R. (1977) Rare earth element patterns and crustal Evolution – II. Archean sedimentary rocks from Kalgoorlie, Australia. *Geochimica et Cosmochimica Acta*, **41**, 225–231.

Nyakairu, G.W.A. and Koeberl, C. (2001) Mineralogical and chemical composition and distribution of rare earth elements in clay-rich sediments from central Uganda. *Geochemical Journal*, **35**, 13–28.

Osborn, S.G., Duffield, L.T., Elliott, W.C., Wampler, J.M., Elmore, R.D., and Engel, M.H. (2014) The timing of diagenesis and thermal maturation of the Cretaceous Marias River Shale, Disturbed Belt, Montana. *Clays and Clay Minerals*, **62**, 112–125.

Pasquarè, G. (1968) Geology of the Cenozoic volcanic area of Central Anatolia. *Atti Della Accademia Nazionale dei Lincei*, *Memorie*, serie VIII, volume **IX**, Roma, 55–204.

Pasquarè, G., Poli, S., Vezzoli, L., and Zanchi, A. (1988) Continental arc volcanism and tectonic setting in Central Anatolia, Turkey. *Tectonophysics*, **146**, 217–230.

Schumacher, R. and Mues-Schumacher, U. (1996) The Kızılkaya ignimbrite-an unusual low-aspect-ratio ignimbrite from Cappadocia, central Turkey. *Journal of Volcanology and Geothermal Research*, **70**, 107–121.

Taylor, K.G. and Macquaker, J.H.S. (2014) Diagenetic alteration in a silt- and clay-rich mudstone succession: an example from the Upper Cretaceous Mancos Shale of Utah, USA. *Clay Minerals*, **49**, 245–259.

Toprak, V. (1998) Vent distribution and its relation to regional tectonics, Cappadocian Volcanics, Turkey. *Journal of Volcanology and Geothermal Research*, **85**, 55–67.

Türkecan, A., Dönmez, M., and Akçay, E.A. (2003) Tertiary volcanics of Kayseri-Niğde-Nevşehir areas. Mineral Research and Exploration Report No. 10575, Ankara (in Turkish, unpublished).

Viereck-Götte, L. and Gürel A. (2003) Klima- und Vegetationswechsel dokumentiert in Obermiozaenen Paläoböden Kappadokiens, Zentralanatolien. *Berichte der Deutschen Mineralogischen Gesellschaft. Beihefte zum, European Journal of Mineralogy*, **15**, pp 211, Stuttgart, Germany.

Viereck-Götte, L., Lepetit, P., Gürel, A., Ganskow, G., Çopuroğlu, İ., and Abratis, M. (2010) Revised volcanostratigraphy of the Upper Miocene to Lower Pliocene Ürgüp Formation, Central Anatolian volcanic province, Turkey. Pp. 85–112 in: *Stratigraphy and Geology of Volcanic Areas* (G. Groppelli and L. Viereck-Götte, editors), *Geological Society of America Special Paper*, 464.

Zhou, L., Zhang, Z., Li, Y., You, F., Wu, C., and Zheng, C. (2013) Geological and geochemical characteristics in the paleo-weathering crust sedimentary type REE deposits, western Guizhou, China. *Journal of Asian Earth Sciences*, **73**, 184–198.

Ziegler, K. (2006) Clay minerals of the Permian Rotliegend Group in the North Sea and adjacent areas. *Clay Minerals*, **41**, 355–393.

(*Received 9 July 2014; revised 17 September 2014; Ms. 895; AE: W.D. Huff*)

Clays and Clay Minerals, Vol. 62, No. 4, 286–312, 2014.

MINERALOGICAL AND ISOTOPIC RECORD OF DIAGENESIS FROM THE OPALINUS CLAY FORMATION AT BENKEN, SWITZERLAND: IMPLICATIONS FOR THE MODELING OF PORE-WATER CHEMISTRY IN A CLAY FORMATION

CATHERINE LEROUGE[1],*, SYLVAIN GRANGEON[1], FRANCIS CLARET[1], ERIC GAUCHER[1], PHILIPPE BLANC[1], CATHERINE GUERROT[1], CHRISTINE FLEHOC[1], GUILLAUME WILLE[1], AND MARTIN MAZUREK[2]

[1] BRGM, 3, avenue Claude Guillemin, F-45060 Orléans Cedex 2, France
[2] University of Bern, Institute of Geological Sciences, Baltzerstrasse 1+3, CH-3012 Bern, Switzerland

Abstract—Argillaceous rocks are considered to be a suitable geological barrier for the long-term containment of wastes. Their efficiency at retarding contaminant migration is assessed using reactive-transport experiments and modeling, the latter requiring a sound understanding of pore-water chemistry. The building of a pore-water model, which is mandatory for laboratory experiments mimicking *in situ* conditions, requires a detailed knowledge of the rock mineralogy and of minerals at equilibrium with present-day pore waters. Using a combination of petrological, mineralogical, and isotopic studies, the present study focused on the reduced Opalinus Clay formation (Fm) of the Benken borehole (30 km north of Zurich) which is intended for nuclear-waste disposal in Switzerland. A diagenetic sequence is proposed, which serves as a basis for determining the minerals stable in the formation and their textural relationships. Early cementation of dominant calcite, rare dolomite, and pyrite formed by bacterial sulfate reduction, was followed by formation of iron-rich calcite, ankerite, siderite, glauconite, (Ba, Sr) sulfates, and traces of sphalerite and galena. The distribution and abundance of siderite depends heavily on the depositional environment (and consequently on the water column). Benken sediment deposition during Aalenian times corresponds to an offshore environment with the early formation of siderite concretions at the water/sediment interface at the fluctuating boundary between the suboxic iron reduction and the sulfate reduction zones. Diagenetic minerals (carbonates except dolomite, sulfates, silicates) remained stable from their formation to the present. Based on these mineralogical and geochemical data, the mineral assemblage previously used for the geochemical model of the pore waters at Mont Terri may be applied to Benken without significant changes. These further investigations demonstrate the need for detailed mineralogical and geochemical study to refine the model of pore-water chemistry in a clay formation.

Key Words—Clay Formation, Diagenesis, Mineralogy, Pore-water Chemistry, Stable Isotopes.

INTRODUCTION

Clay minerals and in particular swelling clay minerals (*i.e.* that have the capacity accommodate various amounts of water molecules, *e.g.* montmorillonite) are amongst the most chemically reactive minerals known on Earth, and also have exceptional mechanical properties. Because of their small size (which may be a result of crystallization at ambient temperature) and incorporation of foreign elements that may act as "poisoning" elements (Meunier, 2006), these minerals have a large density of reactive surface sites that can immobilize cations such as metals efficiently (*e.g.* Tournassat *et al.*, 2013 and references therein). Clays are efficient cation adsorbents and exchangers, with cation exchange capacity (CEC) varying over a wide range depending on the clay mineral: kaolinite: 30−150 meq kg^{-1} (Ma and Eggleton, 1999), mixed-layer illite-smectite: 504−782 meq kg^{-1} (Müller-Vonmoos *et al.*, 1994), illite: 100−400 meq kg^{-1}, (Środoń *et al.*, 1986), smectite: 870−1330 meq kg^{-1} (Müller-Vonmoos *et al.*, 1994; Baeyens and Bradbury, 1997), glauconite: 50−390 meq kg^{-1} (Manghnani and Hower, 1964), chlorite: 40−370 meq kg^{-1} (Martin, 1955). In addition, swelling clays have the ability, when they are in a confined medium, to 'self-heal' (and/or 'self-seal'). For example, cracks in compacted clay materials will, with time, be filled by clays thus reducing the macro-porosity. Compacted (swelling) clays have very low permeability (typically <10^{-12} m s^{-1}; Mazurek *et al.*, 2008, 2009).

All of the above-mentioned characteristics are found in argillaceous rocks, which are thus considered suitable as a geological barrier for the long-term containment of wastes such as nuclear waste or heavy metals (Madsen, 1998). A large part of our knowledge of argillaceous rock behavior is provided by the numerous different experiments conducted in laboratories and *in situ* underground research laboratories dedicated to nuclear-waste storage (ONDRAF/NIRAS, 2001, 2009; NAGRA, 2002; Pearson *et al.*, 2003; Gaucher *et al.*, 2004, 2006, 2009; ANDRA, 2005; Mazurek *et al.*, 2008; Wenk *et al.*, 2008; Weetjens *et al.*, 2009; Mazurek *et al.*, 2009). These experiments and laboratories, and the numerous associated drilling campaigns, were used to obtain samples representative of these formations over large

---

* E-mail address of corresponding author:
c.lerouge@brgm.fr
DOI: 10.1346/CCMN.2014.0620404

spatial extents (Landais *et al.*, 2012). Mineralogical analysis of these samples, associated with the "multi-specimen" approach of X-ray diffraction (XRD) patterns, helped to elucidate the diagenesis of the clay minerals (Claret *et al.*, 2004; Drits *et al.*, 1997; Hubert *et al.*, 2009; Lanson *et al.*, 2009; Sakharov *et al.*, 1999; Ufer *et al.* 2012a, 2012b), and in particular the so-called 'illitization' processes, *i.e.* transformation of smectite, a subject to be discussed with care as suggested by Kaufhold and Dohrmann (2010). Previous studies of the Callovian-Oxfordian formation demonstrated that a discrete smectite phase coexisted with randomly interstratified illite-smectite minerals, the latter consisting mainly of illite layers (Claret *et al.*, 2004). With burial depth, the illitization process manifests itself in the disappearance of the smectite minerals. This phenomenon was originally demonstrated to occur in other clay-rich formations, especially in the extensively studied Texas Gulf Coast, but is beyond the scope of the present study.

The present study provides a full description of the mineralogical assemblage, including the textural relations between the different clay and non-clay phases. This information is essential for a full understanding of the chemical behavior and the waste-retention capacity of clay-rich formations because: (1) clays only minimally immobilize anions, whereas carbonate minerals such as calcite have been shown to be efficient sinks for a number of them, *e.g.* iodine (Claret *et al.*, 2010); (2) clays sorb cations mainly through adsorption reaction, which are to a large extent reversible, whereas other phases such as calcite, which are much less reactive over short timescales, can immobilize cations *via* structural incorporation; and (3) in order to predict the evolution of a storage repository, the understanding of pore-water composition, and its relation to the solid phase must be known. Indeed, much effort has been invested in evaluating the composition of pore water present in argillaceous rock as it will influence both the evolution of the various engineered materials used in the facility (steel, concrete, glass, *etc.*) and the transfer characteristics of elements such as radionuclides through the host rock. Three complementary approaches have been used: (1) geochemical modeling based on knowledge of the concentration of non-reactive solutes in the pore water, the minerals present in the clayrock, and the cation exchange properties of the clay minerals; (2) collection of representative pore-water samples by means of dedicated experiments carried out in *in situ* research laboratories; and (3) the so-called 'natural analog approach' that represents an alternative way of better constraining the long-term behavior of argillaceous rocks by studying their long-term interaction with the naturally occurring isotope of an element of interest for storage (*e.g.* a radioactive element), through their behavior in the geological past, from the time of sedimentation to diagenesis and deformation.

In 1989 the Opalinus Clay formation (Fm), occurring in Switzerland and in southern Germany, was proposed as a target formation for disposal of high-level radioactive waste in Switzerland. Since 1996 the formation has been investigated in the underground research laboratory of Mont Terri at Saint Ursanne (Thury, 2002; Nagra, 2002), the nearby Mont Russelin anticline (Koroleva *et al.*, 2011), and at Benken (deep borehole 30 km N of Zurich: Mazurek *et al.*, 2008, 2009, 2011). Experiments have been aimed at, among other things, determining present-day pore-water chemistry (Vinsot *et al.*, 2008) and the minerals controlling it (Pearson *et al.*, 2003). This has led to a conceptual model of the interstitial water in the Opalinus Clay Fm at Mont Terri (Pearson *et al.*, 2003, 2011). The model considers that present-day pore waters are at equilibrium with the clay mineral-based (illite, smectite...) cation exchanger and a suite of diagenetic minerals in a nearly closed system. This assumption is considered to be locally valid given the long residence time of pore-water chemical constituents, *i.e.* very low advective and diffusive fluxes within the formation. This in turn means that the relative amounts of such divalent cations as Ca^{2+}, Mg^{2+}, Fe^{2+}, and Sr^{2+} on the cation exchanger will reflect equilibrium with respect to the corresponding activities of dissolved species. Activities of Ca^{2+}, Mg^{2+}, and Fe^{2+} are considered to be controlled by three pure carbonate minerals in the present form of the model: calcite (for Ca), dolomite (for Mg), and siderite (for Fe). Sr^{2+} is controlled by the clay cation exchanger. The redox state is imposed by pyrite and sulfate is controlled by celestite saturation. More detailed information concerning the chemical composition of diagenetic minerals at equilibrium with present-day pore waters, as well as their distribution within the geological formation, however, indicates that considering pure carbonate minerals in the model or a phase which is not present throughout the clay formation only approximates the necessary level of detail required to inform geochemical modeling. The present study addresses these various aspects.

The study reported here undertook a petrological and isotopic study of the Opalinus Clay Fm from the Benken borehole for the establishment of a pore-water chemistry model of Opalinus Clay Fm at Benken. The objective of the petrological study was to establish the sequence of formation of diagenetic minerals and to determine the major processes controlling pore-water chemistry over geological time. Particular attention was paid to diagenetic carbonates and sulfides/sulfates, which are the key minerals controlling major cations and redox reactions according to the pore-water chemistry model of Opalinus Clay Fm at Mont Terri (Pearson *et al.*, 2003, 2011). In addition, stable-isotope investigations were performed in order to constrain the temperature of mineral formation and/or the origin of the fluids from which the minerals precipitated.

REGIONAL SETTING

The Benken borehole from which the samples studied here were taken was drilled in the Zürcher Weinland, in the Swiss Molasse Basin, a tectonically quiescent region (Figure 1a). The bedding is nearly horizontal (Birkhäuser *et al.*, 2001; Spillmann *et al.*, 2010), and no large faults are present in the vicinity of the borehole. To the northeast, toward the Hegau-Bodensee Graben, and in the Jura Mountains to the west, the sedimentary rocks become faulted and folded (NAGRA, 2002). The area consequently represents a structurally simple region on the northern edge of a deep basin, bounded by deformed sedimentary rocks to the northeast and west. The drilled profile intersects 70 m of unconsolidated Quaternary deposits, 130 m of Tertiary Molasse, 250 m of Malm limestones, 200 m of Dogger dominated by clay-rich lithologies (including the Opalinus Clay Fm at a depth between 539 and 652 m), 40 m of clay-rich Liassic rocks and 300 m of Triassic (heterogeneous sequence including evaporites) before reaching the top of the crystalline basement at a depth of 983 m (NAGRA, 2002).

The Opalinus Clay Fm present throughout northern Switzerland was deposited ~174 Ma in a shallow marine environment (Marschall *et al.*, 2005). Northern and central Europe in Jurassic times was mostly covered by a structured shelf sea with large expanses of shallow sea plus some deeper marine basins; land areas were isolated massifs (Pearson *et al.*, 2003). At Benken the Opalinus Clay Fm consists of a sequence of dark gray, silty, and calcareous clay sediments. The upper part of the formation (539−590 m) contains abundant carbonate-cemented fine rippled silt laminations and dense carbonate-silt-filled bioturbations. The uppermost part displays lithified burrows, indurated surfaces impregnated by siderite, cm-sized nodules and diffuse patches of pyrite, and cm-sized siderite concretions. The bottom of the formation (590−652 m) is richer in clay minerals, poorer in silt layers, and contains cm-sized siderite concretions at different depths. The base of the formation is marked by a large carbonate content due to a bioclast-rich bed. The sediment variations can be attributed to changes in bottom-water turbulence. The abundance of laminations in the upper part of the Opalinus Clay Fm suggests sediment deposition in an upper offshore environment (~10−30 m below sea level). Turbulent episodes led to mixing of water, inducing variable redox conditions at the sediment surface. The presence of lithified burrows and intense carbonate-silty bioturbations suggests low sedimentation rates (at least episodically) for the upper part of the formation. In contrast, the lower part of the formation was deposited in a lower offshore environment, probably corresponding to a maximum flooding of 50−60 m. The levels where siderite concretions, pyrite nodules, and siderite induration were observed, as well as sampling points, are shown in Figure 1b; characteristic samples are illustrated in Figure 1c.

The Opalinus Clay Fm from Benken was subjected to a complex burial history including two stages of burial, separated by a stage of uplift and erosion (Elie and Mazurek, 2008). A maximum temperature of ~85ºC was reached at ~122 Ma and extended over a period of ~20 Ma in the Early Cretaceous, corresponding to a burial of Opalinus sediments to a depth of 1050 m, caused by subsidence of a large part of Europe associated with lithospheric rifting (Mazurek *et al.*, 2006). The heating rate is assumed to be linear with time, starting with a surface temperature of ~25ºC during deposition. Sediments were uplifted and cooled in the period 102−50 Ma. A linear cooling trend with a final temperature of 43ºC in the Tertiary was inferred. Temperatures of 20−30ºC lower were reached over a shorter period during the second burial stage (maximum burial at 1650 m depth) during the Miocene, due to the Alpine orogeny. Current temperatures are ~38ºC at 650 m depth (Mazurek *et al.*, 2006). Only one sample at 601.90 m (Figure 1c) contains a cm-sized fault, attributed to the Alpine orogeny. Whether the fault is linked to Jura folding further to the west, to the Bodensee-Hegau Graben to the east, or to other tectonic events is unknown.

ANALYTICAL TECHNIQUES

Bulk geochemistry

Major- and trace-element analyses were performed by X-ray fluorescence spectrometry (XRF; Philips model 2400, Amsterdam, The Netherlands) and inductively coupled plasma-mass spectrometry (ICP-MS; Thermo seriX 2, Bremen, Germany). Total carbon and sulfur were analyzed using a Jobin Yvon EMIE 820V carbon/sulfur analyzer (Longjumeau, France).

Mineralogical characterization

The main crystalline phases were identified by powder XRD measurements, conducted on randomly oriented powders, performed using a Bruker D5000 diffractometer (Karlsruhe, Germany) with CoKα radiation (λ Kα_1 = 1.78997 Å), and 10 s counting time per 0.02º2θ (step scan mode). Qualitative identification was achieved by fitting peak positions and relative intensities. The abundant minerals discussed in the present study, and their associated ICDD (International Center for Diffraction Data) records, are (in alphabetical order): ankerite (00-041-0586), anorthoclase (00-009-0478), calcite (00-005-0586), chlorite (clinochlore – 00-029-0701), corundum (00-046-1212), dolomite (00-036-0426), kaolinite (01-075-0938), muscovite (01-086-1385), pyrite (00-042-1340), quartz (00-046-1045), rutile (00-021-1276), and siderite (00-029-0696). Corundum was introduced artificially in the sample to serve as internal calibration for phase quantification and to ensure that both sample height and diffractometer

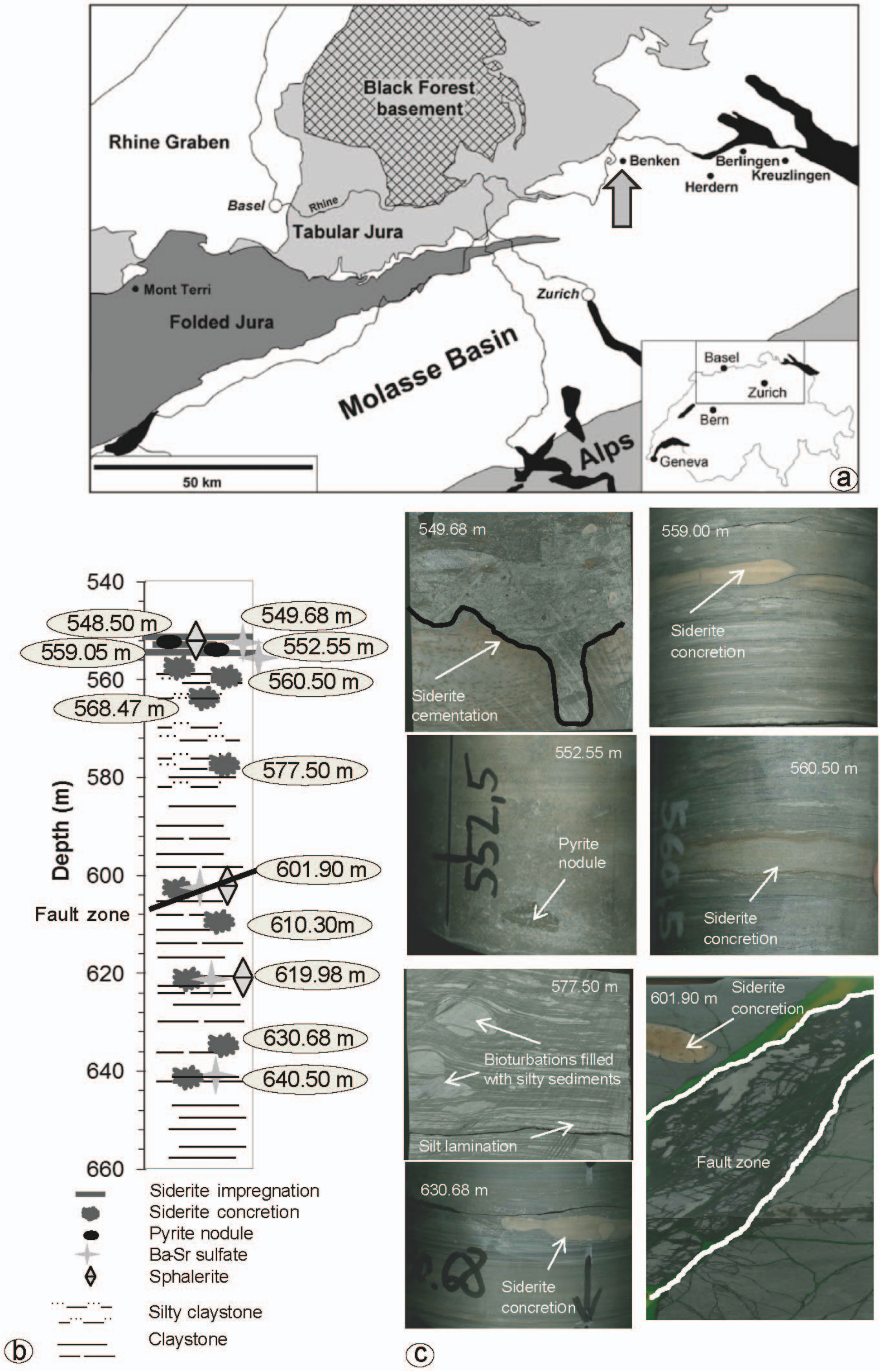

Figure 1. Geological setting and sampling: (a) location of the Benken area on a simplified geological sketch map (Mazurek *et al.*, 2009); (b) lithological log of the Opalinus Clay Fm indicating the levels of siderite concretions, pyrite nodules, siderite induration and the sampling; (c) photographs of some characteristic samples.

alignment were optimal. Note that anorthoclase was chosen as the reference for K-feldspar because it best matched the experimental XRD pattern, but other minerals from this group may actually be present. Similarly, the chlorite record used for identification was the magnesian end-member, but other end-members could also have been used, as chlorite abundance was insufficient to distinguish between them. Finally, the muscovite record was used, but could not be distinguished from illite using powder XRD. Instead, phyllosilicate mineralogy was investigated by recording and analyzing the XRD patterns from oriented preparations of the <2 μm fraction subjected to air-drying, ethylene-glycol (EG) saturation (12 h of contact with EG in saturated air conditions), and heating for 4 h at 490ºC, successively. A semi-quantitative mineralogical reconstitution of the rock samples was realized using the *MINEV* software of P. Blanc (pers. comm., 2013) with XRD data of the <2 μm fraction treated by *ARQUANT* (Blanc *et al.*, 2007) and bulk powder treated using *MODPATTERN* (P. Blanc, pers. comm., 2013) combined with the geochemical composition of the bulk rock and calcimetric data. Refinement of calcite-lattice parameters was performed with the *U-Fit* software (Evain, 1992) by indexing the maximum possible number of calcite Bragg reflections that were not overlapped by other minerals. The number of unambiguous reflections was dependent on the sample studied but was never less than five. This software allows for the calculation of uncertainties on refined lattice parameters, which are reported systematically here.

Observations, analyses, and elemental mapping were performed using a JEOL JSM 6100 scanning electron microscope (SEM) (Tokyo, Japan) coupled with a Kevex Quantum Energy Dispersive Spectrometer (Philadelphia, USA) at 25 kV and 80 nA. Prior to analysis, a thin carbon layer was sputter-coated on the samples (Edwards Auto 306, Genevilliers, France).

The cathodoluminescence (CL) system used was a cold cathode 'Cathodyne' from OPEA (Laboratoire Optique Electronique Appliquée, Fontenay sous Bois, France). The electron beam has adjustable energies up to 26 keV and currents up to 250 mA. The Cathodyne was mounted on an Olympus microscope, allowing magnification up to ×10. The system was equipped with a JVC KYF75U tri-CCD digital camera (Wayne, USA). The three 12 mm-sized sensors had a resolution of 1024 pixels. Cathodoluminescence was used to support the identification of detrital K-feldspar occurring as blue grains and of the different carbonate types: dark orange colors for calcite cement in silty layers, yellow to bright orange colors for rare euhedral dolomite grains, orange–red to dark red colors for biocalcite, bright orange colors for shell recrystallized into diagenetic calcite, and dark red for siderite.

Spot analyses of carbonates, silicates, and sulfates were performed on polished thin sections of samples covered with a carbon coating, using a CAMEBAX SX50 electron microprobe (Genevilliers, France) with an accelerating voltage of 15 kV, a beam current of 12 nA, and a 1–2 μm beam diameter. Peak and background counting times were 10 s for major elements and 60 s for Ba, Sr, and S. Detection limits were 540 ppm for Ba, 570 ppm for Fe, 545 ppm for Mn, 170 ppm for Sr, and 210 ppm for S. Standards used included both well characterized natural minerals and synthetic oxides. Matrix corrections were performed with a ZAF computing program (Merlet, 1994).

Sulfur-isotope analysis of pyrite

Pyrite was separated by handpicking under the binocular microscope and then ground in an agate mortar. Sulfur isotope analyses were performed on ~200–300 μg of pyrite using an elemental analyzer coupled to a Thermo Scientific delta-Plus Isotope Ratio Mass Spectrometer (Bremen, Germany). Sulfur isotopes were not analyzed for sulfate minerals due to the difficulty in separating enough material to analyze.

Carbon and oxygen isotope analysis of carbonates

The conventional method of Rosenbaum and Sheppard (1986) was used to extract, successively, calcite and siderite in siderite concretions from ~400 mg of bulk powder of concretion. The CO_2 samples obtained in this way were analyzed for their isotopic compositions using a Delta S Finnigan-Mat gas-source mass spectrometer.

The 'Carbodevice' is an automatic line which extracts calcite by attack of several hundred μg of powder with phosphoric acid (100% anhydrous) at a temperature of 70ºC for 3 min. It was coupled to a Finnigan MAT Delta S mass spectrometer (Bremen, Germany) for determining $\delta^{13}C$ and $\delta^{18}O$. The fractionation coefficient used for the calculations is from Swart *et al.* (1991).

All the results are reported in δ units relative to international standards, defined by: $\delta = (R_{\mathrm{Sample}}/R_{\mathrm{Standard}} - 1) \times 1000‰$, where R is the measured isotopic ratio in the sample and in the standard: Standard Mean Ocean Water (SMOW) for oxygen, and Pee Dee Belemnite (PDB) for carbon. Reproducibility was ±0.2‰ for oxygen and carbon.

Strontium isotope analysis of carbonates and Ba-Sr sulfate

Strontium isotopic ratios were measured in mineral separates (calcite, Ba-Sr sulfates) or bulk fractions (calcite associated with siderite). Calcite and Ba-Sr sulfates were separated by hand picking on thin sections and pieces of rock used for the thin sections. Strontium was extracted by adding 10 mL of 6 N HCl solution (extra-pure quality concentrated HCl) to crushed mineral separates in covered Teflon beakers.

Calcite present in siderite nodules was extracted by attack with 0.5 N HCl at ambient temperature.

When calcite was not purified and still contained traces of clay particles and feldspars, the sequential extraction procedure described by Lerouge *et al.* (2010) was applied using cobalt hexamine trichloride in a first step to chemically separate strontium hosted in calcite from strontium extracted from clays.

The leachate was purified using an ion-exchange resin (Sr-Spec) before mass analysis according to a method adapted from Pin and Bassin (1992), with blank <1 ng for the entire chemical procedure. After chemical separation, ~150 ng of Sr was loaded onto a tungsten filament with tantalum activator and analyzed using a Finnigan MAT262 multi-collector solid source mass spectrometer (Bremen, Germany). The $^{87}\text{Sr}/^{86}\text{Sr}$ ratios were normalized to a $^{86}\text{Sr}/^{88}\text{Sr}$ ratio of 0.1194. An average internal precision of ±10 ppm ($2\sigma_m$) was obtained and the reproducibility of the $^{87}\text{Sr}/^{86}\text{Sr}$ ratio measurements was tested through repeated analyses of the certified NBS987 standard (0.710240).

RESULTS

Mineralogical composition

Examination of powder XRD patterns showed the systematic and unambiguous presence of phyllosilicates (chlorite, muscovite, and/or illite, kaolinite), tectosilicates (quartz, anorthoclase), carbonates (calcite, siderite), sulfides (pyrite), and oxides (rutile), except samples collected at depths between 610.30 and 610.32 m depth and between 630.64 and 630.68 m, for which pyrite diffracted intensity is very low (Figure 2). In addition to the intensity diffracted by these minerals, powder XRD patterns have a broad diffraction maximum between 35.7 and 36.2º2θ. Although anorthoclase certainly contributes to this maximum, it does not explain it quantitatively. Two minerals common in clayey rocks have an intense diffraction maximum in this range: ankerite and dolomite, the most intense Bragg peaks of which are at 35.86º2θ and 36.09º2θ, respectively. Both minerals thus have their maxima shifted slightly from the broad maximum, which may be explained by a chemical composition deviating from stoichiometry. In the pattern from the sample collected at a depth between 560.43 and 560.53 m, this maximum is sharper, however, and peaks at 35.9º2θ, suggesting the presence of ankerite. Given the low diffracted intensity, however: (1) the presence of dolomite cannot be ruled out; and (2) the combined occurrence of non-stoichiometric variations of both dolomite and ankerite is possible.

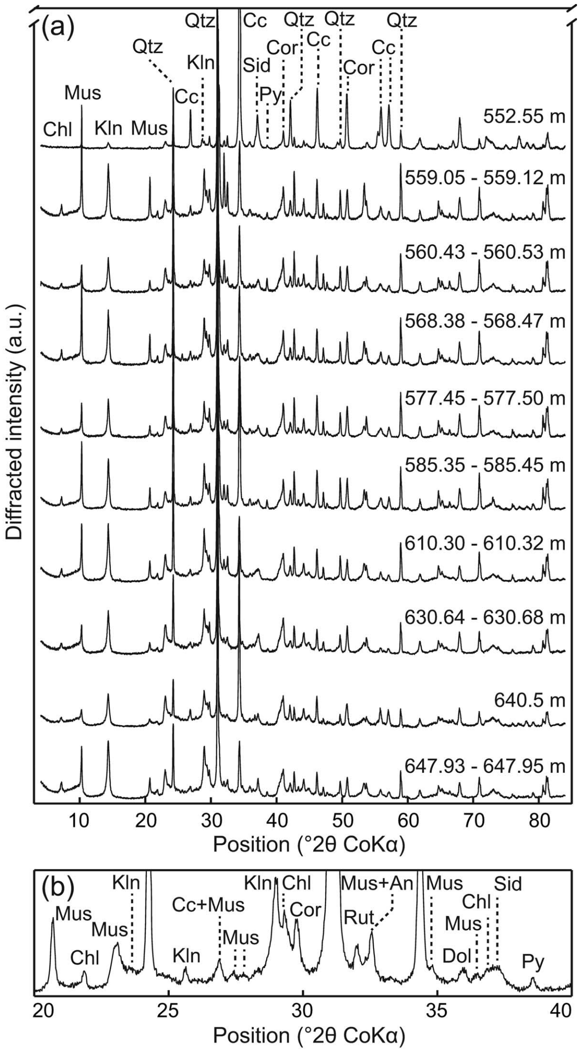

Figure 2. (a) XRD patterns of the 10 samples: From top to bottom, samples collected at depths of 552.55 m, 559.05–559.12 m, 560.43–560.53 m, 568.38–568.47 m, 577.45–577.50 m, 585.35–585.45 m, 610.30–610.32 m, 630.64–630.68 m, 640.5 m, and 647.93–647.95 m; (b) close-up of the XRD pattern between 20 and 40º2θ (CoKα) (sample collected between 568.38 and 568.47 m depth). In the two panels, Chl, Mus, Kln, Qtz, Sid, Cc, Py, Cor, Rut, An, Dol are used to indicate the positions of the main diffraction maxima attributable to chlorite, muscovite, kaolinite, quartz, siderite, calcite, pyrite, corundum, rutile, anorthoclase, and dolomite, respectively.

From quantitative analysis of XRD patterns (Table 1) combined with bulk-rock chemistry (Appendix 1, available at http://www.clays.org/JOURNAL/JournalDeposits.html), sample 552.55 m at the top of the Opalinus Clay Fm is an impure limestone containing ~19 wt.% clay and ~13 wt.% quartz with minor K-feldspar. Most samples of the Opalinus Clay Fm are carbonate-silty-claystone. The silty fraction consists mainly of quartz with minor K-feldspar and plagioclase (<4 wt.%). The carbonate fraction consists mostly of calcite with significant amounts of siderite. The clay fraction comprises ~3–7 wt.% chlorite (chamosite + pyrochlore), ~4–9 wt.% illite, ~25–37 wt.% ordered mixed-layer illite-smectite (I-S, R1 ordered), ~13–21 wt.% kaolinite, and ~3–6 wt.% muscovite. In the upper part of the Opalinus Clay Fm (538–60 m), clay content ranges between 43 and 50 wt.%, associated with an important silty fraction (28–33 wt.%) and a

Table 1. Mineralogy of the BENKEN samples estimated using *MINEV* software (P. Blanc, pers. comm., 2013), the clay contents estimated using *ARQUANT* software (Blanc *et al*., 2007), and the mineral proportions estimated using the *MODPATTERN* software (P. Blanc, pers comm., 2013).

Mineral group	Mineral	Abundance (wt.%)[1]									
		552.55 m	559.05 m	560.43 m	568.38 m	577.35 m	585.35 m	610.30 m	630.64 m	640.50 m	647.93 m
Phyllosilicates	Chlorite	3	4	5	4	4	5	5	6	5	8
	Illite	3	4	8	7	7	7	7	9	6	8
	Illite-smectite MLM[2]	9	21	22	19	20	19	27	28	28	29
	Kaolinite	4	15	15	16	13	13	17	19	21	19
	Muscovite	0	6	3	6	4	3	5	4	4	5
Tectosilicates	Feldspars[3]	2	3	2	4	2	2	2	2	1	1
	Quartz	11	30	26	27	31	31	23	17	10	16
Carbonates	Ankerite/dolomite[4]	<1	<1	1	1	<1	<1	<1	<1	1	2
	Calcite[5]	58	10	8	9	11	14	7	5	16	6
	Siderite[6]	8	4	4	4	4	2	5	5	4	3
Sulfides	Pyrite	1	1	3	1	1	1	<1	<1	<1	1
Oxides	Rutile	<1	1	1	1	1	1	1	1	1	1

[1] Abundance is normalized to 100%. When abundance was <1%, the mineral was detected but its concentration was not given and noted to be <1%.

[2] MLM = mixed-layer mineral; it belongs to the R1 group.

[3] Feldpars mainly belong to the K-feldspar group.

[4] No attempts were made to distinguish between ankerite and dolomite, as both may exist in a non-ideal form (see text for details).

[5] Note that the calcite content determined from modeling of XRD patterns and by calcimetry never differed by more than an absolute value of 2%, with a mean difference of 0.3%.

[6] Siderite may contain significant amounts of impurities as indicated by the shift of its Bragg peaks as compared to the ideal position.

carbonate fraction (12–16 wt.%). In the lower part of the Opalinus Clay Fm, the clay content increases up to 55–63 wt.%, associated with a smaller silty fraction (11–24 wt.%) and a similar sized carbonate fraction (10–21 wt.%). The largest carbonate content, at 640.5 m depth, is due to a bioclast-rich claystone. Kaolinite content ranges between 4 and 21 wt.% with the highest contents at the bottom of the formation.

Petrography

The Opalinus Clay Fm consists of a cm-scale alternation of clay layers with mm- to cm-thick silty layers. The clay and silty layers are characterized by different distributions of detrital and diagenetic minerals. Identification of diagenetic minerals is easier in the silty layers due to larger sizes of primary pores between detrital grains of quartz and feldspars. At Benken, the Opalinus Clay Fm is essentially undeformed on all scales, except for one cm-thick fault at 601.90 m.

Detrital content. The clay layers are composed of dominant <2 μm-sized clay particles with 10–50 μm-sized grains of quartz, minor K-feldspar, calcite, and a variable bioclastic content (Figure 3). Rare 10–100 μm-long flakes of muscovite, biotite, and chlorite define the bedding. Kaolinite pellets were identified only in a siderite nodule of the sample 630.68 m.

Silty layers and carbonate-silty lenses consist of abundant angular detrital grains of quartz with minor K-feldspar, flakes of phyllosilicates (muscovite, biotite, chlorite, and clay particles), and a variable bioclastic content.

Bioclasts disseminated in the clay matrix and in the silty layers consist mainly of carbonate bioclasts occurring essentially as 10–50 μm-sized clasts of colorless shells and tests, with rare calcium phosphate bioclasts with characteristic honey color, and 50–200 μm-sized black particles of organic matter. Examination of carbonate bioclasts under cathodoluminescence in a claystone sample from 640 m depth provided evidence of partial recrystallization into bright orange calcite, whereas the preserved bioclast is dark orange due to the presence of organic carbon.

Diagenetic minerals, textural relationships, and diagenetic mineral sequence. Diagenetic minerals consist of abundant calcite associated with minor dolomite, siderite, glauconite, pyrite, sphalerite, and baryte. Textural relationships between them enabled the chronology of formation of these phases relative to the major stages of sedimentary history – early diagenesis (just after sediment deposition), compaction and burial, and late diagenesis associated with tectonic events (Figure 4) – to be determined.

Four generations of calcite were identified in the matrix of the Opalinus Clay Fm: micritic calcite associated with pyrite (calcite type 1), isolated 20–40 μm-sized euhedral calcite (calcite type 2), isolated

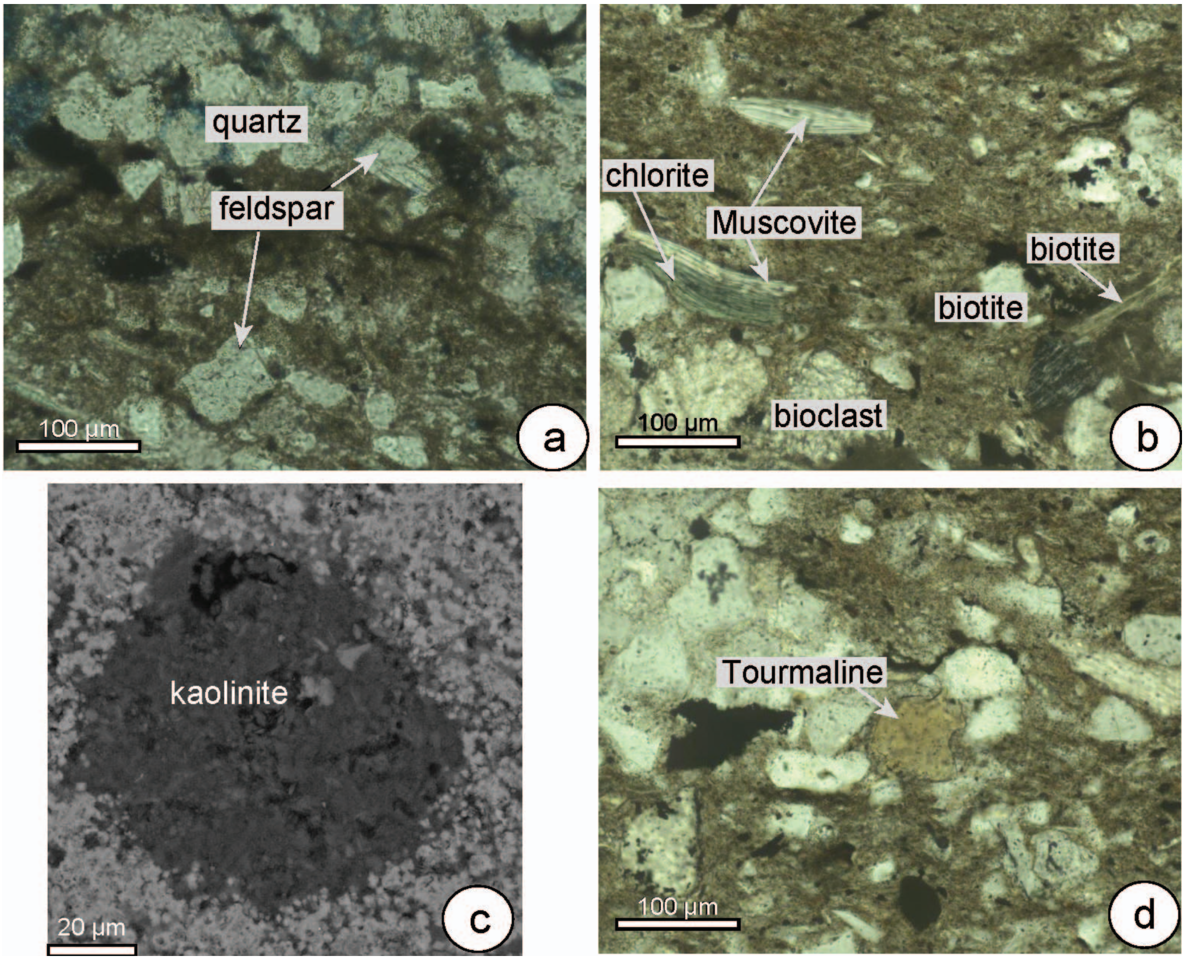

Figure 3. Detrital minerals in Opalinus claystones: (a) quartz and K-feldspar detrital grains in clay matrix (sample 558.98 m; transmitted light); (b) detrital flakes of chlorite, muscovite, and biotite, and bioclasts in clay matrix (sample 586.32 m; transmitted light); (c) detrital residual kaolinite pellet in siderite nodule (sample 630.68 m; BSE image); (d) detrital tourmaline grain (sample 586.32 m; transmitted light).

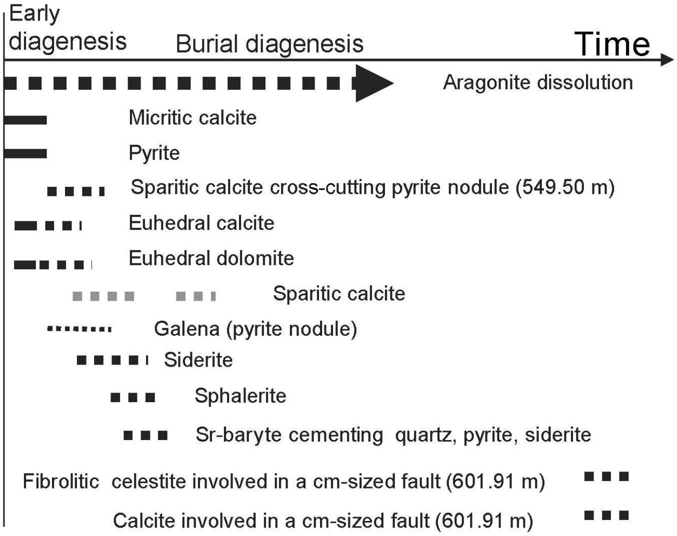

Figure 4. Relative diagenetic sequence determined from observations of textural relationships between the different diagenetic minerals.

rare iron-rich euhedral calcite (calcite type 3), and 50–100 µm-sized sparite cement (calcite type 4) (Figure 5a–d). Calcite types 1 and 2 are the most abundant types in clay layers whereas calcite type 4 is

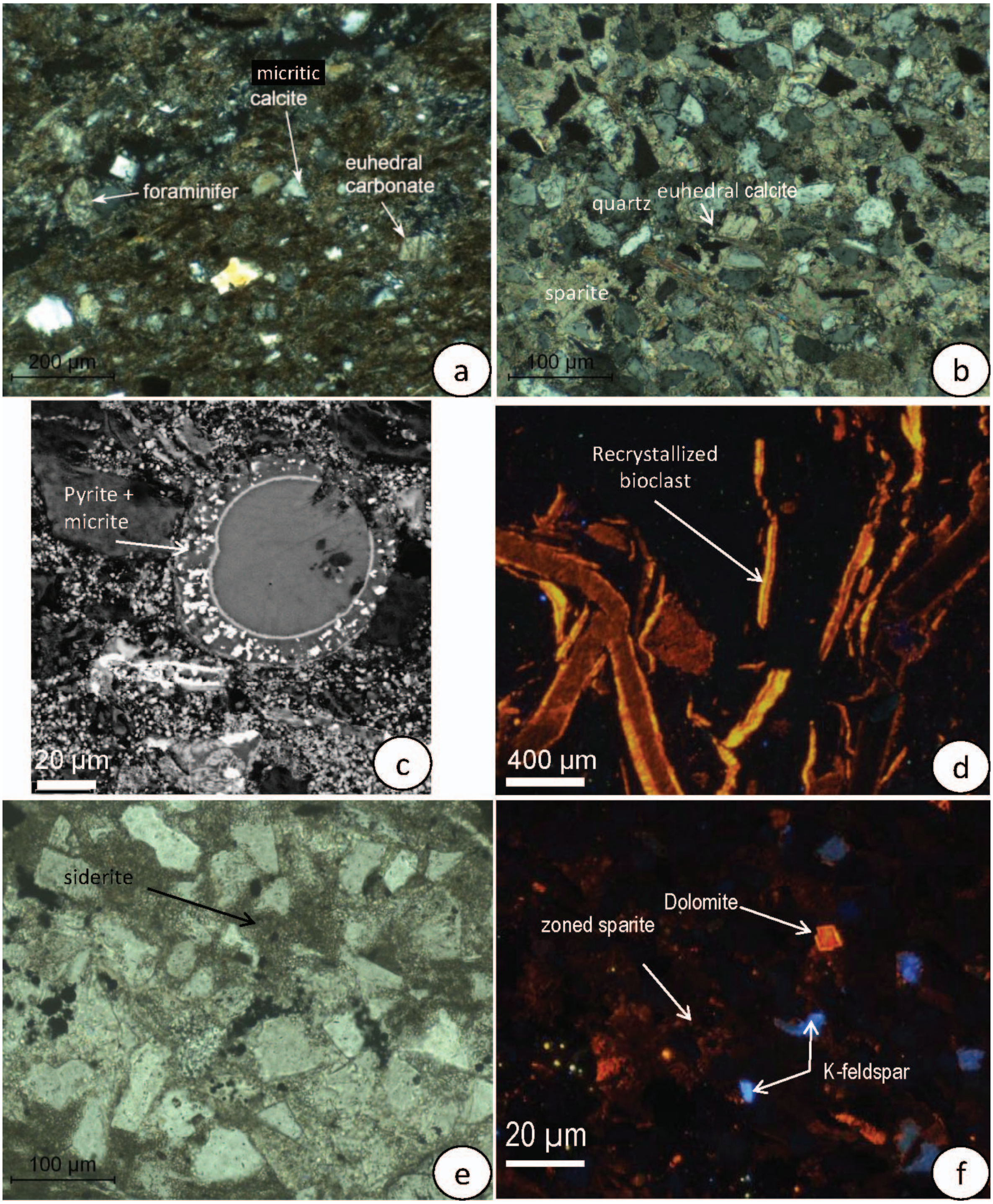

Figure 5. Diagenetic carbonates in Opalinus claystones: (a) euhedral calcite and micrite in clay matrix (sample 619.98 m; BSE image); (b) euhedral calcite grain and sparite cement in silty layer (polarized transmitted light); (c) biocarbonate replaced by micritic calcite and pyrite (sample 619.98 m; BSE image); (d) bivalve shells partially recrystallized (sample 640.50 m; CL); (e) impregnation of the silty sediment by fine-grained siderite (sample 558.98 m; transmitted light); (f) CL image providing evidence of a euhedral grain of dolomite in bright yellow/orange, of zoned calcite cement in dark red/orange, and detrital K-feldspar occurring as blue grains (sample 576.65 m).

dominant in silty layers, carbonate-silty lenses, and nodules. Calcite type 4 of silty layers cements bioclasts and rare grains of calcite type 2, proving that calcite type 4 precipitated later than calcite type 2 in the diagenetic sequence. Limited variations of CL colors (dark orange) and an almost homogeneous gray in a back-scattered electron (BSE) image of calcite type 4 suggest that it has quite an homogeneous chemical composition.

Scarce 5–10 μm-sized euhedral grains of dolomite are identified by a specific bright orange–yellow color under CL (Figure 5f). In silty layers dolomite is cemented by calcite type 4, indicating that calcite type 4 precipitated later than dolomite.

Siderite is common to abundant in the Opalinus Clay Fm. Siderite occurs mainly as impregnations at different depths of the borehole: 548.5 m, 549.68 m, 552.55 m, 558.98 m, 559.05 m, 560.50 m, 568.47 m, 601.91 m, 619.98 m, 630.68 m, and 640.50 m (Figure 5e), but also as disseminated μm-sized grains. Three types of siderite impregnation are distinguished: (1) diffuse impregnation of lime mudstone at the interface with silty sediments (samples 548.5 m, 549.68 m, and 552.65 m) at the top of the Opalinus Clay Fm. These samples are peculiar because lime mudstones are affected by cm-sized burrows and overlain by silty sediments. (2) Yellowish concretions forming flat and roundish masses (samples 558.98 m, 559.05 m, 560.50 m, 601.91 m, 630.68 m and 640.50 m). (3) A yellowish silty layer cross-cut by a burrow filled with silty sediment in a claystone (sample 619.98 m).

Under cathodoluminescence, siderite impregnation imparted a dark red color to the rock. Complementary SEM observations indicated that siderite occurs as numerous disseminated micron-sized euhedral crystals impregnating the matrix extensively; the impregnation decreases and becomes diffuse around concretions. Euhedral grains are often formed around μm-sized undetermined nuclei in the clay matrix but also as growth coronas around calcite type 2 and euhedral dolomite. Disseminated micron-sized grains of siderite clearly precipitated later than pyrite, calcite type 2, and dolomite, as siderite cements all these minerals. No textural features were observed that could provide information on the chronology between siderite and calcite type 2. Diffuse siderite impregnating lime mudstone at the interface with silty sediments at the top of the Opalinus Clay Fm, and the silty layer at the bottom of the Opalinus Clay Fm, is almost absent in sediments filling burrows affecting those sediments. These observations suggest that siderite formed during depositional hiatuses (which could correspond to hard-ground surfaces). The morphologies of concretions (flat and roundish masses) confirm they were also formed in still-porous sediment, *i.e.* before compaction. The homogeneous μm-size of the siderite grains in concretions, their growth around nuclei (*e.g.* impurities of the sediment, dolomite) and their reasonably homogeneous chemical composition suggest that siderite grains formed by crystal growth onto the nuclei at virtually the same time across the entire concretion rather than by radial addition of siderite layers around a central nucleus.

Rare glauconite occurs as pellets in clay layers (Figure 6a). Glauconite's textural relationship with other diagenetic minerals is unclear.

Pyrite occurs as isolated μm-sized framboids or clusters of framboids, but also as <10 μm-sized euhedral grains, disseminated in the clay matrix (Figure 6b), and as partial cement of some silty sediments with calcite type 1 (Figure 6c), throughout the Opalinus Clay Fm. That suggests its early formation at the water/sediment interface, contemporaneous with sedimentation. Some pyrite clusters are included in siderite concretions, suggesting that the former formed earlier than the latter. Rare nodules of pyrite were observed at depths of 548.50 m and ~552.68 m, corresponding to a lithological change between lime mudstone and silty sediments. Rare micro-fractures of sparitic calcite (calcite type 5) with traces of galena cross-cut pyrite nodules (sample 548.50 m: Figure 6g–i), indicating that calcite type 5 crystals were formed during or after compaction.

Sphalerite occurs as <50 μm-sized anhedral and euhedral grains disseminated in clay matrix and in calcite type 4 of silty layers (Figure 6d). Exceptional 300–400 μm-sized euhedral grains of light brownish color are observed in the clay matrix, growing into the microporosity and surrounding fine-grained pyrite, calcite and siderite (Figure 6e,f). These observations indicate that sphalerite precipitated later than siderite.

Rare Ba-Sr sulfates occur as scarce filling of residual porosity in bioclast-rich claystones (552.55 m, 640.5 m), <50 μm-sized anhedral grains cementing framboids of pyrite, μm-sized siderite grains and calcite type 4 in silty layers in sample 619.98 m (Figure 6j) and in siderite nodules, but also as μm-sized grains disseminated in the clay matrix (Figure 6k). Ba-Sr sulfates consequently precipitated later than siderite and other early diagenetic phases. The order of precipitation of sphalerite and Ba-Sr sulfates could not be determined from any textural relationship found. The fissure cross-cutting the pyrite nodule in sample 548.50 m, and which was filled with calcite type 5, is aligned with disseminated Ba-Sr sulfates and sparite in silty sediments. This texture suggests strongly that calcite type 5 is reasonably contemporaneous with Ba-Sr sulfate deposition cementing silty sediments.

Cm-sized fault at 601.91 m. The claystone involved in the fault located at 601.91 m depth has lost its sedimentary structure. The variable competence of the different rock-forming materials has led to heterogeneous deformation (Figure 7). Silty lenses consisting essentially of detrital quartz grains cemented by calcite type 4 are more competent than the surrounding clay matrix. Consequently, silty lenses behave like blocks surrounded by a deformed soft clay matrix. They are less

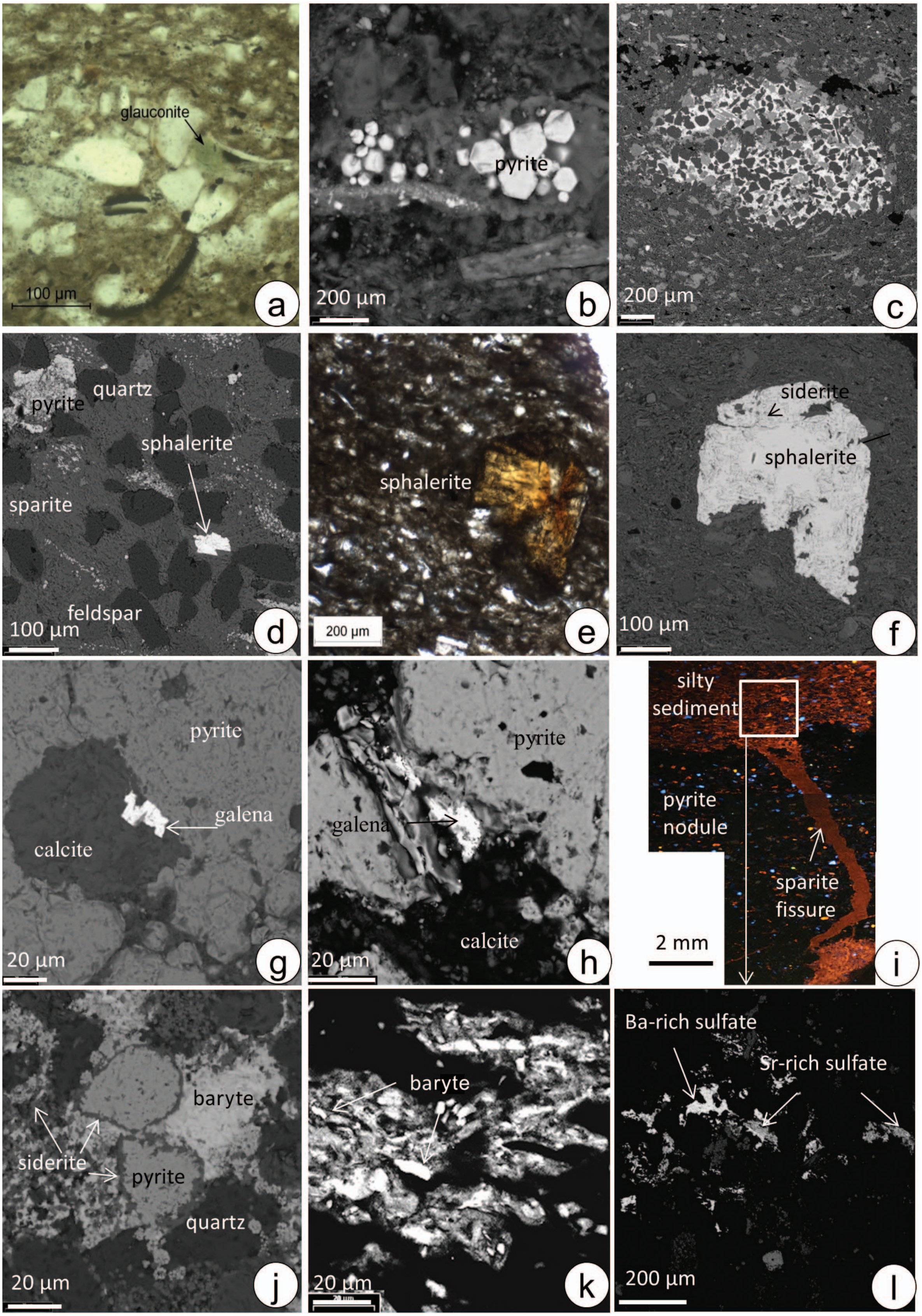
glauconite
100 µm
a
pyrite
200 µm
b
200 µm
c
pyrite
quartz
sphalerite
sparite
feldspar
100 µm
d
sphalerite
200 µm
e
siderite
sphalerite
100 µm
f
pyrite
galena
calcite
20 µm
g
pyrite
galena
calcite
20 µm
h
silty
sediment
pyrite
nodule
sparite
fissure
2 mm
i
baryte
siderite
pyrite
quartz
20 µm
j
baryte
20 µm
k
Ba-rich sulfate
Sr-rich sulfate
200 µm
l

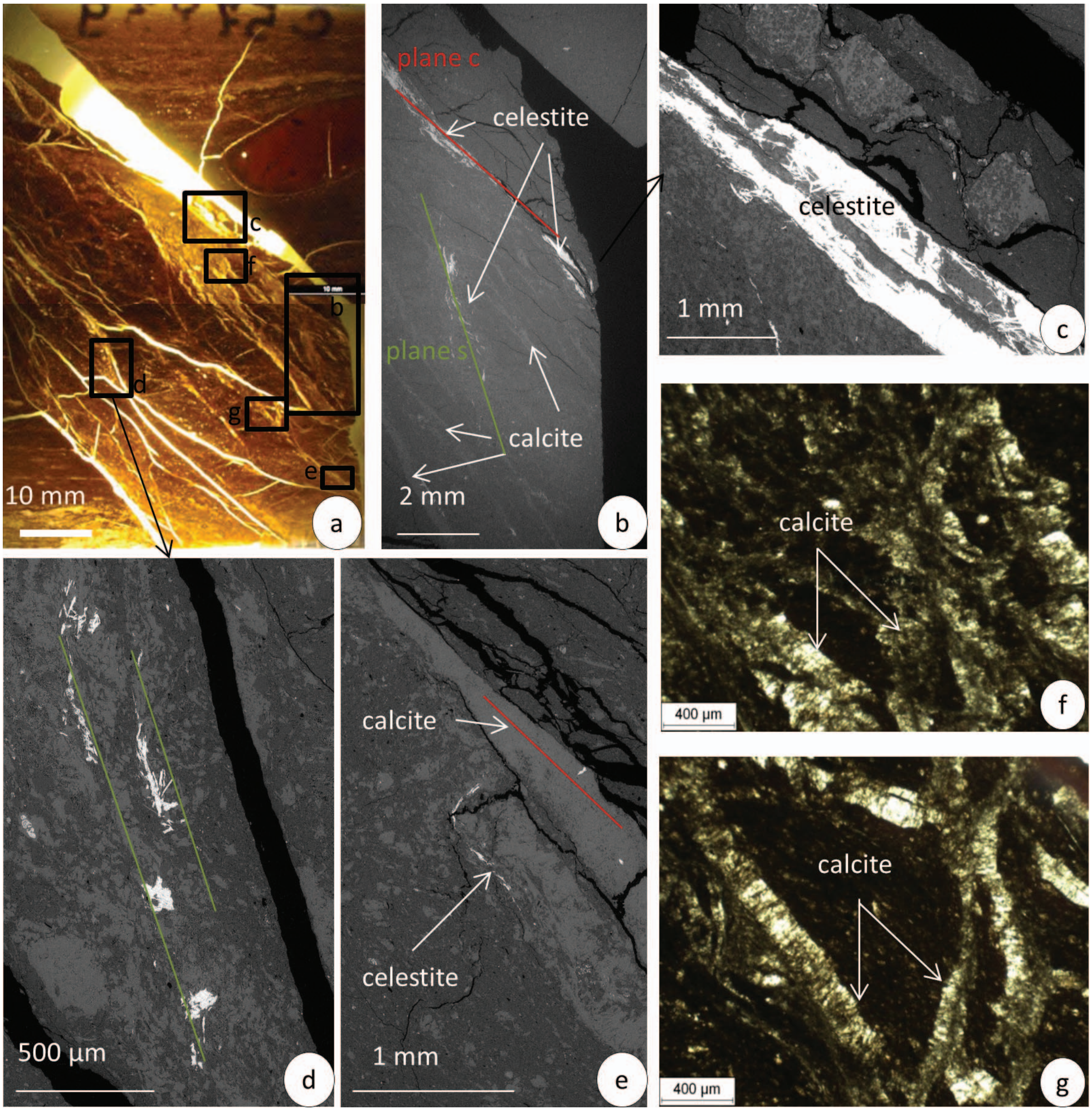

Figure 7. Diagenetic minerals in the fault zone (sample 601.90 m): (a) photograph of the polished thin section; (b) large-scale BSE image showing the presence of massive sulfates along major plane c and of rare fibrolites of sulfates along plane s which is oblique to plane c; (c) mass of fibrolites of sulfates and silty lenses reworked in the fault (natural light); (d) small fibrolites of sulfates along two parallel planes s (BSE image); (e) rare fibrolites of sulfates cross-cutting calcite deposited along a plane s (BSE image); (f) numerous small calcite veinlets cross-cutting the clay matrix along planes s (natural light); (g) network of calcite veinlets (natural light).

Figure 6 (*facing page*). Diagenetic minerals in Opalinus claystones: (a) glauconite in clay matrix (sample 586.32 m; transmitted light); (b) framboidal and euhedral grains of pyrite in clay matrix (sample 619.98 m; BSE image); (c) silty lens cemented essentially by framboids of pyrite (sample 619.98 m; BSE image); (d) euhedral grain of sphalerite associated with sparite cementing detrital grains in a silty layer (sample 576.65 m; BSE image); (e) euhedral grain of sphalerite enclosing detrital clay particles, calcite, pyrite, and siderite (sample 619.98 m; transmitted light); (f) BSE image of sphalerite in part e; (g) 10–20 µm-sized euhedral grains of galena and calcite filling a pore in a pyrite nodule (sample 549.50 m, BSE image); (h) galena and calcite filling a µm-sized micro-crack crosscutting the pyrite nodule (sample 549.50 m, BSE image); (i) sparite fissure cross-cutting the pyrite nodule (sample 549.50 m; CL); (j) baryte cementing pyrite and siderite in a fine silty layer (sample 619.98 m; BSE image); (k) baryte grain in clay matrix (sample 619.98 m; BSE image); (l) BSE image showing detail of a sediment close to a sparite fissure cross-cutting the pyrite in part i, and providing evidence of Ba-Sr sulfate filling residual porosity in silty sediment (sample 549.50 m; BSE image).

deformed than the rest, even though some lenses also seemed to be partially disorganized/recrystallized. The soft clay matrix consists of heterogeneously crushed carbonate and disoriented clay particles. Fluids circulated and Ba-Sr sulfates and calcite type 6 precipitated along deformation planes. Ba-Sr sulfates occur as masses of fibrolites filling microfractures parallel to the major direction of the fault (along c planes) and as small fibrolites in microfractures oblique to the major direction of the fault (secondary s planes). Calcite type 6 fills numerous veinlets cross-cutting claystone preferentially along secondary s planes. Calcite crystallized as elongated crystals perpendicular to the veinlets. The appearance of calcite in the veinlets is slightly gray, due to the presence of clay particles trapped by calcite.

Mineral chemistry

To complement the XRD data and bulk geochemical data the following data were also collected: (1) the chemistry of detrital clay minerals that control cation exchange; and (2) diagenetic minerals precipitated at equilibrium with pore water at different stages of diagenesis, and consequently supposedly recording the evolution of the pore-water chemistry in the clay formation over geological time.

Clay minerals. Electron microprobe analyses were performed on a clay matrix and diagenetic glauconite analyzed in eight samples (Appendix 2, available at http://www.clays.org/JOURNAL/JournalDeposits.html). Analyses of the fine-grained clay matrix, reported on the triangular diagram of Velde (1985), plot mostly in the field of mixed-layer illite-smectite minerals, but, for some analyses, between the field of illite-smectite mixed-layers minerals and the kaolinite end-member (Figure 8). Analyses of particles identified optically as chlorite correspond to analyses of chlorite *sensus stricto* but particles of weathered biotite were found to be chemically between the biotite and chlorite end-members. Their structural formulae calculated on the basis of 11 oxygen atoms shows that K ranges between 0.1 and 0.7 a.p.f.u., demonstrating an interlayer charge deficit. TiO_2 content is significant (up to 1.9 wt.%), consistent with a metamorphic origin of the biotite (Guidotti, 1984). The Fe/(Fe+Mg) ratios (denoted X_{Fe} below) are highly variable (0.20–0.81), probably depending on their origin. Some analyses of muscovite have a low sum of oxides (<96 wt.%), probably due to a slightly low SiO_2 content. The interlayer charge (K+Na+Ca) ranges between 0.9 and 1 (a.p.f.u.), showing a slight deficit of charge for some analyses. Analyses of glauconite pellets showed a variable interlayer charge, ranging between 0.33 and 0.63 (a.p.f.u.). X_{Fe} was high, ranging between 0.68 and 0.76. A few analyses showed traces of Ti.

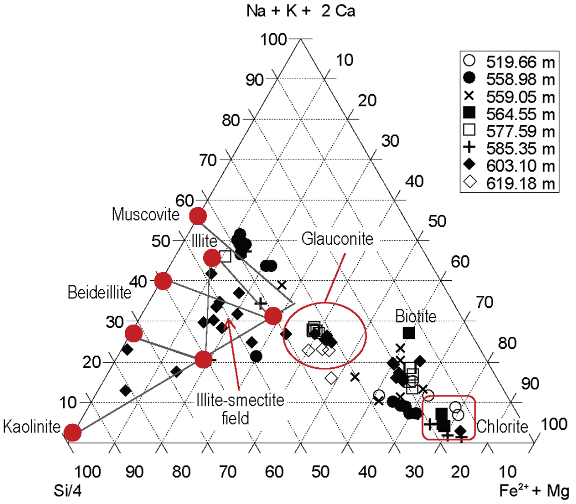

Figure 8. Triangular Si/4–(Na+K+2Ca)–(Fe^{2+}+Mg) diagram providing evidence of the different types of clay minerals according to Velde (1985). The data used for this diagram are based on 2 a.p.f.u. (22 oxygen atoms for illite, mixed-layer ilite-smectite, glauconite, and micas, and 28 oxygen atoms for chlorite).

Carbonates. Electron microprobe analyses performed on preserved (dark orange CL color) and recrystallized (bright orange CL color) detrital bioclasts and on the different generations of diagenetic carbonates exhibit significant chemical variations in terms of X_{Fe} (Figure 9).

Calcite of detrital bioclasts exhibits various Fe, Mg, and Mn contents, but can contain significant amounts of strontium (up to 1400 mg kg^{-1}) and sulfur (up to 2000 mg kg^{-1}) in its structure. The largest Sr and S contents are measured in well preserved parts of bioclasts and are significantly greater than those of diagenetic carbonates (<500 mg kg^{-1}). The variation in the Fe/(Fe+Mg) ratio is probably due to partial recrystallization.

Diagenetic calcite in claystone generally has small Fe and Mg contents compared to calcite in limestone. Among the different generations of calcite, calcite type 1 generally has the lowest X_{Fe} (mean X_{Fe} = 0.49 ± 0.13 in limestone and 0.35 ± 0.23 in claystone). Calcite type 2 (0.43 ± 0.24) exhibits a similar chemical composition to that of calcite type 1. Calcite type 4 (0.71 ± 0.07 in siltstone and 0.60 ± 0.08 in claystone), calcite type 5 (0.61 ± 0.04), and calcite type 6 (0.67 ± 0.04) exhibit the highest X_{Fe} ratios; most of the analyses range between 0.6 and 0.8. Calcite type 4 contains more Fe and Mg than calcite types 5 and 6, although they have the same range of X_{Fe} ratios. Diagenetic calcite is poor in Ba and S (below detection limit) and has low Sr content (<500 ppm) except for calcite type 5 which has an average Sr content of ~1300 mg kg^{-1}.

Calcite composition determined using electron microprobe (Figure 10a) and calcite lattice parameters retrieved from analysis of XRD data (Figure 10b) consistently indicate a significant degree of calcite compositional variation with depth; between 552.50 m

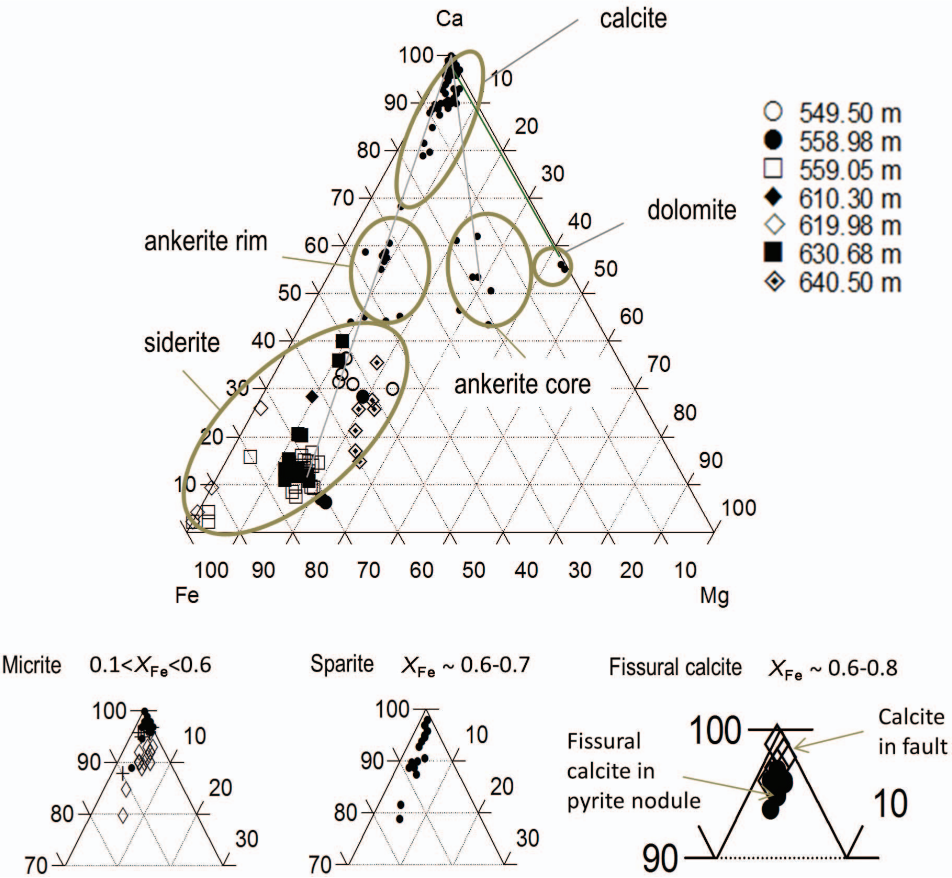

Figure 9. Triangular $CaCO_3$–$FeCO_3$–$MgCO_3$ diagram in which EPMA analyses of the different generations of diagenetic carbonates are plotted. The lines indicate the carbonates which have the same Fe/(Fe+Mg) ratios. Gray circles and lines indicate early-population carbonates, whereas black circles and lines indicate late population of carbonate. The smaller triangles give details of the different generations of diagenetic calcite.

and 560.53 m, the calcite *c* lattice parameter increases, indicating a decreasing concentration with depth of foreign cations that have a ionic radius less than that of Ca (*e.g.* Mg, Fe – Shannon, 1976). From electron microprobe data, the cationic site of calcite is increasingly occupied by Ca. Below 460.53 m the calcite *c* parameter decreases until 585.45 m and then increases consistently, within error, until 647.95 m is reached. Such evolution is in good agreement with electron microprobe data, although accurate comparison is impaired by the following: (1) XRD probes the average composition of a rock sample including different generations of calcite whereas electron microprobe samples the composition of selected grains of the different generations of calcite identified (and thus only those that can be easily identified with a microscope) from a specific horizon; (2) the two methods were not necessarily applied to the same horizons, especially at the bottom; and (3) in some horizons, only a few calcite grains were analyzed using the electron microprobe, which certainly induces bias in the determination of the actual mean calcite composition. Note that the apparent discrepancy between the two methods is in the ~560 m to ~ 568 m depth interval and is certainly related to the fact that the sample analysed using electron microprobe is located at 564.55 m depth, *i.e.* 4 m above and below the samples used for XRD analyses (560.43–560.53 m and 568.38–368.47 m), in a zone where calcite compositional variability is known (from XRD) to be significant. Using quantitative mineralogical composition, the evolution of calcite composition correlates best with rock clay content: the greater the clay content, the lower the concentration of trace elements in the calcite lattice (Figure 10).

The rare grains of ankerite observed in 548.50 m limestone exhibit X_{Fe} ratios of 0.38–0.48 in their cores and of 0.79–0.81 at their rims. Rare grains of ankerite in claystone show various X_{Fe} ratios depending on the sample: 0.35–0.42 (sample 619.18 m), 0.68–0.80 (sample 558.98 m), and 0.68–0.73 (sample 640.50 m).

Analyses of siderite were difficult due to the micrometer-sized grains. Siderite was characterized by its X_{Fe} ratio and also by its Ca/(Ca+Fe+Mg)×100 content. Siderite with significant Ca and Mg contents is also known as sideroplesite, and is very common in marine environments (Mozley, 1989). Siderite overgrowths on

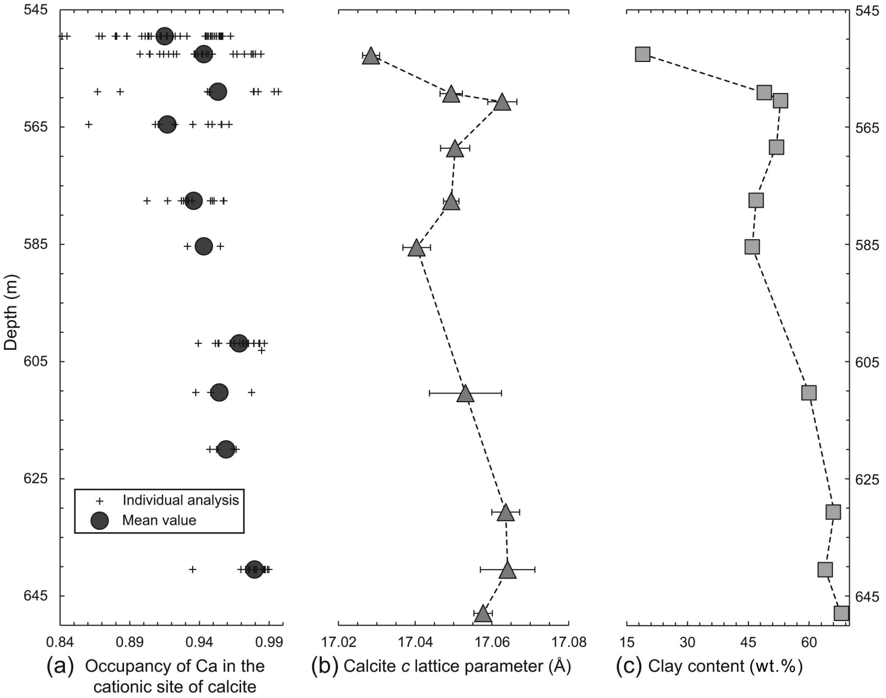

Figure 10. Evolution with depth of (a) Ca occupancy in the cationic site of calcite (determined using EPMA: each cross is an individual measurement, solid circle is the mean value of all values from the same depth); (b) calcite *c* lattice parameter (determined from refinement of calcite Bragg peak positions in the XRD patterns); and (c) clay content (determined from quantitative refinement of XRD patterns and chemical data).

calcite and ankerite in 548.50 m limestone exhibit a major Ca content (32 atom.%) and X_{Fe} ratios of 0.66–0.77. Siderite of nodules in claystones (558.98 m, 559.05 m, 610.30 m, 619.98 m, 630.68 m, and 640.50 m) exhibits different chemical compositions marked by Ca contents ranging between 11 and 28 atom.%, and X_{Fe} ratios ranging between 0.71 and 1.00. An increase in Ca content is observed at the top and at the bottom of the formation in contact with limestones. In contrast, the X_{Fe} ratio attains the maximum value of 1 in the middle of the formation corresponding to the maximum clay zone (Figure 11).

When the chemistry of dolomite/ankerite and siderite is compared with that of calcite, two main populations of diagenetic carbonates characterized by two different X_{Fe} ratios can be distinguished: (1) early populations of carbonates – calcite types 1 and 2 and core of dolomite – which exhibit the lowest Fe contents ($X_{\mathrm{Fe}} \leqslant 0.5$) and are contemporaneous with pyrite deposition; and (2) late populations of carbonates – calcite types 4, 5, and 6, rims of dolomite, ankerite, and siderite – which are marked by the highest values of X_{Fe} ($\approx$ 0.7–0.8) are formed after the deposition of pyrite. Among late calcites, calcite type 6 can be distinguished from calcite types 4 and 5 by its lowest trace-element contents.

Sulfates. Ba-Sr sulfates cementing pyrite, quartz, and carbonates (samples 548.50 m and 640.50 m), and in shear planes of the fault (sample 601.90 m) were analyzed for their Ba/(Ba+Sr) ratio. The Ba-Sr sulfate cement shows a large range of Ba/(Ba+Sr) ratios from one grain to another, but also within a single grain: 0.32–0.89 in sample 548.50 m, 0.23–0.66 in sample 640.50 m and 0.22–0.26 in sample 601.90 m. Fibrolitic Ba-Sr sulfates along shear planes in the fault of the sample 601.90 m exhibit significantly lower Ba/(Ba+Sr) ratios, between 0.02 and 0.12.

Stable isotopes

(C, O, S, Sr) stable isotope ratios were measured in diagenetic minerals of the mineral sequence, in order to

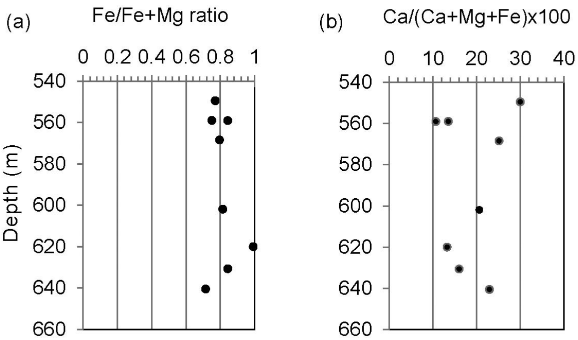

Figure 11. Evolution with depth of (a) the Fe/(Fe+Mg) ratio (denoted X_{Fe} in the text) of siderite and (b) the Ca/(Ca+Fe+Mg) × 100 value of siderite.

constrain their formation processes, estimate their formation temperatures and to discuss the origins of the pore waters from which they precipitated. The analyses were performed on mineral separates whenever possible, *i.e.* pyrite, calcite, siderite, and Ba-Sr sulfates (Table 2).

Sulfur isotopic compositions of pyrite. Sulfur isotopes are widely used with Fe-S minerals and pyrite in marine clay formations in order to constrain their conditions of formation (Ohmoto *et al.*, 1990; Wortmann *et al.*, 2001; Canfield, 2001; Lerouge *et al.*, 2011). Pyrite was analyzed in only five samples at different levels of the Opalinus Clay Fm due to the small pyrite content of the samples in general and because of the difficulty of separating the pyrite itself (Table 2). Negative δ^{34}S values of pyrite in a nodule from sample 548.50 m and of pyrite in replacement and infilling carbonate bioclasts from sample 463.5 m indicate that pyrite at the top of the Opalinus Clay Fm formed by bacterial sulfate reduction in an open marine environment with a continuous sulfate supply. Positive δ^{34}S values of pyrite in other samples (a pyrite nodule at 549.68 m, pyrite cementing silty sediments filling a burrow and impregnating partially bedded silty sediments in sample 576.65 m, and pyrite of bioturbation in sample 647.90 m) indicate that pyrite formed in a marine environment in which the sulfate supply was less than the bacterial sulfate reduction rate.

Carbon and oxygen isotopic compositions of carbonates. Carbon and oxygen isotope ratios of the different generations of diagenetic calcite and of calcite bioclasts were measured using the Carbodevice method on bulk fractions and mineral separates; carbon and oxygen isotope ratios of siderite and associated calcite type 1 of six siderite concretions (samples 559.05 m, 560.50 m, 568.47 m, 630.68 m, and 640.50 m) were measured using the conventional method of Rosenbaum and Sheppard (1986).

Oxygen and carbon isotopic values of siderite concretions, of the different generations of calcite cements, and of calcite bioclasts range from +18.4 to +32.2‰$_{\text{SMOW}}$ for δ^{18}O and from −5.6 to +6.3‰$_{\text{PDB}}$ for δ^{13}C (Table 2; Figure 12). Siderite in siderite concretions is distinguished by the highest δ^{18}O values ranging between +29.9 and +32.2‰$_{\text{SMOW}}$ and their wide range of δ^{13}C values, between −0.8 and +5.3‰$_{\text{PDB}}$ with five out of six values >+3.4‰ for carbon. Associated calcite type 1 in siderite concretions also has high δ^{18}O values up to +30.1‰$_{\text{SMOW}}$ and a large range of δ^{13}C values, between −5.6 and +3.1‰$_{\text{PDB}}$. The largest δ^{13}C values of siderite, up to +5.3‰, and associated calcite type 1 suggest bacterial methanogenic fermentation according to Irwin *et al.* (1977) and Spiro *et al.* (1993). The different generations of diagenetic calcite are distinguished by their δ^{18}O values while their δ^{13}C values are almost homogeneous, ranging between −1.8 to +0.1‰$_{\text{PDB}}$. Calcite type 1 and calcite type 2 in claystone have δ^{18}O values ranging between +22.6 and +25.2‰$_{\text{SMOW}}$; the lowest values (+22.6 to +24.2‰$_{\text{SMOW}}$) are obtained in the lower part of the formation and the highest values (+24.8 to 25.2‰$_{\text{SMOW}}$) in the upper part of the formation. δ^{18}O values of calcite type 4 in the upper part of the formation range between +22.2 and +23.4‰$_{\text{SMOW}}$. Calcite type 5 cross-cutting the pyrite nodule at 548.50 m depth exhibits a δ^{18}O value of 21.6‰$_{\text{SMOW}}$. Calcite type 6 in the fault zone at 601.90 m depth exhibits the smallest δ^{18}O values (+18.4 and +19.0‰$_{\text{SMOW}}$).

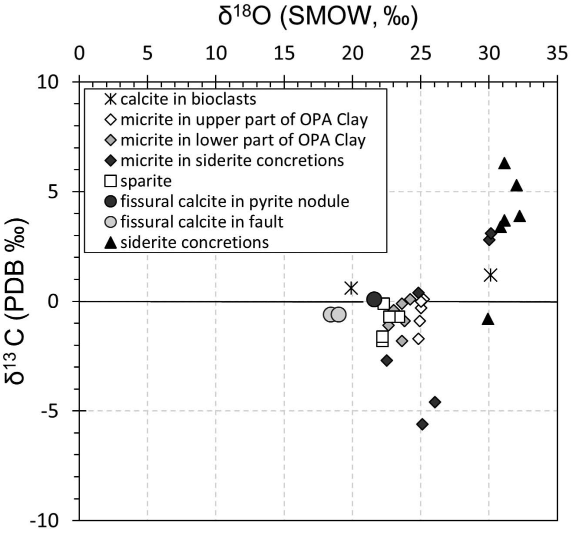

Figure 12. Carbon and oxygen isotopic compositions of the different generations of diagenetic carbonates reported in a δ^{18}O *vs.* δ^{13}C diagram.

Fibrous calcite forming belemnite rostra (sample 549.68 m), and a bivalve shell (sample 640.50 m) were analyzed to obtain the most representative values of seawater contemporaneous with the sedimentation. δ^{13}C and δ^{18}O values of calcite forming belemnite rostra, +1.2‰$_{\text{PDB}}$ and +30.1‰$_{\text{SMOW}}$, respectively, fall within the field of marine carbonates. On the other hand, the small δ^{18}O value of calcite (+19.9‰$_{\text{SMOW}}$) of the bivalve shell indicates a total recrystallization of the shell into diagenetic calcite.

Strontium isotopes. The ^{87}Sr/^{86}Sr values of well preserved belemnite rostra (549.68 m) and crinoids (601.90 m) are 0.70728 and 0.70740. These values fit well with the range of values of Aalenian seawater (Jones and Jenkyns, 2001). The ^{87}Sr/^{86}Sr ratios of a partially recrystallized bivalve shell (640.50 m), of the different generations of calcite, and of Ba-Sr sulfates have greater ^{87}Sr/^{86}Sr values, up to 0.70799. Early diagenetic Ba-Sr sulfate (552.55 m) exhibits an ^{87}Sr/^{86}Sr ratio of 0.70741, slightly higher than Aalenian seawater. Two samples of calcite type 1 associated with siderite in siderite concretions exhibit ^{87}Sr/^{86}Sr ratios of 0.70765

Table 2. Carbon, oxygen, sulfur, and strontium isotopic compositions of diagenetic minerals in the samples from the Benken borehole.

Sample	Exchangeable Strontium $^{87}Sr/^{86}Sr$	Pyrite $\delta^{34}S$‰ /CDT	Ba-Sr sulfate $^{87}Sr/^{86}Sr$	Calcite				Siderite	
				Type of calcite	$\delta^{13}C$‰ /PDB	$\delta^{18}O$‰ /SMOW	$^{87}Sr/^{86}Sr$	$\delta^{13}C$‰ /PDB	$\delta^{18}O$‰ /SMOW
548.50 m		–20.7		fissural calcite crosscutting pyrite nodule	0.1	21.6	0.707517		
549.68 m		4.3		biocalcite (belemnite)	1.2	30.1	0.707281		
552.55 m			0.707406						
559.05 m				siderite concretion	2.8	30.0	0.707649	3.9	32.2
				micrite/euhedral calcite	–0.3	25.0			
				sparite	–0.1	22.3	0.707518		
560.50 m				siderite concretion	0.4	24.8		3.4	30.8
568.47 m				siderite concretion	–5.6	25.1		5.3	32.0
				micrite/euhedral calcite	–0.9	24.9			
				sparite	–0.7	23.4			
					–0.7	22.7			
576.65 m		14.7							
577.50 m				micrite/euhedral calcite	0.1	25.2			
					0.0	25.0			
				sparite	–1.8	22.2			
585.35 m				micrite/euhedral calcite	–1.7	24.8			
				sparite	–1.6	22.2	0.707597		
601.91 m			0.707992	siderite concretion	–2.7	22.5		6.3	31.1
fault									
				biocalcite (crinoid)			0.707396		
				micrite/euhedral calcite	–0.4	23.0			
				fissural calcite	–0.6	19.0	0.707622		
				fissural calcite	–0.6	18.4			
610.30 m	0.708702			micrite/euhedral calcite	0.1	24.2			
623.30 m				micrite/euhedral calcite	–1.1	22.6			
630.68 m	0.708809			siderite concretion	3.1	30.1	0.707762	3.7	31.1
				micrite/euhedral calcite	–0.1	23.6			
640.5 m				siderite concretion	-4.6	26.0		–0.8	29.9
				bioclast (bivalve)	0.6	19.9	0.707590		
				micrite/euhedral calcite	–1.8	23.6			
647.95 m		2.3		micrite/euhedral calcite	–0.9	23.8			

and 0.70776, respectively. Calcite type 4 (559.05 m, 585.35 m) exhibits ^{87}Sr/^{86}Sr ratios of 0.70752 and 70760. Calcite type 5 cross-cutting the pyrite nodule exhibits a ^{87}Sr/^{86}Sr ratio of 0.70752, similar to values obtained for calcite type 4. Calcite type 6 and celestite in the fault zone at 601.90 m depth have ^{87}Sr/^{86}Sr ratios of 0.70762 and 0.70799, respectively. The δ^{18}O *vs.* ^{87}Sr/^{86}Sr diagram displays a coeval increase of ^{87}Sr/^{86}Sr values and decrease of δ^{18}O values from the well preserved bivalve to calcite type 6, except for calcite type 1 in siderite concretions (Figure 13). The ^{87}Sr enrichment of calcite type 1 in siderite concretions could be due to the technique used to extract Sr; 0.5 N HCl attack extracts Sr efficiently from calcite and from that adsorbed on clay particles (0.7087−0.7088) present in the concretions (Lerouge *et al.*, 2010).

DISCUSSION

Diagenetic minerals precipitated at equilibrium with seawater during sedimentation and with pore waters during diagenesis. The chemistry and isotopic signature of the diagenetic minerals recorded the evolution of chemistry and isotopic signature of pore-water chemistry, therefore, and also reflected depositional processes through geological time. Because carbonates were the dominant minerals formed from early to late diagenetic stages from seawater (except in the fault zone), their oxygen isotopic compositions were used to estimate their formation temperatures, though possible partial to total isotopic re-equilibration during diagenesis and loss of the pristine δ^{18}O values cannot be ignored (McIlreath and Morrow 1990; Jenkyns *et al.*, 1994, 2002). Rare carbonate bioclasts were used to obtain the early paleotemperatures of Aalenian seawater. Formation temperatures of calcite combined with the burial curve of the Opalinus Clay Fm provide information on the timing of the cementation. Examination of the textures of pyrite and siderite combined with the stable isotopic study permits an assessment of the conditions under which iron-bearing phases formed in terms of the marine depositional environment and the reduction-oxidation zones of the water column. Comparison with other marine clay formations allows us to define the major geological, mineralogical, and chemical criteria necessary to better constrain pore-water chemistry modeling.

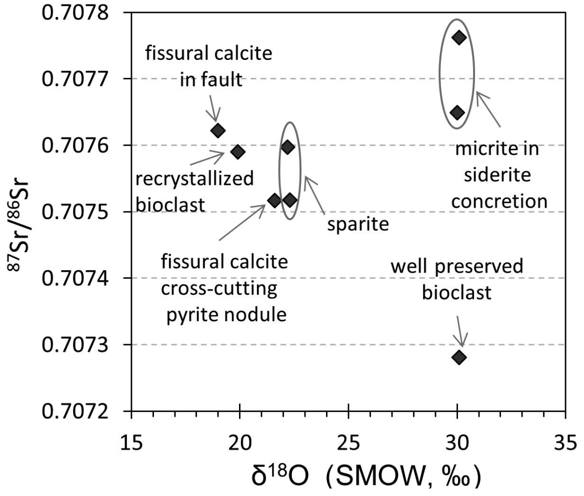

Figure 13. Oxygen isotopic compositions and strontium isotopic ratios of bioclast calcite and the different generations of diagenetic calcites reported in a δ^{18}O *vs.* ^{87}Sr/^{86}Sr ratio diagram.

Oxygen isotopic thermometry based on carbonates

Depositional seawater temperature. The stable oxygen isotope compositions of well preserved marine fossil shells have been used as paleo-temperature indicators of ocean waters for >40 years (Epstein *et al.*, 1953; Bowen, 1966; Lécuyer *et al.*, 2004; Brigaud *et al.*, 2008; Wierzbowski *et al.*, 2013). In the Opalinus Clay Formation bioclasts are scarce. Only three entire shells were separated: a belemnite at the top of the formation (549.68 m), a crinoid (601.90 m), and a bivalve shell at the bottom of the formation (640.50 m). The crinoid was very small and used entirely for strontium analysis. The bivalve shell has been overprinted diagenetically (δ^{18}O value of +19.9‰$_{\text{SMOW}}$, *i.e.* −10.6‰$_{\text{PDB}}$, and ^{87}Sr/^{86}Sr value of 0.70759). The belemnite has presumably kept its primary oxygen composition (δ^{18}O value of +30.1‰$_{\text{SMOW}}$, *i.e.* −0.73‰$_{\text{PDB}}$, and ^{87}Sr/^{86}Sr ratio close to Aalenian seawater). Its δ^{18}O value was used for the standard calculation of temperatures using the following relation (Anderson and Arthur, 1983):

$$T(^{\circ}\text{C}) = 16 - 4.14\,(\delta^{18}\text{O}_{\text{calcite}} - \delta^{18}\text{O}_{\text{seawater}}) + 0.14\,(\delta^{18}\text{O}_{\text{calcite}} - \delta^{18}\text{O}_{\text{seawater}})^2 \qquad (1)$$

where $\delta^{18}\text{O}_{\text{calcite}}$ is the oxygen isotope composition of the shell (‰$_{\text{PDB}}$) and $\delta^{18}\text{O}_{\text{seawater}}$ is the isotopic value (‰$_{\text{SMOW}}$) of seawater in which the shell grew. A $\delta^{18}\text{O}_{\text{Jurassic seawater}}$ of 0‰$_{\text{SMOW}}$ was considered for the calculation, taking into account the dominance of evaporation over precipitation in a shallow-marine reservoir and the potential occurrence of limited ice-sheets during the Jurassic period (Hendry, 1993; Pucéat *et al.*, 2003; Lécuyer *et al.*, 2003). With this assumption, the seawater paleo-temperature during precipitation of the belemnite rostra was estimated to be ~19ºC. This is consistent with the paleo-temperature range inferred from δ^{18}O values recorded by belemnites from several European sections during the early Jurassic (Dera *et al.*, 2009) and bivalve shells in Middle Jurassic carbonate deposits at similar latitudes (Anderson *et al.*, 1994).

Burial curve and formation temperatures of diagenetic carbonates. The formation temperature of siderite concretions was estimated to be between 23 and 33ºC, using the oxygen siderite-water isotopic fractionation of Carothers *et al.* (1988) and a $\delta^{18}\text{O}_{\text{seawater}}$ of 0‰$_{\text{SMOW}}$. Because oxygen isotopes fractionate with temperature during calcite precipitation, an equilibrium fractionation diagram relating calcite δ^{18}O (SMOW) to precipitation temperatures was constructed using the calcite–water oxygen isotopic fractionation data of Kim and O'Neil (1997) and for different $\delta^{18}O_{water}$ values (−10 to 0‰$_{SMOW}$) (Figure 14). δ^{18}O of calcite can be used, on the one hand, to estimate formation temperature of calcite precipitated from a known fluid composition and, on the other hand, to estimate fluid composition from which calcite precipitates at a given temperature.

According to mineral and textural observations, most of the diagenetic calcites (calcite types 1, 4, and 5) were precipitated from mainly marine waters during sedimentation and the first stage of burial, which reached maximum temperatures of 85ºC (Mazurek *et al.*, 2006). The highest δ^{18}O value of calcite type 1 in siderite concretions is consistent with the field of marine carbonates formed at surface temperatures (~20ºC). δ^{18}O of calcite types 1 and 2 formed during early diagenesis from seawater makes it possible to estimate formation temperatures of 40−55ºC. The mean δ^{18}O value of calcite type 4 (22.6 ± 0.5‰$_{SMOW}$) obtained on the bulk silty sediment indicates a range of formation temperatures of ~50−60ºC. The formation temperature was estimated to be ~60−65ºC for calcite type 5 cross-cutting the pyrite nodule at 548.50 m, similar to calcite type 4.

The δ^{18}O value of calcite type 6 in the fault is the lowest value. Lack of knowledge concerning not just the age of the fault but also the age of the filling make it impossible to interpret the value either in terms of temperature or in terms of fluid origin. If calcite filling occurred early in the system, the fluid is assumed to be close to seawater, and a δ^{18}O value of +19‰$_{SMOW}$ corresponds to a formation temperature of ~80ºC. If calcite filling was later than the first uplift, the fluid is assumed to be a mixture of marine and meteoric components, and formed at a temperature of <65ºC. The low trace-element content of calcite type 6 compared to earlier generations of calcite suggests, however, that it precipitated from meteoric-derived dilute fluid rather than from marine fluid.

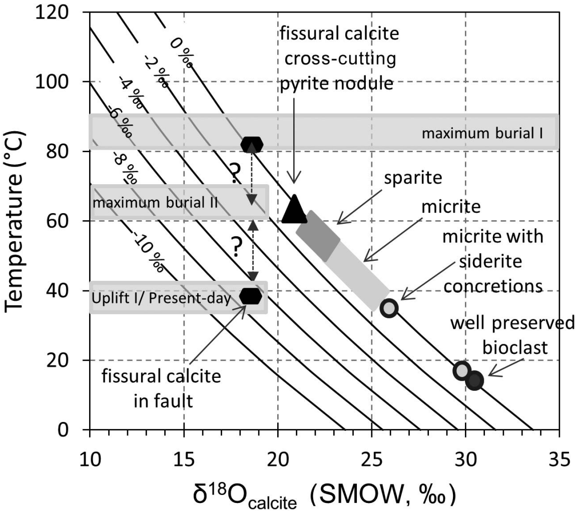

Figure 14. Theoretical temperature curve estimated from calcite δ^{18}O values, using the calcite-water oxygen isotopic fractionation of Kim and O'Neil (1997).

The clay fraction − origin and diagenesis

The distribution of clay minerals in a clay formation allows examination of the flux variation of terrigenous sediments and discussion of the diagenesis of clay minerals. The clay assemblage in the Opalinus Clay Fm is relatively homogeneous and consists mainly of kaolinite and ordered illite-smectite mixed-layer minerals (I-S, R1 ordered, with dominant illite) with minor illite, muscovite, and chlorite. Smectite and disordered illite-smectite mixed-layer minerals are absent. The homogeneity suggests the same source of terrigenous flux throughout the sedimentation of the entire formation. Warm hydrolyzing climates may have favored the formation of kaolinite on emerged lands bordering the basins. Some illite, mixed-layer illite-smectite, and chlorite were probably inherited from Palaeozoic basement material. The decreasing proportions of kaolinite were balanced by slightly increasing proportions of illite, I-S, R1 ordered, chlorite, and glauconite. This change might be explained partially by the mid-Cimmerian unconformity (Ziegler, 1990).

The burial temperatures measured on organic matter (Mazurek *et al.*, 2006; Elie and Mazurek, 2008) and recorded by calcite (present study) and the absence of discrete smectite reveal the influence of burial diagenesis which may disturb the composition of the terrigenous clay assemblages. A signal belonging to the initial terrigenous composition persists. Illite and chlorite contents increase slightly with depth at the expense of the K-feldspar content; this might be interpreted as a breakdown of K-feldspar at the expense of illite and chlorite formation, according to reaction 2 described by Moore and Reynolds (1997):

$$\text{K-feldspar} + \text{smectite} \rightarrow \text{illite} + \text{chlorite} + \text{quartz} \qquad (2)$$

Rare glauconite occurs as pellets. Glauconite is an Fe-rich illite formed near the water/sediment interface in semi-confined marine environments (Odin and Morton, 1988; Baldermann *et al.*, 2013). Traces of Ti in some pellets suggest, however, that some glauconite might have formed from the breakdown of biotite.

Diagenetic cements and evolution of pore waters through geological time

The combination of the isotopic data of diagenetic minerals and the diagenetic mineral sequence allows us to propose a scheme of depositional processes through geological time (Figure 15).

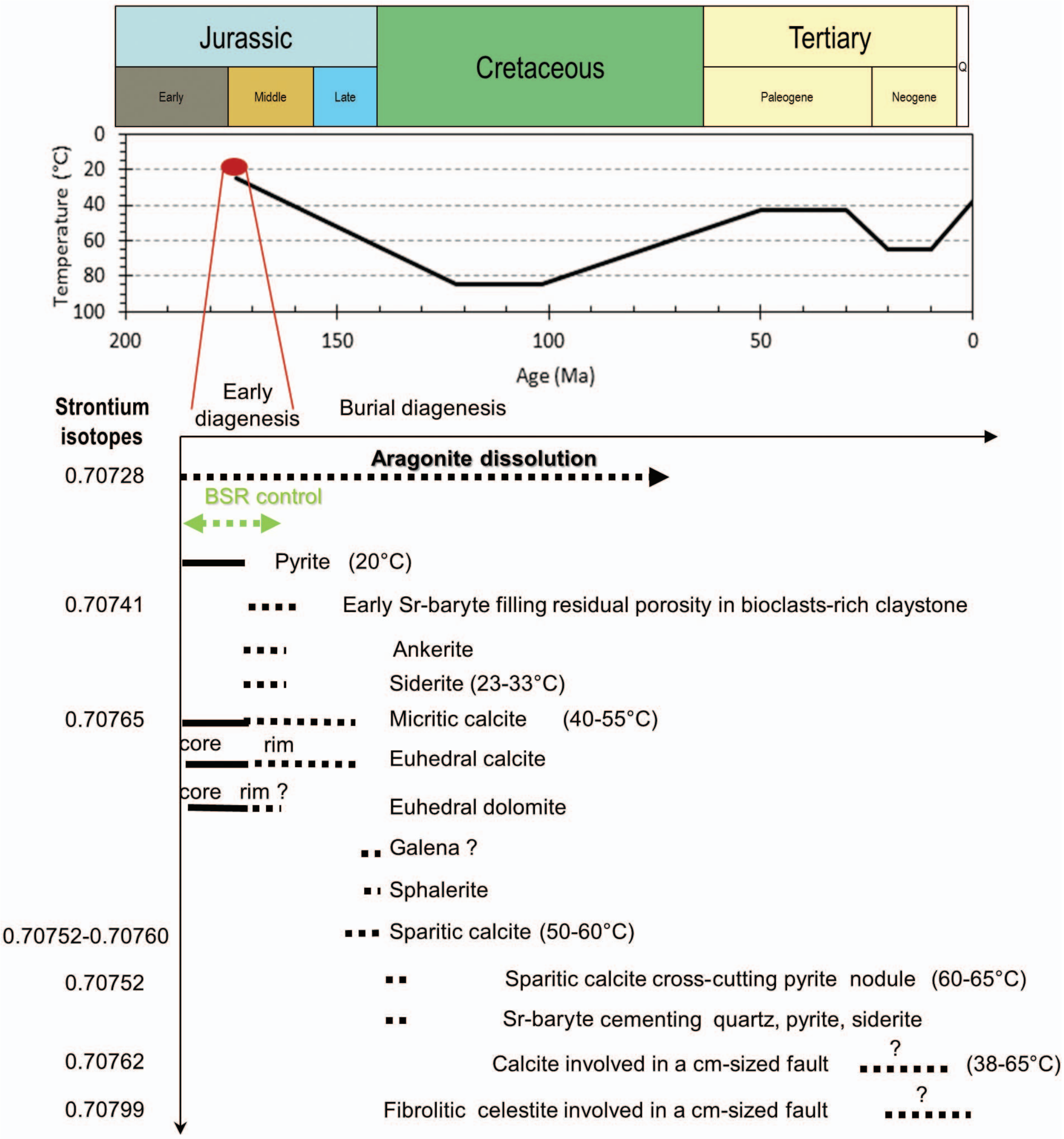

Figure 15. Diagenetic mineral sequence of the Opalinus Clay Fm combined with the burial curve, the formation temperatures of calcite and siderite deduced from their oxygen isotopic compositions, and strontium of fluids deduced from strontium isotopes of carbonates and sulfates. BSR indicates bacterial sulfate reduction.

Sedimentation. Based on petrological observations, most diagenetic phases, calcite types 1 and 2, pyrite framboids, dolomite, and siderite (concretions and disseminations) were formed very early in unconsolidated sediment near the water/sediment interface and are representative of the conditions of sedimentation. The minimal temperatures recorded by calcite type 1 in siderite concretions (~20ºC) are consistent with the formation temperature of well preserved belemnite rostra (~19ºC). The presence of small clusters of framboidal pyrite in siderite concretions indicates that formation of pyrite predated the formation of siderite concretions. The formations of pyrite, dolomite, and siderite are often associated with very variable sedimentation rates, as well as with large clay contents and the presence of organic carbon. The degradation of organic matter takes place over a succession of bacterial depth zones: oxic zone, suboxic zone (Mn and Fe reduction), sulfate reduction, methanogenesis, and fermentation, followed by thermal degradation (Froelich *et al.*, 1979). The formation of pyrite and siderite requires large iron concentrations in pore water that can be reached in the suboxic zone at low sedimentation rates, where Fe can be liberated to pore water from detrital material, especially due to transformations of clay minerals or dissolution of iron (hydro)xides. The ubiquity of pyrite framboids in the clay formation indicates that early sedimentation is close to the sulfate reduction zone, as confirmed by pyrite sulfur stable isotopes. Dolomite is contemporaneous with the bacterial sulfate reduction (BSR), the effect of sulfate inhibition being reduced by the consumption of sulfate during BSR (Compton, 1992) and iron being incorporated readily into sulfides rather than dolomite (Raiswell, 1982).

A rapid cessation of the bacterial reduction of sulfate prevented the total consumption of iron. Once the bacterially mediated sulfate reduction and Fe consumption by pyrite formation ceased, the greater Fe availability in the pore water resulted in an increase of the Fe content and of the Fe/(Fe+Mg) ratio of later diagenetic minerals, as confirmed by the formation of calcite type 3, iron-bearing dolomite, and then ankerite. The iron enrichment was sufficient to achieve siderite saturation. The rapid cessation of BSR and the formation of early siderite concretions could be explained by deposition near a fluctuating boundary between the suboxic iron reduction zone and sulfate reduction zone, or between the sulfate reduction zone and the methanogenesis zone. Large iron concentrations, and a relatively shallow and stormy distal environment associated with periodic arrivals of oxygenated water, are consistent with the precipitation of siderite concretions at a fluctuating boundary near the suboxic zone rather than the methanogenesis zone. Temperatures estimated using siderite (23−33ºC) suggest, however, that some siderite was not formed at the water/sediment interface but continued during burial, and could be associated with a fluctuating boundary between sulfate reduction and the methanogenesis zone, as suggested by carbon isotopic compositions of some siderite concretions and calcite.

Some Ba-Sr sulfates filling voids in sample 552.55 m and showing a ^{87}Sr/^{86}Sr ratio of 0.707406 slightly above the strontium value of Aalenian seawater could also be associated with early diagenesis. Pristine seawater is undersaturated with respect to celestite. Chemical analysis of diagenetic calcite replacing carbonate bioclasts indicates, however, that diagenetic calcite is poorer in Sr than are bioclasts. The remobilized Sr released by the recrystallization of the primary carbonate bioclasts allows celestite saturation to occur.

Burial. The main cementation during burial is represented by calcite type 4 with minor sphalerite in the silty lenses and layers. The range of temperatures of 40−55ºC estimated from bulk calcite (dominant calcite type 1) in clay layers suggest that some calcite type 1 could have continued to precipitate during the beginning of burial. Galena observed in the pyrite nodule of sample 548.50 m could be also associated with this stage. The temperatures estimated from oxygen isotopic compositions of calcite type 4 are 50−60ºC. The consistency of ^{87}Sr/^{86}Sr ratios and formation temperatures between calcite type 4 and fissural calcite (type 5) with minor Ba-Sr sulfates cross-cutting the pyrite nodule strongly suggests that they were almost contemporaneous. At this stage, the slight ^{87}Sr enrichment of the fluid relative to Aalenian seawater could be due to partial disintegration of ^{87}Rb in the fluid and/or support by ^{87}Rb from detrital clay minerals.

Telodiagenesis. Ba-Sr sulfates and calcite type 6 occur as veinlets in the fault zone of the sample 601.90 m, indicating fluid circulation in the cm-scale shear zone. Note that sulfates associated with this stage are Ba-poor celestite, unlike early Ba-Sr sulfates, due either to chemical changes in the fluid or to changes in the conditions. Calcite type 6 is also poor in trace elements, and its Fe/(Fe+Mg) ratio remains constant.

Comparison with other marine clay formations

Diagenetic conditions. Comparison of several marine-reduced clay formations studied for their possible use in the disposal/storage of nuclear waste showed: (1) almost the same mineralogy of cementation that consists of dominant carbonates with minor framboidal pyrite, glauconite, sphalerite, baryte, and celestite; and (2) almost the same diagenetic sequence (Rupelian Boom Clay, Belgium: Laenen and De Craen, 2004; Tournemire Toarcian Clay, France: Peyaud *et al.*, 2006; Bure Callovo-Oxfordian (COx) Clay, France: Lerouge *et al.*, 2011; Opalinus Clay, Switzerland: Mazurek *et al.*, 2008). Calcite is the dominant diagenetic carbonate with minor dolomite, ankerite, and siderite. Carbon and oxygen isotope ratios of most of the carbonates in these formations indicate that are dominantly marine. In deep clay formations such as the Toarcian/Domerian clay formation at Tournemire or the Opalinus Clay formation at Benken for which maximal burial reached temperatures of 80−120ºC and 85ºC, respectively, formation temperatures obtained from late calcite are ~60−65ºC, showing that calcite cementation continued in residual porosity through geological time. Little evidence exists in the data of calcite formed at equilibrium with meteoric waters, such as late filling of cracks in COx clay (Lerouge *et al.*, 2011), recording the slow diffusion of meteoric fluids through the clay formation.

Distribution of siderite in marine clay formations varies from one formation to the next. Siderite concretions are present at the scale of the Opalinus Clay Fm at Benken; they are also present in the Rupelian Boom Clay Fm in Belgium (Laenen and De Craen, 2004) and in the Oxfordian Clay Fm in England (Hudson *et al.*, 2001). In these environments, δ^{18}O values of siderite concretions in the Boom Clay Fm (33−36‰$_{\mathrm{SMOW}}$: Leanen and De Craen, 2004) or in the Opalinus Clay Fm

(30−32‰$_{\rm SMOW}$) are consistent with precipitation from marine-derived water at the water/sediment interface. By comparison, the Toarcian Clay Fm of Tournemire, France, contains siderite dissemination at the scale of the formation whereas the COx Clay Formation at Bure, France, contains little siderite disseminated in the clay matrix and limited to the maximum flooding zone (Lerouge *et al.*, 2011). δ^{18}O values of disseminated siderite in COx Clay (+26 to +29‰$_{\rm SMOW}$) and in the Tournemire Clay (+19 to +22‰$_{\rm SMOW}$) indicate that disseminated siderite formed at temperatures corresponding to the maximal burial attained by these units. According to these data, two types of siderite may be distinguished depending on their occurrence, on their oxygen isotopic signature and their paleo-environment: (1) siderite concretions formed at temperature corresponding to the water/sediment interface at a fluctuating boundary between the suboxic iron reduction and the sulfate reduction zones; and (2) siderite disseminations formed at temperatures near maximum burial and at the fluctuating boundary between sulfate reduction and methanogenesis zones. Note that the chemical compositions of siderite in the clay formation are almost comparable, whatever their distribution and type, *i.e.* rich in Ca and Mg (sideroplesite); this suggests that diagenetic fluids in the different depositional environments evolved in the same trend.

Consequences for the pore-water chemistry and reactive transport modeling

Models of present-day pore waters in the Opalinus Clay Fm are based on data acquired at the Mont Terri Laboratory (Pearson *et al.*, 2003, 2011). Those authors considered cation distribution to be controlled by cation exchange on clay mineral-based exchange sites and equilibrium reactions with diagenetic minerals. In the 2003 model (Pearson *et al.*, 2003), Na, K, and Sr were controlled by the cation exchanger, Ca by calcite saturation, Fe by siderite or goethite saturation, Mg by the cation exchanger or the dolomite saturation. Chlorine was a free solute fixed by the Cl content measured in waters analysed in the boreholes and sulfate was treated as a free solute fixed at the sulfate/chloride ratio of seawater. Redox was controlled by pyrite saturation. In the 2011 model (Pearson *et al.*, 2011), sulfate was controlled by celestite saturation, Mg by the cation exchanger, and calcite saturation was included in all the models, associated with Ca or carbonate concentration. These assumptions need to be validated by the identification of diagenetic minerals at equilibrium with present-day pore waters and their chemistry, and at the scale of the clay formation. This approach is suggested for application to the Opalinus Clay Fm of Benken.

Carbonate control on cation distribution and cation concentration in pore water. According to XRD data on bulk claystone samples from the Benken borehole, the major- and minor-element contents in bulk calcite (Mg, Mn and Fe) are correlated strongly with an inverse relationship with the clay content of the claystone. This suggests that carbonate chemistry is controlled primarily by the amount and the characteristics of the non-carbonate phases such as clay minerals in this case, in agreement with Veizer (1983). The chemical and isotopic evolutions of the different generations of carbonates during diagenesis, such as the $X_{\rm Fe}$ ratio with the bacterial sulfate reduction processes, the trace-element contents in calcite, and δ^{18}O of calcite varying with temperature and/or fluid composition all demonstrate that diagenetic carbonate minerals reflect the chemical evolution of pore waters (Ca/Fe/Mg ratios, δ^{18}O) in the clay formation over geological time. This result is consistent with the role of the clay exchanger and the use of carbonate/pore-water equilibrium as the control of the cation distribution in pore water. The preserved chemical and isotopic variations of carbonates with geological time imply, however, that re-equilibration between precipitated carbonates and pore water is very limited, in agreement with Erbacher *et al.* (2011) and Pellenard *et al.* (2014). Consequently, given the long residence time of pore-water chemical constituents (*i.e.* very low advective and diffusive fluxes within the formation) modeling approaches may need to consider the chemistry of carbonate grain surfaces at equilibrium with present-day pore water in a nearly closed system. The most representative carbonates at equilibrium with pore water at the scale of the Opalinus Clay Fm of Benken are surfaces of dominant calcite type 4 in laminated intervals, surfaces of micrite and euhedral disseminated carbonates (calcite types 1 and 2) in clay-rich zones, and numerous siderite nodules. All the generations of calcite cited above are low in Fe and Mg and are characterized by high $X_{\rm Fe} \approx 0.7$; the euhedral disseminated carbonates other than calcite are ankerite and siderite. Dolomite is scarce and surrounded systematically by ankerite. These observations, made at the scale of the Opalinus Clay Fm, support the assumption of equilibrium of pore waters with pure calcite and pure siderite, and the use of Ca/Mg exchange as the control on Mg concentration rather than dolomite. Siderite in the Opalinus Clay Fm contains significant Ca and Mg contents. Because considerable uncertainty about the thermodynamic data for siderite remains, modeling the equilibrium of pore waters with pure siderite remains a reasonable assumption to a first approximation (Tournassat *et al.*, 2008).

Control of sulfur minerals on redox and sulfate concentration in pore water. Sulfur minerals in the Opalinus Clay Fm of Benken consist of pyrite and (Ba,Sr) sulfates distributed throughout the formation. The pore-water geochemistry model of Pearson (2011) considers present-day pore water to be at equilibrium with pyrite for the control of the redox, and with celestite for the control of sulfate. The morphology and sulfur isotopes of pyrite suggest it was formed at the water/sediment interface during sedimentation as a result of bacterial sulfate reduction. Textural observations of pyrite provide evidence of its stability until the present day. These results justify the assumption of using pyrite to control redox of pore water in the model. (Ba, Sr) sulfates were formed later during diagenesis from residual sulfates dissolved in pore waters in residual porosity, *i.e.* interstitial spaces in silty layers at burial temperatures of ~50–60ºC. Some celestite also occurs as fillings in a cm-thick fault. These data suggest strongly that saturation with celestite was attained and maintained though geological time, and validates the use of celestite to control sulfate concentration in the pore-water model.

Although pyrite and celestite were not formed contemporaneously, but successively, due to the cessation of the BSR, the long residence time of pore-water chemical constituents allows us to assume that pore waters are at equilibrium with diagenetic minerals. Consequently the redox state of the formation might be considered to have been controlled by the pyrite/sulfate couple throughout virtually its entire geological history.

Comparison with pore-water chemistry models in other clay formations. A better understanding of the clay cation exchanger and of mineral equilibrium is needed to improve the pore-water models. In the different reduced clay models (Opalinus Clay Fm at Mont Terri: Pearson *et al.*, 2011; Callovian-Oxfordian clay at Bure: Gaucher *et al.*, 2009; Toarcian clay at Tournemire: Tremosa *et al.*, 2012), good knowledge of the carbonate system and, more specifically of dolomite and siderite, and of sulfate/sulfide equilibrium, allows better constraint of pore-water models. In the pore-water model of the Toarcian clay Fm (Tremosa *et al.*, 2012), Fe was not taken into account in the modeling and sulfate was fixed. Siderite and celestite observed in the clay formation might be used to control Fe and sulfate, respectively. In the Callovian-Oxfordian Clay Fm of Bure, dolomite is present at the scale of the formation and was used to control Mg (Gaucher *et al.*, 2009). Siderite was used to control Fe, though it cannot be considered to have been at equilibrium throughout the formation, due to the fact that its presence is limited to the maximum clay zone (Lerouge *et al.*, 2013).

SUMMARY AND CONCLUSIONS

From the perspective of nuclear-waste disposal in Switzerland, the building of an accurate geochemical model able to predict pore-water chemistry is essential in the evaluation of the potential migration of radionuclides over a long time scale. Pore-water modeling in the Opalinus clay Fm at Mont Terri is based on the clay exchanger and on the minerals at equilibrium with the pore waters (Pearson *et al.*, 2003, 2011). The most recent model (Pearson *et al.*, 2011) demonstrated clearly the necessity to pursue mineralogical investigations of at least two major points: (1) the carbonate system and more specifically the distribution and chemistry of dolomite, ankerite, and siderite throughout the formation; and (2) the presence and distribution of celestite. The present paper provides a detailed mineralogical and geochemical study of the Opalinus Clay formation from Benken, in order to apply the pore-water geochemical model of the Opalinus Clay Fm from Mont Terri to the Benken site.

The semi-quantitative mineralogical assay, based on XRD data and the chemistry of bulk rocks, show that Opalinus claystones at Benken consist of a dominant clay fraction (43–63 wt.%) associated with a carbonate fraction (10–21 wt.%) and a variable silty quartz-feldspar fraction (11–33 wt.%). The upper part of the Opalinus Clay Fm contains a smaller clay fraction than the lower part. Despite variations in the proportions of silty, carbonate, and clay fractions along the vertical profile, the mineralogy of each fraction does not vary significantly. The silty fraction is essentially composed of quartz with minor K-feldspar and plagioclase (<4 wt.%). The carbonate fraction is composed of dominant calcite (8–16 wt.%) with significant amounts of siderite (2–5 wt.%). The clay fraction is composed of ~3–7 wt.% chlorite (chamosite + pyrochlore), ~4–9 wt.% illite, ~25–37 wt.% ordered illite-smectite mixed layers (I-S, R1 ordered), ~13–21 wt.% kaolinite, and ~3–6 wt.% muscovite. Kaolinite and I-S, R1 ordered contents are greater in the lower part of the Opalinus Clay Fm.

Complementary petrological observations of claystone samples enabled the distribution of the major fractions and of diagenetic minerals to be defined. The silty fraction occurs as mm- to cm-thick layers (laminations) alternating with clay-rich layers. The abundant presence of laminations in the upper part of the Opalinus Clay Fm suggests sediment deposition in stormy distal environments at relatively shallow depth. Diagenetic minerals in the Opalinus Clay Fm, in decreasing order, include carbonates, pyrite, sphalerite, (Ba, Sr) sulfates, and glauconite. Among carbonates, different generations of calcite are distinguished and represent the dominant carbonate cement; siderite occurs as disseminated micron-sized grains or as cm-sized nodules distributed at different levels of the formation, whereas dolomite and ankerite are minor. The textural relationships between the different diagenetic minerals in the Opalinus Clay Fm combined with mineral chemistry and stable isotopes enabled the diagenetic mineral sequence, the formation temperatures of minerals, and the processes involved to be determined:

(1) Pyrite associated with micritic calcite and euhedral carbonates (calcite and dolomite) was formed

at an early stage at or near the water/sediment interface. Sulfur isotopic data from pyrite suggest that pyrite was formed by bacterial reduction of sulfate in a 'closed system', *i.e.* in a system in which sulfate supply was less than the BSR rate. These data, obtained essentially in the upper part and at the bottom of the formation, are consistent with a shallow-depth sedimentation environment. The carbonates formed at this early stage are poor in iron due to the consumption of iron by pyrite formation.

(2) At the end of the bacterial reduction of sulfate, iron still available in the pore waters was incorporated in carbonates (sparitic calcite, ankerite, siderite) and in glauconite, whereas available sulfate and strontium released by dissolution of carbonate bioclasts in pore waters was partly incorporated in Ba-Sr sulfates.

Siderite is abundant, occurring as cm-scale concretions in the Opalinus Clay Fm of Benken. This morphology and oxygen isotopes indicate that these concretions were formed at an early stage close to the water/sediment interface at the fluctuating boundary between suboxic iron reduction and sulfate reduction zones. The quite regular occurrence of siderite concretions at different levels of the Opalinus Clay Fm could suggest small sedimentation cycles with the formation of siderite linked to pauses in sedimentation and iron enrichment of pore waters. However, some carbon and oxygen isotopic data on siderite also suggest that some of it continued to precipitate during burial at the fluctuating boundary between sulfate reduction and the methanogenesis zone.

Sparitic calcite was formed at temperatures of 50–60ºC from marine-derived fluids. Galena and sphalerite are associated with sparitic calcite.

Ba-Sr sulfates were formed later than sparitic calcite and contemporaneously with fissural calcite cross-cutting the pyrite nodule. Oxygen data from fissural calcite indicates formation temperatures of 60–65ºC from marine-derived fluids, *i.e.* during burial.

(3) Celestite and calcite occur as veinlets in the only 1 cm-thick fault observed in sample 601.90 m.

Based on these mineralogical and geochemical data of the Benken claystones, the mineral assemblage used for the geochemical model of the pore waters at Mont Terri might be applied at Benken without significant adjustment. The scarcity of dolomite and the presence of an ankerite corona surrounding dolomite suggest that present-day pore waters are not at equilibrium with dolomite. Rather it is suggested that Mg concentration in pore waters is controlled by Ca/Mg exchange, according to Pearson *et al.* (2011). The observation of celestite through the formation is consistent with the use of celestite saturation to control sulfate concentration (Pearson *et al.*, 2011). These investigations show the need for a detailed mineralogical and geochemical study to refine the pore-water chemistry model in a clay formation.

ACKNOWLEDGMENTS

This research was supported financially by the University of Bern and by the BRGM. The authors acknowledge Antoine de Haller for providing the crinoïd separate and Eric Lasseur for helpful discussions. They are also grateful to Dr Gregory Connelly (Scientific Translations Limited) for proofreading and editing the English. The Editors in Chief, Drs Joseph W. Stucki and Michael A. Velbel, the Associate Editor, Dr Reiner Dohrmann, and Dr F.J. Pearson and two other anonymous referees are thanked for their constructive comments which led to significant improvements in the manuscript.

REFERENCES

Anderson, T.F. and Arthur, M.A. (1983) Stable isotopes of oxygen and carbon and their application to sedimentologic and paleonvironmental problems. Pp. 1–151 in: *Stable Isotopes in Sedimentary Geology* (I.R. Kaplan, J. Veizer, and L.S. Land, editors). Society of Economic Paleontologists and Mineralogists Short Course, **10**, SEPM, Tulsa, Oklahoma, USA.

Anderson, T.F., Popp, B.N., Williams, A.C., Ho, L.Z., and Hudson, J.D. (1994) The stable isotopic records of fossils from the Peterborough Member, Oxford Clay Formation (Jurassic), UK: paleoenvironmental implications. *Journal of the Geological Society*, **151**, 125–138.

ANDRA (2005) Evaluation de la faisabilite′ du stockage géologique en formation argileuse, Dossier 2005. Collection Les Rapports.

Baldermann, A., Warr, L.N., Grathoff, G., and Dietzel, M. (2013) The rate and mechanism of deep sea glauconite formation at the Ivory coast-Ghana marginal ridge. *Clays and Clay Minerals*, **61**, 258–276.

Baeyens, M.H. and Bradbury, B., editors (1997) Far-field sorption data bases for performance assessment of a L/ILW repository in an undisturbed Palfris marl host rock. Paul Scherrer Institut, Switzerland.

Birkhäuser, P., Roth, P., Meier, B., and Naef, H. (2001) 3D-Seismik: Räumliche Erkundung der mesozoischen Sedimentschichten im Zürcher Weinland (3D seismics: exploration of the Mesozoic sediments in the Zürcher Weinland). Nagra Technical Report, NTB 00-03, Nagra, Wettingen, Switzerland.

Blanc, P., Legendre, O., and Gaucher, E. (2007) Estimate of clay minerals amounts from XRD pattern modelling: the ARQUANT model. *Physics and Chemistry of the Earth*, **32**, 135–144.

Bowen, R. (1966) Oxygen isotopes as climatic indicators. *Earth-Science Reviews*, **2**, 199–224.

Brigaud, B., Pucéat, E., Pellenard, P., Vincent, B., and Joachimski, M.M. (2008) Climatic fluctuations and seasonality during the Late Jurassic (Oxfordian–Early Kimmeridgian) inferred from $\delta^{18}O$ of Paris Basin oyster shells. *Earth and Planetary Science Letters*, **273**, 58–67.

Canfield, D.E. (2001) Biogeochemistry of sulphur isotopes. Pp. 603–636 in: *Stable Isotope Geochemistry* (J.W. Valley and D.R. Cole, editors). Reviews in Mineralogy, **43**. Mineralogical Society of America, Washington, D.C.

Carothers, W.W., Adami, L.H., and Rosenbauer, R.J. (1988) Experimental oxygen isotope fractionation between siderite-water and phosphoric acid liberated CO_2-siderite. *Geochimica et Cosmochimica Acta*, **52**, 2445–2450.

Claret, F., Sakharov, B.A., Drits, V.A., Velde, B., Meunier, A., Griffault, L., and Lanson, B. (2004) Clay minerals in the Meuse-Haute Marne Underground Laboratory (France): possible influence of organic matter on clay mineral evolution. *Clays and Clay Minerals* **52**, 515–532.

Claret, F., Lerouge, C., Laurioux, T., Bizi, M., Conte, T., Ghestem, J.P., Wille, G., Sato, T., Gaucher, E.C., Giffaut, E., and Tournassat, C. (2010) Natural iodine in a clay formation: implications for iodine fate in geological disposals. *Geochimica et Cosmochima Acta*, **74**, 16–29.

Compton, J.S. (1992) Early diagenesis and the origin of diagenetic carbonate in sediment recovered from the Argo basin, northeastern Indian Ocean (Site 765). Pp. 77–88 in: Proceedings of the Ocean Drilling Program, Scientific Results, **123**, (F.M. Gradstein, J.N. Ludden *et al.*, editors).

Dera, G., Pucéat, E., Pellenard, P., Neige, P., Delsate, D., Joachimski, M., Reisberg, L., and Martinez, M. (2009) Water mass exchange and variations in seawater temperature in the NW Tethys during the Early Jurassic: Evidence from neodymium and oxygen isotopes of fish teeth and belemnites. *Earth and Planetary Science Letters*, **286**, 198–207.

Drits, V.A., Lindgreen, H., Sakharov, B.A., and Salyn, A.S. (1997) Sequence structure transformation of illite-smectite-vermiculite during diagenesis of Upper Jurassic shales, North Sea. *Clay Minerals*, **35**, 351–371.

Elie, M. and Mazurek, M. (2008) Biomarker transformations as constraints for the depositional environment and for maximum temperatures during burial of Opalinus Clay and Posidonia Shale in northern Switzerland. *Applied Geochemistry*, **23**, 3337–3354.

Epstein, S., Buchsbaum, R., Lowenstam, H.A., and Urey, H.C. (1953) Revised carbonate-water isotopic temperature scale. *Geological Society of America Bulletin*, **64**, 1315–1325.

Erbacher, J., Friedrich, O., Wilson, P.A., Lehmann, J., and Weiss, W. (2011) Short-term warming events during the boreal Albian (mid-Cretaceous). *Geology*, **39**, 223–226.

Evain, M. (1992) U-FIT: A Cell Parameter Refinement Program. IMN Nantes, France.

Froelich, P.N., Klinkhammer, G.P., Bender, M.L., Luedtke, N.A., Heath, G.R., Cullen, D., Dauphin, P., Hammond, D., Hartman, B., and Maynard, V. (1979) Early oxidation of organic matter in pelagic sediments of the eastern equatorial Atlantic suboxic diagenesis. *Geochimica et Cosmochima Acta*, **43**, 1075–1090.

Gaucher, E., Robelin, C., Matray, J.M., Negrel, G., Gros, Y., Heitz, J.F., Vinsot, A., Rebours, H., Cassagnabere, A., and Bouchet, A. (2004) ANDRA underground research laboratory: interpretation of the mineralogical and geochemical data acquired in the Callovian–Oxfordian formation by investigative drilling. *Physics and Chemistry of the Earth*, **29**, 55–77.

Gaucher, E.C., Blanc, P., Bardot, F., Braibant, G., Buschaert, S., Crouzet, C., Gautier, A., Girard, J.P., Jacquot, E., Lassin, A., Negrel, G., Tournassat, C., Vinsot, A., and Altmann, S. (2006) Modelling the pore water chemistry of the Callovian-Oxfordian formation at a regional scale. *Comptes Rendus Geoscience*, **338**, 917–930.

Gaucher, E.C., Tournassat, C., Pearson, F.J., Blanc, P., Crouzet, C., Lerouge, C., and Altmann S. (2009) A robust model for pore-water chemistry of clayrock. *Geochimica et Cosmochimica Acta*, **73**, 6470–6487.

Guidotti, V. (1984) Micas in metamorphic rocks. Pp. 357–467 in: *Micas* (S.W. Bailey, editor). Reviews in Mineralogy, **13**, Mineralogical Society of America, Washington, D.C.

Hendry, J.P. (1993) Geological control on regional subsurface carbonate cementation: anisotopic paleohydrologic investigation of middle Jurassic limestones in Central England. Pp. 231–260 in: *Diagenesis and Basin Development* (A.D. Horbury and A.G. Robinson, editors), American Association for Petroleum Geologists Studies in Geology, AAPG **36**.

Hubert, F., Caner, L., Meunier, A., and Lanson, B. (2009) Advances in characterization of soil clay mineralogy using X-ray diffraction: from decomposition to profile fitting. *European Journal of Soil Science*, **60**, 1093–1105.

Hudson, J.D., Coleman, M.L., Barreiro, B.A., and Hollingworth, N.T.J. (2001) Septarian concretions from the Oxford Clay (Jurassic, England, UK): involvement of original marine and multiple external pore fluids. *Sedimentology*, **48**, 507–531.

Irwin, H., Curtis C.D., and Coleman M.L. (1977) Isotopic evidence for the source of diagenetic carbonates formed during burial of organic-rich sediments. *Nature*, **269**, 209–213.

Jenkyns, H.C., Gale, A.S., and Corfield, R.M. (1994) Carbon- and oxygen-isotope stratigraphy of the English Chalk and Italian Scaglia and its palaeoclimatic significance. *Geological Magazine*, **131**, 1–34.

Jenkyns, H.C., Jones, C.E., Gröcke, D.R., Hesselbo, S.P., and Parkinson, D.N. (2002) Chemostratigraphy of the Jurassic System: applications, limitations and implications for palaeoceanography. *Journal of the Geological Society*, **159**, 351–374.

Jones, C.E. and Jenkyns, H.C. (2001) Seawater strontium isotopes, oceanic anoxic events, and seafloor hydrothermal activity in the Jurassic and Cretaceous. *American Journal of Science*, **301**, 112–149.

Kaufhold, S. and Dohrmann, R. (2010) Stability of bentonites in salt solutions II. Potassium chloride solution – Initial step of illitization? *Applied Clay Science*, **49**, 98–107.

Kim, S.-T. and O'Neil, J.R. (1997) Equilibrium and nonequilibrium oxygen isotope effects in synthetic carbonates. *Geochimica et Cosmochimica Acta*, **61**, 3461–3475.

Koroleva, M., Alt-Epping, P., and Mazurek, M. (2011) Large-scale tracer profiles in a deep claystone formation (Opalinus Clay at Mont Russelin, Switzerland): Implications for solute transport processes and transport properties of the rock. *Chemical Geology*, **280**, 284–296.

Laenen, B. and De Craen, M. (2004) Eogenetic siderite as an indicator for fluctuations in sedimentation rate in the Oligocene Boom Clay Formation (Belgium). *Sedimentary Geology*, **163**, 165–174.

Landais, P., Dohrmann, R., and Kaufhold, S. (2012) Overview of the clay mineralogy studies presented at the 'Clays in natural and engineered barriers for radioactive waste confinement' meeting, Montpellier, October 2012. *Clay Minerals*, **48**, 149–152.

Lanson, B., Sakharov, B.A., Claret, F. and Drits, V.A. (2009) Diagenetic smectite-to-illite transition in clay-rich sediments: A reappraisal of X-ray diffraction results using the multi-specimen method. *American Journal of Science*, **309**, 476–516.

Lécuyer, C., Picard, S., Garcia, J.-P., Sheppard, S.M.F., Grandjean, P., and Dromart, G. (2003) Thermal evolution of Tethyan surface waters during the Middle–Late Jurassic: evidence from $\delta^{18}O$ values of marine fish teeth. *Paleoceanography*, **18**, 1076.

Lécuyer, C., Reynard, B., and Martineau, F. (2004) Stable isotope fractionation between mollusc shells and marine waters from Martinique Island. *Chemical Geology*, **213**, 293–305.

Lerouge, C., Gaucher, E.C., Tournassat, C., Negrel, P., Crouzet, C., Guerrot, C., Gautier, A., Michel, P., Vinsot, A., and Buschaert, S. (2010) Strontium distribution and origins in a natural clayey formation (Callovian-Oxfordian. Paris Basin. France): A new sequential extraction procedure. *Geochimica et Cosmochimica Acta*, **74**, 2926–2942.

Lerouge, C., Grangeon, S., Gaucher, E.C., Tournassat, C., Agrinier, P., Guerrot, C., Widory, D., Flehoc, C., Wille, G., Ramboz, C., Vinsot, A., and Buschaert, S. (2011) Mineralogical and isotopic record of biotic and abiotic diagenesis of the Callovian–Oxfordian clayey formation of Bure (France). *Geochimica et Cosmochimica Acta*, **75**, 2633–2663.

Lerouge, C., Grangeon, S., Fléhoc, C., Buschaert, S., Mazurek, M., Matray, J.-M., and Tournassat, C. (2012) Diagenetic carbonates in clay-rich marine formations. Abstract: International meeting "Clays in Natural and Engineered Barriers for Radioactive Waste Confinement", France.

Lerouge, C., Vinsot, A., Grangeon, S., Wille, G., Flehoc, C., Gailhanou, H., Gaucher, E.C., Madé, B., Altmann, S., and Tournassat, C. (2013) Controls of Ca/Mg/Fe activity ratios in pore water chemistry models of the Callovian−Oxfordian Clay Formation. *Water Rock Interaction WRI 14, Procedia Earth and Planetary Science*, **7**, 475−478.

Ma, C. and Eggleton, R.A. (1999) Cation exchange capacity of kaolinite. *Clays and Clay Minerals*, **47**, 174−180.

Madsen, F.T. (1998) Clay mineralogical investigations related to nuclear waste disposal. *Clay Minerals*, **33**, 109−129.

Manghnani, M.H. and Hower, J. (1964) Glauconite: cation exchange capacities and infrared spectra. Part I. The cation exchange capacity of glauconite. *The American Mineralogist*, **49**, 586−598.

Martin, R.T. (1955). Reference chlorite characterization for chlorite identification in soil clays. *Clays and Clay Minerals*, **3**, 117−145.

Marschall, P., Horseman, S., and Gimmi, T. (2005) Characterisation of gas transport properties of the Opalinus Clay, a potential host rock formation for radioactive waste disposal. *Oil & Gas Science and Technology − Revue d'IFP Energies*, **60**, 121−139.

Mazurek, M., Hurford, A.J., and Leu, W. (2006) Unravelling the multi-stage burial history of the Swiss Molasse Basin: integration of apatite fission track, vitrinite reflectance and biomarker isomerisation analysis. *Basin Research*, **18**, 27−50.

Mazurek, M., Gautschi, A., Marschall, P., Vigneron, G., Lebon, P., and Delay, J. (2008) Transferability of geoscientific information from various sources (study sites, underground rock laboratories, natural analogues) to support safety cases for radioactive waste repositories in argillaceous formations. *Physics and Chemistry of the Earth*, **33**, 95−105.

Mazurek, M., Alt-Epping, P., Bath, A., Gimmi, T., and Waber, H.N. (2009) Natural tracer profiles across argillaceous formations: The CLAYTRAC project. OECD/NEA Rep. 6253. OECD Nuclear Energy Agency, Paris.

Mazurek, M., Alt-Epping, P., Bath, A., Gimmi, T., Waber, H. N., Buschaert, S., Cannière, P. De Craen, M.D., Gautschi, A., Savoye, S., Vinsot, A., Wemaere, I., and Wouters, L. (2011) Natural tracer profiles across argillaceous formations. *Applied Geochemistry*, **26**. 1035−1064.

McIlreath, I.A. and Morrow, D.W., editors (1990) *Diagenesis.* Geological Association of Canada. St. John's, Newfoundland.

Merlet, C. (1994) An accurate computer correction program for quantitative electron probe microanalysis. *Mikrochimica Acta*, **114−115**, 363−376.

Moore, D.M. and Reynolds, R.C. (1997) Structure, nomenclature, and occurrences of clay minerals. Pp. 138−195 in: *X-ray Diffraction and the Identification and Analysis of Clay Minerals*. Oxford University Press, New York.

Mozley, P.S. (1989) The internal structure of carbonate concretions in mudrocks: a critical evaluation of the conventional concentric model of concretion growth. *Sedimentary Geology*, **103**, 85−91.

Müller-Vonmoos, M., Kahr, G., and Madsen, F.T. (1994) Intracrystalline swelling of mixed-layer illite-smectite in K-bentonites. *Clay Minerals*, **29**, 205−213.

Meunier, A. (2006) Why are clay minerals small? *Clays and Clay Minerals*, **41**, 551−566.

Nagra (2002) Project Opalinus Clay − Safety Report. Demonstration of Disposal Feasibility for Spent Fuel, Vitrified High-level Waste and Long-lived Intermediate-level Waste (Entsorgungsnachweis). Nagra Technical Report NTB 02-05, Nagra, Wettingen, Switzerland.

Odin, G.S. and Morton, A.C. (1988) Authigenic green particles from marine environments. Pp. 213−264 in: *Diagenesis* (G.V. Chiligarian and K.H. Wolf, editors). Developments in Sedimentology, **43**, Elsevier, Amsterdam.

Ohmoto, H., Kaiser, C.J., and Geers, K.A. (1990) Systematics of sulphur isotopes in recent marine sediments and ancient sediment-hosted basemetal deposits. Pp. 70−120 in: *Stable Isotopes and Fluid Processes in Mineralization*, **23** (H.K. Herbert and S.E. Ho, editors). Geology Department and University extension, the University of Western Australia.

ONDRAF/NIRAS (2001) SAFIR-2: Second Safety Assessment and Interim Report. ONDRAF/NIRAS, Brussels, Report NIROND 2001-06 E.

ONDRAF/NIRAS (2009) The Long-term Safety strategy for the Geological Disposal of Radioactive Waste, second full draft, ONDRAF/NIRAS report NIROND-TR 2009-12E.

Pearson, F.J., Arcos, D., Gaucher, E.C., and Waber, H.N. (2003) Porewater chemistry and geochemical modelling. Pp. 67−104 in: *Mont Terri Project − Geochemistry of water in the Opalinus Clay Formation at the Mont Terri Rock Laboratory*. Reports of the Federal Office for Water and Geology (FOWG). Geology Series N°5.

Pearson, F.J., Tournassat, C., and Gaucher, E.C. (2011) Biogeochemical processes in a clay formation in situ Experiment: Part E − Equilibrium Controls on Chemistry of Pore Water from the Opalinus Clay, Mont Terri Underground Research Laboratory, Switzerland. *Applied Geochemistry*, **26**, 990−1008.

Pellenard, P., Tramoy, R., Pucéat, E., Huret, E., Martinez, M., Bruneau, L., and Thierry, J. (2014) Carbon cycle and seawater palaeotemperature evolution at the Middle-Late Jurassic transiton, eastern Paris Basin (France). *Marine and Petroleum Geology*, **53**, 30−43.

Peyaud, J.B., Pagel, M., Cabrera, J., and Pitsch, H. (2006) Mineralogical, chemical and isotopic perturbations induced in shale by fluid circulation in a fault at the Tournemire experimental site (Aveyron, France). *Journal of Geochemical Exploration*, **90**, 9−23.

Pin, C. and Bassin, C. (1992) Evaluation of a strontium specific extraction chromatographic method for isotopic analysis in geological materials. *Analytica Chimica Acta*, **269**, 249−255.

Pucéat, E., Lécuyer, C., Sheppard, S.M.F., Dromart, G., Reboulet, S., and Grandjean, P. (2003) Thermal evolution of Cretaceous Tethyan marine waters inferred from oxygen isotope composition of fish tooth enamels. *Paleoceanography*, **18**, 1029−1040.

Raiswell, R. (1982) Pyrite texture, isotopic composition and the availability of iron. *American Journal of Science*, **82**, 1244−1263.

Rosenbaum, J. and Sheppard, S.M. (1986) An isotopic study of siderites, dolomites and ankerites at high temperatures. *Geochimica et Cosmochimica Acta*, **50**, 1147−1150.

Sakharov, B.A., Lindgreen, H., Salyn, A., and Drits, V.A. (1999) Determination of illite-smectite structures using multispecimen XRD profile fitting. *Clays and Clay Minerals*, **47**, 555−566.

Shannon, R.D. (1976) Revised effective ionic radii and systematic studies of interatomic distances in halides and chalcogenides. *Acta Crystallographica* **A32**, 751−767.

Spillmann, T., Blümling, P., Manukyan, E., Marelli, S., Maurer, H.R., Greenhalgh, S.A., and Green, A.G. (2010) Geophysics applied to nuclear waste disposal investigations in Switzerland. *Near Surface Geoscience, first break*, **28**, August 2010 special topic (www.firstbreak.org © 2010 EAGE), 39−50.

Spiro, B., Gibson, P.J., and Shaw, H.F. (1993) Eogenetic siderites in lacustrine oil shales from Queensland, Australia, a stable isotope study. *Chemical Geology*, **106**, 415−427.

Środoń, J., Morgan, D.J., Eslinger, E.V., Eberl, D.D., and Karlinger, M.R. (1986) Chemistry of illite/smectite and end-member illite. *Clays and Clay Minerals*, **34**, 368−378.

Swart, P.K., Burns, S.J., and Leder, J.J. (1991) Fractionation of the stable isotopes of oxygen and carbon in carbon dioxide during the reaction of calcite with phosphoric acid as a function of temperature and technique. *Chemical Geology*, **86**, 89−96.

Thury, M. (2002) The characteristics of the Opalinus Clay investigated in the Mont Terri underground rock laboratory in Switzerland. *Comptes Rendus Physique*, **3**, 923−933.

Tournassat, C., Grangeon, S., Leroy, P., and Giffaut, E. (2013) Modeling specific pH-dependent sorption of divalent metals on montmorillonite surfaces. A review of pitfalls, recent archievements and current challenges. *American Journal of Science*, **313**, 395−451.

Tremosa, J., Arcos, D., Matray, J.M., Bensenouci, F., Gaucher, E.C., Tournassat, C., and Hadi, J. (2012) Geochemical characterization and modelling of the Toarcian/Domerian pore water at the Tournemire underground research laboratory. *Applied Geochemistry*, **27**, 1417−1431.

Ufer, K., Kleeberg, R., Bergmann, J., and Dohrmann, R. (2012a) Rietveld refinement of disordered illite-smectite mixed layered structures by a recursive algorithm. I: One-dimensional patterns. *Clays and Clay Minerals*, **60**, 507−534.

Ufer, K., Kleeberg, R., Bergmann, J., and Dohrmann, R. (2012b) Rietveld refinement of disordered illite/smectite mixed layered minerals with a recursive algorithm. II: powder pattern refinement and quantitative phase analysis. *Clays and Clay Minerals*, **60**, 535−552.

Veizer, J. (1983) Trace elements and isotopes in sedimentary carbonates. Pp. 265−299 in: *Carbonates: Mineralogy and Chemistry* (R.J. Reeder, editor). Reviews in Mineralogy, **11**, Mineralogical Society of America, Washington, D.C.

Velde, B. (1985) *Clay Minerals: a Physico-chemical Explanation of their Occurrence*. Elsevier, 426 pp.

Vinsot, A., Appelo, C.A.J., Cailteau, C., Wechner, S., Pironon, J., De Donato, P., De Cannière, P., Mettler, S., Wersin, P., and Gabler, H.E. (2008) CO_2 data on gas and pore water sampled in situ in the Opalinus Clay at the Mont Terri rock laboratory. *Physics and Chemistry of the Earth*, *Supplement 1*, **33**, S54−S60.

Weetjens, E., Marivoet, J., and Govaerts, J. (2009) Preparatory Safety Assessment, Conceptual Model Description of the Reference Case. External Report of the Belgian Nuclear Centre: SCK·CEN-ER-215, B. Leterme (editor). 12/Ewe/P-42.

Wenk, H.-R., Voltolini, M., Mazurek, M., Van Loon, L.R., and Vinsot, A. (2008) Preferred orientations and anisotropy in shales: Callovo-Oxfordian shale (France) and Opalinus clay (Switzerland). *Clays and Clay Minerals*, **56**, 285−306.

Wierzbowski, H., Rogov, M., Matyja, B., Kiselev, D., and Ippolitov, A. (2013) Middle-Upper Jurassic (Upper Callovian-Lower Kimmeridgian) stable isotope and elemental records of the Russian Platform: Indices of oceanographic and climatic changes. *Global and Planetary Change*, **109**, 196−212.

Wortmann, U.G., Bernasconi, S.M., and Boettcher, M.E. (2001) Hypersulfidic deep biosphere indicates extreme sulphur isotope fractionation during single-step microbial sulphate reduction. *Geology*, **29**, 647−650.

Ziegler, P.A. (1990) Tectonic and palaeogeographic development of the North Sea rifts. Pp 1−36 in: *Evolution of North Sea Rifts* (D.J. Blundell and A.D. Gibbs, editors). Clarendon Press, Oxford, UK.

(*Received 11 March 2014; revised 20 August 2014; Ms. 856; AE: R. Dohrmann*)

Clays and Clay Minerals, Vol. 62, No. 4, 313–323, 2014.

THE DYNAMIC SHEAR MODULUS AND DAMPING RATIO OF CLAY NANOCOMPOSITES

Z. NESE KURT* AND SUAT AKBULUT

Ataturk University, Department of Civil Engineering, 25240 Erzurum, Turkey

Abstract—Clay soils are very useful as liners in geotechnical structures such as landfill sites, dams, water channels, *etc*. Swelling is a common problem in clay liners, however. To better understand swelling properties, in the present study clay nanocomposites were produced by means of the sol gel method, using a hydrophobic clay, polymers (locust bean gum, latex, glycerine, vinyl acrylic copolymer), and rubber powder. The study focused on the swelling and dynamic properties (secant shear modulus and damping ratio) of the clay nanocomposites researched experimentally in laboratory conditions. The dynamic tests were conducted on samples compacted using two different compaction energy levels. The test results were compared with those of natural clay and hydrophobic organo-clay. The test results revealed that the damping ratios and secant shear modulus of clay nanocomposites without rubber (CNC) and with rubber (CNCr) that were compacted with both the E1 and E2 energy levels were increased and decreased, respectively. In addition, with increasing percentage of vinyl acrylic in nanoclay composites, the secant shear modulus values were decreased and damping ratio values were increased. Consequently, the test results found that the swelling and dynamic properties of clay nanocomposites can be optimized in order to attenuate the negative effects of dynamic loads on clay liners.

Key Words—Clay nanocomposite, Damping Ratio, Hydrophobic Clay, Secant Shear Modulus, Swelling

INTRODUCTION

Determination of dynamic soil properties is an extremely important aspect of geotechnical earthquake engineering (Kumar *et al.*, 2013). The dynamic response of soils is an important engineering property because soils can underlay critical support structures such as highway bridges or levees (Bate, 2010). The dynamic shear modulus and damping ratio of clay soils are important parameters for constructing engineering structures which may be subjected to dynamic loads such as earthquakes, machine vibrations, and waves. Shear modulus is a measure of the shear stiffness of the soil. The secant shear modulus can also be used to approximate dynamic loading over a cycle of loading at any given strain amplitude (Darendeli, 2001). At moderate to high strains, the secant shear modulus is used to represent the average soil stiffness. The material damping ratio is a measure of the amount (or magnitude) of energy dissipated by the soil when undergoing shear or plastic deformation (Zhang *et al.*, 2005; Aghaei Araei *et al.*, 2010). The most important dynamic parameters of soils are shear modulus and damping ratio (Aghaei Araei *et al.*, 2010; Bate and Burns, 2012). Determination of the secant shear modulus and material damping ratio are important for soils, therefore.

Energy-absorbing systems find applications in many situations where excess energy needs to be managed without causing damage to surrounding objects (Chaudhari *et al.*, 2005). Energy-absorbing materials are produced from rubber-based elastomers (Moon *et al.*, 2002; Kilar and Koren, 2009). In recent years, polymer/layered silicate nanocomposites have been investigated widely because of their excellent properties which are different from either clay or polymer. Polymer/layered silicate nanocomposites are composite materials, obtained from clay which has interacted chemically and physically with polymer (Alexandre and Dubois, 2000; Ray and Okamoto, 2003; Tjong, 2006; Pavlidou and Papaspyrides, 2008). Biopolymers are naturally occurring polymers that are found in all living organisms. Biopolymers are therefore considered to originate from renewable sources; consequently, their use is expected to have a less negative effect on the environment than petroleum-based materials. At present, biopolymers are used in a variety of applications such as therapeutic aids, medicines, coatings, food products, and packaging materials (Petersson and Oksman, 2006).

Surfactants are substances that cause a hydrophilic or a hydrophobic surface which can increase or decrease the surface tension. Clay nanocomposites (polymer/layered silicate nanocomposites) are prepared by incorporating finely dispersed layered silicate materials in a polymer matrix. In recent years polymer/layered silicate nanocomposites have attracted great interest from researchers (LeBaron *et al.*, 1999; Paiva *et al.*, 2008; Mittal, 2009; Akbulut *et al.*, 2010, 2012, 2013). The dynamic properties of organo-clays have also been investigated. The dynamic properties of organo-bentonites using resonant column tests were investigated by Bate and Burns (2012).

---

* E-mail address of corresponding author:
znkurt@atauni.edu.tr
DOI: 10.1346/CCMN.2014.0620405

The fundamental properties and preparation of clay nanocomposites (polymer/layered silicate nanocomposites) were investigated by previous researchers (Lagaly, 1999; Alexandre and Dubois, 2000; Fischer, 2003; Ray and Okamoto, 2003; Liu, 2007; Pavlidou and Papaspyrides, 2008). A number of these studies have focused on the thermal and mechanical properties of polymer/layered silicate nanocomposites (Burmistr *et al.*, 2005; Tjong, 2006; Yasmin *et al.*, 2006; Hbaieb *et al.*, 2007; Zare-Shahabadi *et al.*, 2011). The mechanical properties of silicon rubber consisting of blended silicone gums with varied vinyl contents were improved by Xu *et al.* (2010). Tanniru *et al.* (2006) compared the mechanical response of a clay-reinforced polyethylene nanocomposite with un-reinforced polyethylene under identical processing conditions. Those authors found that the addition of clay to polyethylene led to retention of adequately high-impact strength in the temperature range investigated −40 to +70ºC (Tanniru *et al.*, 2006). Zhu and Wool (2006) synthesized a new bio-based elastomer from soybean oil filled with nanoclay to generate an elastic nanocomposite and observed that the mechanical properties were improved significantly by the addition of organoclays.

Other studies focused on the barrier properties and flame-retardant properties of polymer/layered silicate nanocomposites (Koh *et al.*, 2008; Mohan and Kanny, 2011; Mishra *et al.*, 2012). A series of rubber/clay nanocomposites prepared by the latex-compounding method (He *et al.*, 2010) was shown to have low cost/performance ratios, excellent tensile strength, superior gas-barrier properties, improved flame-retardant properties, and outstanding anti-fatigue properties. The advantages of using nanocomposite materials in civil engineering over those of the more conventional construction materials were listed by Hackman and Hollaway (2006) who noted that the tensile modulus and flexural modulus of nanocomposites were increased.

The damping ratios and secant shear modulus of clay nanocomposites were investigated by a number of researchers. One of these studies focused on improving clay nanocomposites using latex and glycerin. The damping ratios of these clay nanocomposites were investigated (Majedi, 2013) in an attempt to modify clay nanocomposites and to investigate the effects of locust bean gum (biopolymer-LBG), latex (LTX), glycerin (GLC), vinyl acrylic (VA), and rubber powder (RP) on the swelling properties, secant shear modulus, and damping ratio of the natural clay (C) and hydrophobic clay (HOC). The hydrophobic clay was used to eliminate the negative effects caused by the swelling of clayey soils.

To better understand the swelling and dynamic properties (secant shear modulus and damping ratio) swelling of the clay nanocomposites, the present study produced clay nanocomposites by means of the sol gel method, using a hydrophobic clay, polymers (locust bean gum, latex, glycerine, vinyl acrylic copolymer), and rubber powder, and determined swelling and dynamic properties of different combinations and preparations.

MATERIALS

Natural clay

The clayey soil samples came froma clay pit in the Oltu-Narman deposits in Erzurum, Turkey and are classified as high-plasticity clay (CH), according to the Unified Soil Classification System (USCS), and also based on some engineering properties of natural clay (Table 1). Natural clay was used as the template sample.

Hydrophobic organo-clay

In the present study, hydrophobic organo-clay (Table 1) was prepared using the procedure of Kurt (2009). A cationic surfactant, dialkyl ammonium meta

Table 1. Some engineering properties of natural and hydrophobic clays (after Kurt, 2009).

Some properties			Clay	Hydrophobic organo-clay
Clay content	<0.002 mm	(%)	56	–
Specific gravity	G_s		2.62	2.52
Liquid limit	w_L	(%)	72	–
Plasticity index	I_p	(%)	39	–
Contact angle		º	37	88
Cation exchange capacity	(meq/100 g of dry soil)		26.25	21.62
Optimum moisture content*	w_{opt}	(%)	16.5	14
Maximum dry density*	γ_{dmax}	(kN/m^3)	17.55	16.67
Unconfined compression strength*	q_{uu}	(kPa)	1048	998
BET (N_2) surface area		(m^2/g)	10,19	5
Soil classification,	(USCS)		CH	–
Damping ratio*	D	(%)	12.74	16.9
Secant shear modulus*	G_{sec}	MPa	2.843	2.757

* The results were investigated from samples compacted with energy level E1.

Table 2. Properties of LBG, latex, glycerine, vinyl acrylic copolymer, and rubber powder.

Properties	Locust bean gum (LBG)	Latex (LTX)	Glycerine (GLC)	Vinyl acrylic copolymer (VA)	Rubber (RP)
Chemical formula	(1−4) linked beta-D mannose residues and the side chain of (1−6) linked alpha-D galactose.	C_3H_3N	$C_3H_8O_3$	–	–
Chemical composition	Galactomannan (a group of hydrocolloids)	Styrene Butadiene Emulsion	Glycerol	Vinyl acrylic copolymer emulsion	Styrene Butadiene Copolymer
pH	5−7	8−12	7	5 ± 1	–
Viscosity (cps)	2000−3500	–	1200	1000−5000	–
Density (g/cm^3)	–	1.015	1.261	1.03	1.15−1.198

sulfate (DAMS), was used in the preparation of hydrophobic organo-clay. First, 40 g of clay was dispersed in 8 L of deionized water and stirred with a magnetic stirrer at 1000 rpm for 2 h. Previously prepared surfactant solution (DAMS and deionized water) was added slowly to the clay suspension at 30ºC. The modified product (hydrophobic clay) was dried at room temperature. The surfactant included 5% (250 ppm) by weight of clay.

Polymers and other materials

In the present study, locust bean gum, latex, glycerine, vinyl acrylic copolymer, and rubber powder (Tables 2, 3) were used to improve the clay nanocomposites.

Locust-bean gum (LBG). The conventional use of locust-bean gum as an excipient in drug products utilizes its thickening, gel forming, and stabilizing properties (Dey *et al.*, 2012). Locust-bean gum is a virtually neutral

Table 3. Chemical structures of LBG, latex, glycerine, and vinyl acrylic copolymer.

	Chemical structure
Locust bean gum	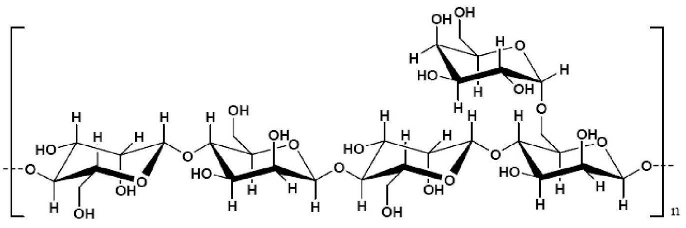
Latex	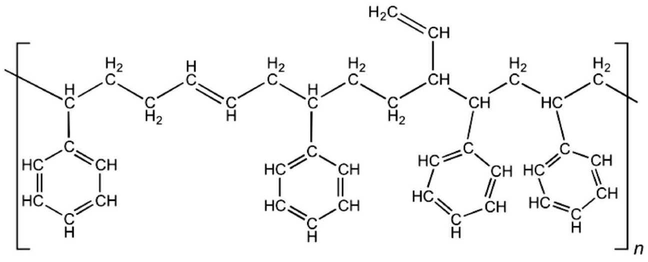
Glycerine	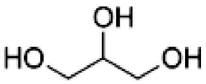
Vinyl acrylic copolymer	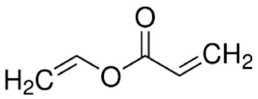

galactomannan polymer extracted from the seeds of the carob tree (Lopes da Silva *et al.*, 1994). Locust-bean gum increases the strength of the gel markedly and changes the gel character of the nanocomposite from brittle to elastic (Maier *et al.*, 1993). The LBG was used in the experiments in order to increase the gel strength of the clay nanocomposites.

Latex (LTX). Latex, which was the other polymer used in the experiments, is an elastomer. Natural rubber is produced from the latex of the *Hevea brasiliensis* tree (Hamed, 2001). Latex as an elastomer was used in the experiments in order to improve the elastic properties of the nanocomposites.

Glycerine (GLC). The presence of glycerine is essential for preparing nanocomposites (Lin *et al.*, 1993). In some previous studies for preparing nanocomposites, glycerine was used as the plasticizer (de Carvalho *et al.*, 2001; Tang *et al.*, 2008; Rhim, 2011).

Vinyl acrylic copolymer emulsion (VA). Vinyl acrylic copolymer emulsion is a water-based resin (Barmar *et al.*, 2010). Such resins are often used as the adhesive component of the composition (Murphy *et al.*, 1977). The pigment-binding and film-forming properties of the vinyl acrylic copolymer are significant and its water stability is also notable. Vinyl acrylic copolymer was also used for its adhesive properties.

Rubber powder (RP). The rubber powder used in the present study was purchased from Kahya Rubber, Sakarya, Turkey. Due to its light-weight nature and its capacity for damping energy, the rubber powder can be used to mitigate seismic forces and to absorb earthquake vibrations (Nakhaei *et al.*, 2012). The use of waste fiber materials in geotechnical applications was investigated by Akbulut *et al.* (2007) to evaluate the effects of scrap tire rubber and synthetic fibers on the unconfined compressive strength parameters, and on the dynamic behavior, of clayey soils. Soil samples reinforced with scrap-tire rubber fibers were investigated and the results indicated that increased use of scrap-tire rubber could lead to improved damping ratios and shear moduli of clayey soils.

CHARACTERIZATION OF COMPOSITES

Sample preparation and tests

The clay nanocomposites were obtained by the sol- gel method (Schadler 2003). First, LBG (0.5%) was added to 2 L of water and mixed using a mechanical stirrer at 4000 rpm until dissolved. During stirring, latex (10%) was added and mixed for 20 min. Then, glycerine (10%) was added and the solution was mixed for 10 min. Next, 2500 g of hydrophobic organo-clay and 1 L of water were added and mixed for 1 h. Finally, vinyl acrylic copolymer was added in different proportions (0%, 5%, 10%) and mixed with a mechanical stirrer. (These products were clay nanocomposite samples without rubber powder additive CNC). Rubber powder (5%) was also added and mixed for 10 min to produce clay nanocomposite samples with rubber powder additive (CNCr). The leach products (clay nanocomposites) were dried at room temperature for 48 h. All of the percentages of polymers and additives were used as the percentages of clay weight. The materials used for nanocomposites are listed in Table 4 with the percentage of dry hydrophobic clay weight.

In order to prepare the clay nanocomposite samples for swelling and dynamic simple shear tests, bulk samples of clay nanocomposites were compacted with an automatic compactor. The maximum dry unit weight (γ_{dmax}) and optimum moisture content (w_{omc}) were determined in the clay nanocomposite samples in accordance with standard ASTM D 1557 (2012). To compare the swelling and damping properties of clay nanocomposites with different compactive energy levels and moisture contents, two different energy levels were applied to the samples. The samples were compacted in a 152.4 mm diameter mold with a 44.48 N rammer dropped from a height of 457.2 mm. The samples were added to the mold in five layers and each layer was tamped 25 times. The calculated compactive effort was 2597 kJ/m^3 (energy level E1). In addition, the samples were also added to the mold in five layers in the mold and each layer was tamped 50 times. The calculated compactive effort in this case was 5192 kJ/m^3 (energy level E2). The leach samples with optimum moisture content were then used to prepare samples for swelling tests and dynamic simple shear tests.

Table 4. Clay nanocomposite contents (see Table 2 for abbreviations).

	Content
C	Natural clay
HOC	Hydrophobic clay
CNC0	HO-%0.5LBG-%10LTX-%10GLC
CNC5	HO-%0.5LBG-%10LTX-%10GLC-%5VA
CNC10	HO-%0.5LBG-%10LTX-%10GLC-%10VA
CNCR0	HO-%0.5LBG-%10LTX-%10GLC-%5RP
CNCR5	HO-%0.5LBG-%10LTX-%10GLC-%5VA-%5RP
CNCR10	HO-%0.5LBG-%10LTX-%10GLC-%10VA-%5RP

The swelling tests were carried out in accordance with ASTM D 4546 Method C. The tests were conducted on the compacted samples with optimum moisture contents using a consolidation test apparatus manufactured by ELE (Bedfordshire, UK). The swelling tests were conducted on the natural clay, hydrophobic organoclay and clay nanocomposite (CNC and CNCr) samples.

Dynamic simple shear tests

The dynamic simple shear test apparatus used in this study is a GeocompTM ShearTrac II-DSS system (Geocomp, 2007) (Figure 1). The dynamic simple shear (DSS) tests were carried out in accordance with ASTM D 6528 (2007) on the natural clay, hydrophobic organo-clay, and clay nanocomposite samples compacted with energy levels E1 and E2. The device allows load-controlled constant-volume DSS tests with a load frequency up to 1 Hz on a consolidated soil specimen. A computer controls the micro-stepper motors that apply vertical and horizontal loads to the specimen. A soil specimen of diameter 63.5 mm was confined by a rubber membrane supported by Teflon-covered aluminum rings instead of conventional reinforced membranes.

Natural clay, hydrophobic clay, and clay nanocomposite samples were consolidated under a vertical stress of 100 kPa which was greater than the estimated preconsolidation pressure. In the experiments, the frequency of cyclic load (f) was 1.0 Hz. The cyclic stress ratio (CSR) was 0.40. To compare the effect of VA on the clay nanocomposites, the DSS tests were conducted at a single CSR. The maximum peak to peak strain is ±2.5%.

With the raw data taken from the tests performed on hydrophobic clay and clay nanocomposite, shear strain and shear stress values of the second cycle were determined and the graphs of second cycles were plotted. The hysteresis loop is a stress-strain path. The secant shear modulus (G) and damping ratios (D) were determined from idealized hysteresis loops (Figure 2) produced by cyclic loading. G is defined in equation 1 where τ is the shear stress and γ is the shear strain.

$$G = \tau / \gamma \tag{1}$$

The material damping ratio, D, is the proportion of dissipated energy to the maximum retained strain energy during each cycle at a given strain amplitude (Figure 2). The energy dissipated over a loading cycle is represented by the gray area within the hysteresis loop (A_L), and the maximum retained strain energy is represented by the triangular area (A_T) that is calculated using peak shear stress and peak shearing strain (Kramer, 1996; Darendeli, 2001).

$$D = A_L / (4\pi A_T) \tag{2}$$

The material damping ratio is a result of friction between soil particles, strain rate effects, and non-linearity of the stress-strain relationship in soils

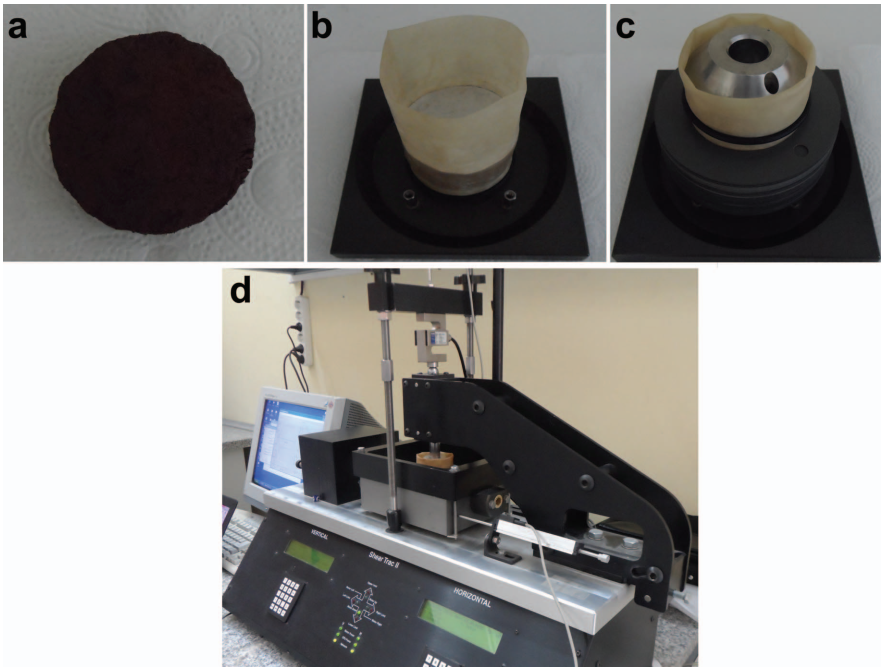

Figure 1. Specimen preparation for DSS tests: (a) the test sample, (b) covering the specimen with a membrane, (c) fixing the membrane to the bottom plate by O-rings and installing Teflon-covered rings around the specimen, (d) the DSS device includes the sample.

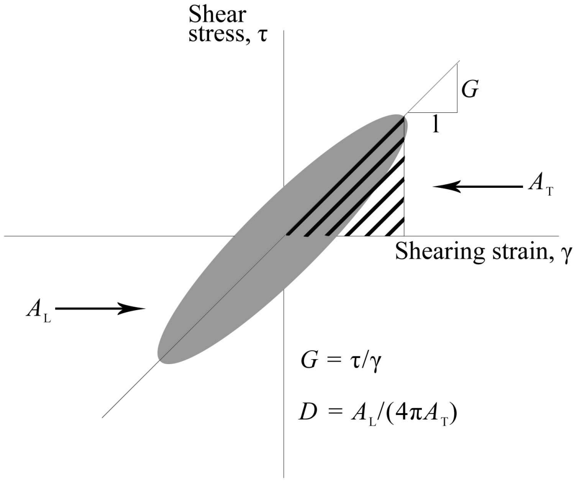

Figure 2. Determination of secant shear modulus, and damping ratios from the idealized hysteresis loop produced by cyclic loading (after Darendeli, 2001).

(Darendeli, 2001). Some of the tests were repeated as many as three times to assure the repeatability of the results.

RESULTS AND DISCUSSION

Swelling tests

The swelling test results (Figure 3) revealed that the swelling pressures of clay nanocomposites (CNC and CNCr) were lower than those of hydrophobic clay. The decrease in the swelling pressures of clay nanocomposite samples are due to the hydrophobic properties of clay nanocomposites (Akbulut *et al.*, 2013). The negative effects of swelling of clayey soils were eliminated by decreasing the swelling pressures of the clay nanocomposites.

Dynamic simple shear test results

Hysteresis loops. The hysteresis loops from second cycles (Figure 4) indicated that the secant shear modulus (determined using equation 1) of clay nanocomposites compacted with energy levels E1 and E2 were decreased when compared with natural clay and hydrophobic clay. The damping ratio values (determined from equation 2) of clay nanocomposites compacted with energy levels E1 and E2 were increased.

Shear modulus. The dynamic simple shear test results (Figure 5) showed that the secant shear modulus of E1- and E2-compacted clay nanocomposites (CNC and CNCr samples) decreased when compared with both C and HOC. Similarly, the secant shear modulus of E1-and E2-compacted clay nanocomposites decreased with increased addition of VA.

The test results (Table 5) showed that the secant shear modulus of hydrophobic organo-clay compacted with the energy level E1 decreased by 3% relative to the natural clay. The secant shear modulus of clay nanocomposite (CNC) samples decreased by 39% and 35%, respectively, relative to natural clay and hydrophobic organo-clay. Similarly, the secant shear modulus of hydrophobic organo-clay compacted with energy level E1 decreased by 17% relative to the natural clay. The secant shear modulus of clay nanocomposites (CNC)

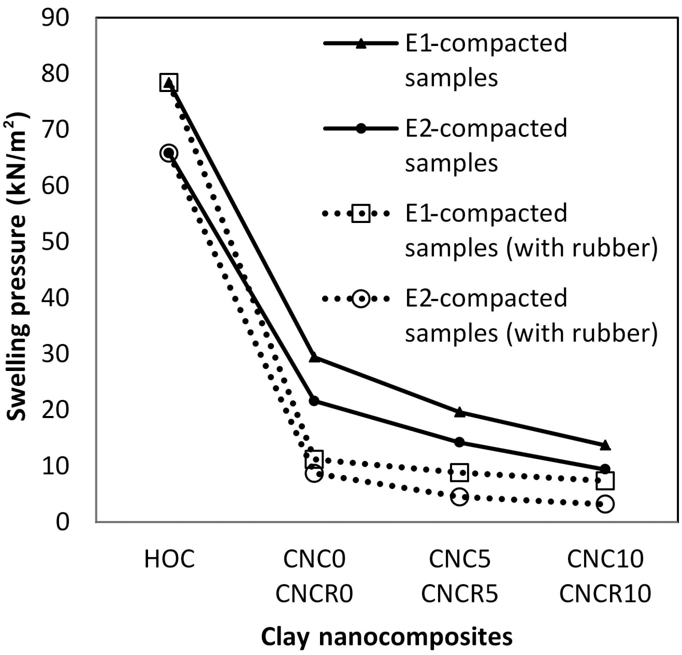

Figure 3. Swelling pressures of clay nanocomposite samples.

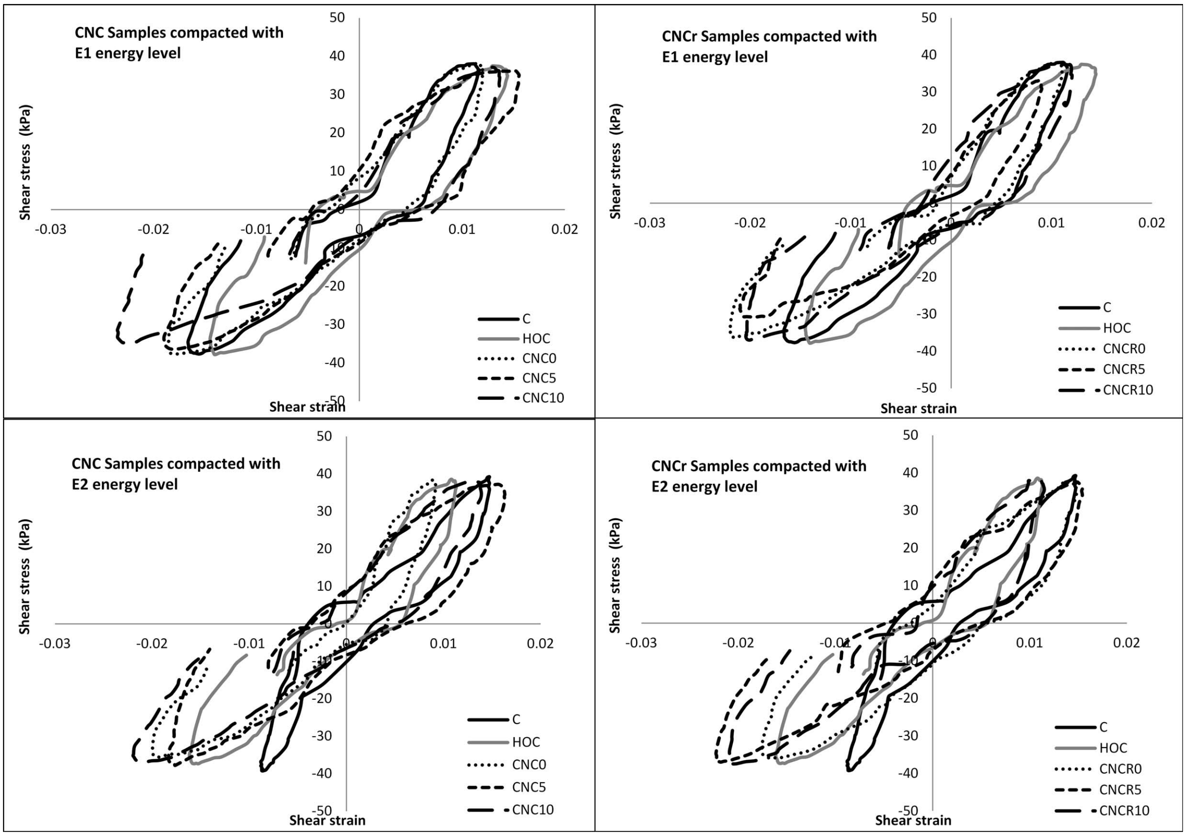

Figure 4. Hysteresis loops at the second cycle of samples.

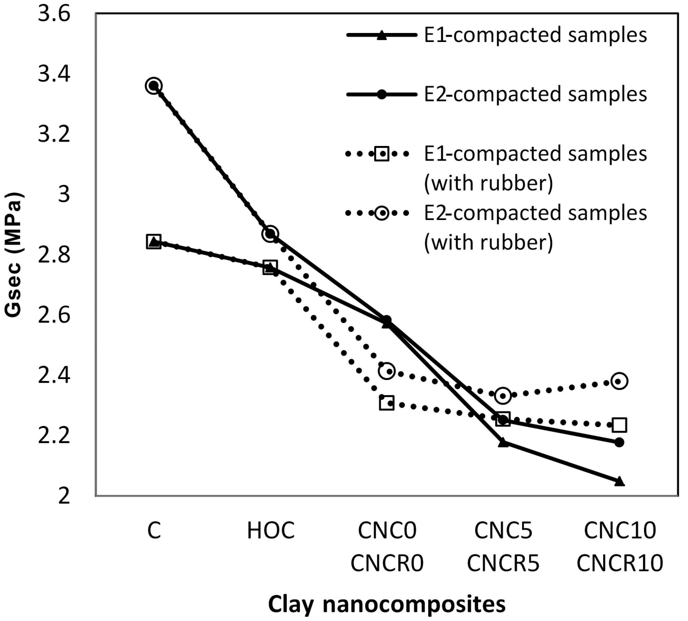

Figure 5. Secant shear modulus values of compacted clay nanocomposite samples.

Table 5. Secant shear modulus values of clay nanocomposite samples compacted with energy levels E1 and E2.

	E1 energy			E2 energy		
	Gsec (MPa)	Decreasing, % (relative to C)	Decreasing, % (relative to HOC)	Gsec (MPa)	Decreasing, % (relative to C)	Decreasing, % (relative to HOC)
C	2,843	–	–	3,360	–	–
HOC	2,757	3	–	2,868	17	–
CNC0	2,572	11	7	2,582	30	11
CNC5	2,178	31	27	2,251	49	27
CNC10	2,048	39	35	2,177	54	32
CNCR0	2,308	23	20	2,414	39	19
CNCR5	2,255	26	22	2,331	44	23
CNCR10	2,234	27	23	2,380	41	21

decreased by 54% and 32%, respectively, relative to natural clay and hydrophobic organo-clay. The secant shear modulus of the CNCr samples compacted with energy level E1 also decreased by 27% and 23%, respectively, relative to natural clay and hydrophobic organo-clay. Similarly, the secant shear modulus of clay nanocomposites (CNCr) compacted with energy level E2 decreased by 41% and 21%, respectively, relative to natural clay and hydrophobic organo-clay.

The test results demonstrated that the secant shear modulus values of E2-compacted natural clay samples were greater than E1-compacted natural clays. The secant shear modulus values of clay nanocomposites increased slightly with increasing energy.

Furthermore, secant shear modulus values in clay nanocomposites decreased when the percentage of VA increased. Large stiffness values may lead to negative dynamic effects, such as reduction of damping; in general, few materials possess both significant damping and rigidity properties (Finegan and Gibson, 1999; Finegan and Gibson, 2000; Ludwigson *et al.*, 2002; Chung, 2003; Rivin, 2007) . This problem was overcome by Finegan and Gibson (2000) who used hybrid composites (with a combination of coated and uncoated fibers) which appear to be a good compromise for obtaining improved damping without much loss of rigidity. The unconfined compressive strengths of clay nanocomposites decreased with the increased VA percentage.

Damping ratios. The dynamic simple shear test results (Figure 6) revealed that the damping ratios of E1- and E2-compacted clay nanocomposites (CNC and CNCr samples) had increased when compared with hydrophobic organo-clay and natural clay. Similarly, the E1- and E2-compacted clay nanocomposites increased when the VA percentage increased.

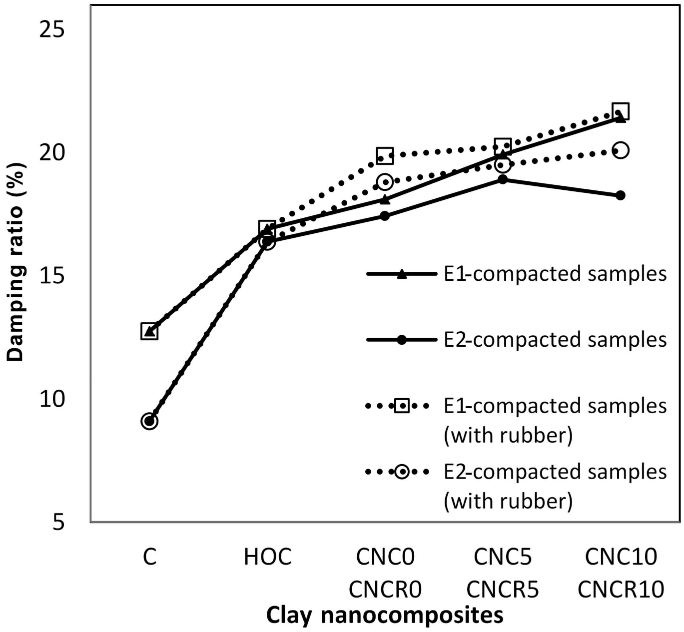

Figure 6. Damping ratios of compacted clay nanocomposite samples.

Previous research indicated that the initial damping ratio decreases when the mean effective stress is increased (D'Onofrio and Penna, 2003). The effective stress increased when the pore-water pressure decreased (Das, 1998). The experimental results revealed that the damping-ratio values of samples compacted at lower moisture contents were less than those of samples compacted at greater moisture contents and these results supported the findings of previous research.

The test results (Table 6) showed that the damping ratio of hydrophobic organo-clay compacted with energy level E1 increased by 33% relative to natural clay. The damping ratio of clay nanocomposites (CNC) increased by 68% and 27%, respectively, relative to natural clay and hydrophobic organo-clay. Similarly, the damping ratio of hydrophobic organo-clay compacted with the energy level E1 increased by 80% relative to natural clay. The damping ratio of clay nanocomposites (CNC) increased by 101% and 11%, respectively, relative to natural clay and hydrophobic organo-clay. The damping ratio of clay nanocomposites (CNCr) increased by 70% and 28%, respectively, relative to natural clay and hydrophobic organo-clay. Similarly, the damping ratio of clay nanocomposites (CNCr) compacted with the energy level E2 increased by 121% and 23%, respectively, relative to natural clay and hydrophobic organo-clay.

The test results also showed that the damping ratio values of E2-compacted natural clay samples were less than E1-compacted natural clays. The damping ratio values of clay nanocomposites decreased slightly with increasing energy, however.

The damping ratios of clay nanocomposites increased when the VA percentage increased. According to Kyminas *et al.* (1989), coating films, which are tough and flexible, which adhere well to various substrates with very low water-vapor permeability, and which have improved weather resistance, contain vinyl acrylic copolymers. The clay nanocomposites could gain these properties from the flexible structure of VA.

In civil engineering, 'base isolation systems' were used in buildings to decrease the negative effects of dynamic loads. 'Base isolation' is a technique in which isolation bearings are installed in structure foundations to reduce the damaging motion transmitted by horizontal earthquakes to those structures (Moon *et al*., 2002). Seismic base isolation is a valuable earthquake-resistant technique for structures such as buildings and bridges (Ashkezari, 2008). The energy-absorbing ability was increased with increase in the damping ratios of the CNC and CNCr samples. Eventually, the clay nanocomposites may be used as a damper rather like a seismic isolator, under buildings. The clay nanocomposites can also be used as a damper liner between the building and soil because of the decrease in swelling pressures.

CONCLUSIONS

The present study was undertaken to investigate the swelling properties and dynamic properties (secant shear modulus and damping ratio) of some clay nanocomposites and to compare the swelling pressure, damping ratio, and secant shear modulus values with those of natural clay and hydrophobic organo-clay. The swelling pressures of clay nanocomposites that compacted with energy levels E1 and E2 were decreased when compared with hydrophobic organo-clay. The experimental results indicated that the secant shear modulus and damping ratios of clay nanocomposites changed significantly in comparison with those of natural clay and hydrophobic organo-clay. The secant shear modulus values of clay nanocomposite samples without rubber (CNC) and with rubber (CNCr) compacted with energy levels E1 and E2 decreased when compared with natural clay and hydrophobic organo-clay. The secant shear modulus of clay nanocomposites compacted with energy level E1 was less than that for clay nanocomposites compacted with energy level E2.

The damping ratios of clay nanocomposites without rubber (CNC) and with rubber (CNCr) compacted with energy levels E1 and E2 increased when compared with natural clay and hydrophobic organo-clay. The damping ratios of clay nanocomposites compacted with energy level E1 were greater than clay nanocomposites compacted with energy level E2. The secant shear modulus

Table 6. Damping ratios of clay nanocomposite samples compacted with energy levels E1 and E2.

	E1 energy			E2 energy		
	D (%)	Increasing, % (relative to C)	Increasing, % (relative to HOC)	D (%)	Increasing, % (relative to C)	Increasing, % (relative to HOC)
C	12.74	–	–	9.09	–	–
HOC	16.9	36	–	16.38	80	–
CNC0	18.1	42	7	17.42	92	6
CNC5	19.92	57	18	18.9	108	15
CNC10	21.41	68	27	18.25	101	11
CNCR0	19.86	56	18	18.8	107	15
CNCR5	20.24	59	20	19.5	115	19
CNCR10	21.67	70	28	20.09	121	23

and damping ratios of clay nanocomposites decreased and increased, respectively, with increased VA percentage.

The improvement of clay nanocomposites by decreasing swelling pressures and increasing damping ratios could help to solve the dynamic problems of clayey soils, which could then be used as a damper for soils under buildings as a 'base isolation system'.

ACKNOWLEDGMENTS

The present study was conducted under project 2011/122, supported by the Research Development Centre of Ataturk University.

REFERENCES

Aghaei Araei, A., Razeghi, H.R., Hashemi Tabatabaei, S., and Ghalandarzadeh, A. (2010) Dynamic properties of gravelly materials. *Transactions A: Civil Engineering*, **17**, 245–261.

Akbulut, S., Arasan, S., and Kalkan, E. (2007) Modification of clayey soils using scrap tire rubber and synthetic fibers. *Applied Clay Science*, **38**, 23–32.

Akbulut, S., Kurt, Z.N., and Arasan, S. (2010) Electrokinetic properties of surfactant modified clays. *International Journal of Civil and Structural Engineering*, **1**, 354– 361

Akbulut, S., Kurt, Z.N., and Arasan, S. (2012) Surfactant modified clays' consistency limits and contact angles. *Earth Sciences Research Journal*, **16**, 13–19.

Akbulut, S., Kurt, Z.N., Arasan, S., and Pekdemir, Y. (2013) Geotechnical properties of some organoclays. *Sadhana*, **38**, 317–329.

Alexandre, M. and Dubois, P. (2000) Polymer-layered silicate nanocomposites: preparation, properties and uses of a new class of materials. *Materials Science and Engineering*, **28**, 1–63.

Ashkezari, G.D., Aghakouchak, A.A., and Kokabi, M. (2008) Design, manufacturing and evaluation of the performance of steel like fiber reinforced elastomeric seismic isolators. *Journal of Materials Processing Technology*, **197**, 140–150.

ASTM D 1557 (2012) Standard Test Method for Laboratory Compaction Characteristics of Soil Using Modified Effort. ASTM, West Conshohocken, Pennsylvania, USA.

ASTM D 4546 (2008) Standard Test Methods for One-Dimensional Swell or Collapse of Cohesive Soils. ASTM, West Conshohocken, Pennsylvania, USA.

ASTM D 6528 (2007) Standard Test Method for Consolidated Undrained Direct Simple Shear Testing of Cohesive Soils. ASTM, West Conshohocken, Pennsylvania, USA.

Barmar, M., Kaffashi, B., and Barikani, M. (2010) Investigating the Uni-HEUR thickener performance considering hydrophilic segment length. *Colloids and Surfaces A: Physicochemical and Engineering Aspects*, **364**, 105–108.

Bate, B. (2010) Engineering behavior of fine-grained soils modified with a controlled organic phase. PhD thesis, Georgia Institute of Technology, Atlanta, USA.

Bate, B. and Burns, S. (2012) Influencing factors on the dynamic properties of organobentonites. Geo-Congress 2012, Oakland, California, USA.

Burmistr, M.V., Sukhyy, K.M., Shilov, V.V., Pissis, P., Spanoudaki, A., Sukha, I.V., Tomilo, V.I., and Gomza, Y.P. (2005) Synthesis, structure, thermal and mechanical properties of nanocomposites based on linear polymers and layered silicates modified by polymeric quaternary ammonium salts (ionenes). *Polymer*, **46**, 12226–12232.

Chaudhari, T.D., Thiagarajan, C., Theethira, P.K., Shuler, S., and Jaarda, E.J. (2005) Energy absorbing articles. *United States Patent Application Publication*, US 2005/0287371 A1.

Chung, D.D.L. (2003) Structural composite materials tailored for damping. *Journal of Alloys and Compounds*, **355**, 216–223.

D'Onofrio, A. and Penna, A. (2003) Small strain behaviour of lime-treated silty sand. Pp. 329–336 in: *Deformation Characteristics of Geomaterials* (H. Di Benedetto, T. Doanh, H. Geoffroy, and C. Sauzeat, editors). Swets & Zeitlinger, Lisse, The Netherlands.

Darendeli, M.B. (2001) Development of a new family of normalized modulus reduction and material damping curves. PhD thesis, Faculty of the Graduate School of The University of Texas at Austin, Texas, USA.

de Carvalho, A.J.F., Curvelo, A.A.S., and Agnelli, J.A.M. (2001) A first insight on composites of thermoplastic starch and kaolin. *Carbohydrate Polymers*, **45**, 189–194.

Dey, P., Maiti, S., and Sa, B. (2012) Locust bean gum and its application in pharmacy and biotechnology: an overwiew. *International Journal of Current Pharmaceutical Research*, **4**, 7–11.

Das, B.M. (1998) *Principles of Geotechnical Engineering*. PWS Publishing Company, Boston, Massachusetts, USA.

Finegan, I.C. and Gibson, R.F. (1999) Recent research on enhancement of damping in polymer composites. *Composite Structures*, **44**, 89–98.

Finegan, I.C. and Gibson, R.F. (2000) Analytical modeling of damping at micromechanical level in polymer composites reinforced with coated fibers. *Composites Science and Technology*, **60**, 1077–1084.

Fischer, H. (2003) Polymer nanocomposites: from fundamental research to specific applications. *Materials Science and Engineering*, **23**, 763–772.

Geocomp, (2007) Cyclic Direct Simple Shear User's Manual: Control and Report Sorftware for Fully Automated Cyclic Direct Simple Shear Tests on ShearTrac-II Systems Using MS-Windows® 2000 or XP Software, Version 5.0, Boxborough, Massachusetts, USA.

Hackman, I. and Hollaway, L. (2006) Epoxy-layered silicate nanocomposites in civil engineering. *Composites*, **37**, 1161–1170.

Hamed, G.R. (2001) Materials and compounds. Pp. 13–34 in: *Engineering with Rubber: How to Design Rubber Components* (A.N. Gent, editor). Carl Hanser, Verlag, Munich, Germany.

Hbaieb, K., Wang, Q.X., Chia, Y.H.J., and Cotterell, B. (2007) Modelling stiffness of polymer/clay nanocomposites. *Polymer*, **48**, 901–909.

He, S.J., Wang, Y.Q., Wu, Y P, Wu X.H., Lu, Y.L., and Zhang, L.Q. (2010) Preparation, structure, performance, industrialisation and application of advanced rubber/clay nanocomposites based on latex compounding method. *Plastics, Rubber and Composites*, **39**, 33–42.

Kilar, V. and Koren, D. (2009) Seismic behaviour of asymmetric base isolated structures with various distributions of isolators. *Engineering Structures*, **31**, 910–921.

Koh, H.C., Park, J.S., Jeong, M.A., Hwang, H.Y., Hong, Y.T., Ha, S.Y., and Nam, S.Y. (2008) Preparation and gas permeation properties of biodegradable polymer/layered silicate nanocomposite membranes. *Desalination*, **233**, 201–209.

Kramer, S.L. (1996) *Geotechnical Earthquake Engineering*. Prentice Hall, New Jersey, USA.

Kumar, S.S., Krishna, A.M., and Dey, A. (2013) Parameters influencing dynamic soil properties: a review treatise. National Conference on Recent Advances in Civil Engineering November, pp. 15–16.

Kurt, Z.N. (2009) Investigation of the strength properties of surfactant modified clay. Master Thesis, Graduate School of Natural and Applied Sciences, Ataturk University, Erzurum, Turkey (Turkish with an English abstract).

Kyminas, S.C., Philips, J.C., and Einhaus, B.J. (1989) Coating for roof surfaces. *United States Patent Documents*, 4.859.723.

Lagaly, G. (1999) Introduction: from clay mineral–polymer interactions to clay mineral–polymer nanocomposites. *Applied Clay Science*, **15**, 1–9.

LeBaron, P.C., Wang, Z., and Pinnavaia, T.J. (1999) Polymer–layered silicate nanocomposites: an overview. *Applied Clay Science*, **15**, 11–29.

Lin, J.T,, Jong, S.J., and Cheng, S. (1993) A new method for preparing microporous titanium pillared clays. *Microporous Materials*, **1**, 287–290.

Liu, P. (2007) Polymer modified clay minerals: A review. *Applied Clay Science*, **38**, 64–76.

Lopes da Silva, J.A., Gonçalves, M.P., and Rao, M.A. (1994) Influence of temperature on the dynamic and steady-shear rheology of pectin dispersions. *Carbohydrate Polymers*, **23**, 77–87.

Ludwigson, M.N., Swan, C.C., and Lakes, R.S. (2002) Damping and stiffness of particulate SiC–InSn composite. *Journal of Composite Materials*, **35**, 1–10.

Maier, M., Anderson, M., Karl, C., and Magnuson, K. (1993) Guar, locust bean, tara, and fenugreek gums. Pp. 205–213 in: *Industrial Gums: Polysaccharides and their Derivatives* (3rd edition) (R.L. Whistley and J.N. BeMiller, editors). Academic Press, New York.

Majedi, P. (2013) Examination of some geotechnical and dynamic properties of hydrophobic clay that mixed by polymer. Masters thesis, Graduate School of Natural and Applied Sciences, Ataturk University, Erzurum, Turkey (Turkish with English abstract).

Mishra, A.K., Bose, S., Kuila, T., Kim, N.H., and Lee, J.H. (2012) Silicate-based polymer-nanocomposite membranes for polymer electrolyte membrane fuel cells. *Progress in Polymer Science*, **37**, 842– 869.

Mittal, V. (2009) Polymer layered silicate nanocomposites: a review. *Materials*, **2**, 992–1057.

Mohan, T.P. and Kanny, K. (2011) Water barrier properties of nanoclay filled sisal fibre reinforced epoxy composites. *Composites*, **42**, 385–393.

Moon, B.Y., Kang, G.J., Kang, B.S., and Kelly, J.M. (2002) Design and manufacturing of fiber reinforced elastomeric isolator for seismic isolation. *Journal of Materials Processing Technology*, **130-131**, 145–150.

Murphy, R.E.J., Haemer, L.F., and Scholl, E.C. (1977) Method for installing surface covering or the like. *United States Patent Documents*, 4.036.673.

Nakhaei, A., Marandi, S.M., Sani Kermani, S., and Bagheripour, M.H. (2012) Dynamic properties of granular soils mixed with granulated rubber. *Soil Dynamics and Earthquake Engineering*, **43**, 124–132.

Paiva, L.B., Morales, A.N., and Diaz, F.R.V. (2008) Organoclays: Properties, preparation and applications. *Applied Clay Science*, **42**, 8–24.

Pavlidou, S. and Papaspyrides, C.D. (2008) A review on polymer-layered silicate nanocomposites. *Progress in Polymer Science*, **33**, 1119–1198.

Petersson, L. and Oksman, K. (2006) Biopolymer based nanocomposites: comparing layered silicates and microcrystalline cellulose as nanoreinforcement. *Composites Science and Technology*, **66**, 2187–2196.

Ray, S.S. and Okamoto, M. (2003) Polymer/layered silicate nanocomposites: a review from preparation to processing. *Progress in Polymer Science*, **28**, 1539–1641.

Rhim, J.W. (2011) Effect of clay contents on mechanical and water vapor barrier properties of agar-based nanocomposite films. *Carbohydrate Polymers*, **86**, 691–699.

Rivin, E.I. (2007) Use of stiffness/damping/natural frequency criteria in vibration control. IFToMM World Congress Besanson, June 2–6.

Schadler, L.S. (2003) Polymer-based and polymer-filled nanocomposites. Pp. 77–153 in: *Nanocomposite Science and Technology* (P.M. Ajayan, L.S. Schadler, and P.V. Braun, editors). Wiley-VCH Verlag GmbH & Co. KGaA, Weinheim, Germany.

Tang, X., Alavi, S., and Herald, T.J. (2008) Effects of plasticizers on the structure and properties of starch-clay nanocomposite films. *Carbohydrate Polymers*, **74**, 552–558.

Tanniru, M., Yuan, Q., and Misra, R.D.K. (2006) On significant retention of impact strength in clay-reinforced high-density polyethylene (HDPE) nanocomposites. *Polymer*, **47**, 2133–2146.

Tjong, S.C. (2006) Structural and mechanical properties of polymer nanocomposites. *Materials Science and Engineering*, **53**, 73–197.

Winkworth-Smith, C. and Foster, T.J. (2013) *General Overview of Biopolymers: Structure, Properties, and Applications. Handbook of Biopolymer-Based Materials From Blends and Composites to Gels and Complex Networks* (S. Thomas, D. Durand, C. Chassenieux, and P. Jyotishkumar, editors). Wiley-VHC Verlag GmbH&Co. KgaA, Weinheim, Germany.

Xu, Q., Pang, M., Zhu, L., Zhang, Y., and Feng, S. (2010) Mechanical properties of silicone rubber composed of diverse vinyl content silicone gums blending. *Materials and Design*, **31**, 4083–4087.

Yasmin, A., Luo, J.J., and Daniel, I.M. (2006) Mechanical and thermal behavior of clay/epoxy nanocomposites. *Composites Science and Technology*, **66**, 2415–2422.

Zare-Shahabadi, A., Shokuhfar, A., Ebrahimi-Nejad, S., Arjmand, M., and Termeh, M. (2011) Modeling the stiffness of polymer/layered silicate nanocomposites: More accurate predictions with consideration of exfoliation ratio as a function of filler content. *Polymer Testing*, **30**, 408–414.

Zhang, J., Andrus, R.D., and Juang, C.H. (2005) Normalized shear modulus and material damping ratio relationships. *Journal of Geotechnical and Geoenvironmental Engineering*, 453–464.

Zhu, L. and Wool, R.P. (2006) Nanoclay reinforced bio-based elastomers: Synthesis and characterization. *Polymer*, **47**, 8106–8115.

(*Received 20 March 2013; revised 20 August 2014; Ms. 857; AE: D.P. Jaisi*)

Clays and Clay Minerals, Vol. 62, No. 4, 324–335, 2014.

MINERALOGICAL CHARACTERIZATION OF Ni-BEARING SMECTITES FROM NIQUELÂNDIA, BRAZIL

ELIANA SATIKO MANO[1,*], LAURENT CANER[2], SABINE PETIT[2], ARTHUR PINTO CHAVES[1], AND ANDRÉ SAMPAIO MEXIAS[3]

[1] Escola Politécnica, Universidade de São Paulo. Av. Prof. Mello Moraes 2.373, 05508-900, São Paulo, Brazil
[2] Université de Poitiers, CNRS IC2MP-HydrASA UMR 7285, Poitiers, France
[3] Universidade Federal do Rio Grande do Sul, Instituto de Geociências, UFRGS, Campus do Vale Av. Bento Gonçalves, 9500 - Porto Alegre - RS - Brazil

Abstract—Nickel-lateritic ore is the most common source of nickel in Brazil. The Niquelândia deposit, located in State of Goias, is one of the most famous deposits due to the large amounts of nickel associated with both oxidized and mainly silicated ores. The terms oxidized and silicated ores are used to specify two different ores formed exclusively by oxides and silicate (clay) minerals, respectively. The aim of the present study was to characterize thoroughly the silicated ore to identify the Ni-bearing clay minerals and their crystal chemistry in support of developing a better mineral-processing method or optimizing the current one to improve Ni recoveries. X-ray diffraction, chemical analyses, scanning electron microscopy, and Fourier transform infrared (FTIR) spectroscopy demonstrated that nickel is associated with Ni-rich stevensite and to a lesser extent with Fe-rich montmorillonite. The crystal chemistry performed by FTIR spectroscopy revealed that Ni is present in the octahedral positions, substituting for Mg or Fe, which results in significant chemical and layer-charge heterogeneity in the samples. This heterogeneity seems to be responsible for reduction in Ni recoveries during the hydrometallurgical process.

Key Words—Clay Minerals, Crystal Chemistry, Fe-montmorillonite, Nickel, Smectite, Stevensite.

INTRODUCTION

Nickel is important as a metal or as an alloying element in steels because of its low rate of oxidation and consequent resistance to corrosion. In nature, Ni is associated with sulfides and lateritic deposits. According to Dalvi *et al.* (2004), 70% of nickel worldwide is contained in lateritic deposits, and production of Ni-laterites increased from 140 kt/year to 1200 kt/year between 1950 and 2003. For this reason, extensive research into Ni-bearing clay minerals has been carried out. Nickel is associated with a wide variety of clay minerals such as serpentine, talc/kerolite/pimelite, and smectite.

Nickel exhibits a specific geochemical affinity for mantle-derived (mafic and ultramafic) rocks (Christidis and Mitsis, 2006). Mafic and ultramafic intrusions were responsible for the formation of the Niquelândia ultrabasic massif during the Archean period (Marini *et al.*, 1984). The combination of relief and seasonal alternations of large and small amounts of precipitation led to intense weathering of dunites, peridotites, and pyroxenites and to the formation of clay minerals.

Previous mineral characterization studies conducted at Niquelândia have indicated that the nickel is associated with a mixture of di- and trioctahedral smectites and talc (Bosio *et al.*, 1975; Brindley and de Souza, 1975; de Souza *et al.*, 1978; Colin *et al.*, 1985, 1990; Decarreau *et al.*, 1987; Oliveira, 1990; Coelho *et al.*, 2000; Raous *et al.*, 2013). Ni-bearing smectite is one of the secondary phases formed during low-temperature weathering processes of ultrabasic rocks – these smectites contain Fe^{3+} as the main octahedral cation with small amounts of Ni, ~<0.4 atoms per half formula unit (p.h.f.u.) (Bosio *et al.*, 1975; Gaudin *et al.*, 2004a). Nickel grades were observed to vary from 10 to 84% of occupancy in the octahedral sites of trioctahedral smectites in Niquelândia (Colin *et al.*, 1990). A Ni-rich stevensite has also been reported from Othrys, Greece (Christidis and Mitsis, 2006). The complex crystal chemistry of the clay minerals in Niquelândia may be the cause of significant variability in the ores which affects the recovery rates of Ni from the hydrometallurgical process. In the present study, the clay minerals in the silicated ore were characterized, focusing on the Ni-stevensite and Fe/Ni-montmorillonite. A detailed characterization of the Ni-bearing clay minerals in the samples, including the variability in the silicated ores, will help us to understand smectite formation and will provide pathways for improving Ni recovery from the hydrometallurgical process.

MATERIALS AND METHODS

The Niquelândia deposit is located in the State of Goias, central Brazil (Figure 1). The relief seen at Niquelândia reveals dunites and peridotites making up an old plateau covered by silcrete; pyroxenites are found in valley regions. Different parent rocks are responsible for different grades (high, intermediate, and low) of Ni in the silicated ore. In order to characterize these three

---

* E-mail address of corresponding author:
elli_mano@hotmail.com
DOI: 10.1346/CCMN.2014.0620406

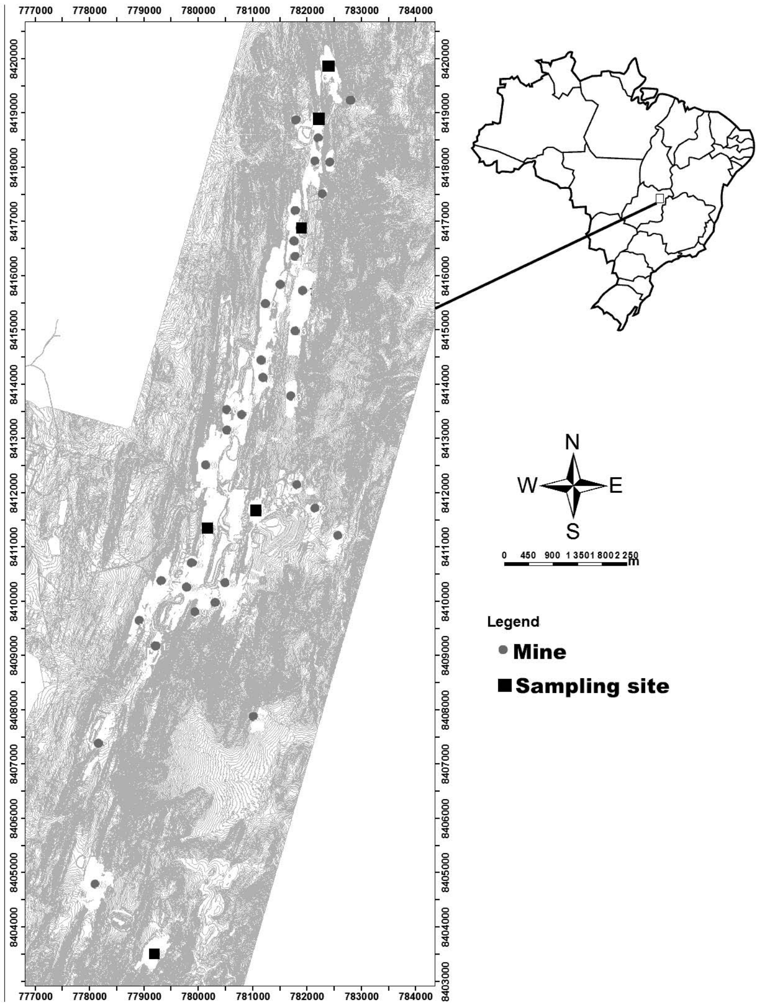

Figure 1. Topographic and sampling-site map of Niquelândia, Brazil (image courtesy of Votorantim Metais Níquel).

silicated ore types, seven samples were collected throughout the deposit (Figure 1). Chemical analyses of the bulk samples were performed using inductively coupled plasma-atomic emission spectroscopy (ICP-AES) for the main elements (Mg, Si, Fe, Ni, Al, Cu, Co, Mn, and Cr) and confirmed the broad chemical variability, especially for NiO and Fe_2O_3. Loss on ignition (LOI) was also measured.

Sample AS-ANi3 represents a partially altered peridotite with large amounts of NiO (lowermost part of the weathering profile). Sample ASL-I5 corresponds to the intensely altered part of the profile (uppermost), near the oxidized zone, which results in large Fe_2O_3 contents. Samples from peridotites located near quartz veins, such as AS-BNi2, contain low grades of NiO. The other samples have intermediate amounts of Ni and Fe, varying according to their location in the weathering profile.

In order to identify the clay minerals, the <2 μm fraction was extracted from each of the bulk samples. Initially, the samples were dispersed in distilled water. The fine fractions (<50 μm) were separated from coarse material (>50 μm) by wet sieving. The coarse fractions were discarded. The fine fractions (<50 μm) were saturated with 1 mol L^{-1} NaCl (Moore and Reynolds, 1989) to deflocculate the particles. The clay fraction (<2 μm) was obtained by centrifugation (according to Stokes' law). A proportion of the <2 μm fraction of each sample was subsequently flocculated and saturated with 0.5 mol L^{-1} $CaCl_2$. Ca-saturated clay fractions were washed with distilled water to remove excess salts. The remainder was kept in suspension for extraction of <0.1 μm fractions.

Oriented preparations of Ca-saturated <2 μm fractions were obtained by depositing clay suspensions on glass slides which were dried at room temperature (air-dried: AD) and also saturated with ethylene glycol (EG) vapor at 50ºC for 16 h.

In order to distinguish high- from low-charge smectites, the Ca/K/Ca sequence of saturation was carried out

(Calarge *et al.*, 2003). First, the samples were saturated with 0.5 mol L^{-1} $CaCl_2$, followed by 1 mol L^{-1} KCl; then, a further Ca saturation step was performed. Ultimately, the samples were washed to eliminate the excess salts. Smectites with high tetrahedral charge remained collapsed at ~10 Å in AD and EG states, whereas smectites with low tetrahedral charge re-expanded to ~15 Å in AD and ~16–17 Å in EG states, once Ca replaced K in the last saturation step. For samples AS-ANi3, VSL-R2, and ASL-AN3, the <0.1 µm fractions were obtained by repeated centrifugation cycles until the supernatant became clear. Later, the fractions were Ca-saturated and prepared using the same procedure as adopted for the <2 µm fractions.

Lithium saturations were performed to characterize the octahedral (Oc) and tetrahedral (Te) locations of the charge (*e.g.* Hofmann and Klemen, 1950). Samples were saturated with 1 mol L^{-1} LiCl and washed with ethanol to remove the excess salts; they were then heated overnight at 300ºC. The first step involved a complete exchange of the interlayer cations by Li^+ and the second step involved migration of the Li^+ to the octahedral vacancies of the dioctahedral smectites and, consequently, neutralization of the octahedral layer charge. The swelling properties of the clays are affected in different ways, depending on the layer charge and on the location of the charge. According to Petit *et al.* (2002) and Gaudin *et al.* (2004a), layers having tetrahedral charge of <0.18 per half unit cell do not swell following the Hofmann-Klemen (HK) treatment and EG solvation, whereas layers with tetrahedral charge >0.18 per half unit cell are expandable. For trioctahedral smectites with octahedral charge, Li-saturation followed by heating (HK treatment) results in only partial neutralization and compensates approximately half of the charge (Li^+ *vs.* Mg^{2+} or Ni^{2+}) and the layers remain expandable (Petit *et al.*, 2008).

X-ray diffraction (XRD) patterns for oriented preparations were recorded using a Bruker D8 Advance diffractometer (CuKα radiation, 40 kV, 40 mA, Lynxeye detector) from 2.5 to 35º2θ in 0.012º2θ steps and a counting time per step of 96 s. The XRD patterns were obtained from oriented Ca-saturated clay in AD and EG states, oriented Ca/K/Ca saturations in AD and EG states, and after Li-saturated preparation, in AD and EG states, heated overnight at 300ºC ($Li_{300}H$) and followed by solvation with EG ($Li_{300}H$ EG).

The $d_{06\text{-}33}$ on randomly oriented powders of <2 µm fractions were used to distinguish between di- and trioctahedral clay minerals. The samples were prepared using the back-loading procedure (Moore and Reynolds, 1989). Powder XRD patterns were obtained by scanning from 57 to 63º2θ in 0.02º2θ steps at 96 s/step. The *HighScore Plus*® software (PANanalytical/Spectris, Netherlands) was used to analyze the patterns.

Microanalyses were performed by EDX (energy dispersive X-ray spectroscopy) (INCA, Oxford, UK) using 20 kV with SDD (silicon drift detector), coupled to a scanning electron microscope (SEM) (LEO-Stereoscan 440 from Leica). A JEOL JSM-5600LV coupled to a BRUKER X-Flash 4010 EDS spectrometer was also used to analyze the <2 µm powders. The EDX microanalyses of the clay particles were plotted on ternary diagrams to compare the different smectite compositions.

Fourier-transform infrared (FTIR) spectroscopy was used to constrain the crystal chemistry of the Fe-Ni smectites studied as well as to further refine the layer-charge distribution using ammonium saturations (Petit *et al.*, 1998). Mid-infrared (MIR) analyses were performed using a Nicolet Magna-IR 760 spectrometer in the 400–4000 cm^{-1} range with a 2 cm^{-1} resolution. The spectra were obtained from pressed KBr pellets, prepared by mixing 1 mg of sample with 150 mg of KBr and pressing at 10 t cm^{-2} and drying overnight at 110ºC. Near-infrared (NIR) spectra from 4000 to 10,000 cm^{-1} were obtained at a resolution of 4 cm^{-1} on powder in glass vial, using a Thermo Scientific Integrating Sphere (diffuse reflectance) with an internal InGaAs detector coupled to a Thermo Scientific Nicolet 6700 FTIR spectrometer.

Before and after Li treatment, the samples were saturated with 1 mol L^{-1} NH_4Cl five times and washed with ethanol until free of NH_4 salts. This procedure was performed to quantify the amounts of NH_4^+ in the NH_4-saturated smectites. The detailed procedure was given by Petit *et al.* (1998, 2006). The NH_4^+ fixed by the bulk smectites corresponds to the total layer charge (permanent Te + Oc + variable edge charges), *i.e.* the cation exchange capacity (CEC) (at the pH of the NH_4Cl solution). After Li saturation and heating for 16 h at 300ºC (Hofmann-Klemen treatment), the amount of NH_4^+ adsorbed corresponds to the remaining charge after neutralization by Li fixation. As a result, the difference between them was attributed to the neutralized charge by the Li treatment, *i.e.* the octahedral charge for the dioctahedral smectites (montmorillonites) and half of the octahedral charge for the trioctahedral smectites (stevensite) as described by Petit *et al.* (2008). The IR spectra of NH_4^+-saturated samples (NH_4^+ and $Li_{300}NH_4$) were recorded using the same amount of clay and they were normalized to the main SiO band around 1020 cm^{-1} using *Omnic*® software (Thermo Fisher Scientific Inc, United States) as the samples contain both dioctahedral and trioctahedral smectites and are devoid of quartz. The integrated intensity of the NH_4 deformation (υ_4NH_4) band at 1400 cm^{-1} was measured before and after Li treatment (area: ANH_4; range 1353–1500 cm^{-1}) in arbitrary units using the *Omnic*® software. The surface area of the υNH_4 band (after normalization) was correlated to the CEC of the sample (Petit *et al.*, 1998, 2002, 2008; Gaudin *et al.*, 2005). The ratio of the integrated intensity of $ALi_{300}NH_4/ANH_4$ corresponded to the percentage of the charge remaining after Li treatment.

Table 1. Chemical composition (wt.%) determined using ICP-AES, for all samples.

Samples	NiO	Fe_2O_3	Al_2O_3	MgO	SiO_2	Cr_2O_3	LOI
AS-BNi2	2.11	17.7	3.95	4.87	51.0		8.45
AS-ANi3	23.4	5.23	2.45	7.44	39.9		6.82
ASL-I5	1.16	32.4	4.76	5.07	44.6	1.96	6.68
VSL1A	9.60	10.9	8.52	7.45	44.1	2.39	7.91
VSL-R2	4.74	10.1	3.93	19.1	35.1	1.08	3.71
ASL-AN3	7.75	13.4	5.07	12.4	40.1	1.33	5.53
CSL-G8	2.08	15.3	5.07	10.5	50.7	1.39	

RESULTS

Chemical analyses

The chemical compositions (main elements) of the bulk samples are shown in Table 1. Samples with abundant SiO_2 and LOI between 6 and 8 wt.% suggest the presence of clay minerals. High abundances of NiO (23.4%) for sample AS-ANi3 and Fe_2O_3 (32.4%) for sample ASL-I5 were measured. The samples VSL-R2 and ASL-AN3 contained 4.7 and 7.7% of NiO and 19.1% and 12.4% of MgO, respectively. The sample VSL1A had similar amounts of NiO and Fe_2O_3 (10−11%) and the largest Al_2O_3 content (8.5%). Finally, AS-BNi2 and CSL-G8 contained 17.7 and 15.3% Fe_2O_3, respectively, and a small amount of NiO and Al_2O_3 ($\leqslant$5%). Sample AS-BNi2 contained <5% MgO, whereas CSL-G8 had 10.5% MgO.

X-ray diffraction

The XRD patterns of the Ca-saturated clay fraction of the different samples were similar and showed a main peak at $d_{001\text{AD}} \approx 15$Å that expanded to $d_{001} \approx 16.5$ Å following the EG solvation (Figure 2). The peak at 8.3 Å was attributed to the 002 reflection of glycolated smectite. The peaks in the AD and EG states were symmetrical and the samples exhibited uniform swelling, supporting the presence of pure smectite layers and the absence of mixed layers with swelling and non-swelling layers in the different samples.

Powder XRD patterns exhibited asymmetrical *hk* reflections that are characteristic of turbostratic stacking of layers typical of smectites. The samples AS-BNi2, ASL-AN3, ASL-I5, CSL-G8, and VSL1A revealed $d_{06\text{-}33}$ values which varied from 1.50 to 1.51 Å (Figure 3) indicating that they consist essentially of dioctahedral Fe-rich smectites as described, for example, by Desprairies (1983), Petit *et al.* (1992), and Gaudin *et al.* (2004a, 2004b). The samples VSL-R2 and AS-ANi3 exhibited a large $d_{06\text{-}33}$ peak (Figure 3) probably due to the possible overlapping of different smaller peaks that hinder the identification of the di- or trioctahedral

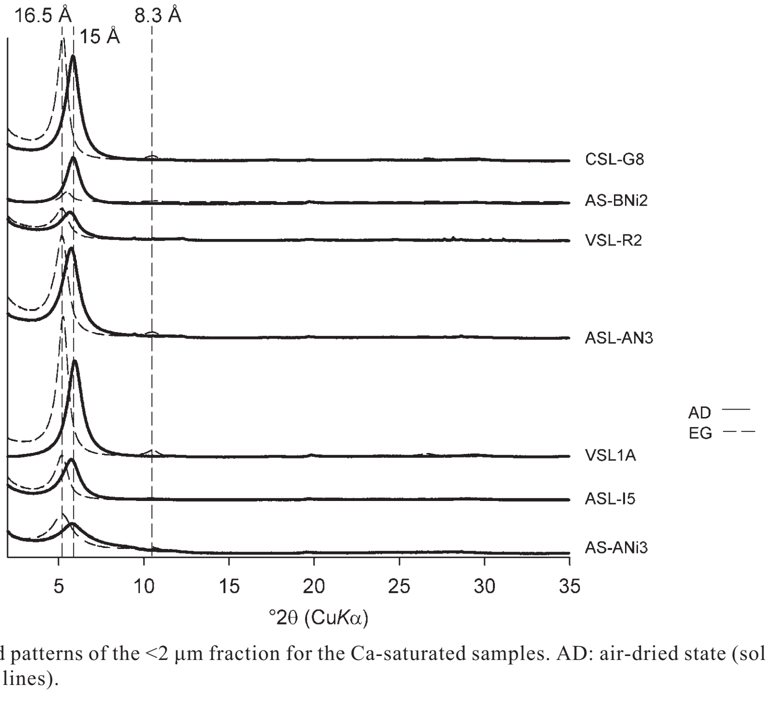

Figure 2. XRD oriented patterns of the <2 μm fraction for the Ca-saturated samples. AD: air-dried state (solid lines); EG: ethylene glycol-treated (dashed lines).

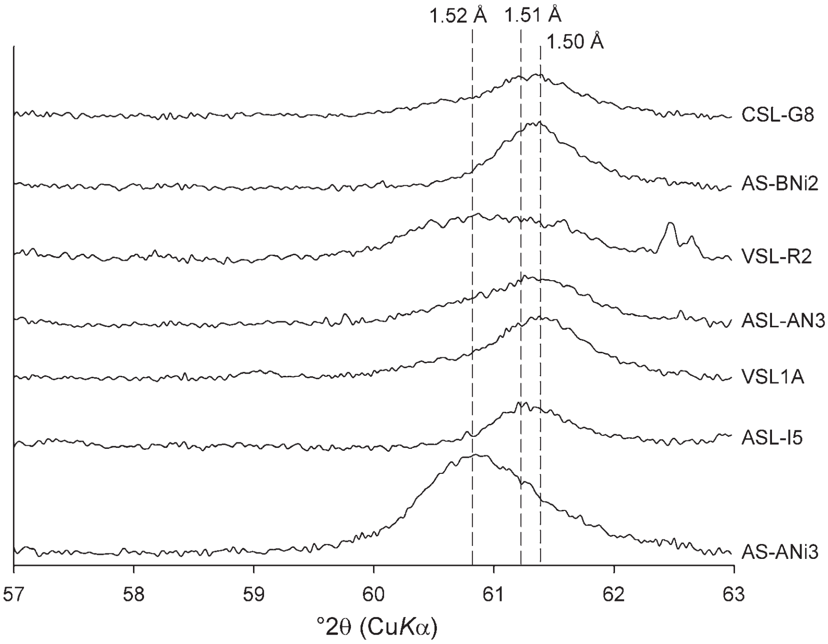

Figure 3. $d_{06\text{-}33}$ reflections. VSL-R2 presents a large $d_{06\text{-}33}$ peak attributed to mixtures of di- and trioctahedral smectites. AS-ANi3 consists essentially of trioctahedral smectites, whereas ASL-I5 consists of entirely of dioctahedral smectites.

character. Sample AS-ANi3 ($d_{06\text{-}33}$ = 1.52 Å), however, appeared to belong to the trioctahedral type, whereas VSL-R2 showed a mix of di- and trioctahedral mineral characteristics.

Following K^+ saturation, all the samples collapsed from 10.8–12.4 Å (AD) to 9.5–9.9 Å after heating at 550ºC (patterns not shown). The XRD patterns for Ca/K/Ca samples were very close to those of the Ca-saturated samples (not shown) suggesting a rather small tetrahedral charge of the layers for all of the samples, as K is replaced by Ca in the third saturation step.

The layer-charge distribution was determined by the HK procedure (Figure 4). The XRD patterns after HK treatment indicated a collapse of the layers between 9.3 and 9.6 Å. Following EG solvation, the 001 and 002 reflections broadened and the d_{001} values varied between 16 and 16.7 Å for different samples. For samples VSL-R2 and CSL-G8, HK swelling was almost complete for all layers after EG solvation. For most of the samples, however, the different d spacings and non-harmonic d_{001} and d_{002} values indicated different swelling behaviors that are related to the presence of HK-swelling and HK-non-swelling layers (random mixed layers). The smectites from Niquelândia have a heterogeneous layer-charge distribution, therefore, within the same population and between different samples, making it difficult to

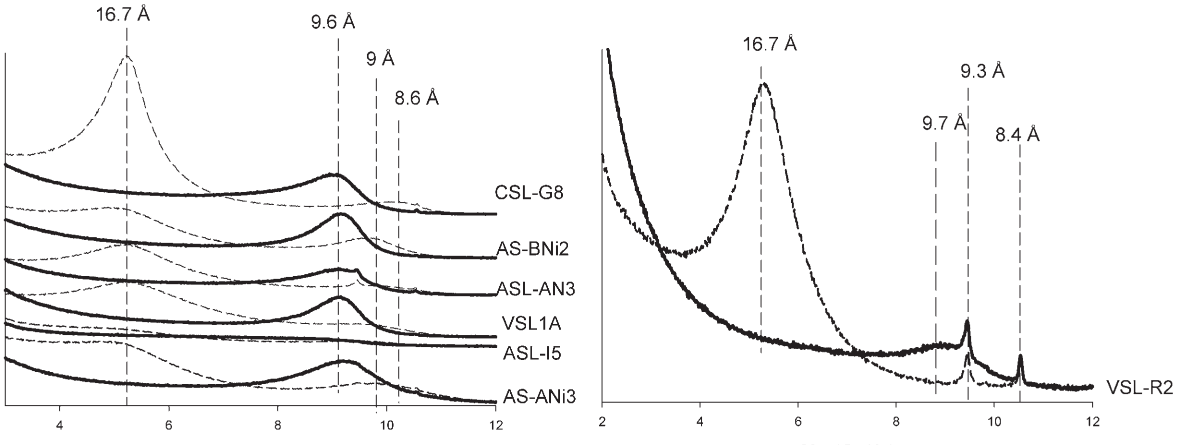

Figure 4. XRD patterns of samples after Hofmann-Klemen treatment. The solid lines correspond to $Li_{300}H$ and the dashed lines to $Li_{300}HEG$ samples, respectively.

further refine the distribution of the layer charge from these XRD measurements.

Infrared results

Three categories of samples were differentiated by MIR spectroscopy: dioctahedral samples (ASL-I5, CSL-G8, and AS-BNi2 – Group A), trioctahedral samples (AS-ANi3 – Group B) and a mixture of these two types (VSL-R2, ASL-AN3, and VSL1A – Group C).

Dioctahedral samples ASL-I5, CSL-G8, and AS-BNi2 (Group A) consist mainly of dioctahedral smectites with a small amount of trioctahedral clays. In the OH-bending region, the bands at 820 cm^{-1} and at ~765 cm^{-1} (Figure 5) were assigned to δFe^{3+}Fe^{3+}OH and to δFe^{3+}MgOH (and/or maybe δFe^{3+}NiOH), respectively, and the band at 870 cm^{-1} was attributed to δAlFe^{3+}OH (Farmer, 1974; Petit *et al.*, 2002; Bishop *et al.*, 2002; Gaudin *et al.*, 2004a, 2004b, 2005).

In the OH-stretching region (Figure 5), the wide band at ~3555 cm^{-1} was attributed to υFe^{3+}Fe^{3+}OH superimposed on the υFe^{3+}MgOH band at 3575 cm^{-1} (Farmer, 1974; Wilson, 1994; Petit *et al.*, 2002; Petit, 2005; Gaudin *et al.*, 2004a, 2004b, 2005; Gates, 2005; Decarreau *et al.*, 2008; Andrieux and Petit, 2010). These features are characteristic of Fe-rich montmorillonites with Mg (and/or probably Ni) in the octahedral sites and indicate that Fe, Mg (and/or probably Ni) may occur in adjacent octahedral sites responsible for the heterogeneity of the samples. The IR spectra of Niquelândia dioctahedral smectite (ASL-I5, CSL-G8, AS-BNi2 – Figure 5) are very similar to the Fe-montmorillonite characterized in weathered ultrabasic nodules in Ölberg, Germany (Köster *et al.*, 1999; Petit *et al.*, 2002) or in pyrite-bearing calcareous sediments in the Costa Rica margin (Gaudin *et al.*, 2005).

Trioctahedral sample AS-ANi3 (Group B) consists mainly of trioctahedral Ni-smectites. Bands at 3624 cm^{-1} and 710 cm^{-1} (Figure 5) were assigned to νNi$_3$OH and δNi$_3$OH, respectively, as described for kerolite and talc (Wilkins and Ito, 1967; Farmer, 1974; Gerard and Herbillon, 1983; Petit, 2005; Christidis and Mitsis, 2006). This is in agreement with the large Ni content determined by chemical analysis.

Samples VSL-R2, ASL-AN3, and VSL1A (Group C) correspond to the mixture of dioctahedral and trioctahedral smectites described above and thus showed the characteristic bands of both smectite groups.

The NIR spectra corroborated the MIR results. A narrow band at 7185 cm^{-1} (Figure 6) was assigned to the 2υMg$_3$-OH vibration of talc (Petit *et al.*, 2004; Petit, 2005; Madejová *et al.*, 2011), for samples AS-ANi3 and VSL-R2.

Layer-charge reduction by Li treatment

The IR spectra of all samples (but to a lesser extent in sample AS-ANi3) are affected by the HK treatment (Figures 7, 8).

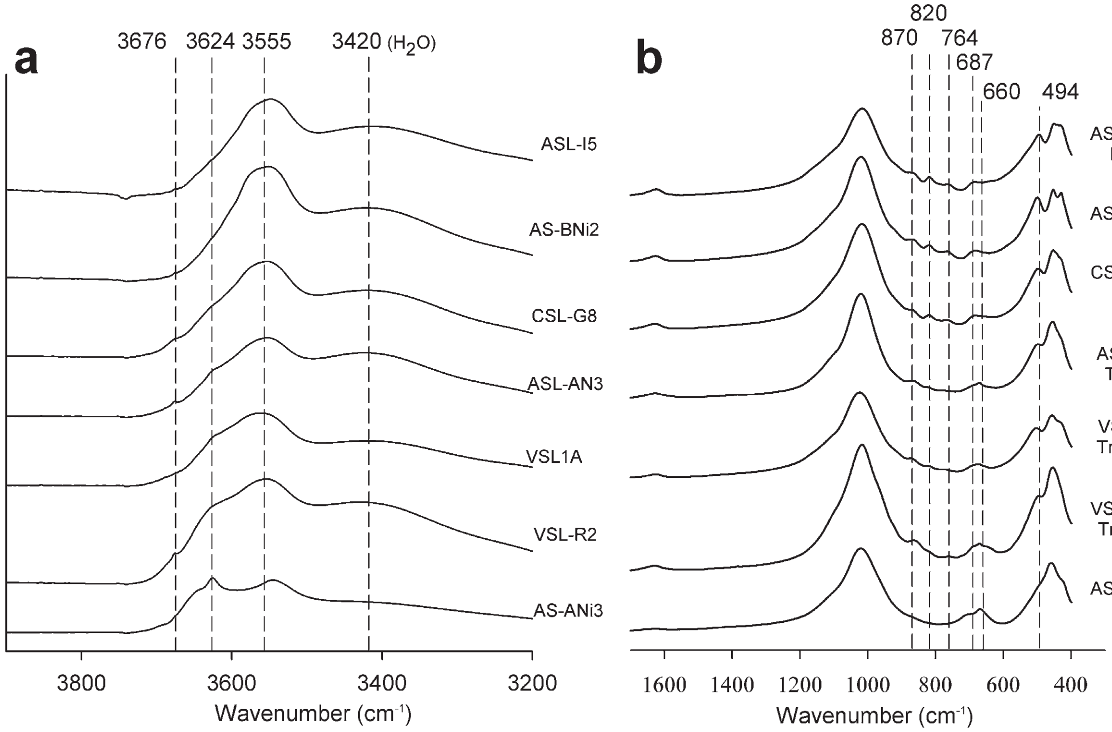

Figure 5. MIR spectra of all samples: VSL1A, ASL-AN3, VSL-R, AS-ANi3, AS-BNi2, CSL-G8, and ASL-I5. (a) The Ni-rich trioctahedral smectites present bands at 3624 cm^{-1} attributed to υNi$_3$OH. (b) The Fe-rich smectites present bands at 870 and 820 cm^{-1}, related to δAlFe^{3+}OH and δFe^{3+}Fe^{3+}OH, respectively.

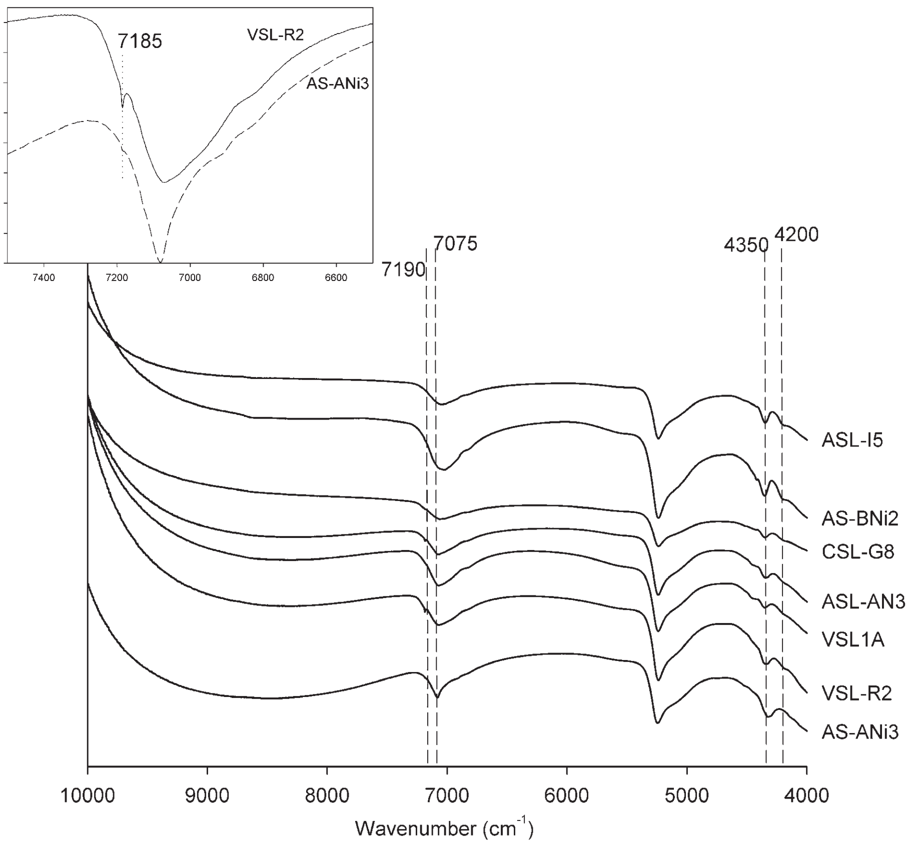

Figure 6. NIR spectra of samples VSL-R2, ASL-AN3, AS-ANi3, AS-BNi2, CSL-G8, VSL1A, and ASL-I5. The characteristic band for talc, at 7185 cm^{-1}, is noted.

For the dioctahedral samples, the structural changes after Li treatment were similar to those described for the Ölberg sample (Petit *et al.*, 2002). In the OH-stretching region, the bands at 3675 cm^{-1}, 3645 cm^{-1}, and the shoulder at ~3600 cm^{-1} were observed after Li saturation (Figure 6). They were attributed to

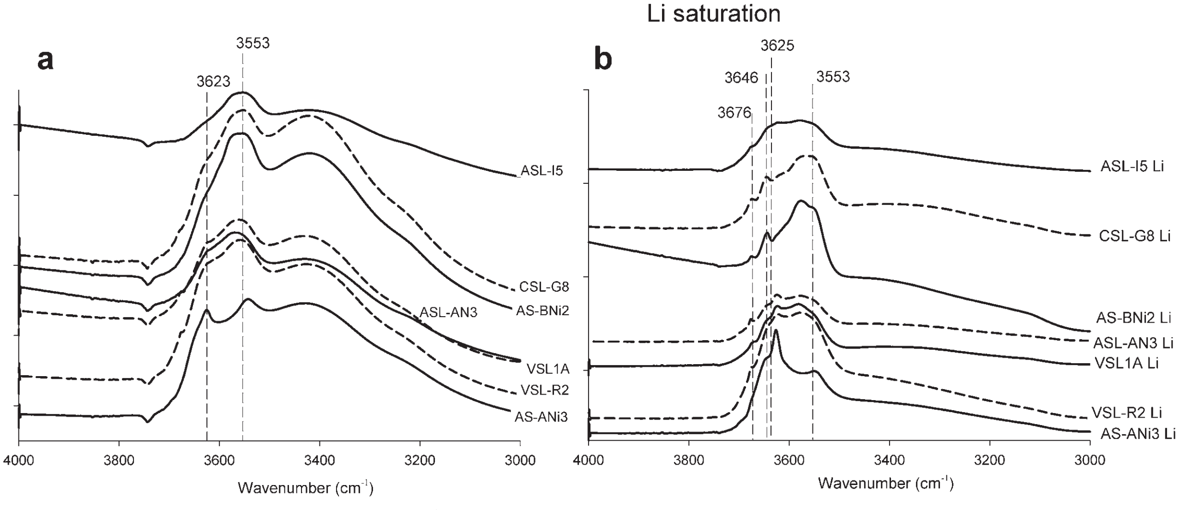

Figure 7. MIR spectra (range: 3000–4000 cm^{-1}) of bulk samples (a) and after HK treatment (b) for samples VLS1A, ASL-AN3, VSL-R2, AS-ANi3, AS-BNi2, CSL-G8, and ASL-I5. New bands were observed after Li treatment (3675 cm^{-1}, 3645 cm^{-1}, and a shoulder at 3600 cm^{-1}).

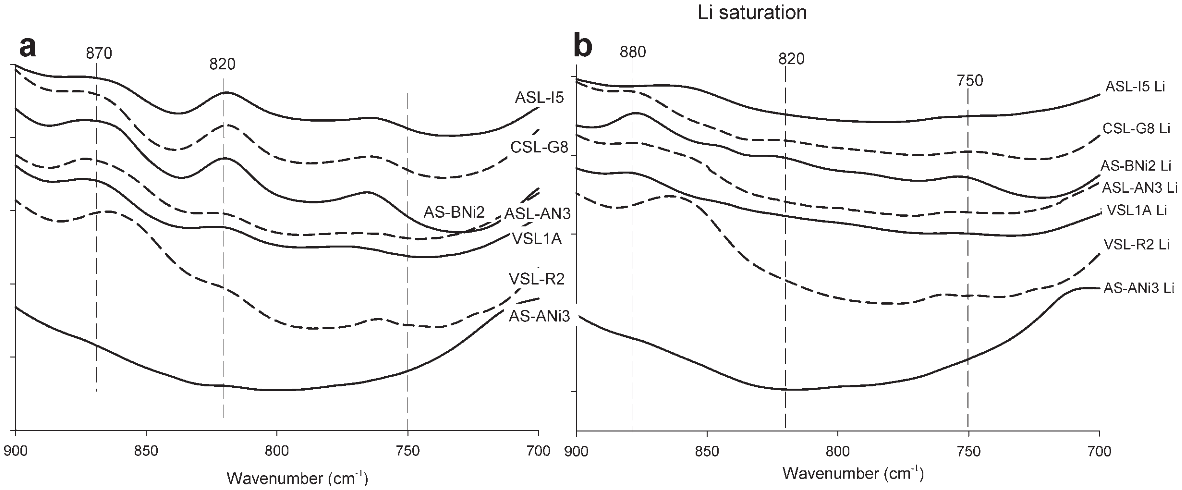

Figure 8. MIR spectra (range: 1000–400 cm^{-1}) of bulk samples (a) and after HK treatment (b) for samples VSL1A, ASL-AN3, VSL-R2, AS-ANi3, AS-BNi2, CSL-G8, and ASL-I5.

$\upsilon\mathrm{Li}R^{2+}\mathrm{OH}$ vibrations (R being Mg^{2+}, Fe^{3+} or Ni^{2+}) by Petit *et al.* (2002) and Gaudin *et al.* (2005). In addition, the intensity of the band at 3555 cm^{-1} decreased. In the OH-bending region, structural changes were also observed (Figure 8). After Li treatment, the $\delta\mathrm{AlFe}^{3+}\mathrm{OH}$ band at 870 cm^{-1} shifted to 880 cm^{-1}, the intensity of the band at 820 cm^{-1} ($\delta\mathrm{Fe}^{3+}\mathrm{Fe}^{3+}\mathrm{OH}$) decreased, and a band appeared at 750 cm^{-1} (AS-BNi2Li). The latter band is attributed to the trioctahedral domains created by the migration of Li into the vacant sites (Petit *et al.*, 2002).

For the trioctahedral samples, the changes in IR spectra after Li treatment were more subtle as observed by Petit *et al.* (2008) for synthetic Zn-stevensite.

The decrease in layer charge after Li treatment was obtained from the decrease in the integrated intensity of the $\upsilon_4\mathrm{NH}_4$ band at 1400 cm^{-1} (Figure 9, Table 2) showing about half of the CEC (44% for VSL-R2 and 63% for CSL-G8) determined for the <2 μm fraction of all the samples. For dioctahedral smectites, the remaining charge not neutralized by Li^+ was attributed to tetrahedral plus variable charges. For trioctahedral smectites (*e.g.* AS-ANi3), the remaining charge was ~50% of the total layer charge, consistent with the 50% neutralization of the octahedral charge by Li^+ in the stevensite structure ($[\mathrm{NH}_4]_{2x}\mathrm{Si}_4[\mathrm{Mg, Ni}]_{3-x}\square_x\mathrm{O}_{10}[\mathrm{OH}]_2 \rightarrow [\mathrm{NH}_4]_x\mathrm{Si}_4[\mathrm{Mg, Ni}]_{3-x}\langle\mathrm{Li}\rangle_x\mathrm{O}_{10}[\mathrm{OH}]_2$; □ being a vacancy), as described by Petit *et al.* (2008) for synthetic Zn-stevensite.

The CEC values for samples ASL-I5 and AS-ANi3, measured independently using the ammonium acetate method, were 81 and 41 meq/100 g, respectively. Using these values and integrated intensities of the 1400 cm^{-1} band of the NH_4-saturated samples, the CEC of the other samples was estimated (Petit *et al.*, 1998). The CEC of the <2 μm fractions ranged from 41 (AS-ANi3) to 100 meq/100 g (AS-BNi2) (Table 2). The <2 μm and <0.1 μm fractions of sample AS-ANi3 revealed the same

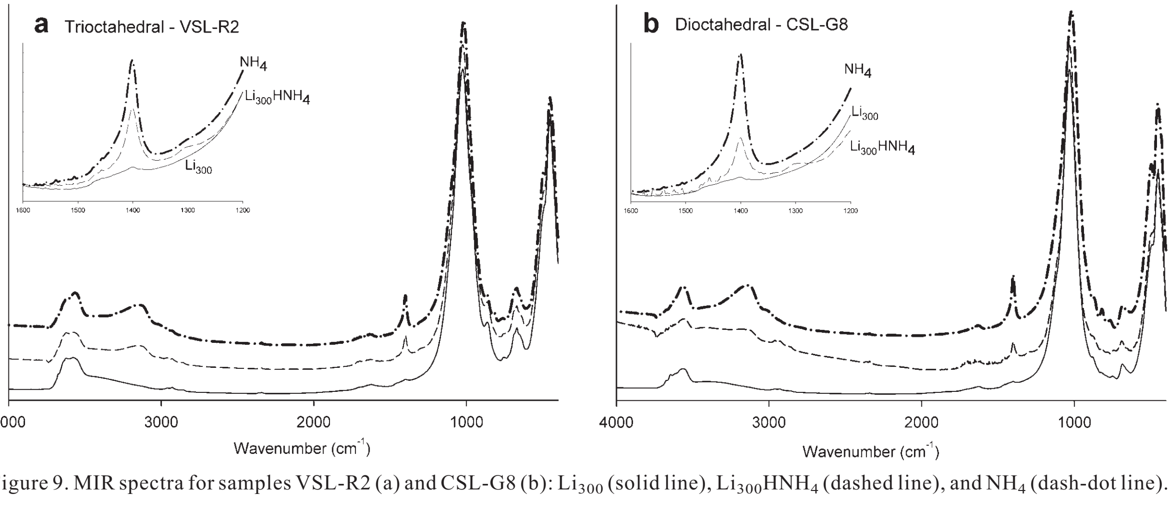

Figure 9. MIR spectra for samples VSL-R2 (a) and CSL-G8 (b): Li_{300} (solid line), $\mathrm{Li}_{300}\mathrm{HNH}_4$ (dashed line), and NH_4 (dash-dot line).

Table 2. CEC and octahedral charge obtained for Niquelândia smectite samples.

Samples	AS-BNi2 Di	AS-ANi3 Tri		ASL-I5 Di	VSL-R2 Di+Tri		CSL-G8 Di	VSL1A Di+Tri	ASL-AN3 Di+Tri	
Size (μm)	<2	<2	<0.1	<2	<2	<0.1	<2	<2	<2	<0.1
CEC (meq/100 g)	100	41	39	81	60	77	79	83	67	89
Ratio of charge neutralized by Li^+ (%)	55	48	52	57	44	71	63	54	49	69

CEC and origin of charge (Table 2). This is in agreement with the similarity of the FTIR spectra for both size fractions (Figure 10). In contrast, for samples VSL-R2 and ASL-AN3, which are mixtures of di and tri-octahedral smectites, the CEC and the origin of charge varied significantly between the <2 μm and <0.1 μm fractions, with a larger CEC value and higher ratio of charges neutralized by Li^+. In fact, the FTIR spectra of the two fractions of these samples revealed that the <0.1 μm fractions are relatively enriched in Fe-montmorillonite compared to the <2 μm fractions with a relative increase in the band at 820 cm^{-1} and an increase in the band at 670–710 cm^{-1} (trioctahedral smectites).

Scanning electron microscopy

The typical morphology of smectites, honeycomb structure and wavy flakes (Figure 11), was observed in the Ni-rich sample (AS-ANi3) and in the Mg-rich sample (VSL-R2).

The SEM-EDX microanalysis data of the K-saturated <2 μm fractions plotted in ternary diagrams (Figure 12) revealed chemical heterogeneities for the different samples. Sample AS-ANi3 contains a remarkable amount of Ni (31 ± 2.4%; Figures 12b and 12c) and corresponds to the trioctahedral Ni-rich stevensite end-member (Figure 12a). The samples ASL-I5 and AS-BNi2 are enriched in Fe (Figures 12b and 12c) and correspond to the dioctahedral end-member (Fe-montmorillonite) (Figure 12a). Samples CSL-G8, VSL1A, VSL-R2, and ASL-AN3 have chemical compositions intermediate between the two end-members described above (Figure 12b,c).

For samples VSL-R2 and ASL-AN3, the oriented trend toward the Mg pole (Figure 12d) may be attributable to the presence of talc as revealed by other techniques.

The average structural formulae of the two di- and trioctahedral end-members of the Niquelândia smectites were estimated roughly from powder analyses of samples ASL-I5 and AS-ANi3 based on 11 oxygens, expressing Fe as Fe^{3+}, and taking into account FTIR structural data (Table 3). The octahedral charge was adjusted to take into account the results of FTIR and $Li_{300}H$-NH_4 saturations.

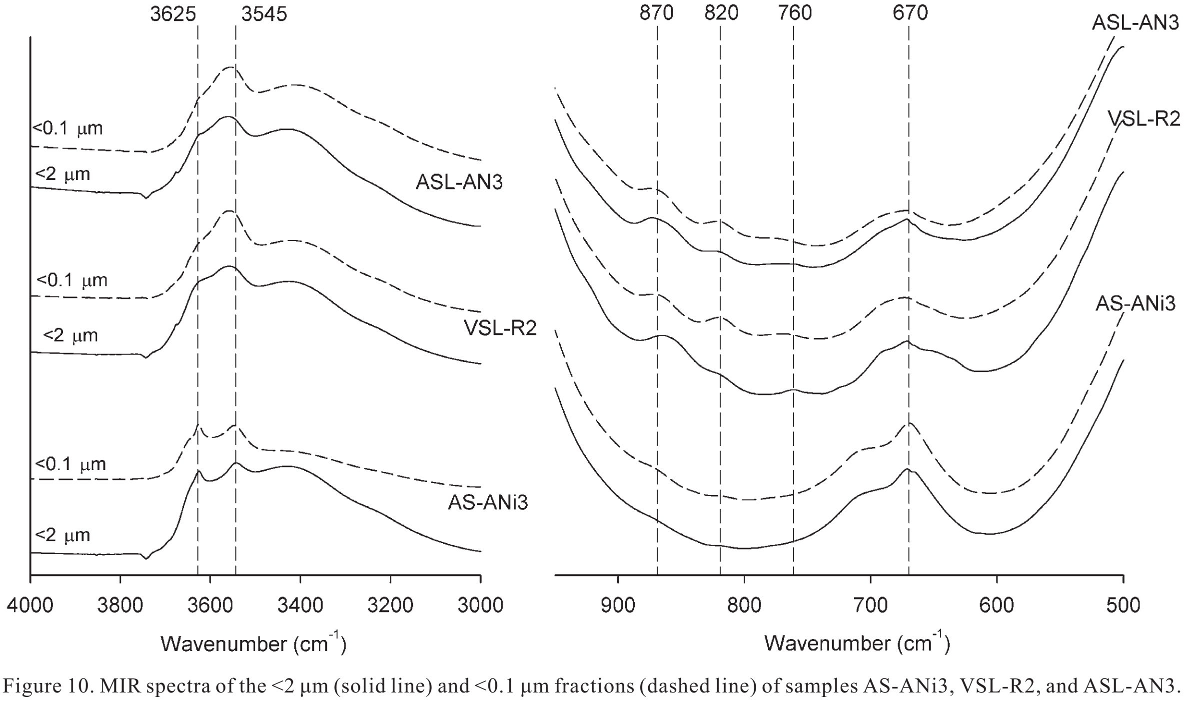

Figure 10. MIR spectra of the <2 μm (solid line) and <0.1 μm fractions (dashed line) of samples AS-ANi3, VSL-R2, and ASL-AN3.

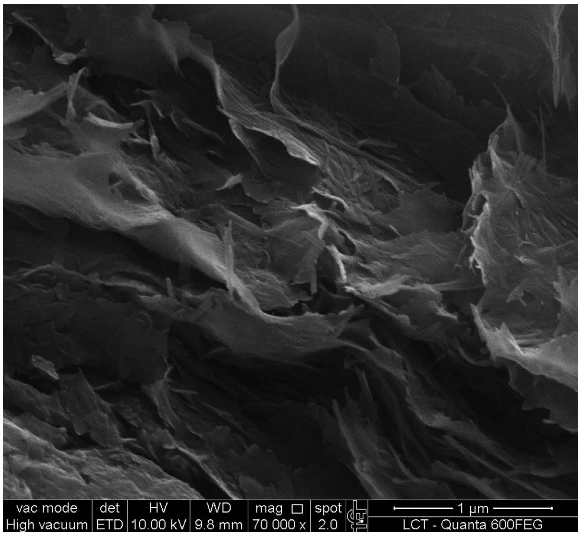

Figure 11. SEM-SE (secondary electron) image of smectite in sample VSL-R2 with typical wavy-flake particles.

The dominant octahedral cation of the dioctahedral end-member is Fe^{3+} (1.50 atoms per half unit cell), which is in the range of values obtained by Petit *et al.* (2002) and Gaudin *et al.* (2004a) for Fe-montmorillonites. For trioctahedral smectites, the dominant octahedral cation is Ni (>2 atoms per half unit cell).

DISCUSSIONS AND CONCLUSIONS

The results for the <2 μm fractions confirmed that most of the samples are formed by mixtures of Fe-montmorillonite and Ni-stevensite with traces of talc for some samples.

The calculated structural formulae (Table 3) obtained by EDX and FTIR analysis show that there is no chemical substitution in tetrahedral sheets for trioctahedral smectites (AS-ANi3). For dioctahedral smectites, Si^{4+} is replaced by Al^{3+} in small proportions (0.14 atoms per half unit cell).

With respect to the octahedral sheet, the Ni^{2+} is the dominant cation for trioctahedral smectites, reaching 2.2 Ni atoms per half unit cell. Ni-rich smectites are rare in

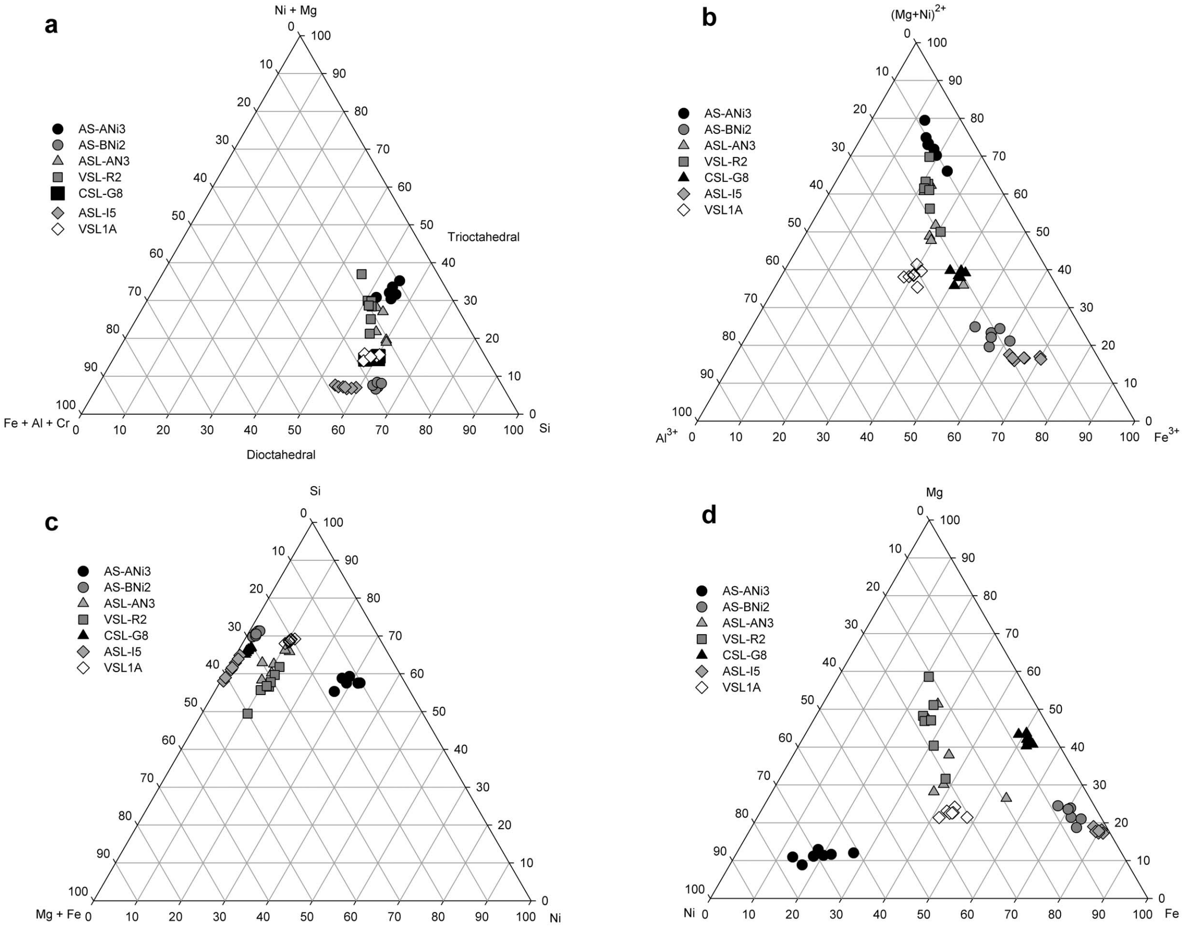

Figure 12. SEM-EDX microanalysis of K-saturated powders plotted in ternary diagrams (atom.%).

Table 3. Structural formulae of Niquelândia smectites (on the basis of 11 oxygens) from SEM-EDX analyses of powders of K-saturated samples. The layer-charge distribution is adjusted on the basis of FTIR data. Tri = AS-ANi3; Di+Tri = VSL-R2, VSL1A, and ASL-AN3; Di = ASL-I5.

		Di	Tri
IV	Si^{4+}	3.86	4
IV	Al^{3+}	0.14	0
IV	Fe^{3+}	0	0
VI	Al^{3+}	0.25	0
VI	Fe^{3+}	1.50	0.20
VI	Mg^{2+}	0.16	0.21
VI	Cr^{3+}	0.04	0.07
VI	Ni^{2+}	0.05	2.2
inter	K^{+}	0.31	0.33
Σ IV		4.00	4.00
ΣVI		2.17	2.69
Charge IV		−0.50	0
Charge VI		−0.66	0.33
Total charge		−1.15	0.33
% charge VI		57	100
% charge $Li_{300}H$		57	48

nature; a dioctahedral Ni-smectite which does not exceed 0.4 Ni atoms per half unit cell was studied by Bosio *et al.* (1975), Brindley and de Souza (1975), and Gaudin *et al.* (2004a). Only Christidis and Mitsis (2006) found a Ni-smectite in Othrys, Greece, with >2 Ni per half unit cell. For the dioctahedral smectites, Fe^{3+} is the dominant octahedral cation (1.5 Fe atoms per half unit cell). Niquelândia dioctahedral smectites show an over-occupancy of octahedral sheets (2.17 atoms p.h.f.u.).

Lithium saturations and structural formulae showed that the layer charge arises especially in octahedral sheets for most samples, confirming that Fe-montmorillonites are characteristic dioctahedral smectites in ultrabasic weathered rocks as described by Gaudin *et al.* (2004a, 2004b). Another Fe-rich octahedral charged smectite was also described in deep-sea pyrite-rich sediments (Gaudin *et al.*, 2005; Wiewióra *et al.*, 2001).

The samples AS-ANi3 and VSL-R2, located at the bottom of the profile, consist essentially of Mg and Ni-rich smectites and also of some preserved pyroxene grains, suggesting that Mg- and Ni-rich smectites were formed from alteration of peridotites and pyroxenite. A trioctahedral Mg-bearing smectite was observed (Oliveira, 1990; Nahon *et al.*, 1982; Colin *et al.*, 1990) to have formed by incongruent and congruent dissolution of olivines and pyroxenes. The olivine from the peridotites is a continuous source of Ni capable of replacing Mg in trioctahedral smectites. The intense weathering process and continuous Mg and Ni leaching transformed trioctahedral smectite into an Fe-rich dioctahedral smectite (Colin *et al.* 1990). This interpretation was confirmed by the infra-micrometric fractionation study that showed that Fe-montmorillonite coexists, at the smallest size (<0.1 μm), in the trioctahedral Ni-Fe stevensite samples. This also agrees with the results of Decarreau and Bonnin (1986) who determined that a nontronite-like smectite formed from an Fe-stevensite in atmospheric oxidized conditions.

The great heterogeneity of Ni distribution in both dioctahedral and trioctahedral smectites seems to be responsible for the large variation in Ni recovery during ore processing. Differences in the clay-mineral structure due to chemical substitutions may require different ore behaviors during the leaching process. Likewise, for the same smectite, different dissolution rates for one sample treated with Li^{+} and another treated with Ni^{2+} were observed by Pálková *et al.* (2003) due to structural modifications.

ACKNOWLEDGMENTS

This study was supported by CAPES (Coordenação de Aperfeiçoamento de Pessoal de Nível Superior/Brazilian Coordination for the Improvement of Higher Education Personnel) – Project CAPES/COFECUB: 9075/12-7–Te 761/12 and FAPESP (Fundação de Apoio à Pesquisa do Estado de São Paulo/ the São Paulo State Research Foundation) – project 10/50849-4. The authors thank the Votorantim Metais Níquel Company for all their contributions. The authors also thank the editors and reviewers for their constructive reviews and careful editing of the manuscript.

REFERENCES

Andrieux, P. and Petit, S. (2010) Hydrothermal synthesis of dioctahedral smectites: The Al–Fe^{3+} chemical series: Part I: Influence of experimental conditions. *Applied Clay Science*, **48**, 5–17.

Bishop, J., Murad, E., and Dyar, M.D. (2002) The influence of octahedral and tetrahedral cation substitution on the structure of smectites and serpentines as observed through infrared spectroscopy. *Clay Minerals*, **37**, 617–628.

Bosio, N.J., Hurst, V.J., and Smith, R.L. (1975) Nickeliferous nontronite, a 15 Å garnierite, at Niquelândia, Goiás, Brazil. *Clays and Clay Minerals*, **23**, 400–403.

Brindley, G.W. and de Souza, J.V. (1975) Nickel-containing montmorillonites and chlorites from Brazil, with remarks on schuchardtite. *Mineralogical Magazine*, **40**, 141–152.

Calarge, L., Lanson, B., Meunier, A., and Formoso, M.L. (2003) The smectitic minerals in a bentonite deposit from Melo (Uruguay). *Clay Minerals*, **38**, 25–34.

Christidis, G.E. and Mitsis, I. (2006) A new Ni-rich stevensite from the ophiolite complex of Othrys, Central Greece. *Clays and Clay Minerals*, **54**, 653–666.

Coelho, A.C.V., Poncelet, G., and Ladrière, J. (2000) Nickel, iron-containing clay minerals from Niquelânida deposit, Brazil – 1 Characterization. *Applied Clay Science*, **17**, 163–181.

Colin, F., Noack, J., Trescases, J., and Nahon, D. (1985) L'altération latéritique débutante des pyroxénites de Jacuba, Niquelândia, Brésil. *Clay Minerals*, **20**, 93–113.

Colin, F., Nahon, D., Trescases, J.J., and Melfi, A.J. (1990) Lateritic weathering of pyroxenites at Niquelândia, Goias, Brazil: The supergene behavior of nickel. *Economic Geology*, **85**, 1010–1023.

Dalvi, A., Bacon, G., and Osborne, R. (2004) The past and the future of nickel laterites. Pp. 7–10 in: PDAC 2004

International convention, Toronto, Canada. *Trade show and investors exchange*. Prospectors and Developers Association of Canada, Toronto.

de Oliveira, S.M.B. (1990) *Os depósitos de Níquel Lateríticos do Brasil*. PhD thesis, Universidade de São Paulo, Instituto de Geociências, São Paulo, Brazil.

De Souza, J.V., Santos, P.S., and Santos, H.S. (1978) Caracterização mineralógica de algumas argilas niquelíferas brasileiras. *Revista Cerâmica*, **24**, 434–446.

Decarreau, A. and Bonnin D. (1986) Synthesis and crystallogenesis at low temperature of Fe(III)-smectites by evolution of coprecipitated gels: Experiments in partially reducing conditions. *Clay Minerals*, **21**, 861–877.

Decarreau, A., Colin, F., Herbillon, A., Manceau, A., Nahon, D., Paquet, H., Trauth-Badaud, D., and Trescases, J.J. (1987) Domain segregation in Ni-Fe-Mg smectites. *Clays and Clay Minerals*, **35**, 1–10.

Decarreau, A., Petit, S., Martin, F., Farges, F., Vieillard, P., and Joussein, E. (2008) Hydrothermal synthesis, between 75 and 150ºC, of high-charge, ferric nontronites. *Clays and Clay Minerals*, **56**, 322–337.

Desprairies, A. (1983) Relation entre le paramètre b des smectites et leur contenu en fer et magnesium. Application à l'étude des sédiments. *Clay Minerals*, **18**, 165–175.

Farmer, V.C. (1974) *Infrared Spectra of Minerals*. Monograph **4**, The Mineralogical Society, London.

Gates, W.P. (2005) Infrared spectroscopy and the chemistry of dioctahedral smectites. Pp. 125–168 in: *The Application of Vibrational Spectroscopy to Clay Minerals and Layered Double Hydroxides* (J.T. Kloprogge, editor). CMS Workshop Lectures, **13**, The Clay Minerals Society, Aurora, Colorado, USA.

Gaudin, A., Grauby, O., Noack, Y., Decarreau, A., and Petit, S. (2004a) Accurate crystal chemistry of ferric smectites from the lateritic nickel ore of Murrin Murrin (Western Australia). I. XRD and multi-scale chemical approaches. *Clay Minerals*, **39**, 301–315.

Gaudin, A., Petit, S., Rose, J., Martin, F., Decarreau, A., Noack, Y., and Borschneck, D. (2004b) The accurate crystal chemistry of ferric smectites from the lateritic nickel ore of Murrin Murrin (Western Australia). II. Spectroscopic (IR and EXAFS) approaches. *Clay Minerals*, **39**, 453–467.

Gaudin, A., Buatier, M.D., Beaufort, D., Petit, S., Grauby, O. and Decarreau, A. (2005) Characterization and origin of Fe^{3+}-montmorillonite in deep-water calcareous sediments (Pacific Ocean, Costa Rica margin). *Clays and Clay Minerals*, **53**, 452–465.

Gerard, P. and Herbillon, A.J. (1983) Infrared studies of Ni-bearing clay minerals of the kerolite-pimelite series. *Clays and Clay Minerals*, **31**, 143–151.

Hofmann, U. and Klemen, R. (1950) Verlust der Austauschfähigkeit von Lithiuminonenan Bentonitdurch Erhitzung. *Zeitschrift für anorganische und allgemeine Chemie*, **262**, 95–99.

Köster, H.M., Ehrlicher, U., Gilg, H.A., Jordan, R., Murad, E. and Onnich, K. (1999) Mineralogical and chemical characteristics of five nontronite and Fe-rich smectites. *Clay Minerals*, **34**, 579–599.

Madejová, J., Balán, E., and Petit, S. (2011) Application of vibrational spectroscopy to the characterization of phyllosilicates and other industrial minerals. Pp. 171–226 in: *Advances in the Characterization of Industrial Minerals* (G.E. Christidis, editor). EMU Notes in Mineralogy, **9**, European Mineralogical Union and the Mineralogical Society of Great Britain and Ireland, London.

Marini, O.J., Fuck, R.A., Dardenne, M.A., and Danni, J.C.M. (1984) Província Tocantins – Setores Central e Sudeste. Pp. 205–264 in: *O pré-cambriano do Brasil* (F.F.M. de Almeida and Y. Hasui, editor). Edgard Blucher, São Paulo.

Moore, D.M. and Reynolds, R.C. Jr. (1989) *X-ray Diffraction and the Identification and Analysis of Clay Minerals*. Oxford University Press, New York.

Nahon, D., Colin, F., and Tardy, Y. (1982) Formation and distribution of Mg, Fe, Mn-smectites in the first stages of the lateritic weathering of forsterite and tephroite. *Clay Minerals*, **17**, 339–348.

Pálková, H., Madejová, J., and Righi, D. (2003) Acid dissolution of reduced-charge Li- and Ni-montmorillonites. *Clays and Clay Minerals*, **51**, 133–142.

Petit, S. (2005) Crystal-chemistry of talcs: a NIR and MIR spectroscopic approach. Pp. 41–64 in: *The Application of Vibrational Spectroscopy to Clay Minerals and Layered Double Hydroxides* (J.T. Kloprogge, editor). CMS Workshop Lectures Series, **13**, The Clay Minerals Society, Aurora, Colorado, USA.

Petit, S., Prot, T., Decarreau, A., Mosser, C., and Toledo-Groke, M.C. (1992) Crystallochemical study of a population of particles in smectites from a lateritic weathering profile. *Clays and Clay Minerals*, **40**, 436–445.

Petit, S., Righi, D., Madejová, J., and Decarreau, A. (1998) Layer charge estimation of smectites using infrared spectroscopy. *Clay Minerals*, **33**, 579–591.

Petit, S., Caillaud, J., Righi, D., Madejová, J., Elsass, F., and Köster, H.M. (2002) Characterization and crystal chemistry of an Fe-rich montmorillonite from Ölberg, Germany. *Clay Minerals*, **37**, 283–297.

Petit, S., Martin, F., Wiewióra, A., De Parseval, P., and Decarreau, A. (2004) Crystal-chemistry of talc: A near infrared (NIR) spectroscopy study. *American Mineralogist*, **89**, 319–326.

Petit, S., Righi, D., and Madejová, J. (2006) Infrared spectroscopy of NH_4^+-bearing and saturated clay minerals: A review of the study of layer charge. *Applied Clay Science*, **34**, 22–30.

Petit, S., Righi, D., and Decarreau, A. (2008) Transformation of synthetic Zn-stevensite to Zn-talc induced by the Hofmann-Klemen effect. *Clays and Clay Minerals*, **57**, 645–654.

Raous, S., Echevarria, G., Sterckeman, T., Hanna, K., Thomas, F., Martins, E.S., and Becquer, T. (2013) Potentially toxic metals in ultramafic mining materials: Identification of the main bearing and reactive phases. *Geoderma*, **192**, 111–119.

Wiewióra, A., Giresse, P., Petit, S., and Wilamowski, A. (2001) A deep-water glauconitization process on the Ivory Coast–Ghana marginal ridge (ODP site 959): determination of Fe^{3+}-rich montmorillonite in green grains. *Clays and Clay Minerals*, **49**, 540–558.

Wilkins, R.W.T. and Ito, J. (1967) Infrared spectra of some synthetic talcs. *American Mineralogist*, **52**, 1649–1661.

Wilson, M. (1994) *Clay Mineralogy: Spectroscopic and Chemical Determinative Methods*. Chapman & Hall, London.

(*Received 18 February 2014; revised 2 September 2014; Ms. 849; AE: R. Kukkadapu*)

Clays and Clay Minerals, Vol. 62, No. 4, 336–353, 2014.

EXPANSION BEHAVIOR OF OCTADECYLAMMONIUM-EXCHANGED LOW- TO HIGH-CHARGE REFERENCE SMECTITE-GROUP MINERALS AS REVEALED BY HIGH-RESOLUTION TRANSMISSION ELECTRON MICROSCOPY ON ULTRATHIN SECTIONS

Dirk Schumann[1,2,*], Reinhard Hesse[3,4], S. Kelly Sears[5], and Hojatollah Vali[3,5]

[1] Fibics Incorporated, 1431 Merivale Road, Suite 100, Lower Level, Ottawa, ON, K2E 0B9, Canada
[2] Department of Earth Sciences, Western University, 1151 Richmond Street N., London, ON, N6A 5B7, Canada
[3] Department of Earth and Planetary Sciences, McGill University, 3450 University Street, Montréal, QC, H3A 0E8, Canada
[4] Department of Geo- and Environmental Sciences, Section Geology, Ludwig Maximilian University, Luisenstr. 37, D-80333, München, Germany
[5] Facility for Electron Microscopy Research, McGill University, 3640 University Street, Montréal, QC, H3A 2B2, Canada

Abstract—Ultrathin sections of reference 2:1 layer silicates treated with octadecylammonium cations were examined using high-resolution transmission electron microscopy (HRTEM) to establish the layer structure. Hitherto, few HRTEM ultrathin-section data existed on the expansion behavior of smectite-group minerals with different interlayer-charge values. Without such information, the expansion behavior of both low-charge and high-charge smectite minerals cannot be characterized and the structures observed in HRTEM images of clay-mineral mixtures cannot be interpreted reliably. Reference smectite-group minerals (Upton, Wyoming low-charge montmorillonite; Otay, California high-charge montmorillonite; a synthetic fluorohectorite; and a Jeanne d'Arc Basin offshore Newfoundland clay sample) with a range of layer charge values were examined. To prevent possible intrusion of epoxy resin into interlayers during embedding, the clay samples were first embedded in epoxy, sectioned with an ultra microtome, and then treated with octadecylammonium cations before examination using HRTEM. Lattice-fringe images showed that lower-charge (<0.38 eq/$O_{10}(OH)_2$) 2:1 layers had 13−14 Å spacings, whereas higher-charge (>0.38 eq/$O_{10}(OH)_2$) 2:1 layers had 21 and 45 Å spacings. These differently expanded silicate layers can occur within the same crystal and an alternation of these layer types can generate rectorite-like structures. For comparison, clay samples were also treated with octadecylammonium before epoxy embedding and sectioning and then examined with HRTEM. These samples mostly had highly expanded interlayers due to epoxy intrusion in the interlayer space. The reference clay minerals embedded in epoxy resin, sectioned, and treated with octadecylammonium cations were used to characterize smectite-group minerals in a natural clay sample from the Jeanne d'Arc Basin, Eastern Canada. Smectite-group minerals in this sample revealed similar structures in lattice-fringe images to those observed in the pure reference clay samples. Rectorite-like structures observed in lattice-fringe images were in fact smectite crystals with short, alternating sequences of low-charge and high-charge smectite layers rather than illite-smectite (I-S) phases with expanded smectite layers and non-expanded 10 Å illite layers.

Key Words—Clay Minerals, High-resolution Transmission Electron Microscopy, Lattice-fringe Images, *n*-alkylammonium Cations, Mixed-layer Illite/smectite, Rectorite-like Structures, Smectite-group Minerals.

INTRODUCTION

Organic compounds such as glycerol and ethylene glycol are commonly used to identify expandable smectite-group clay minerals and to differentiate them from non-expandable clay minerals such as illite and chlorite (MacEwan, 1944; Brindley, 1966). The expansion of the 2:1 layer silicates, caused by the replacement of inorganic interlayer cations by *n*-alkylammonium cations, is used to determine layer-charge magnitude and distribution (Lagaly and Weiss, 1969; 1970a, 1970b, 1970c). This method became a frequently used technique in various subsequent studies to estimate layer charge and charge distribution in expandable 2:1 layer silicates (Lagaly and Weiss, 1971; Stul and Mortier, 1974; Rühlicke and Kohler, 1981, Stanjek and Friedrich, 1986; Laird *et al.*, 1989a; Olis *et al.*, 1990) but limitations and problems associated with the method were also identified (Mermut, 1994). X-ray diffraction (XRD) analysis has been the usual method for routine identification and structural characterization of clay minerals. However, XRD patterns average signals over thousands of unit cells and particles and therefore cannot provide the micro- and nano-scale information required for a reliable identification of clay minerals, particularly of mixed-layer minerals.

Transmission electron microscopy (TEM), however, can be used to obtain this crucial information about clay

* E-mail address of corresponding author:
dschumann@fibics.com
DOI: 10.1346/CCMN.2014.0620407

materials. A detailed review of the preparation methods of clay-mineral and soil samples for TEM investigations was given by Elsass *et al.* (2008). Special preparation techniques have been developed to examine silicate layers perpendicular to the stacking axis direction (Eberhart and Triki, 1972; Lee *et al.*, 1975). The *n*-alkylammonium cation-exchange method was first combined with TEM lattice-fringe imaging of different 2:1 clay-mineral ultrathin sections (Vali and Köster, 1986) to investigate structure and expansion behavior. This approach, in which *n*-alkylammonium cation exchange is performed before clay minerals are embedded in epoxy resin (Figure 1: method 1), was also applied in various other studies (Graf von Reichenbach *et al.*, 1988; Ghabru *et al.*, 1989; Laird *et al.*, 1989b; Laird and Nater, 1993; Malla *et al.*, 1993; Cetin and Huff, 1995).

Previous smectite-group minerals studies (Vali, 1983; Vali and Köster, 1986; Malla *et al.*, 1993) that prepared samples using method 1 always found larger spacings in TEM lattice-fringe images than those determined by XRD analyses (Table 3). The additional expansion observed in TEM images was attributed to incorporation of epoxy resin into clay interlayers during the embedding of *n*-alkylammonium-treated smectite-group minerals in epoxy.

In order to avoid resin infiltration in the interlayer space, Vali and Hesse (1990) developed a new method in which samples are first embedded in epoxy resin. After ultrathin sections are cut and transferred to TEM grids, the treatment with *n*-alkylammonium cations is performed on the ultrathin sections (see Figure 1: method 2, and Table 1). This method was used subsequently in several studies that used HRTEM to examine 2:1 layer silicates from various geological settings. Most clay minerals prepared according to the Vali and Hesse (1990) method (method 2) for HRTEM examination were reference high-charge 2:1 layer silicates (Marblehead Illite, Zempleni Illite, Llano and Jefferson vermiculite) and clay mixtures from various geological environments that contained different proportions of smectite-group minerals, illite, vermiculite, and mica (Vali *et al.*, 1991, 1993, 1994; Vali and Hesse, 1992; Sears *et al.*, 1998; Lee *et al.*, 2003; Shata *et al.*, 2003).

The only reference smectite-group sample prepared for HRTEM examination that was alkylammonium-exchanged after epoxy embedding and sectioning was the SWa-1 nontronite (Vali and Hesse, 1990). No reference smectite-group minerals other than nontronite have been prepared using method 2 and examined with HRTEM (Figure 1). Without knowing the expanding behavior of low-charge and high-charge smectite-group minerals prepared using this method (method 2), however, correct interpretation of the structures in silicate clay-mineral mixtures or explanation of the discrepancies between the *d* values obtained from HRTEM lattice-fringe images and XRD analyses is impossible.

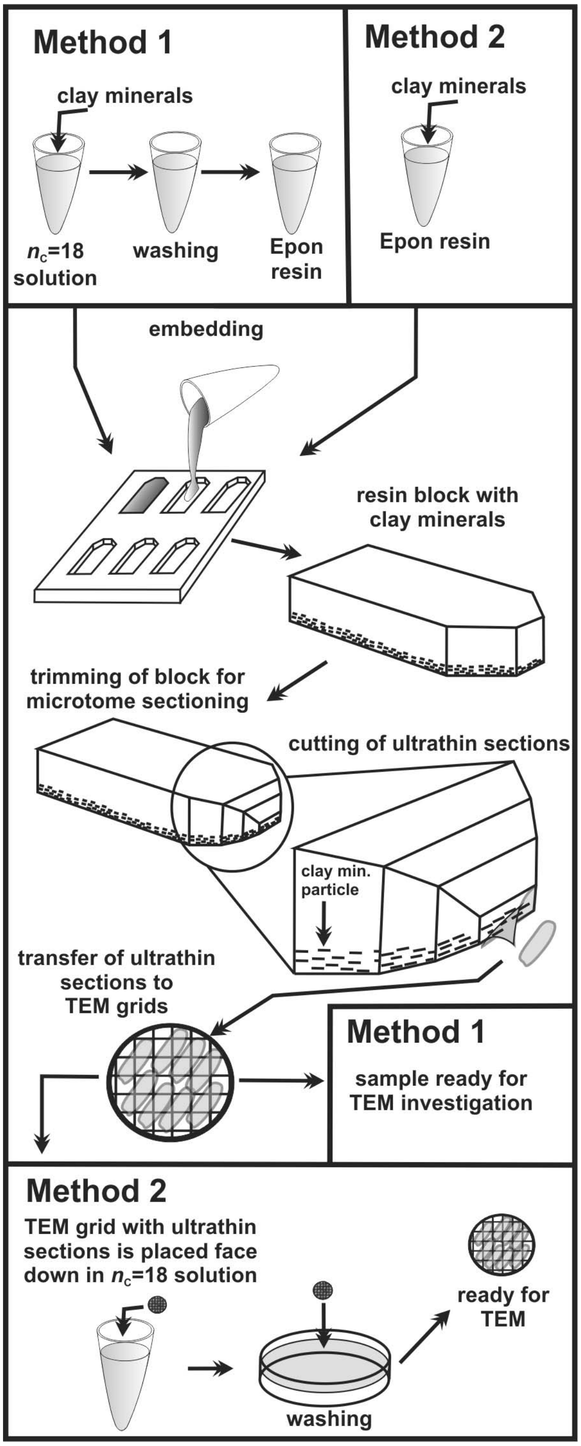

Figure 1. Sample preparation for examination by HRTEM using methods 1 and 2.

The objectives of the present study were, therefore, to: (1) embed in epoxy resin smectite-group minerals with a range of layer charge, prepare stacking axis-parallel ultrathin sections, treat the ultrathin sections

Table 1. Procedural steps describing the different embedding and octadecylammonium cation-exchange treatment methods on the copper grid as well as the octadecylammonium cation treatment before embedding in epoxy resin.

Sample	Method 1 octadecylammonium cation exchange treatment before embedding			Method 2 octadecylammonium cation exchange treatment after embedding and cutting of ultrathin sections		
	1. exchange	2. washing	3. embedding	1. embedding	2. exchange	3. washing
Upton Montm.	20 minutes					
Upton Montm.	5 days	with 100% ethanol up to 20 times	in Epon resin	in Epon resin	20 min	gently submerge TEM grid in a Petri dish with preheated distilled H_2O (65ºC)
Otay Montm.						
Fluorohectorite (0.4)						
Fluorohectorite (0.6)						

with octadecylammonium (n_C = 18) cations (Figure 1, method 2), examine them with HRTEM; and (2) compare the *d* values obtained from HRTEM lattice-fringe images to *d* values from XRD analyses and HRTEM lattice-fringe *d* values from the same clay samples treated with octadecylammonium before embedding in epoxy resin and sectioning (Figure 1, method 1).

MATERIALS AND METHODS

Samples

The two montmorillonite and two hectorite samples selected as reference materials for this study were Upton montmorillonite from Wyoming (reference No. 25 of the American Petroleum Institute (A.P.I.)), Otay montmorillonite from California (A.P.I. No. 24), and synthetic fluorohectorites. Samples of synthetic fluorohectorite with interlayer charges of 0.4 and 0.6 eq/$O_{10}(OH)_2$ were synthesized and provided by Josef Breu, University of Bayreuth, Germany (Breu *et al.*, 2001; Malikova *et al.*, 2007). The reference clay minerals have the following structural formulae:

Upton montmorillonite:
$R^{n+}_{0.36/n}$ $m$$H_2O$ ($Al_{1.58}Fe^{3+}_{0.12}Fe^{2+}_{0.02}Mg_{0.28}$)
[$Al_{0.06}Si_{3.94}$]$O_{10}(OH)_2$ (Vogt and Köster, 1978)

Otay montmorillonite:
$Na_{0.42}Mg_{0.09}Ca_{0.01}$$m$$H_2O$($Al_{1.35}Fe^{3+}_{0.06}Mg_{0.59}$)
[$Al_{0.02}Si_{3.98}$]$O_{10}(OH)_2$ (Schultz, 1969)

Synthetic fluorohectorite:
$Na_{0.4}$$m$$H_2O$($Mg_{2.6}Li_{0.4}$)[$Si_{4.0}$]$O_{10}F_2$ and
$Na_{0.6}$$m$$H_2O$($Mg_{2.4}Li_{0.6}$)[$Si_{4.0}$]$O_{10}F_2$.

One argillaceous rock sample from an area that is currently undergoing active burial diagenesis in the Jeanne d'Arc Basin, offshore Newfoundland, Canada, was selected in order to study the <0.1 μm fraction of natural smectite-group minerals. The sample was collected at the core storage facility of the Canada-Newfoundland and Labrador Offshore Petroleum Board (C-NLOPB) in St John's (Newfoundland) from core cuttings that came from the well Adolphus D-50 (AD-D50) (C-NLOPB Schedule of Wells, 2007). The sampled core cuttings were obtained from 2035 m depth from the Paleocene to Pliocene Banquereau Formation that represents the Tertiary passive-margin sediment fill of the Jeanne d'Arc Basin (Sinclair, 1988). The <0.1 μm grain size fraction of this sample was described by Abid *et al.* (2004) as R = 0 randomly interstratified I-S mixed-layer clay minerals with 34% illite in I-S.

The Jeanne d'Arc Basin well cuttings of sample AD-D50 (2035 m) were dispersed and washed several times in distilled water. The <0.1 μm factions of samples AD-D50 (2035 m), Upton montmorillonite, and Otay montmorillonite were separated using a high-speed, bench-top, Beckman Coulter AllegraTM 21R centrifuge at $10730 \times g$ using a fixed-angle rotor. The clay-mineral suspensions were frozen and freeze-dried. The synthetic fluorohectorite material was used as received.

n-alkylammonium cation-exchange method

The *n*-alkylammonium cation-exchange method developed by Lagaly and Weiss (1969) is a tool to determine the interlayer-charge density, layer charge, and charge distribution of expandable 2:1 layer silicates, such as smectites, vermiculite, and illitic minerals in XRD. An *n*-alkylammonium cation consists of an alkyl chain ($C_{n_C}H_{2n_C+1}$) and an ammonium group (NH_3^+) with the general formula $C_{n_C}H_{(2n_C+1)}NH_3^+$ (n_C = number of carbon atoms in the chain).

Alkylammonium-cation arrangements within 2:1 layer-silicate interlayers depend on layer-charge magnitude and density. Low-charge smectite-group minerals have monolayer (~13.6 Å), bilayer (~17.7 Å), or pseudotrimolecular (21.7 Å) arrangements. Long-chain *n*-alkylammonium cations, such as octadecylammonium, form 25 to >30 Å paraffin-type arrangements (Figure 2)

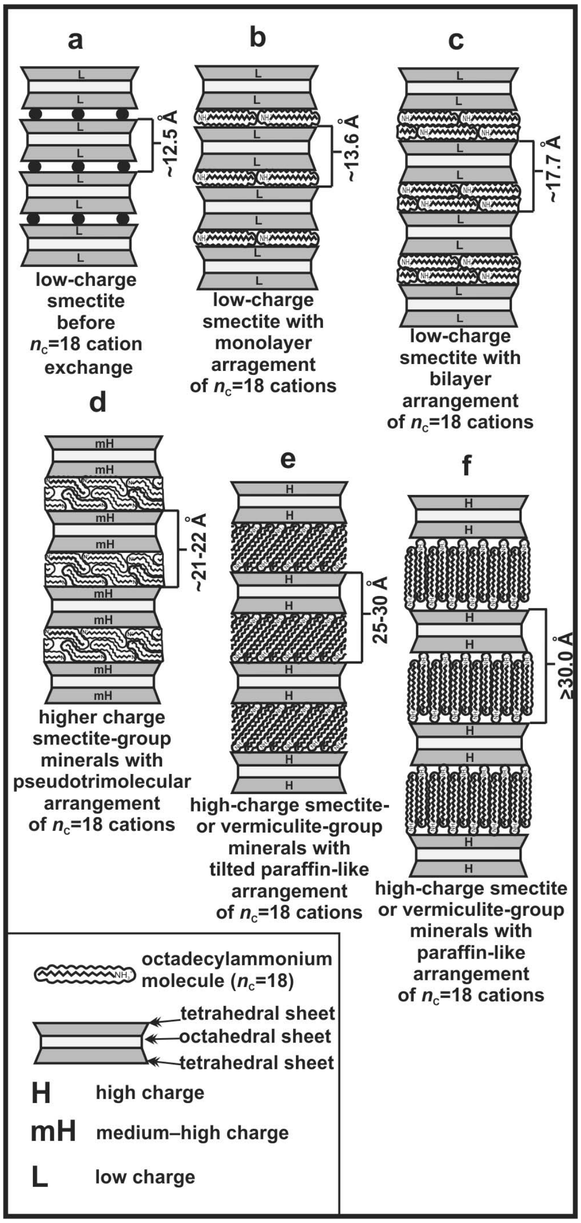

Figure 2. Schematic model showing smectite-group and vermiculite-group 2:1 layer silicates before and after treatment with octadecylammonium (n_C = 18) cations (not to scale): (a) low-charge smectite-group mineral; (b–c) low-charge smectite-group mineral with a monolayer (13.6 Å) and bilayer (17.7 Å) arrangement of the octadecylammonium cations; (d) high-charge smectite-group or vermiculite-group 2:1 layer silicates with a pseudotrimolecular (21–22 Å) arrangement of octadecylammonium cations; (g–f) paraffin-like arrangement of octadecylammonium cations with different tilt angles of the alkyl chains. Diagrams based on the original drawings of Lagaly and Weiss (1969, 1970c), Lagaly (1981), and Vali *et al.* (1994).

in high-charge smectite-group minerals, vermiculite-group minerals, expandable illite, or altered micas (Lagaly and Weiss, 1969, 1970a, 1970c; Lagaly, 1981, 1982). A pseudotrimolecular arrangement can form in 2:1 layer silicates with a layer charge of >0.4 eq/$O_{10}(OH)_2$ whereas paraffin-type orientations of the alkyl chain occur at interlayer charges >0.63 eq/$O_{10}(OH)_2$ (Lagaly, 1982; Malla and Douglas, 1987; Lagaly and Dekany, 2005). For a detailed summary of the theoretical background of the *n*-alkylammonium cation-exchange method and additional references see Sears *et al*. (1998) as well as Laird and Fleming (2008).

XRD and TEM

To prepare octadecylammonium cation-exchanged samples for XRD analysis, ~40 mg of freeze-dried clay material were placed in 1.5 mL polypropylene Eppendorf micro-test tubes (Eppendorf Canada Limited, Streetsville, ON, Canada) and dispersed in a 0.05 M solution of octadecylammonium hydrochloride (n_C = 18) (Acros Organics, Thermo Fisher Scientific, New Jersey, USA) and left in an oven at 65ºC for 24 h. This exchange procedure was repeated four times. The samples were washed thoroughly up to 20 times with 100% ethanol to remove excess alkylammonium salts. The washed clays were dispersed in ~1 mL of 100% ethanol and pipetted onto glass slides, dried at room temperature, and X-rayed. The XRD analyses were performed using a Siemens D5000 diffraction system equipped with a Sol-X solid-state detector with CoKα1,2 radiation in the Département des sciences de la Terre et de l'atmosphère of Université du Québec à Montréal (Québec, Canada). The following analytical conditions were used: operating voltage of 40 kV, beam current of 30 mA, step-size of 0.02º2θ, counting time of 2 s per step, 0.02 mm receiving slit, and scanning range of 1.75 to 55º2θ. After analyses the Co-Kα1,2 radiation was converted numerically into CuKα radiation and the background as well as the Kα2 signal were removed from the XRD patterns.

For HRTEM investigations the samples were embedded in Epon epoxy resin (Electron Microscopy Sciences, Hatfield, Pennsylvania, USA) (Figure 1: method 2). For this procedure, ~10–20 mg of freeze-dried clay samples were placed in 1.5 mL polypropylene Eppendorf micro-test tubes and dehydrated for 48 h by adding 100% acetone to remove adsorbed water. After centrifugation at 16060 × *g* for 15 min with an accuSpin Micro bench-top centrifuge (Fisher Scientific Company, Ottawa, ON, Canada), the supernatant was removed and the clay material dispersed in a mixture of 10% Epon resin and 90% acetone. These steps were repeated with mixtures containing 30%, 50%, 70%, and 100% resin. The dispersion of the material in the acetone resin mixtures was achieved through stirring and agitation using an electrical shaker. Each incubation step lasted 24 h and during that time the samples were placed on a rotating plate to ensure continuous agitation of the material. The resin-clay mixture was transferred into embedding molds after the fifth incubation step (100% Epon resin). After a settling time of 1–2 h the embedding molds (Electron Microscopy Sciences, Hatfield, PA, USA) were placed in an oven for 48 h at 65ºC. Ultrathin sections (~80 nm) were obtained from the polymerized resin blocks using a Reichert-Jung Ultracut E microtome (C. Reichert AG, Vienna, Austria) and transferred to 300-mesh copper TEM grids with carbon support film (Structure Probe, Inc. West Chester, Pennsylvania, USA).

The octadecylammonium cation-exchange treatment was carried out using a modified version of the procedure described by Vali and Hesse (1990). Each grid was placed face down in a 1.5 mL micro-test tube on the surface of the octadecylammonium cation solution diluted to 50% (0.025 M). The micro-test tubes were left for 20 min in an oven at 65ºC. The grids were removed from the tubes, held submerged in a Petri dish filled with 65ºC preheated distilled water and agitated gently for several minutes in order to remove excess alkylammonium solution and salts.

Some aliquots of the Upton and Otay montmorillonite were first treated with octadecylammonium cations and then embedded in Epon resin (Figure 1: method 1). These samples were treated in a 5-day cation-exchange reaction like those that were prepared for XRD analyses. An additional sample of Upton montmorillonite was only treated with octadecylammonium cations for 20 min, washed and embedded. The different treatment methods were chosen in order to compare possible differences in the expansion behavior caused by the different order of the treatment steps.

All samples were studied in bright-field illumination mode at an acceleration voltage of 200 kV with a Philips CM200-TEM at the Facility for Electron Microscopy Research (FEMR) of McGill University (Montreal, Canada). The TEM is equipped with a Gatan Ultrascan 1000 2k × 2k CCD Camera and an EDAX Genesis Energy-Dispersive X-Ray Spectroscopy system (EDS). The spherical aberration coefficient for the TEM is 1.2 mm. Lattice-fringe images were taken at Scherzer defocus (underfocus) conditions at magnifications of 59000–75000 (Vali *et al.*, 1991; Vali and Hesse, 1992). Lattice-fringe measurements were taken, when possible, on sets of lattice fringes. For *d* values of single bilayers, measurements were taken throughout the images on similar layers in order to obtain representative *d* values. The *d*-value measurements were taken using the graphics program *CorelDRAW*® X3 and calculated in Microsoft® *EXCEL*.

RESULTS AND DISCUSSION

Upton and Otay montmorillonite (<0.1 μm)

The incubation of the <0.1 μm grain-size fraction of Upton montmorillonite in octadecylammonium cations for 20 min and for 5 days resulted in similar XRD patterns. A sharp first-order reflection appeared at 5.02º2θ (17.58 Å) followed by integral reflections at 8.77 Å (002), 5.83 Å (003), 4.37 Å (004), 3.50 Å (005), 2.92 Å (006), and 1.95 Å (009) (Table 2).

The Otay montmorillonite <0.1 μm grain-size fraction exchanged with octadecylammonium cations showed a first-order reflection at 20.32 Å in the XRD pattern followed by nearly integral reflections at 10.39 Å (002), 6.98 Å (003), 5.44 Å (004), 4.36 Å (005), 3.54 Å (006), and 3.07 Å (007) (Table 2).

20 min octadecylammonium cation-exchange treatment of ultrathin sections after embedding and sectioning (method 2). Lattice-fringe images of ultrathin sections of Upton montmorillonite after treatment with octadecylammonium cations showed thick packets or ribbons of 2:1 layer-silicate sequences with a spacing ranging between 13 and 14 Å (Figure 3a). The spacings measured in the lattice-fringe images are different from those obtained from the XRD pattern of the octadecylammonium-treated sample. The 13–14 Å sequences suggest a monolayer arrangement of the octadecylammonium cations in the interlayer space whereas the first-order XRD reflection of 17.58 Å is typical for a bilayer arrangement (Figure 2b,c).

Lattice-fringe images of Otay montmorillonite ultrathin sections treated with octadecylammonium cations showed short sequences of two to five 2:1 silicate layers with a spacing between 13 and 14 Å (white half circles), highly expanded sequences of two to eight 2:1 silicate layers with spacing ranging between 26 and 45 Å (white diamonds), and sequences of 2:1 silicate layers containing both low (13 to 14 Å) and highly (26 to 45 Å)

Table 2. XRD peaks of the octadecylammonium cation-exchanged <0.1 μm grain-size fractions of Upton montmorillonite (UM) and Otay montmorillonite (OM).

Sample	Treatment	001 2θ / Å	002 2θ / Å	003 2θ / Å	004 2θ / Å	005 2θ / Å	006 2θ / Å	007 2θ / Å	009 2θ / Å
Upton	octadecylammonium cations for 20 min	5.02 / 17.58	10.08 / 8.77	15.18 / 5.83	20.30 / 4.37	25.42 / 3.50	30.54 / 2.92		46.44 / 1.95
Upton	octadecylammonium cations for 5 days	5.02 / 17.58	10.08 / 8.77	15.18 / 5.83	20.30 / 4.37	25.42 / 3.50	30.54 / 2.93		46.44 / 1.95
Otay	octadecylammonium cations for 20 min	4.34 / 20.32	8.49 / 10.39	12.66 / 6.98	16.28 / 5.44	20.34 / 4.36	25.13 / 3.54	28.97 / 3.08	

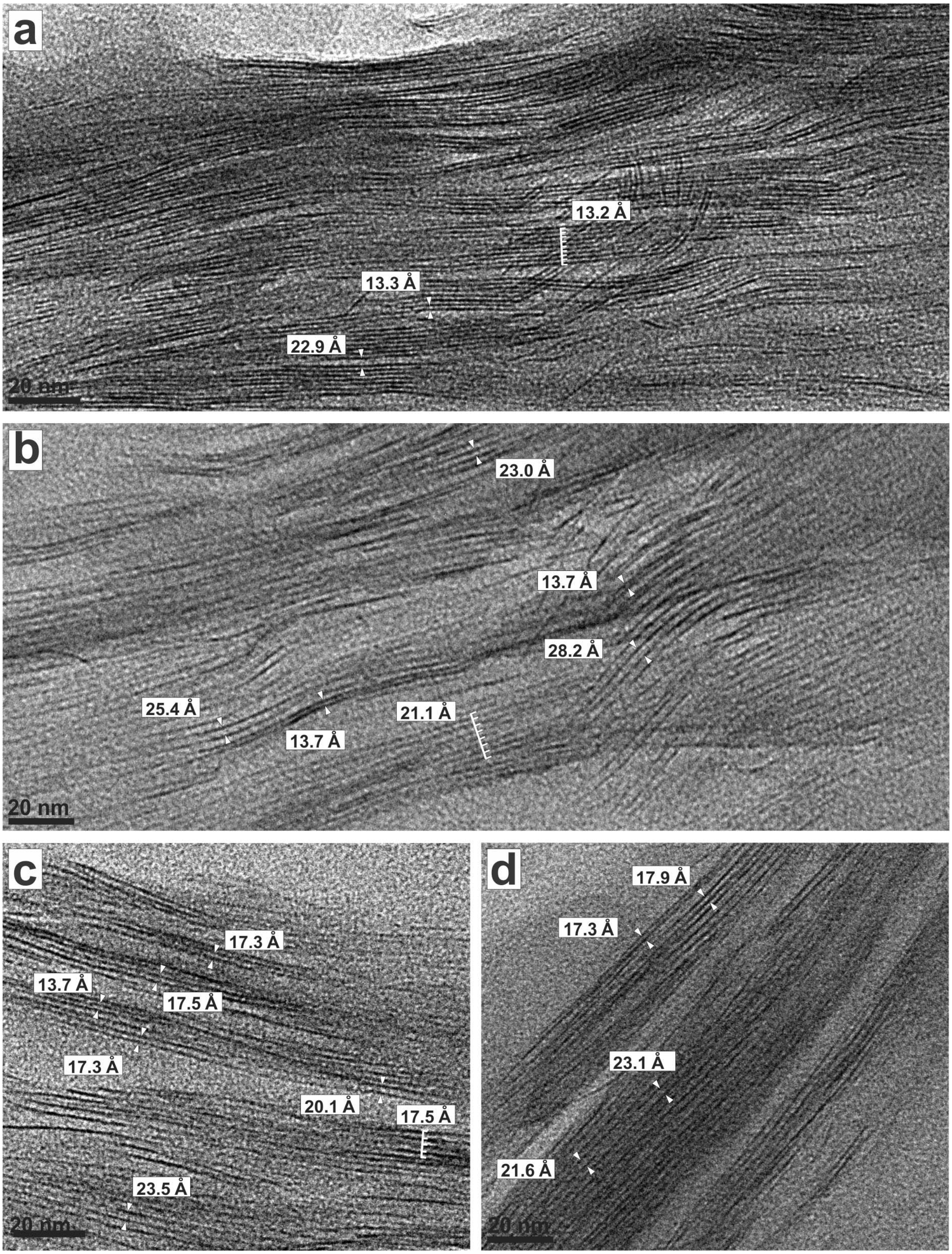

Figure 3. TEM lattice-fringe images of the ultrathin sections of Upton montmorillonite: (a) HRTEM image of an ultrathin section after treatment for 20 min with octadecylammonium cations (method 2) with sequences of silicate layers spacings of 13–14 Å; (b) lattice-fringe images of Upton montmorillonite treated for 20 min with octadecylammonium cations before embedding in resin (method 1). Most crystals are expanded significantly with spacings of between 21 and 26 Å. Some double layers or short sequences show 13–14 Å spacings; (c–d) Lattice-fringe images of Upton montmorillonite exchanged for 5 days with octadecylammonium cations before embedding (method 1). Most crystals show sequences with spacings of 21–25 Å and 17–18 Å. Some crystals have short sequences with 13 to 14 Å spacings.

expanded interlayers in a random distribution (Figure 4a–e). Lattice-fringe images also showed the presence of short sequences composed of alternating low (13–14 Å) and highly (26–45 Å) expanded 2:1 silicate layers resembling a rectorite-like structure (Figure 4b,d,e: white star). The spacings measured using HRTEM contrast with the results obtained by XRD. The 20.32 Å spacing observed in the XRD pattern suggests a pseudotrimolecular arrangement of the octadecylammonium cations (Figure 2e). The 13–14 Å layers in lattice fringes have a monolayer structure while the highly expanded 26–45 Å sequences could be interpreted as a paraffin-type arrangement of octadecylammonium cations (Figure 2b,e,f).

20 min octadecylammonium cation-exchange treatment before embedding (method 1). Lattice-fringe images of Upton montmorillonite treated with octadecylammonium cations for 20 min before embedding mainly showed disrupted 2:1 silicate-layer sequences. The majority of the sequences consisted of highly expanded 2:1 silicate layers with spacings ranging between 21 and 26 Å (Figure 3b). Some sequences showed spacings as large as ~34 Å (not illustrated in any of the figures). Other 2:1 silicate layers showed expansions of 13–14 Å similar to the spacings observed in lattice-fringe images of the ultrathin sections treated with octadecylammonium cations after embedding.

Five days of octadecylammonium cation-exchange treatment before embedding (method 1). Lattice-fringe images of Upton montmorillonite treated for 5 days with octadecylammonium cations before embedding showed highly expanded sequences of 2:1 silicate layers with spacings of 21–25 Å, short sequences with spacings between 17 and 18 Å, and minor amounts of 2:1 silicate layers with 13–14 Å spacings (Figure 3c,d). Some highly expanded sequences reached spacings of up to 34 Å. The measured *d* values between 17 and 18 Å were in the same range of spacings obtained from the XRD analyses of the material exchanged with octadecylammonium cations (Table 2).

The Otay montmorillonite sample treated with octadecylammonium cations before embedding showed packets of highly expanded sequences of 2:1 silicate layers with spacings ranging between 20 and 26 Å (Figure 4f).

Synthetic fluorohectorite

Lattice-fringe images of ultrathin sections of the 0.4 eq/$O_{10}(OH)_2$ fluorohectorite treated with octadecylammonium cations after embedding and sectioning (method 2) showed both crystals with highly expanded 21–27 Å silicate layers and others with a spacing of 13–14 Å (Figure 5a,b). These structures occur, in many instances, within the same crystal (Figure 5c, d). They resemble a rectorite-like structure if they occur in an alternating manner (Figure 5d: white stars). Some of the 2:1 silicate layers changed their expansion behavior within one layer from a small spacing (13 to 14 Å) to a large expansion (21 to 27 Å) (Figure 5a,c,d: white arrows). Some highly expanded sequences reached spacings of up to 30 Å.

Lattice-fringe images of ultrathin sections of the 0.6 eq/$O_{10}(OH)_2$ fluorohectorite treated with octadecylammonium cations revealed the predominance of thick sequences of highly expanded 2:1 silicate layers with *d* values ranging between 21 and 27 Å (Figure 5e, f). Some layers reached spacings of up to 30 Å. In some cases, layers with 13–14 Å spacing occurred within these highly expanded sequences (Figure 5f).

Comparison between d values obtained from XRD and TEM treatment method 1 and 2

Upton montmorillonite exchanged with octadecylammonium cations showed a first-order reflection of 17.58 Å in XRD pattern. In TEM lattice-fringe images, the same exchanged material embedded in epoxy resin (method 1) showed disrupted and highly expanded packets of 2:1 silicate layers with spacings ranging from 21 to 34 Å. Similar highly expanded packets of 2:1 silicate layers were observed by Vali (1983) and Vali and Köster (1986) for Upton montmorillonite and hectorite (Hector, California) in lattice-fringe images despite the slightly different pre-treatment procedure. Those authors' samples were also saturated with Na before they were exchanged for only 3 h with octadecylammonium cations and embedded in epoxy resin (Table 3).

Otay montmorillonite from the present study prepared according to method 1 also showed highly expanded sequences of 2:1 silicate layers in lattice-fringe images (20–26 Å) (Figure 4f) but only 20.32 Å as a first-order XRD reflection (Table 3). Similar discrepancies between XRD peak maxima and measured stacking periodicities on HRTEM images were observed by Malla *et al.* (1993) for the montmorillonite samples SWy-1 and SAz-1 exchanged with dodecylammonium ($n_C = 12$) cations and embedded in Spurr resin. The XRD patterns showed first-order reflections of 17.70 Å while lattice-fringe images showed highly expanded packets ranging from 20 to 48 Å (compare column 3 and 4 for smectites in Table 3). The large expansion of the 2:1 silicate layers in the lattice-fringe images of material treated with *n*-alkylammonium cations before embedding (method 1) can be attributed to the intrusion of epoxy resin into the interlayer spaces that were already expanded by the intercalation of *n*-alkylammonium cations (Vali and Köster, 1986; Laird *et al.*, 1989b; Malla *et al.*, 1993).

Different expansion behaviors of smectite-group minerals can be observed if the samples are treated with *n*-alkylammonium cations after embedding and cutting of ultrathin sections (method 2). For example,

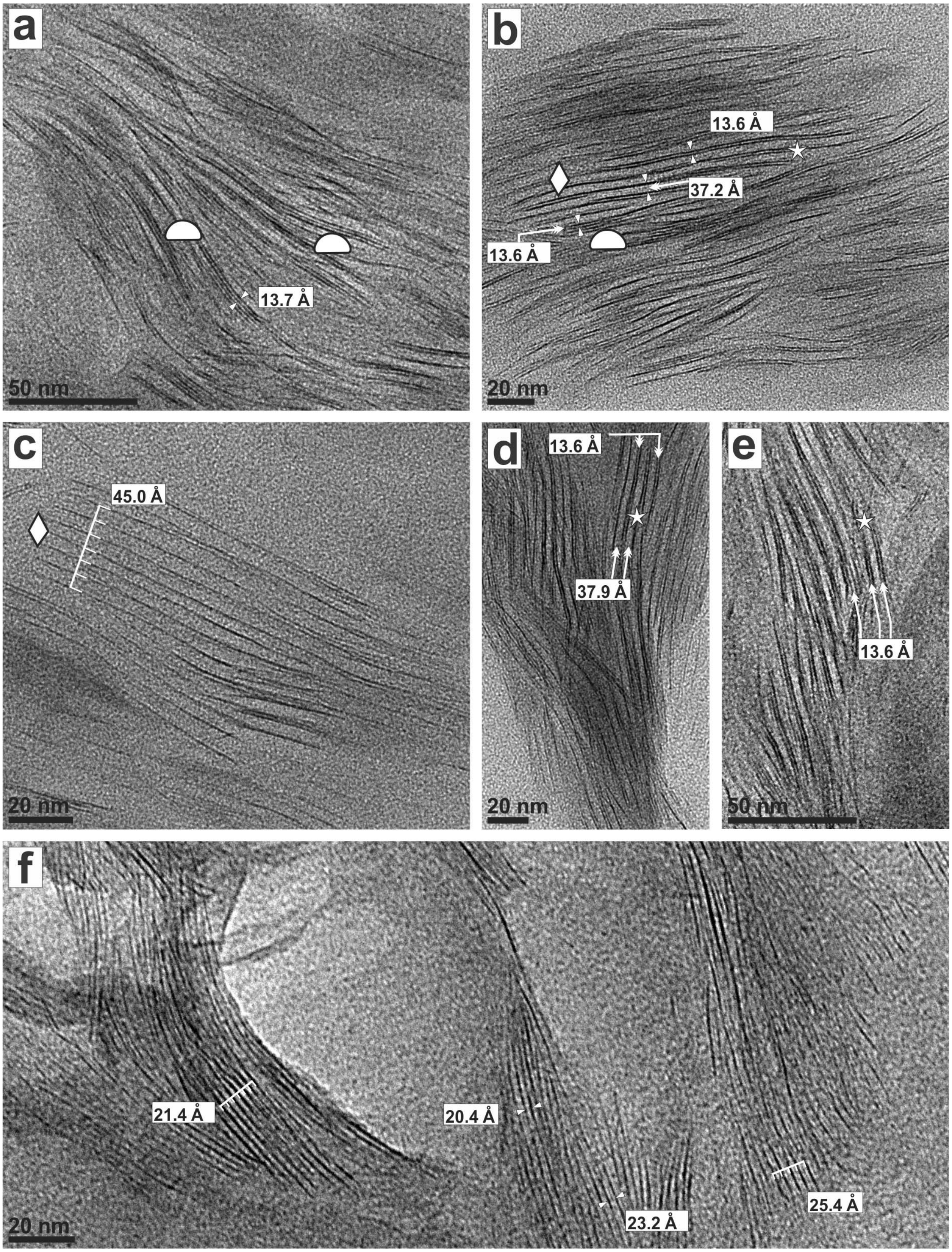

Figure 4. (a–e) HRTEM lattice-fringe images of Otay montmorillonite after treatment with octadecylammonium cations (method 2) showing the different expanded 2:1 silicate layer sequences. Short sequences of 2:1 silicate layers with *d* values of 13–14 Å (white half-circles in parts a and b). Sequences with highly expanded 26–45 Å silicate layers (white diamonds in parts b and c). Both structures may also occur within the same crystal (b,d,e). Some crystals also contain alternating highly expanded layers (26–45) and 13–14 Å layers which resemble rectorite-like structures (white stars in parts b, d, and e). (f) Lattice-fringe images of Otay montmorillonite treated with octadecylammonium cations before embedding in epoxy resin (method 1) showing the predominance of disrupted, highly expanded sequences of 2:1 silicate layers with 20–26 Å spacings. The different expansion behavior of the silicate layers which are due to interlayer-charge differences can only be observed in samples prepared according to method 2.

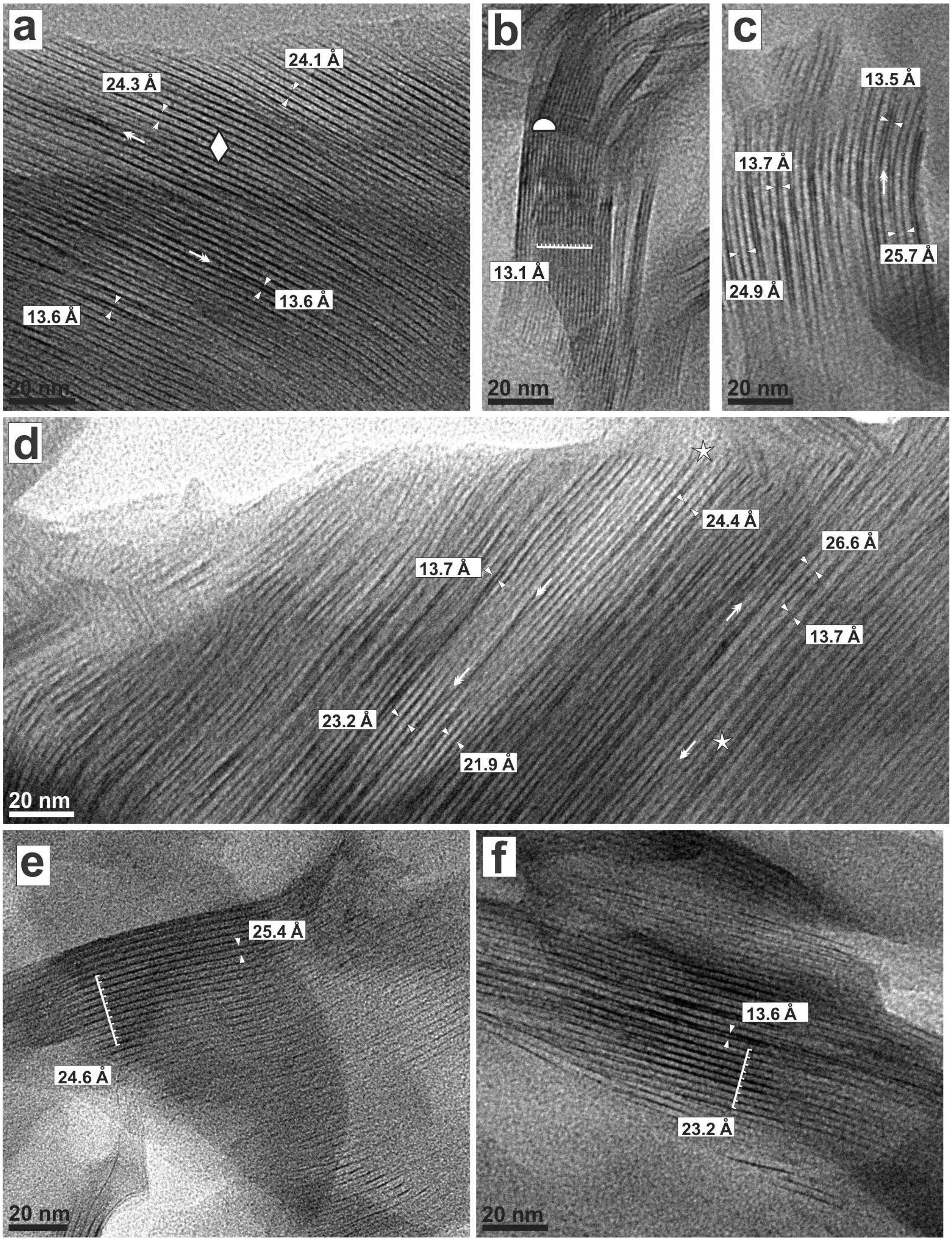

Figure 5. HRTEM lattice-fringe images of synthetic fluorohectorite samples with layer charges of 0.4 and 0.6 eq/$O_{10}(OH)_2$. The ultrathin sections of the of 0.4 eq/$O_{10}(OH)_2$ fluorohectorite treated according to method 2 reveal several different expanded structures: (a) large crystals with highly expanded 2:1 silicate layers with 24–25 Å spacings (white diamond). Some layers show expansions of 13–14 Å.(b) Crystals that only have layers with an expansion of 13–14 Å (white half circle). (c–d) Highly expanded silicate layers (21–27 Å) and 13–14 Å layers commonly occur within the same crystal. In many cases, the alternation of these layers generate short sequences resembling rectorite-like structures (white stars in d). The expansion behavior can also change laterally within the same silicate layer indicating a change in layer charge (white arrows in a, c, and d). (e–f) Lattice-fringe images of 0.6 eq/$O_{10}(OH)_2$ fluorohectorite show crystals with highly expanded silicate layers of between 23 and 26 Å. Some of these highly expanded sequences can contain 13–14 Å layers.

Table 3. List of *d* values of smectite-group mineral samples after treatment with *n*-alkylammonium cations obtained from XRD analyses and TEM lattice-fringe measurements. Column 3 shows the spacings obtained from XRD analyses. Columns 4 and 5 list spacings from TEM lattice-fringe measurements. Values in column 4 were obtained from samples that were treated with *n*-alkylammonium cations before embedding in epoxy resin and the preparation of ultrathin sections (method 1). Values in column 5 are from samples that were treated with *n*-alkylammonium cations after embedding in epoxy resin and the preparation of ultrathin sections (method 2). The cation-exchange procedure was performed on ultrathin sections on the TEM grids.

1	2	3	4	5	6
		XRD	TEM		
Sample	Layer charge	*n*-alkylammonium cation exchange †($n_C = 18$ for 5 days); ‡($n_C = 18$ for 20 min); §($n_C = 18$ for 2 days); *($n_C = 12$ for 2 days)	*n*-alkylammonium cation exchange (method 1)	*n*-alkylammonium cation exchange (method 2)	Reference (grain-size fraction)
	eq/$O_{10}(OH)_2$	d_{001}	d_{001}	d_{001}	
Smectite-group minerals					
Upton montmorillonite (A.P.I. No. 25)	0.36[1] 0.38[2]	17.58 Å†	Majority 21–25 Å† and 17–18 Å†; max. ~31 Å; a few 13–14 Å	13–14 Å	Present study (<0.1 µm)
		17.58 Å‡	Majority 21–26 Å‡; a few 13–14 Å‡; max. ~34 Å		
		17.80 Å§	20–30 Å§		(Vali, 1983; Vali and Köster, 1986) (<0.6 µm)
Otay montmorillonite (A.P.I. No. 24)	0.38–0.60[2] 0.62[3];	20.32 Å†	20–26 Å†	2 kinds of layers: 13–14 Å; 26–45 Å	Present study (<0.1 µm)
Chisholm montmorillonite (A.P.I No. 21)	0.36[1]	19.70 Å§	~20 Å§		(Vali and Köster, 1986) (<0.6 µm)
SWy-1 Na-montmorillonite	0.21–0.37[4]; 0.34[5]	17.70 Å*	20–48 Å*		(Malla *et al.*, 1993)
		16.51 Å*	15–16 Å*		(Klimentidis and Mackinnon, 1986) (<2.0 µm)
SAz-1 Ca-montmorillonite	0.31–0.49[4]	17.70 Å*	20–44 Å*		(Malla *et al.*, 1993)
Hectorite, Hector, California	0.31[6]	17.30 Å§	20–34 Å§		(Vali and Köster, 1986) (<0.6 µm)
Fluorohectorite, synthetic	0.40[7]			2 kinds of layers: 13–14 Å; 21–27 Å (max. 30 Å)	Present study

		— §(n_C = 18 for 2 days) —			
Fluorohectorite, synthetic	0.60^8			2 kinds of layers: majority 21–27 Å (max. 30 Å); a few 13-14 Å	this study
Smectite-group minerals (continued)		d_{001}	d_{001}	d_{001}	
Nontronite, Hundsangen	0.39^9, 0.36^{10}	22.00 Å§	22–25 Å§		(Vali and Köster, 1986) (<0.6 μm)
Nontronite SWa-1	0.50^{11} 0.54^{12}			20–28 Å	(Vali and Hesse, 1990)

[1] Vogt and Köster (1978); [2]Schultz (1969); [3]Hetzel and Doner (1993); [4]Malla and Douglas (1987a, 1987b); [5]Jaynes and Bigham (1987); [6]Ames *et al.* (1958); [7]Dr J. Breu (unpublished results); [8]Kalo *et al.* (2010); [9]Kerschreiter (1975); [10]Köster *et al.* (1999); [11]Bujdak *et al.* (1998); [12]Rozenson and Heller-Kallai (1976); (n_C = 18) = octadecylammonium cations; (n_C = 12) = dodecylammonium cations.

the treatment of ultrathin sections of Upton montmorillonite does not result in the large expansion of the silicate layers that was observed in lattice-fringe images of the same material treated with octadecylammonium cations before embedding and cutting (method 1). Lattice-fringe images showed thick sequences of 2:1 silicate layers with a uniform expansion of 13–14 Å (Figure 3a).

Lattice-fringe images of other smectite-group minerals such as Otay montmorillonite or synthetic fluorohectorite showed sequences of highly expanded 2:1 silicate layers (26–45 Å) and sequences with an expansion of 13–14 Å (Figures 4a–e, 5a–d; Table 3, column 5). Both layer types also occurred frequently within the same crystal in short alternating sequences that resemble rectorite-like structures (Figures 4b,d,e, 5c,d: white stars). Instead of containing non-expanded ~10 Å double layers as in rectorite, however, the double layers in the Otay montmorillonite and the fluorohectorite are silicate layers with a spacing of 13–14 Å.

What is the reason for these differences? Why did Upton montmorillonite only show sequences of 13–14 Å in lattice-fringe images while Otay montmorillonite showed both 13–14 Å and highly expanded structures of 26–45 Å? What caused the difference in the spacings obtained from XRD analyses and those measured in HRTEM lattice-fringe images?

The 13–14 Å silicate layers in lattice-fringe images (method 2)

A possible reason for the discrepancy between spacings obtained from XRD for Upton montmorillonite (17.58 Å) and those measured in lattice-fringe images (13–14 Å and 26–45 Å) was the different treatment methods (methods 1 and 2). The expansion behavior of smectite-group minerals in ultrathin sections treated with octadecylammonium cations depends essentially on the level of the layer charges. Based on XRD analyses, the transition from a monolayer (~13.6 Å) to a bilayer arrangement is achieved if the layer charge of the 2:1 layer silicate is $>0.24/O_{10}(OH)_2$ (Maes *et al.*, 1979).

Upton montmorillonite has an average interlayer charge of $0.36/O_{10}(OH)_2$ and the bilayer arrangement of octadecylammonium cations (17.58 Å) was achieved both in a 20 min and a 5-day exchange process for XRD samples (Table 2). The evaluation of the XRD patterns alone would suggest that the time period of the exchange treatment does not have an influence on the arrangement of octadecylammonium cations in the interlayer space. However, evaluation of the HRTEM lattice-fringe images of the sample treated for 20 min and for 5 days with octadecylammonium cations before the embedding (method 1) suggested that time did indeed play a role. Both samples showed the predominance of disrupted highly expanded sequences with 21 to 34 Å spacings that were originally 17–18 Å structures with bilayer arrangement before the intrusion of resin into the interlayer space during the embedding. The ‘20 min’ sample (method 1) also contains minor amounts of double layers and short sequences with an expansion of 13 to 14 Å (Figure 3b, Table 3).

The sample exchanged for 5 days (method 1), in addition to highly expanded sequences, also showed silicate layers with spacings of 17−18 Å and only very few silicate layers with expansions of 13−14 Å (Figure 3c,d). The silicate layers with spacings of 13−14 Å and 17−18 Å in both the ‘20 min’ and the ‘5 day’ samples did not experience additional intrusion of the embedding resin. The presence of the 13−14 Å layers in the lattice-fringe images of the ‘20 min’ sample suggests that the time of 20 min was not sufficiently long to completely form a bilayer arrangement in the very low-charge 2:1 silicate-layer sequences. However, a bilayer arrangement of the octadecylammonium cations in the lower-charge interlayers was achieved after a 5 day exchange period, which is shown by the 17−18 Å layers in the lattice-fringe images (Figure 3c,d). The minor amount of 13−14 Å layers that were still observable in lattice-fringe images of the ‘5 day’ sample probably originated from silicate layers with a charge of $<0.24/O_{10}(OH)_2$ as a transition from monolayer to bilayer is only achieved by charges $>0.24/O_{10}(OH)_2$ (Maes *et al.*, 1979).

The short time period of 20 min for the octadecylammonium cation-exchange treatment of ultrathin sections (method 2) of Upton montmorillonite could have been one reason why lattice-fringe images only showed sequences with a spacing of 13 to 14 Å (Figure 3a). The layer charges were simply not high enough to achieve greater expansion during the short exchange period. The possibility that a bilayer arrangement (17−18 Å) of the octadecylammonium cations could have been achieved if the exchange time for method 2 was extended to 5 days was tested. Large crystals of octadecylammonium salts form everywhere on the TEM copper grid during this long exchange time and cover the ultrathin sections of the clay minerals, however, which makes it impossible to investigate the layer structure in TEM. An intensive washing procedure with ethanol in order to remove the octadecylammonium salts as was done for the XRD sample materials was not an option because the ethanol would have destroyed the epoxy ultrathin sections that contain the clay minerals on the TEM grids. The gentle washing of the TEM grids with preheated distilled water (method 2) in a Petri dish works reasonably well for removing excess octadecylammonium solution from the surface of the ultrathin sections that were exchanged for 20 min but not for ultrathin sections on TEM grids that were exchanged for 5 days.

Exchange kinetics may play a role for samples prepared according to method 2 but the interlayer charges also have an influence on the expansion behavior. While Upton montmorillonite only shows sequences with 13–14 Å layers, Otay montmorillonite ultrathin sections treated with octadecylammonium cations (method 2) showed both highly expanded silicate layers (26−45 Å) and layers with spacings of 13−14 Å within the same crystal (Figure 4a−e). Otay montmorillonite is a smectite-group mineral with a heterogeneous interlayer charge distribution ranging between 0.38 and 0.62 $eq/O_{10}(OH)_2$ (Schultz, 1969; Hetzel and Doner, 1993). The occurrence of sequences that contain both layer types illustrates the presence of differently charged 2:1 silicate layers within the same crystal.

The same material treated with octadecylammonium cations before the resin impregnation, however, showed lattice-fringe images of highly expanded sequences of 2:1 silicate layers with spacings ranging from 20 to 26 Å (Figure 4f). No significant spacing differences (interlayer-charge heterogeneities), either laterally or in the stacking direction, were observed in Otay montmorillonite crystals prepared using method 1. The interlayer-charge heterogeneities that are revealed in lattice-fringe images from octadecylammonium cation-exchanged ultrathin sections (method 2) cannot be seen in these images (Figure 4a−e,f).

The lattice-fringe images from the different embedding and octadecylammonium cation treatment methods for the Upton and Otay montmorillonite as well as the data from Vali and Köster (1986) and Malla *et al.* (1993) confirmed that smectite-group minerals treated with *n*-alkylammonium cations before embedding in epoxy resin (method 1) will appear mainly as highly expanded sequences of 2:1 silicate layers, due to the additional incorporation of resin molecules into the interlayer space (Table 3, columns 2 and 4). The evaluation of such lattice-fringe images would, therefore, lead to an incorrect interpretation of the interlayer charge properties of members of this 2:1 layer silicate group, if the effects of sample treatment were not taken into consideration.

The highly expanded 2:1 silicate layers in lattice-fringe images (method 2)

The question that has to be answered next is the discrepancy between the relatively large expansions of 26−45 Å observed in lattice-fringe images of the Otay montmorillonite prepared according to method 2 and the spacing of 20.32 Å obtained from the XRD pattern (Table 2, Figure 4b−e; Table 3, columns 3, 5). The difference in the values can be explained by the different preparation techniques. In method 2, the clay minerals were embedded without pre-treatment (Figure 1) and therefore the intrusion of epoxy resin into the interlayer space of the Otay montmorillonite silicate layers sequences was less likely, which contrasts with the smectite-group minerals that were treated with octadecylammonium cations before embedding (method 1).

Observations by TEM showed that clay-mineral aggregates were engulfed by resin during the embedding process (method 2) and only some clay minerals on the outsides of the particles were affected by resin infiltration, not crystals in the interior parts of larger crystal aggregates. During the treatment procedure of the ultrathin sections on the TEM grids, the exchangeable inorganic interlayer cations are replaced by *n*-alkylammonium cations which expand the 2:1 clay-mineral structures according to their layer charges. After this exchange reaction, additional pairs of *n*-alkylammonium cations can enter the interlayer space and are held there through van der Waals interactions (Lee and Kim, 2002; He *et al.*, 2004). The gentle washing process of the TEM grid with the ultrathin sections in preheated distilled water did not completely remove all excess *n*-alkylammonium molecules from the interlayer space. The use of ethanol for the washing was not an option for carbon-coated TEM grids that contain ultrathin sections of clay minerals in Epon epoxy resin, because the ethanol would destroy the carbon film and the epoxy resin.

Additional incorporation of *n*-alkylammonium cations into the interlayers of 2:1 silicate layers holding a certain threshold interlayer charge could be a reasonable explanation for the observed high expansion. This conclusion was supported by a study of Lee and Kim (2002) who investigated the effect of different concentrations of hexadecyltrimethylammonium (HDTMA) solutions on the expansion behavior of smectite-group minerals. The XRD patterns of their study showed first-order reflections of 27.6 and 40.5 Å for smectite-group minerals treated with a 0.01 M HDTMA solution that had a concentration equivalent to 1.5–2.5 times the cation exchange capacity (CEC) of the sample (104.3 meq/100 g). Additional incorporation of HDTMA molecules in the interlayer space and subsequent expansion up to 40 Å occurs through hydrophobic bonding if the alkylammonium molecule concentration increases beyond the CEC of the material (figures 2a, 10d of Lee and Kim, 2002).

Otay montmorillonite has a CEC of 121.0 meq/100 g (Maes and Cremers, 1977). The octadecylammonium hydrochloride solution used in the present study had a concentration of 0.025 M. The highest concentration of HDTMA used by Lee and Kim (2002) was close to 0.01 M and caused interlayer expansions of >40 Å. This concentration was still 0.015 M less than the concentration of the octadecylammonium solution (0.025 M) used in the present study. In the light of these results, the high concentration of the exchange solution in the present study probably caused the additional incorporation of octadecylammonium molecules into the interlayer space, generating the highly expanded (26–45 Å) 2:1 silicate layers. The arrangement of the octadecylammonium cations in the interlayer space is not known. They may be aligned in a dense paraffin-like arrangement in double layers (Lagaly, 1981; He *et al.*, 2004) or in a less dense irregular paraffin-type configuration as proposed by Lee and Kim (2002) (Figure 6b,c).

The question now arises as to why the XRD pattern of the octadecylammonium cation-exchanged Otay montmorillonite did not show these large expansions that were described for the smectite-group minerals used in the study of Lee and Kim (2002)? The difference was due to the different washing procedures used by Lee and Kim and in the present study. Their samples were washed only once with distilled water, whereas the octadecylammonium cation-exchanged samples of this study were washed up to 20 times with 100% ethanol before XRD analyses with the purpose of removing the excess *n*-alkylammonium molecules. On the other side, the gentle washing procedure of the TEM grids with the ultrathin sections after the octadecylammonium exchange treatment (method 2) in preheated distilled water, as used in this study, was indeed comparable to the "one-time" washing procedure of Lee and Kim (2002). This, however, was not sufficient to remove all excess *n*-alkylammonium molecules from the interlayer space and led to the observed highly expanded 2:1 silicate layers.

These findings showed once again that the arrangement of the alkylammonium cations within the 2:1 layer silicate interlayers depends upon the magnitude of the layer charge, the charge density, the concentration of the exchange solution, and the washing procedure (Lagaly and Weiss, 1969, 1970c; Lagaly, 1981, 1994; Lee and Kim, 2002).

As little about the washing procedure of the TEM grids with the ultrathin sections in preheated distilled water can be changed, future studies should test whether the excess incorporation of alkylammonium cations into the interlayer space of clay minerals prepared according to method 2 could be prevented by using lower concentrations of octadecylammonium cation exchange solutions. The solutions that should be tested in future studies should have concentrations of 0.01 M, 0.005 M, 0.0025 M, and 0.0001 M or even lower. Ultrathin sections (microtome sections) of one higher-charge smectite-group mineral, *e.g.* Otay montmorillonite, should be treated with these exchange-solution concentrations according to method 2. Lattice-fringe images of these samples will then show how the interlayer spacing is influenced by the concentration of the octadecylammonium exchange solution.

At what interlayer-charge threshold does the additional incorporation of n-alkylammonium cations in the interlayer space of smectite-group minerals occur?

The average interlayer charge for Upton montmorillonite is 0.36 eq/$O_{10}(OH)_2$ (Table 3). Lattice-fringe images of this sample showed only thick sequences with spacings of 13–14 Å. In contrast, the interlayer charges for Otay montmorillonite range from 0.38 to 0.62 eq/$O_{10}(OH)_2$ which is reflected in the different spacings observed in the lattice-fringe images (Figure 4b–e, Table 3). The minimum charge of 0.38 eq/$O_{10}(OH)_2$ probably corresponded to the limit for the 13–14 Å expansion.

Synthetically produced fluorohectorite with known interlayer charges was chosen in order to estimate the charge at which smectite 2:1 silicate layers in ultrathin sections showed large expansions after the treatment with octadecylammonium cations. Lattice-fringe images of the 0.4 eq/$O_{10}(OH)_2$ fluorohectorite also showed crystals both with highly expanded (21−30 Å) and less expanded (13−14 Å) 2:1 silicate layers (Figure 5a,b). Numerous fluorohectorite (0.4 eq/$O_{10}(OH)_2$) crystals also have rectorite-like sequences with alternating highly expanded 2:1 silicate layers (21−27 Å) and 13−14 Å layers (Figure 5c,d). The occurrence of such rectorite-like sequences was assumed by Breu *et al.* (2001) in a synthetic fluorohectorite with an average interlayer charge of 0.5 eq/$O_{10}(OH)_2$. The XRD patterns of the fluorohectorite (0.5 eq/$O_{10}(OH)_2$) treated with *n*-alkylammonium cations suggest a certain amount of regular interstratification of an R1-ordered structure containing monolayers and bilayers of *n*-alkylammonium cations (figure 10 in Breu *et al.*, 2001).

The expansion behavior of the 0.4 eq/$O_{10}(OH)_2$ fluorohectorite crystallites suggested that not all crystals have the same interlayer-charge values. The charge values even differ within the same crystal, as shown by sequences containing both 13−14 Å and highly expanded 2:1 layers which are similar to the Otay montmorillonite. Therefore, the interlayer charge of 0.4 eq/$O_{10}(OH)_2$ for the fluorohectorite must be interpreted as an average value.

The proportion of highly expanded sequences of 2:1 silicate layers increases in lattice-fringe images of smectite-group minerals if the interlayer charge increases beyond 0.4 eq/$O_{10}(OH)_2$ as observed in images of the more highly charged fluorohectorite (0.6 eq/$O_{10}(OH)_2$). It showed crystals with highly expanded 2:1 silicate layers (Figure 5e, f). Some silicate layers with a monolayer arrangement (13−14 Å) also occurred within these sequences, but less frequently than in the lower-charge fluorohectorite (0.4 eq/$O_{10}(OH)_2$) (Figure 5f). These observations showed that even high-charge smectite-group minerals still contain some 2:1 silicate layers with low interlayer charges of <0.4 eq/$O_{10}(OH)_2$.

From the expansion behavior of the synthetic fluorohectorite, the Upton montmorillonite, and the

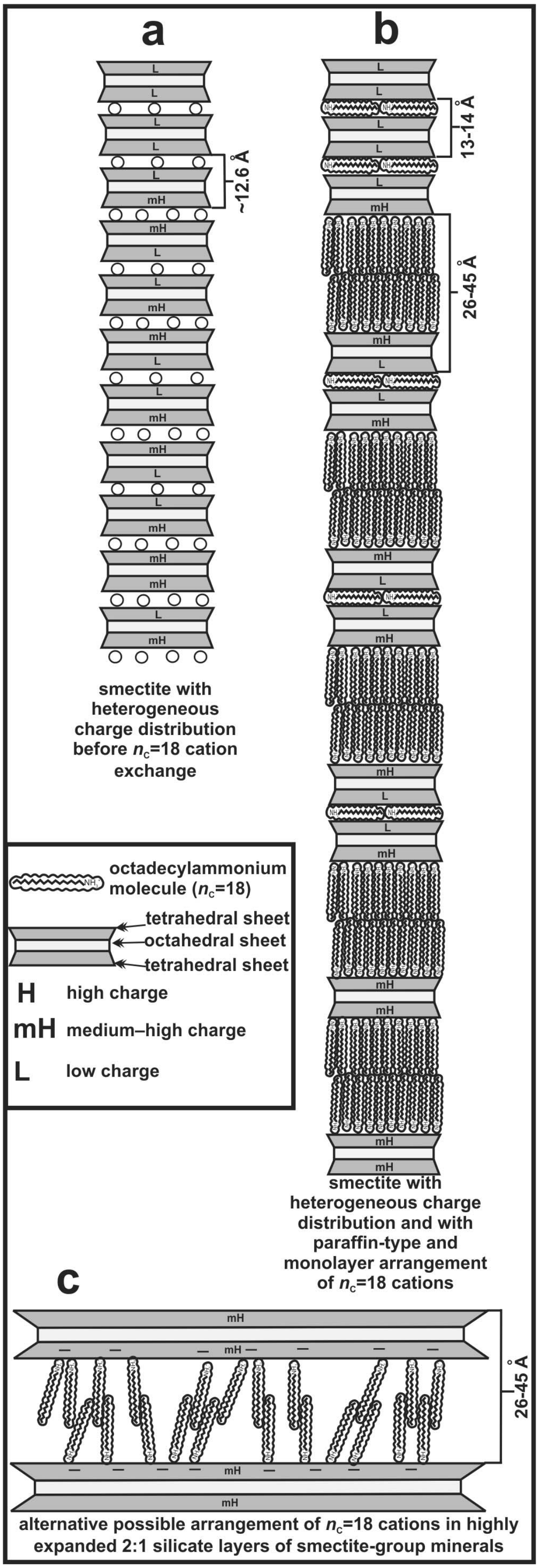

Figure 6. Models showing a smectite-group mineral with heterogeneous charge distribution before (a) and after (b) treatment with octadecylammonium cations (not to scale). This model illustrates the observations made in lattice-fringe images of Otay Montmorillonite and synthetic fluorohectorite (method 2). The 2:1 silicate layers with spacings of 13−14 Å are interpreted to have a monolayer arrangement of the octadecylammonium cations. The sequences with highly expanded 2:1 silicate layers can have a double-layer paraffin-like arrangement or may form some sort of irregular arrangement of the octadecylammonium cations as shown in model (c) (Lee and Kim, 2002). Diagrams (a) and (b) are modifications of original drawings by Lagaly and Weiss (1969, 1970a, 1970b, 1970c), Lagaly (1981), and Vali *et al.* (1994).

Otay montmorillonite, the critical interlayer charge at which the silicate layers become highly expanded 2:1 silicate layers in the ultrathin sections is probably ~0.40 eq/$O_{10}(OH)_2$ with a minimum value of 0.38 eq/$O_{10}(OH)_2$ which is the lower value of the interlayer-charge range of the Otay montmorillonite (Table 3).

The fact that the Upton montmorillonite consists of sequences of 13–14 Å silicate layers in lattice-fringe images suggests that the layer charges are below the threshold of 0.38–0.40 eq/$O_{10}(OH)_2$ in order to develop expansions as in Otay montmorillonite or fluorohectorite.

The treatment of smectite-group minerals with octadecylammonium cations after preparation of the ultrathin sections (method 2) not only prevented disintegration of the primary arrangement of layers and additional expansion from infiltration of resin into the alkylammonium-expanded interlayer space of 2:1 layer silicates as suggested by Sears *et al.* (1998), it also allowed the distinction between differently charged 2:1 silicate layers within the same crystal. This treatment method illustrated well the differences in interlayer charges from layer to layer within the crystals. It made charge heterogeneities visible that occur within the same 2:1 silicate layer (Figure 5c,d: white arrows).

Reference samples vs. sample AD-D50 2035 m

Lattice-fringe images of the octadecylammonium cation-exchanged <0.1 μm size fraction of sample AD-D50 (2035 m) showed expanded structures of smectite-group minerals that are similar to those observed in lattice-fringe images of Otay montmorillonite and the synthetic fluorohectorite. The sample contained both smectite crystals that have highly expanded 2:1 silicate layers (white diamonds) ranging from 22 to 27 Å (maximum values up to 33 Å) and short sequences of silicate layers with an expansion between 13 and 14 Å (white half circles, Figure 7a,b). Both layer types occurred within the same crystal in random distribution but could also be observed as short rectorite-like sequences (Figure 7b). Minor amounts of illite packets (I) with 3–6 non-expanded ~10 Å layers also occur between smectite-group minerals (Figure 7a).

The observations made in lattice-fringe images from Otay montmorillonite, the synthetic fluorohectorite, and the sample AD-D50 (2035 m) suggest that crystals of smectite-group minerals may have, like rectorite, polar 2:1 silicate layers (Lagaly, 1979; Ahn and Peacor, 1986; Güven, 1991; Vali *et al.*, 1994). In rectorite, one of the tetrahedral sheets in the 2:1 silicate layers has a low charge and one a high charge. The low-charge layers in rectorite have a beidellite-like composition. Beidellite is a dioctahedral smectite-group mineral in which the majority of the interlayer charges originate from the tetrahedral sheets due to isomorphous substitution of Si^{4+} by Al^{3+}. The interlayer charges in the dioctahedral smectite mineral, montmorillonite, however, originates mainly from isomorphous substitution of trivalent (Al^{3+}, Fe^{3+}) by divalent cations (Fe^{2+}, Mg^{2+}) in the octahedral sheet. This charge can increase by reduction of Fe^{3+} to Fe^{2+} or decrease by oxidation of Fe^{2+} to Fe^{3+}. The synthetic fluorohectorite is a trioctahedral smectite in which the charge originates from the octahedral sheet due to isomorphous substitution of Mg^{2+} by Li^{+}. The rectorite-like appearance of 2:1 silicate layers in lattice-fringe images of Otay montmorillonite and synthetic fluorohectorite is, therefore, probably due to the heterogeneity of the occupancy in the octahedral sheets which causes a dissymmetry of the charges on the basal surfaces (interlayers) of the 2:1 silicate layers.

The fact that smectite-group minerals show rectorite-like expansion behavior in lattice-fringe images is an important finding for the characterization of clay-mineral assemblages that were previously interpreted to contain mixed-layer illite-smectite clay minerals (*e.g.* Abid *et al.*, 2004).

Rectorite-like, R1-ordered I-S structures, for example, were described from lattice-fringe images in studies by Vali *et al.* (1993) (their figure 4a–c), Sears *et al.* (1998) (their figure 6b), and Sears (2001). A reevaluation of the lattice-fringe images from those studies in light of present findings concluded that many of those R1-ordered structures are in fact smectite-group crystals with short sequences of alternating low-charge and high-charge silicate layers rather than I-S phases with expanded smectite layers and non-expanded (10 Å) illite double layers. They are smectite crystals with charge heterogeneities in the tetrahedral or octahedral sheets that cause a rectorite-like expansion behavior.

SUMMARY AND CONCLUSIONS

Alkylammonium cation exchange on ultrathin sections of smectite-group minerals and their subsequent examination using HRTEM can reveal layer-to-layer charge heterogeneities within crystals or even within the same 2:1 silicate layer. The treatment of the ultrathin sections with octadecylammonium cations after embedding in epoxy resin (method 2) made charge-density heterogeneities visible that could not be observed if the samples were treated with octadecylammonium cations before embedding (method 1). Treatment of the smectite-group minerals with octadecylammonium cations before resin impregnation expanded the 2:1 silicate layers and facilitated the intrusion of embedding resin into the interlayer space. This led to additional expansion and layer-sequence disintegration. Such charge heterogeneities within single smectite crystals, revealed by HRTEM imaging of ultrathin sections (method 2), were not revealed in XRD patterns.

The treatment of smectite-group minerals with octadecylammonium cations after ultrathin-section preparation (method 2) prevented disintegration of the primary layer arrangement and the additional expansion

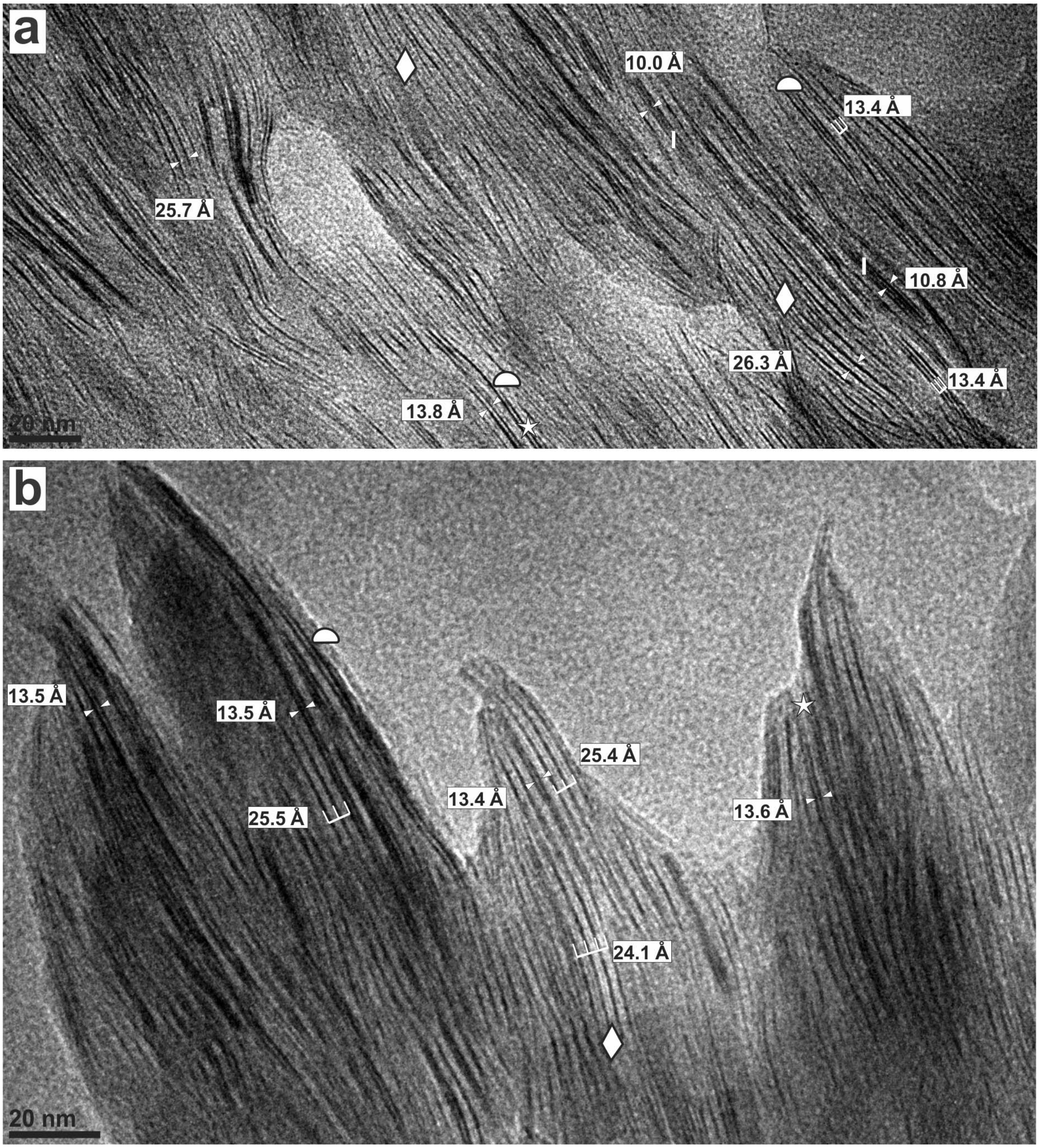

Figure 7. HRTEM lattice-fringe images of the octadecylammonium-exchanged <0.1 μm size fraction of sample AD D-50 (2035 m) showing smectite crystal aggregates with an expansion behavior that is similar to those observed in Otay montmorillonite and synthetic fluorohectorite. (a−b) Sequences of highly expanded (white diamonds) 2:1 silicate layers of smectite phases with 22−27 Å spacings. Sequences of low-charge smectite layers (13−14 Å) occur as separate phases or within high-charge smectite crystals (white half circles). Alternating low-charge and high-charge layers (white stars). Note the presence of minor amounts of authigenic illite (I) with spacings of 10−11 Å in image (a) that grow between the smectite-group mineral crystals.

due to resin infiltration into alkylammonium-expanded interlayers.

Smectite-group minerals with layer charges <0.38 eq/$O_{10}(OH)_2$ had spacings of 13−14 Å in lattice-fringe images, while silicate layers with >0.38 eq/$O_{10}(OH)_2$ showed spacings between 26 and 45 Å. Smectite crystals can also contain short sequences of highly-expanded (higher-charge) silicate layers that alternate with 13−14 Å silicate layers (lower charge) and resemble rectorite-like structures. This demonstrates that smectite-group minerals, similar to rectorite, may have alternating low- and high-charge 2:1 silicate layers. This finding is important for a correct interpretation of lattice-fringe images of clay-mineral assemblages that were previously thought to contain mixed-layer illite-smectite minerals.

Knowledge of the expansion behavior of 2:1 layer silicates, such as smectite-group minerals with a range of layer charge, can be used to distinguish the minerals in the clay-mineral assemblages from argillaceous rocks of sedimentary basins, soils, or in hydrothermal alteration zones. For example, smaller crystallites of vermiculite with no non-expanded and only highly expanded silicate layers are difficult to differentiate in clay-mineral assemblages from high-charge smectite-group minerals due to their similarity in lattice-fringe images. However, high-charge smectite-group crystals might also contain lower-charge 2:1 silicate layers due to charge heterogeneities. Thus, the existence of 13−14 Å layers within a highly expanded 2:1 silicate layer sequence indicates a high-charge smectite-group mineral with some low-charge layers. In contrast, unexpanded 2:1 silicate layers in vermiculite crystals with 9.3−10.5 Å spacings can be distinguished easily from the 13−14 Å layers that can occur in high-charge smectite-group minerals.

The results of this study also suggest that the discrepancies between *d* values measured in lattice-fringe images and those obtained from XRD analyses are related to HRTEM and XRD sample-preparation methods. Highly-expanded 2:1 silicate layers observed in lattice-fringe images of high-charge smectite-group minerals are caused by additional *n*-alkylammonium cations incorporated into the interlayers.

REFERENCES

Abid, I.A., Hesse, R., and Harper, J.D. (2004) Variations in mixed-layer illite/smectite diagenesis in the rift and post-rift sediments of the Jeanne d'Arc Basin, Grand Banks offshore Newfoundland, Canada. *Canadian Journal of Earth Sciences*, **41**, 401−429.

Ahn, J.H. and Peacor, D.R. (1986) Transmission electron-microscope data for rectorite − Implication for the origin and structure of fundamental particles. *Clays and Clay Minerals*, **34**, 180−186.

Breu, J., Seidl, W., Stoll, A.J., Lange, K.G., and Probst, T.U. (2001) Charge homogeneity in synthetic fluorohectorite. *Chemistry of Materials*, **13**, 4213−4220.

Brindley, G.W. (1966) Ethylene glycol and glycerol complexes of smectites and vermiculites. *Clays and Clay Minerals*, **6**, 237−260.

Cetin, K. and Huff, W.D. (1995) Characterization of untreated and alkylammonium ion-exchanged illite/smectite by high-resolution transmission electron-microscopy. *Clays and Clay Minerals*, **43**, 337−345.

C-NLOPB Schedule of Wells (2007) Well 44, Adolphus D-50, http://www.cnlopb.ca/well_alpha.shtml (accessed 24 June 2013)

Eberhart, J.P. and Triki, R. (1972) Method for obtaining thin sections of clay-minerals − Application to investigation of mixed-layer clay-minerals. *Journal of Microscopy*, **15**, 111−120.

Elsass, F., Chenu, C. and Tessier, D. (2008) Transmission electron microscopy for soil samples: preparation methods and use. Pp. 235−267 in: *Methods of Soil Analysis. Part 5. Mineralogical Methods* (A.L. Ulery and L.R. Drees, editors). Soil Science Society of America, Madison, Wisconsin, USA.

Ghabru, S.K., Mermut, A.R., and Starnaud, R.J. (1989) Layer-charge and cation-exchange characteristics of vermiculite (weathered biotite) isolated from a Gray Luvisol in northeastern Saskatchewan. *Clays and Clay Minerals*, **37**, 164−172.

Graf von Reichenbach, H.G., Wachsmuth, H., and Marcks, C. (1988) Observations at the mica-vermiculite interface with HRTEM. *Colloid and Polymer Science*, **266**, 652−656.

Güven, N. (1991) On a definition of illite/smectite mixed-layer. *Clays and Clay Minerals*, **39**, 661−662.

He, H., Frost, R.L., Deng, F., Zhu, J., Wen, X., and Yuan, P. (2004) Conformation of surfactant molecules in the interlayer of montmorillonite studied by ^{13}C MAS NMR. *Clays and Clay Minerals*, **52**, 350−356.

Hetzel, F. and Doner, H.E. (1993) Some colloidal properties of beidellite − comparison with low and high charge montmorillonites. *Clays and Clay Minerals*, **41**, 453−460.

Lagaly, G. (1979) Layer charge of regular interstratified 2:1 clay minerals. *Clays and Clay Minerals*, **27**, 1−10.

Lagaly, G. (1981) Characterization of clays by organic-compounds. *Clay Minerals*, **16**, 1−21.

Lagaly, G. (1982) Layer charge heterogeneity in vermiculites. *Clays and Clay Minerals*, **30**, 215−222.

Lagaly, G. (1994) Layer charge determination by alkylammonium ions. Pp. 1−46 in: *Layer Charge Characteristics of 2:1 Clay Minerals* (A. Mermut, editor). CMS Workshop Lectures, **6**, The Clay Minerals Society, Boulder, Colorado, USA.

Lagaly, G. and Dekany, I. (2005) Adsorption on hydrophobized surfaces: Clusters and self-organization. *Advances in Colloid and Interface Science*, **114**, 189−204.

Lagaly, G. and Weiss, A. (1969) Determination of layer charge in mica-type layer silicates. *Proceedings of the International Clay Conference*, **1**, 61−80.

Lagaly, G. and Weiss, A. (1970a) Inhomogeneous charge distribution in mica-type layer silicates. Pp. 179−187 in: *Reunión Hispano-Belga de Minerales de la Arcilla* (L. Heller, editor). Consejo Cuperior de Investigaciones Cientificas, Madrid.

Lagaly, G. and Weiss, A. (1970b) Arrangement and orientation of cationic surfactants on plane silicate surfaces. 1. Preparation of normal-alkylammonium derivates of mica type laminated silicates. *Kolloid-Zeitschrift und Zeitschrift für Polymere*, **237**, 266−273.

Lagaly, G. and Weiss, A. (1970c) Arrangement and orientation of cationic tensides on silicate surfaces. 3. Paraffin-like structures in alkylammonium layer silicates with an average layer load (vermiculite). *Kolloid-Zeitschrift und Zeitschrift für Polymere*, **238**, 485−493.

Lagaly, G. and Weiss, A. (1971) Anordnung und Orientierung kationischer Tenside auf Silikatoberflächen 4. Anordnung von *n*-Alkylammoniumionen bei niedrig geladenen Schichtsilikaten. *Kolloid-Zeitschrift und Zeitschrift für Polymere*, **243**, 48−55.

Laird, D. and Fleming, P. (2008) Analysis of layer charge, cation and anion exchange capacities, and synthesis of reduced charge clays. Pp. 485−509 in: *Methods of Soil Analysis. Part 5. Mineralogical Methods* (A.L. Ulery and L.R. Drees, editors). Soil Science Society of America, Madison, Wisconsin, USA.

Laird, D.A. and Nater, E.A. (1993) Nature of illitic phase associated with randomly interstratified smectite illite in soils. *Clays and Clay Minerals*, **41**, 280−287.

Laird, D.A., Scott, A.D., and Fenton, T.E. (1989a) Evaluation of the alkylammonium method of determining layer charge. *Clays and Clay Minerals*, **37**, 41−46.

Laird, D.A., Thompson, M.L., and Scott, A.D. (1989b) Technique for transmission electron-microscopy and X-ray-powder diffraction analyses of the same clay mineral specimen. *Clays and Clay Minerals*, **37**, 280–282.

Lee, S.Y. and Kim, S.J. (2002) Expansion of smectite by hexadecyltrimethylammonium. *Clays and Clay Minerals*, **50**, 435–445.

Lee, B.D., Sears, S.K., Graham, R.C., Amrhein, C., and Vali, H. (2003) Secondary mineral genesis from chlorite and serpentine in an ultramafic soil toposequence. *Soil Science Society of America Journal*, **67**, 1309–1317.

Lee, S.Y., Jackson, M.L., and Brown, J.L. (1975) Micaceous occlusions in kaolinite observed by ultramicrotomy and high-resolution electron-microscopy. *Clays and Clay Minerals*, **23**, 125–129.

MacEwan, D.M.C. (1944) Identification of the montmorillonite group of minerals by X-rays. *Nature*, **154**, 577–578.

Maes, A. and Cremers, A. (1977) Charge-density effects in ion-exchange. 1. Heterovalent exchange equilibria. *Journal of the Chemical Society – Faraday Transactions I*, **73**, 1807–1814.

Maes, A., Stul, M.S., and Cremers, A. (1979) Layer charge-cation-exchange capacity relationships in montmorillonite. *Clays and Clay Minerals*, **27**, 387–392.

Malikova, N., Cadene, A., Dubois, E., Marry, V., Durand-Vidal, S., Turq, P., Breu, J., Longeville, S., and Zanotti, J.M. (2007) Water diffusion in a synthetic hectorite clay studied by quasi-elastic neutron scattering. *Journal of Physical Chemistry C*, **111**, 17603–17611.

Malla, P.B. and Douglas, L.A. (1987) Identification of expanding layer silicates: layer charge vs. expansion properties. International Clay Conference, Denver, The Clay Minerals Society, Bloomington, Indiana, pp. 277–283.

Malla, P.B., Robert, M., Douglas, L.A., Tessier, D., and Komarneni, S (1993) Charge heterogeneity and nanostructure of 2:1 layer silicates by high-resolution transmission electron-microscopy. *Clays and Clay Minerals*, **41**, 412–422.

Mermut, A.R. (1994) Problems associated with layer charge characterization of 2:1 phyllosilicates. Pp. 106–122 in: *Layer Charge Characteristics of 2:1 Clay Minerals* (A. Mermut, editor). CMS Workshop Lectures, **6**, The Clay Minerals Society, Boulder, Colorado, USA.

Olis, A.C., Malla, P.B., and Douglas, L.A. (1990) The rapid estimation of layer charges of 2:1 expanding clays from a single alkylammonium ion expansion. *Clay Minerals*, **25**, 39–50.

Rühlicke, G. and Kohler, E.E. (1981) A simplified procedure for determining layer charge by the *n*-alkylammonium method. *Clay Minerals*, **16**, 305–307.

Schultz, L.G. (1969) Lithium and potassium absorption, dehydroxylation temperature, and structural water content of aluminous smectites. *Clays and Clay Minerals*, **17**, 115–149.

Sears, S.K. (2001) The study of crystal structure in the evolution of interstratified 2:1 clay minerals, Reindeer D-27 well, Mackenzie Delta – Beaufort Sea region, Arctic Canada. PhD thesis, McGill University, Montreal, Canada, 271 pp.

Sears, S.K., Hesse, R., and Vali, H. (1998) Significance of n-alkylammonium exchange in the study of 2:1 clay mineral diagenesis, Mackenzie Delta Beaufort Sea region, Arctic Canada. *The Canadian Mineralogist*, **36**, 1485–1506.

Shata, S., Hesse, R., Martin, R.F., and Vali, H. (2003) Expandability of anchizonal illite and chlorite: Significance for crystallinity development in the transition from diagenesis to metamorphism. *American Mineralogist*, **88**, 748–762.

Sinclair, I.K. (1988) Evolution of Mesozoic–Cenozoic sedimentary basins in the Grand Banks area of Newfoundland and comparison with Falvey's (1974) rift model. *Bulletin of Canadian Petroleum Geology*, **36**, 255–273.

Stanjek, H. and Friedrich, R. (1986) The determination of layer charge by curve-fitting of Lorentz- and polarization-corrected X-ray diagrams. *Clay Minerals*, **21**, 183–190.

Stul, M.S. and Mortier, W.J. (1974) The heterogeneity of the charge density in montmorillonites. *Clays and Clay Minerals*, **22**, 391–396.

Vali, H. (1983) Vergleichende elektronenoptische und röntgenographische Untersuchungen zur Kristallstruktur und Morphologie von quellfühigen und nicht quellenden 2:1-Schichtsilikaten. PhD, Technische Universität München, Germany, 94 pp.

Vali, H. and Hesse, R. (1990) Alkylammonium ion treatment of clay minerals in ultrathin sections – A new method for HRTEM examination of expandable layers. *American Mineralogist*, **75**, 1443–1446.

Vali, H. and Hesse, R. (1992) Identification of vermiculite by transmission electron microscopy and X-ray diffraction. *Clay Minerals*, **27**, 185–192.

Vali, H. and Köster, H.M. (1986) Expanding behavior, structural disorder, regular and random irregular interstratification of 2:1 layer silicates studied by high-resolution images of transmisson electron microscopy. *Clay Minerals*, **21**, 827–859.

Vali, H., Hesse, R., and Kohler, E.E. (1991) Combined freeze-etch replicas and HRTEM images as tools to study fundamental particles and the multiphase nature of 2:1 layer silicates. *American Mineralogist*, **76**, 1973–1984.

Vali, H., Martin, R.F., Amarantidis, G., and Morteani, G. (1993) Smectite-group minerals in deep-sea sediments – Monomineralic solid-solutions or multiphase mixtures? *American Mineralogist*, **78**, 1217–1229.

Vali, H., Hesse, R., and Martin, R.F. (1994) A TEM-based definition of 2:1 layer silicates and their interstratified constituents. *American Mineralogist*, **79**, 644–653.

Vogt, K. and Köster, H.M. (1978) Mineralogy, crystallography and geochemistry of some montmorillonites from bentonites. *Clay Minerals*, **13**, 25–43.

(*Received 24 July 2013; revised 27 September 2014; Ms. 792; AE: P.B. Malla*)

Clays and Clay Minerals, Vol. 62, No. 4, 354–355, 2014.

BOOK REVIEWS

Spectroscopic Methods in Mineralogy and Materials Sciences. Grant S. Henderson, Daniel R. Neuville, and Robert T. Downs, editors. Reviews in Mineralogy and Geochemistry v. **78**, Mineralogical Society of America and the Geochemical Society, Chantilly, VA, ISBN 978-0-939950-84-3. Price: $50.

Spectroscopic analysis is a powerful tool for analyzing the composition and structure of materials. Some spectroscopic methods, such as powder X-ray diffractometry, are widely used in the earth sciences, whereas others are more specialized and their use is confined to a smaller number of laboratories. An understanding of spectroscopic methods is critical to 21st century researchers in mineralogy, petrology, geochemistry, and related fields, as they produce most of the data underpinning the current understanding of geomaterials.

The application of various spectroscopic methods to geologic materials was previously covered in volume 18 of 'Reviews in Mineralogy and Geochemistry' (RiMG), published in 1988. The underlying theory has not changed in the 26 intervening years, and the older volume can still be consulted profitably for that information; however, the practical use of many techniques has changed dramatically since that time. Technological advances in instrumentation have improved the reliability, reproducibility, resolution, and detection limits of many techniques, while improvements in computer equipment and control software have increased ease of use and of data collection, storage, analysis, and sharing. The increased availability of very bright synchrotron radiation sources has expanded the sensitivity of established techniques such as infrared spectroscopy and X-ray diffractometry, and has permitted *in situ* monitoring of experiments in real time. Newer analytical methods have also been adopted profitably for application to earth materials. The intention of this new RiMG volume is to present both updated information on techniques covered in the previous volume, and descriptions of newer techniques that are not currently as well known. This is a massive undertaking, and the editors are to be commended for producing such a valuable work for earth scientists.

The 19 chapters in this book cover X-ray diffractometry, X-ray absorption fine structure and near-edge spectroscopy, X-ray photoelectron spectroscopy, Fourier transform infrared spectroscopy, nuclear magnetic resonance spectroscopy, electron paramagnetic resonance spectroscopy, optical spectroscopy, Brillouin scattering, Raman and X-ray Raman, and luminescence spectroscopy. Additional chapters discuss remote sensing spectroscopic techniques, transmission electron and atomic force microscopy, sampling errors, theoretical modeling, and *in situ* spectroscopy of high-pressure and high-temperature experiments. Many of the chapters discuss techniques that were also covered in the previous volume, and these focus mostly on developments since that time, but all chapters provide at least some theoretical background.

One particular factor that has changed dramatically since 1988 is the wide availability of powerful computing resources and of specialized software for data processing, theoretical modeling, and the management of very large datasets (*i.e.* datacubes). This has expanded tremendously the capability to make full use of modern analytical instruments and the torrents of data they often produce. It has also allowed the development of advanced computational modeling techniques such as those discussed in depth by Jahn and Kowalski in chapter 17 of this volume, and more briefly in other chapters.

Researchers familiar with the techniques described in various chapters will find them to be excellent resources for training students. The great usefulness of most of the chapters in this book is that they include not only good descriptions of the theoretical principles underlying the techniques and their specific usefulness, with examples of recent applications to geologically interesting problems, but also valuable practical tips from experienced users on how to obtain the best results. The chapters on techniques with which this reviewer is familiar with are clearly written and very readable, particularly the chapter by Newville on Fundamentals of XAFS and that by Henderson, de Groot, and Moulton on XANES. Among the many other well written and informative chapters in this book, chapter 12 by Hofmeister may be of the greatest general value in training students to use laboratory analytical techniques. It discusses the various sources of error in infrared and ultraviolet spectroscopic measurements and how they must be considered in different applications, with several specific examples of past issues and how they have been or might be resolved. Even when IR or UV spectroscopy are not specifically being used, this chapter should be tremendously useful reading for those students who tend to think of a laboratory instrument as a magical box that tells only perfect truth.

The book is generally well edited, and although certain chapters suffer from more typographical errors than others, there are few for such a large volume. As of this writing, one erratum is posted on the Mineralogical Society of America website, a correction to Figure 14 in chapter 13 (Advances in Raman Spectroscopy).

This book will be very valuable to the student who needs to learn new techniques, to the researcher who may wish to understand more about unfamiliar methods, and to anyone training new users of these techniques. It will be an excellent companion volume to RiMG v. 18, and deserves a place in the row of white volumes on the shelf of every geochemist, petrologist, and mineralogist.

LESLIE BAKER
University of Idaho

The Geochemistry of Geologic CO_2 Sequestration. Reviews in Mineralogy and Geochemistry v. **77**, Mineralogical Society of America and the Geochemical Society, Chantilly, VA, ISBN 978-0-939950-92-8. Price: $40.

If we continue our business-as-usual greenhouse emissions, our species will need to sequester (*i.e.* prevent from reaching the atmosphere) trillions of tons of carbon dioxide over the next 100 years if we are to avoid dangerous climate change. *The Geochemistry of Geologic CO_2 Sequestration* collects together the underpinning science of CO_2 storage in underground rock formations in 15 chapters. As you might expect from the RiMG series, this volume focuses on the molecular and pore-scale processes occurring in a CO_2 reservoir. One hundred pages were dedicated to a comprehensive review of the kinetic and thermodynamic properties of CO_2–H_2O–mineral interaction in high-pressure systems (chapters 3, 4, and 5). Chapter 3 is a formidable review of carbonate mineral thermodynamics in which citations from the 1970s (*e.g.* the classic work of Robie and Hemingway) are interspersed with recent work on more exotic carbonate minerals. Chapter 3 is an excellent summary of brine–CO_2 interaction, which is a critical factor in evaluating the storage capacity of a reservoir, but which lacks fundamental experimental data.

This leads neatly to the state-of-the-art geochemical modeling currently employed to describe these environments, and attempts to connect the pore-scale processes (chapter 8), with the larger-scale rheology of a CO_2 storage formation (chapter 12). A contribution by Bickel *et al*. (chapter 2) presents some of the natural analogs of underground CO_2 storage, including methods of monitoring and quantifying leakage from these systems. Power *et al*. (chapter 9) present a summary of carbon mineralization, an alternative pathway to sequestration involving the chemical transformation of CO_2 into carbonate minerals.

The widespread acceptance of underground carbon sequestration for climate change mitigation is presently held back by uncertainties in the capacity and longevity of the storage reservoirs. While this book discusses contemporary investigations of these, including a section on cap-rock fracture (chapter 13), the natural examples of leaking CO_2-rich aquifers (chapter 2), and the relative and time-dependent contribution of physical and chemical trapping (throughout), there are no overarching conclusions or normative statements that might decrease this uncertainty. These uncertainties, of course, can only be resolved by reservoir-specific studies, and it is probably too much to ask of this volume. I would encourage anyone with interests in CO_2 sequestration to acquire a copy of this book as it is likely that CO_2 reservoir engineers of the future will call heavily upon it as a standard reference text.

PHIL RENFORTH
Cardiff University, UK